



LUND UNIVERSITY

Identified Hadron Production as a Function of Event Multiplicity and Transverse Sphericity in pp Collisions at $\sqrt{s} = 7$ and 13 TeV with the ALICE Detector

Vislavicius, Vytautas

2018

Document Version:

Publisher's PDF, also known as Version of record

[Link to publication](#)

Citation for published version (APA):

Vislavicius, V. (2018). *Identified Hadron Production as a Function of Event Multiplicity and Transverse Sphericity in pp Collisions at $\sqrt{s} = 7$ and 13 TeV with the ALICE Detector*. Lund University, Faculty of Science, Department of Physics.

Total number of authors:

1

General rights

Unless other specific re-use rights are stated the following general rights apply:

Copyright and moral rights for the publications made accessible in the public portal are retained by the authors and/or other copyright owners and it is a condition of accessing publications that users recognise and abide by the legal requirements associated with these rights.

- Users may download and print one copy of any publication from the public portal for the purpose of private study or research.
- You may not further distribute the material or use it for any profit-making activity or commercial gain
- You may freely distribute the URL identifying the publication in the public portal

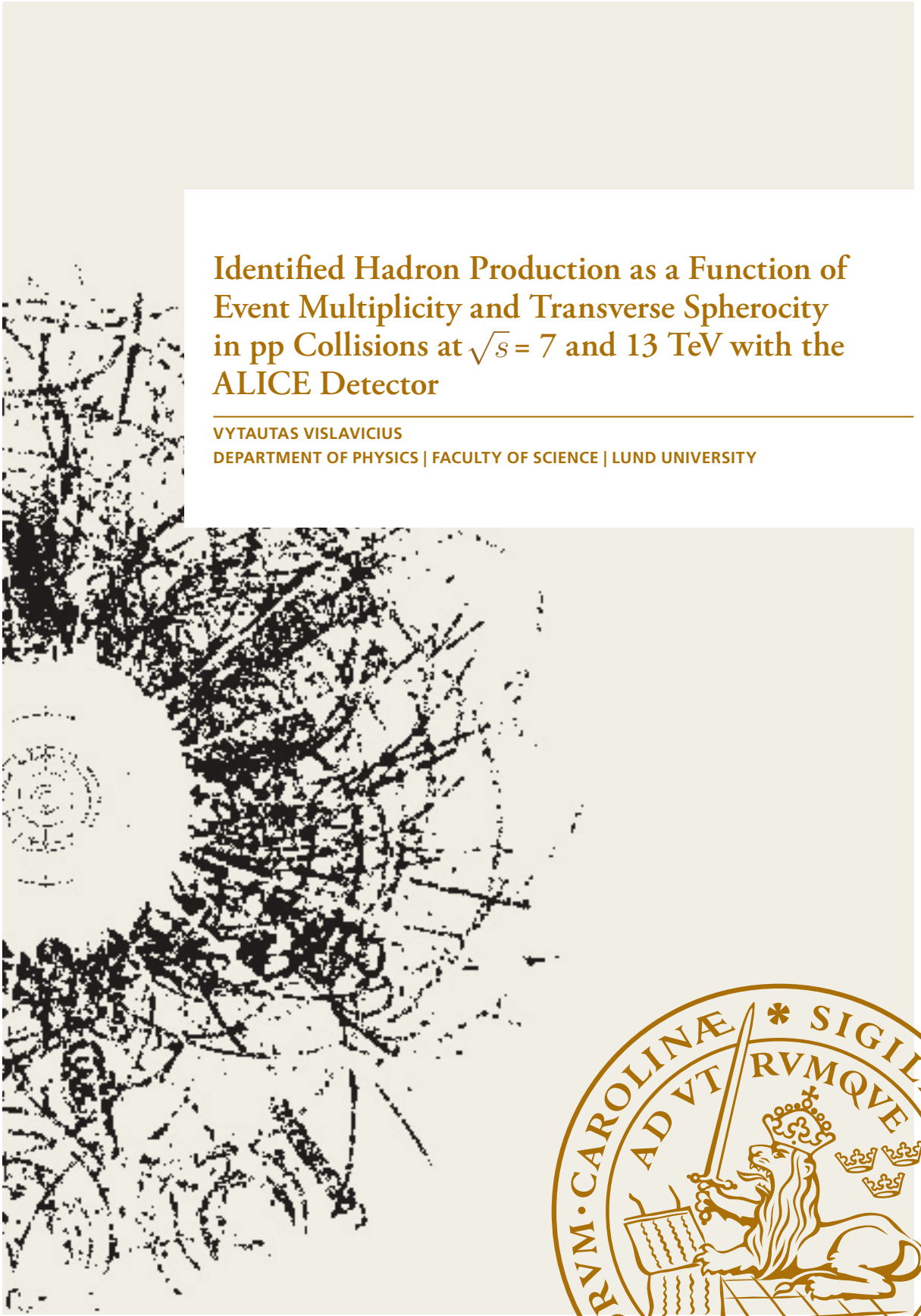
Read more about Creative commons licenses: <https://creativecommons.org/licenses/>

Take down policy

If you believe that this document breaches copyright please contact us providing details, and we will remove access to the work immediately and investigate your claim.

LUND UNIVERSITY

PO Box 117
221 00 Lund
+46 46-222 00 00

A large, complex visualization of a particle collision event, likely from the ALICE detector. It shows a dense network of black lines representing particle tracks, with a central bright yellow and orange region indicating the collision point. The tracks radiate outwards, forming a complex web of connections. The background is a light beige color.

Identified Hadron Production as a Function of Event Multiplicity and Transverse Sphericity in pp Collisions at $\sqrt{s} = 7$ and 13 TeV with the ALICE Detector

VYTAUTAS VISLAVICIUS

DEPARTMENT OF PHYSICS | FACULTY OF SCIENCE | LUND UNIVERSITY



Identified Hadron Production as a Function of Event Multiplicity and Transverse Spherocity in pp Collisions at $\sqrt{s} = 7$ and 13 TeV with the ALICE Detector


by Vytautas Vislavicius



LUND
UNIVERSITY

Thesis for the degree of Doctor of Philosophy
Faculty opponent: Prof. Thomas Hemmick

To be presented, with the permission of the Faculty of Science of Lund University, for
public criticism in the Rydberg lecture hall (Rydbergsalen) at the Department of
Physics on Friday, the 23rd of March 2018 at 13:00.

Organization LUND UNIVERSITY Department of Physics Box 118 SE-221 00 LUND Sweden		Document name DOCTORAL DISSERTATION	
Author(s) Vytautas Vislavicius		Date of disputation 2018-03-23	
		Sponsoring organization	
Title Identified Hadron Production as a Function of Event Multiplicity and Transverse Sphericity in pp Collisions at $\sqrt{s} = 7$ and 13 TeV with the ALICE Detector			
Abstract This study reports on identified hadron production as a function of event multiplicity ($\langle dN_{\text{ch}}/d\eta \rangle$) and transverse sphericity (S_0) in proton-proton collisions at $\sqrt{s} = 7$ and 13 TeV measured with the ALICE detector at the LHC. The particle spectra and their ratios measured in high-multiplicity events show signatures of an expanding medium. Integrated particle yields as a function of multiplicity measured in pp collisions at $\sqrt{s} = 7$ and 13 TeV are compared to those measured in p-Pb and Pb-Pb collisions. Hadrochemical composition of particles are found to be similar in different colliding systems under different \sqrt{s} , provided similar multiplicities are compared. This suggests that hadron yields are dominantly driven by $\langle dN_{\text{ch}}/d\eta \rangle$, and not the colliding system or center-of-mass energy. On the other hand, particle spectra measured in pp collisions at $\sqrt{s} = 13$ TeV is harder than that at 7 TeV, when similar $\langle dN_{\text{ch}}/d\eta \rangle$ are compared. In addition, hadron production as a function of multiplicity is studied in the context of statistical, hydrodynamical and pQCD-inspired models. In order to disentangle the soft QCD component from the hard, high-multiplicity pp collisions at $\sqrt{s} = 13$ TeV are studied as a function of transverse sphericity. It is found that the amount of flow-like effects in the data sample can be controlled using event shape observables.			
Key words LHC, ALICE, small systems, QGP, collectivity, multiplicity, sphericity, event shapes, pp collisions			
Classification system and/or index terms (if any)			
Supplementary bibliographical information		Language English	
ISSN and key title		ISBN 978-91-7753-596-6 (print) 978-91-7753-597-3 (pdf)	
Recipient's notes		Number of pages 219	Price
		Security classification	
I, the undersigned, being the copyright owner of the abstract of the above-mentioned dissertation, hereby grant to all reference sources the permission to publish and disseminate the abstract of the above-mentioned dissertation.			
Signature 		Date 2018-02-12	

Identified Hadron Production as a
Function of Event Multiplicity and
Transverse Spherocity in pp
Collisions at $\sqrt{s} = 7$ and 13 TeV
with the ALICE Detector

by Vytautas Vislavicius



LUND
UNIVERSITY

Cover illustration front: an event display from a proton-lead collision measured by the ALICE detector. Original image credits: CERN.

© Vytautas Vislavicius 2018

Faculty of Science, Department of Physics

ISBN: 978-91-7753-596-6 (print)

ISBN: 978-91-7753-597-3 (pdf)

Printed in Sweden by Media-Tryck, Lund University, Lund 2018



ABSTRACT

This study reports on identified hadron production as a function of event multiplicity ($\langle dN_{\text{ch}}/d\eta \rangle$) and transverse sphericity (S_{O}) in proton-proton collisions at $\sqrt{s} = 7$ and 13 TeV measured with the ALICE detector at the LHC. The particle spectra and their ratios measured in high-multiplicity events show signatures of an expanding medium. Integrated particle yields as a function of multiplicity measured in pp collisions at $\sqrt{s} = 7$ and 13 TeV are compared to those measured in p-Pb and Pb-Pb collisions. Hadrochemical composition of particles are found to be similar in different colliding systems under different \sqrt{s} , provided similar multiplicities are compared. This suggests that hadron yields are dominantly driven by $\langle dN_{\text{ch}}/d\eta \rangle$, and not the colliding system or center-of-mass energy. On the other hand, particle spectra measured in pp collisions at $\sqrt{s} = 13$ TeV is harder than that at 7 TeV, when similar $\langle dN_{\text{ch}}/d\eta \rangle$ are compared. In addition, hadron production as a function of multiplicity is studied in the context of statistical, hydrodynamical and pQCD-inspired models. In order to disentangle the soft QCD component from the hard, high-multiplicity pp collisions at $\sqrt{s} = 13$ TeV are studied as a function of transverse sphericity. It is found that the amount of flow-like effects in the data sample can be controlled using event shape observables.

POPULÄRVETENSKAPLIG SAMMANFATTNING

Över 30 år av forskning inom tungjonsfysik, Quantum ChromoDynamics (QCD) och kosmologi har etablerat vår nuvarande syn på universums tidigare stadie: kort efter Big Bang var universum fyllt av ett mycket hett och kompakt medium bestående av fria kvarkar och gluoner, den så kallade Kvarkgluon plasman (Quark–Gluon Plasma, QGP). Detta medium expanderade snabbt, och kyldes ner tills beståndsdelarnas växelverkan blev så stark att de individuella kvarkarna bands samman till hadroner. Efter ytterligare expansion kombinerades hadronerna till elektriskt laddade atomkärnor, vilka så småningom formade atomer genom att koppla ihop sig med elektroner. Idag lever vi i en värld där den förhistoriska kvarkgluonplasman har hadroniserats.

Att studera kvarkgluonplasmans utveckling är ett viktigt steg i att förstå universum. Den enda nu förväntade naturligt förekommande kvarkgluonplasman finns djupt inne kärnan hos neutronstjärnor, och de är inte åtkomliga med dagens verktyg. Vi kan istället skapa droppar av QGP i *små bangs* genom att kollidera tunga atomkärnor vid relativistiska energier. Detta har gjorts i flera decennier, och resulterat i ett flertal etablerade teorimodeller – även om hela teorin om allt som sker i kollisioner mellan tunga joner är långt ifrån fullständig.

Hittills har man trott att energitätheten som krävs för att producera QGP endast kan möjliggöras genom tungjonskollisioner. Detta paradigm har ifrågasatts efter att nyligen ha observerat QGP-liknande signaturer i kollisioner av proton-bly-kärnor (p-Pb). Upptäckten av de nya signalerna i det mindre kollisionssystemet leder till den naturliga frågan om ännu mindre system, såsom proton-proton-kollisioner (pp), också genererar likartade QGP-karaktäristiska signaler. I den här avhandlingen studeras spektrat av identifierade hadroner, uppmätt i pp-kollisioner vid två olika kollisionensenergier. Den partikeldynamik och hadrokemi som resultaten visar, implicerar vagt en förekomst av ett expanderande medium även i detta kollisionssystem, och indikerar således att Pb-Pb-kollisioner skulle kunna tolkas som en förlängning av pp-kollisioner. Dessa implikationer är banbrytande, och skulle kräva en omarbetning av vår nuvarande förståelse av både kvantkromodynamik och tungjonsfysik.

ACKNOWLEDGMENTS

The following thesis would have never seen the daylight if not for the involvement of many people, who have contributed not only to my professional development, but also had a major impact on my personal life. Unfortunately, expressing my gratitude to every single person would require a separate book, therefore here I will only mention the highlights.

First of all I would like to sincerely thank my supervisor Peter Christiansen for providing guidance throughout the four years of my PhD and always pointing me the right directions; for having patience whenever I would mess something up; for giving me enough freedom to do what I want and trusting in me, even when I doubted myself; for all those “viking-aristocrat” conversations and karaoke evenings in the most peculiar places around the world.

I would also like to express my gratitude to Alexander Kalweit, who became my “unofficial” supervisor at CERN and introduced me to the studies which became the main focus of my thesis; for always having time to discuss yet another issue in my analysis; for all the dinners in R1 (and outside) and social activities at CERN; for always having my back.

Many thanks go to the past and current members and students of Lund ALICE group (my Lund family): Anders, for his brilliant knowledge of detectors and his patience explaining it in a way that even I could understand; Evert, for always having a witty comment that I could never top; David for always having the most positive attitude; Tuva, for taking over my duties when I could just not do it, and for always being *really* supportive and helpful when I needed it; Martin, for all the tag-popping, beverage evenings, adventures in the conferences and long discussions beyond physics; Ben (although not in ALICE, but who cares) for providing us the roof when we did not have one; Jonatan, for taking over the office after I leave; all the master students: Maria, Madeleine, other Madeleine, Adam, Adrian, and Rickard for contributing to the very pleasant office environment.

I am very grateful to Maria, who stood by me through ups and downs and supported me in some really desperate situations; for all the horror movies and video game evenings; for showing me the bright side of hiking and embarking on travels with me; for making me realize that there is so much more to life than just work.

I would also like to explicitly thank all the previous ATLAS PhD students in our division for making the best social working environment: Lene, Sasha, Anthony, Anders. I do miss you all (but just *lagom*).

A very special thanks to Bozena (dzięki!), who took her best care of me and other PhD students – I am still convinced that everything that works out, it is because of her. I am also grateful to Else, who took her time to read my thesis and provided valuable feedback. In general, I would like to thank to all the people in the division for contributing to the nice social environment during the last four years.

In addition, I would like thank Alice and Leticia for the nerd dinners; Christian Bierlich for *hamburguesa* in Mexico; Christian Bourjau for the adventures before/during/after all the conferences around the world; NBI ALICE PhD students who became my friends throughout the years; Antonio, who has been a friend and the coordinator of the SPECTRA PAG, and Francesca who has been the convener of the PWG-LF.

Last but not least, I would very much like to thank my parents – Inga and Gintas, my brother Mindaugas and his family, Brigita and my lovely niece Sofija, for providing me the support and a place to retreat whenever things would get out of hand, and most importantly – for their boundless care.

It was a crazy ride, for which I thank you all!

Contents

1	Introduction	5
1.1	The Aim of This Thesis	6
1.2	Outline	6
1.3	My Contributions	7
2	The Standard Model and the Strong Force	9
2.1	The Standard Model	9
2.2	The Coupling Constant in QED	11
2.3	The Coupling Constant in QCD	14
2.4	Lattice QCD	17
2.5	Color Deconfinement	22
3	Quark–Gluon Plasma in Large Systems	23
3.1	Formation of QGP	24
3.1.1	Jet Quenching	25
3.1.2	Heavy Quarkonia Dissociation	28
3.2	Hydrodynamical Evolution	30
3.2.1	Hydrodynamical Flow	30
3.3	Chemical Freeze-out	33
3.3.1	Strangeness Enhancement	36
3.4	Kinetic Freeze-out	36
4	Microscopic and Macroscopic Models	41
4.1	Lund String Model	42
4.1.1	Multi-Partonic Interactions and Color Reconnection	44
4.2	Color Ropes	48
4.3	Boltzmann–Gibbs Blast Wave Model	49

4.3.1	Thermal Source Spectra	50
4.3.2	Feed-down from Resonance Decays	51
4.3.3	Longitudinal Flow	52
4.3.4	Transverse Flow	54
4.4	Thermal Model	56
4.4.1	The Grand-Canonical Ensemble	57
4.4.2	The Strangeness-Canonical Ensemble	58
4.4.3	Excluded Volume Corrections	59
4.4.4	Model Predictions and the Data	61
4.5	Core-Corona Model	63
5	The ALICE Detector	69
5.1	A Large Ion Collider Experiment	69
5.1.1	The Inner Tracking System	72
5.1.2	The Time-Projection Chamber	75
5.1.3	The Time-Of-Flight Detector	78
5.1.4	VZERO Multiplicity Estimator	80
5.2	Multiplicity and Centrality Estimation	81
5.2.1	Collision Centrality and Glauber MC	82
5.3	Track Reconstruction	85
6	Event, Vertex, Track Selection and Transverse Sphericity	89
6.1	Event Selection Criteria	89
6.1.1	Out-of-Bunch Pileup	90
6.2	Vertex Selection	91
6.3	Track Selection for Spectral Analysis	91
6.4	Transverse Sphericity	94
6.4.1	Sphericity Selection Track Cuts	95
6.4.2	Detector Response to Sphericity Selection	98
7	Particle Identification	105
7.1	Particle Identification with the TOF Detector	105
7.1.1	Track Cuts Specific to TOF Analysis	107
7.1.2	Raw Yield Extraction	107
7.1.3	Mismatched Tracks	112
7.1.4	From p to p_T	114
7.1.5	Normalization to Rapidity	115
7.2	Particle Identification with Time-Projection Chamber	116

7.2.1	Raw Yield Extraction	116
7.3	Efficiency Corrections	120
7.4	Feed-down	122
7.5	Geant3, Geant4 and Fluka Corrections	124
8	Results	127
8.1	Proton-Proton Collisions at $\sqrt{s} = 7$ TeV	128
8.2	Proton-Proton Collisions at $\sqrt{s} = 13$ TeV	131
8.3	Systematic Uncertainties	138
9	Discussion	147
9.1	Spectral Shapes	148
9.2	Integrated Hadron Yields	156
9.3	Center-of-Mass Energy Scaling	164
9.4	Event Shape Studies	168
10	Conclusions	177
A	List of Acronyms	193
B	Different Sources of Tracking Uncertainties	195
C	Systematic Uncertainties on Particle Spectra	197
D	Blast Wave Fits in pp Collisions at $\sqrt{s} = 7$ TeV	203
E	Blast Wave Fits in pp Collisions at $\sqrt{s} = 13$ TeV	207

Chapter 1

Introduction

The unprecedented energies available at the Large Hadron Collider (LHC) have provided new opportunities to study the deconfined colored medium known as the Quark–Gluon Plasma (QGP). While a complete theoretical description of the formation and evolution of the QGP has not yet been achieved, the “standard model of heavy-ion physics”¹ has been adopted by the community. In this framework it is assumed that energy densities which are only accessible in the relativistic heavy-ion collisions are required to form the QGP.

At the LHC, quark–gluon plasma is produced by colliding lead–lead (Pb–Pb) at a center-of-mass energy $\sqrt{s_{\text{NN}}} = 2.76$ TeV since 2010 and at 5.02 TeV since 2015. In addition, the proton–lead (p–Pb) collisions at $\sqrt{s_{\text{NN}}} = 5.02$ TeV delivered by the LHC in 2012–2013 were expected to isolate the cold nuclear matter effects such as hadronic rescatterings or reabsorption. However, the multiplicity dependent studies of hadron production and particle correlations in p–Pb collisions revealed trends similar to those observed in Pb–Pb, indicating that a hot and dense QCD medium might already be produced in proton–nucleus collisions. These observations provided inspiration to search for similar signatures in even smaller systems, such as proton–proton (pp).

One of the features characteristic of QGP is radial flow, which originates from the expansion of the medium and results in a mass-dependent boost of hadrons. This effect can be studied by measuring the spectra

¹The “standard model of heavy-ion physics” is a phenomenological framework which describes the main aspects of each stage of the collision evolution.

of identified particles and comparing them to hydrodynamical models. In addition, strange particle production rates in the QGP are enhanced as compared to “conventional” pp physics. These two phenomena can be used to search for QGP-like effects as will be discussed in the next section.

1.1 The Aim of This Thesis

This work investigates the production of π , K and p as a function of transverse sphericity and charged-particle multiplicity in pp collisions at $\sqrt{s} = 7$ and 13 TeV measured with the ALICE detector. In order to build a more complete picture, the study of pp collisions at $\sqrt{s} = 7$ TeV was performed together with the measurements of strange, multistrange and resonance hadron yields in a wide transverse momentum range. Note that the (multi) strange hadrons were not measured by the author.

To study the center-of-mass energy dependence of hadron production, π , K and p spectra were also measured in pp collisions at $\sqrt{s} = 13$ TeV. Moreover, event shape analysis was performed on the highest multiplicity pp events in order to isolate QGP-like effects. The single and double-differential study of identified hadron spectra measured in pp collisions at $\sqrt{s} = 13$ TeV was performed by the author alone.

Finally, the results obtained from the spectral analysis are compared to the predictions from several models commonly used in high energy physics. Both heavy-ion and pp models are considered in comparisons.

1.2 Outline

The Standard Model of elementary particle physics is briefly explained in Chapter 2 with the main focus on quantum chromodynamics and the strong force. This is followed by a description of the formation and evolution of the quark–gluon plasma in Chapter 3, where the most important QGP observables are also discussed. The ideas behind several models used to study particle production in pp and nucleus-nucleus collisions are explained in Chapter 4, followed by a short description of the ALICE detector in Chapter 5, where different multiplicity estimation techniques are also covered. Event and track selection used for this analysis is described in Chapter 6, where the transverse sphericity observable is also introduced,

together with a discussion on the detector response to the event shape selection. In Chapter 7, particle identification techniques developed for this study are explained. The measured particle spectra in different multiplicity and transverse sphericity classes in pp collisions at $\sqrt{s} = 7$ and 13 TeV are presented in Chapter 8. This is followed by a comprehensive discussion of particle dynamics and hadrochemistry in the context of both micro- and macroscopic models in Chapter 9. Finally, the work presented in this thesis is concluded in Chapter 10. Note that a list of acronyms used in this work is given in Chapter A.

1.3 My Contributions

My first contribution to the Light Flavor Spectra analysis group was in 2013, where as a CERN Summer Student I was studying different multiplicity estimators in pp collisions at $\sqrt{s} = 7$ TeV. In 2014, the group started working on the identified hadron spectra as a function of multiplicity in pp collisions at 7 TeV and my role was to measure π , K and p spectra using the time-projection chamber (TPC) and the time-of-flight (TOF) detectors. This was the first time such a study was carried out in pp collisions and many people across different analysis groups were involved.

Once the analysis of the 7 TeV data converged, I studied particle production in the context of a thermal model. The study was prepared as a preprint and it was then agreed to include it in an upcoming ALICE publication. Afterwards, I moved on to the measurements of π , K and p spectra as a function of charged-particle multiplicity and transverse sphericity in pp collisions at $\sqrt{s} = 13$ TeV using TPC and TOF detectors.

In addition to my activities in the analysis group, I have also been involved in the upgrade of the TPC read-out electronics. My part there was to prepare the testing software for the new modules and I have participated in their installation afterwards. In addition, I have also been involved in the simulations of ion backflow in the TPC. Finally, I have also contributed to the ALICE collaboration by taking detector-control-system operator and shift leader shifts during the data taking periods in 2015–2017.

The list of publications that I have contributed thus far:

1. “Enhanced production of multi-strange hadrons in high-multiplicity proton-proton collisions”, J. Adam *et al.* [ALICE Collaboration], Nature

Phys. **13**, 535 (2017).

[*This publication reports on strange particle production as a function of multiplicity in pp collisions at $\sqrt{s} = 7$ TeV and is a part of a larger study. In this publication, my results of π and p are used.*]

2. “Multiplicity dependence of light flavour hadron production at LHC energies in the strangeness canonical suppression picture”, V. Vislavicius and A. Kalweit. e-Print: arXiv:1610.03001 [nucl-ex]

[*This preprint reports on the study that I have performed on particle production as a function of multiplicity in the framework of thermal hadronization model. The results reported in the preprint will be published as a part of an upcoming ALICE publication.*]

3. “Multiplicity dependence of identified particle production in proton-proton collisions with ALICE”, V. Vislavicius [ALICE Collaboration], Nucl. Phys. A **967**, 337 (2017).

[*This is a proceeding of a talk that I have given in the Quark Matter 2017 conference and reports on the new results on particle production in pp collisions at $\sqrt{s} = 7$ and 13 TeV. The proceeding is written by me.*]

4. “New results related to QGP in small systems with ALICE”, V. Vislavicius [ALICE Collaboration]. PoS LHCP **2016**, 117 (2016)

[*This is a proceeding of a talk I have given in the Large Hadron Collider Physics 2016 conference and reports on the multiplicity dependence of particle production in pp collisions at $\sqrt{s} = 7$ TeV. The proceeding is written by me.*]

5. “Universal scaling dependence of QCD energy loss from data driven studies”, P. Christiansen, K. Tywoniuk and V. Vislavicius. Phys. Rev. C **89**, no. 3, 034912 (2014)

[*This publication reports on the study of energy loss of high transverse momenta partons in the QGP. The study was performed by me for the MSc degree.*]

Chapter 2

The Standard Model and the Strong Force

Ordinary nuclear matter is comprised of protons and neutrons, which in turn are sets of three quarks (q) bound together by gluons (g). The two most abundant quarks in the universe are *up* (u) and *down* (d) quarks; a set of two u and one d quark forms a positively charged proton, and a set of two d and one u quark – a neutron, with an electrical charge of zero. Bound states of multiple quarks are called *hadrons*. To this day, no evidence of internal structure of quarks or gluons has been found, and it is therefore thought that they are *elementary* particles.

In this chapter I will briefly introduce the Standard Model and the particles and forces within it. I will then focus on strong interactions between quarks and gluons, which are governed by quantum chromodynamics (QCD). I will discuss the strength of QCD coupling in parallel with quantum electrodynamics (QED) and pinpoint the main features of strong interactions at very high energies.

2.1 The Standard Model

In the Standard Model (SM) framework, all matter is composed of 12 elementary particles (quarks and leptons), four gauge bosons and a recently discovered Higgs boson (see Fig. 2.1). All particles within the SM have a quantum number known as *spin*, which describes the intrinsic angular

momentum of the particle and can be either $1/2$ or $1(0)$. The former are called *fermions*, while the latter – *bosons*. In addition, each fermion has a distinct antiparticle, which has the same mass but opposite charge. In nature, fermions interact via exchange of bosons.

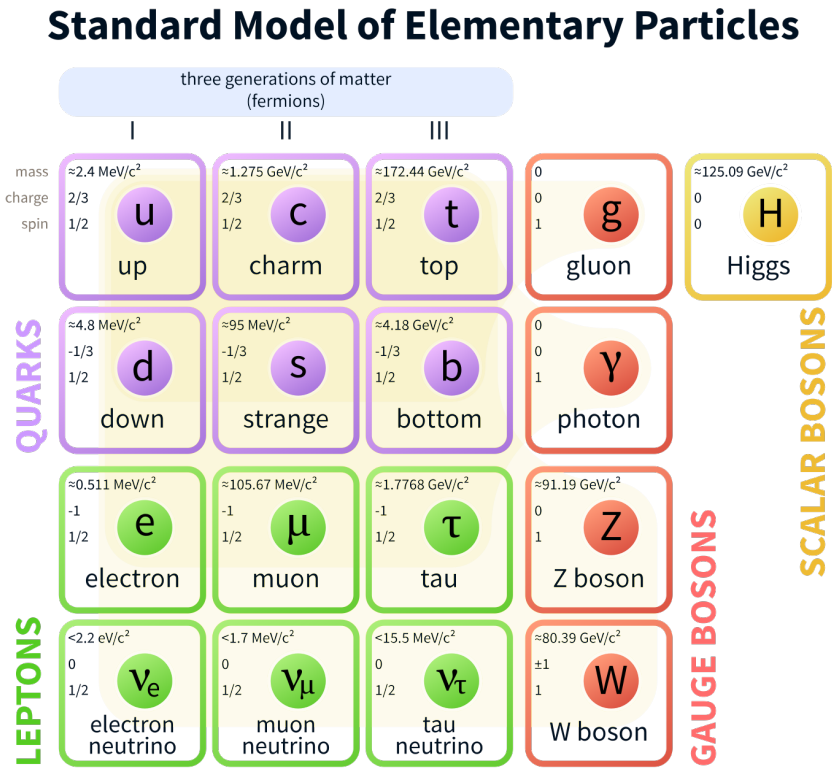


Figure 2.1: All fundamental particles within the Standard Model. Figure taken from [1].

All fermions can be divided into three generations. The first generation, containing the u and d quarks, the electron e and the electron neutrino ν_e are the lightest known particles (with a possible exception of ν_e) and are the most abundant particles in the Universe. There is a remarkable mass ordering between different generations, as shown in Fig. 2.1, with fermions

in generation III being the heaviest. This is also reflected in the timeline of experimental observations of different particles, as heavier fermions can only be produced at increasingly higher energies. It is not clear whether neutrino masses also follow the generation mass ordering, as the current state of the Standard Model predicts them to be massless. Moreover, experimental attempts to directly measure their mass are consistent with zero, and only more recent observations of neutrino oscillations indicate that they are massive [2, 3].

The three fundamental forces described by the Standard Model are strong, electromagnetic (EM) and weak interactions. The latter two are unified into the *electroweak* force – a theoretical achievement, which earned the Nobel Prize in 1979 [4]. The electroweak force is mediated via exchange of *massive* W and Z bosons (weak interactions) and the *massless* photon (EM interactions), while the strong force is carried by the *massless* gluons.

The fermions are classified into *quarks* and *leptons*. The former have a non-zero color charge and therefore interact *strongly*, while the latter are always color-neutral and therefore participate in electroweak interactions only. There are three colors a quark can have: **red** (r), **green** (g) and **blue** (b), and corresponding anticolors for antiquarks. Gluons carry a color and an anti-color, forming eight linearly independent states known as a *color octet*. As will be shown later, the fact that gluons are massless colored objects has important implications on the way the strong force behaves, e.g. binding quarks into color-neutral hadrons. However, before discussing the dependence of strong coupling on the energy scales involved, let us first study how this dependence looks in electromagnetic interactions.

2.2 The Coupling Constant in QED

In quantum field theories like QED or QCD, the strength of a particular interaction is characterized by the respective coupling constant (α). In QED, this constant is defined as $\alpha_{\text{EM}} = \frac{e^2}{4\pi}$, with e being the elementary charge. Each vertex represented by a dot in Fig. 2.2 contributes to the amplitude of the process with a factor $\sqrt{\alpha_{\text{EM}}}$. For the simple process shown in Fig. 2.2, the amplitude can be written as:

$$A = \bar{u}(k')(-ie\gamma^\mu)u(k)\frac{-ig_{\mu\nu}}{q^2}\bar{u}(l')(-ie\gamma^\nu)u(l) \quad (2.1)$$

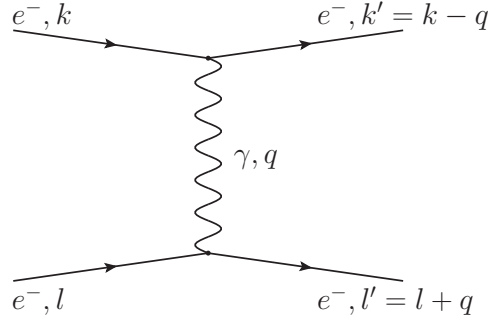


Figure 2.2: Electron scattering via photon exchange

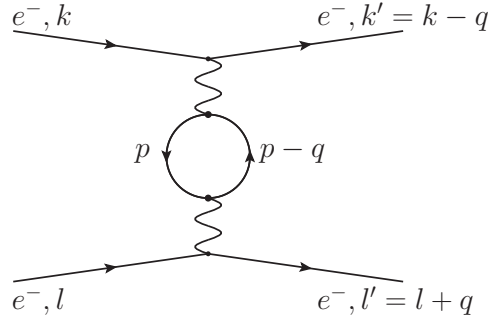


Figure 2.3: One-loop correction for electron scattering via photon exchange

where u and \bar{u} are the annihilation and creation operators of electrons with the respective four momenta. Note that the overall probability for such a process is

$$P(k, q) \propto |\mathcal{M}|^2 \propto |A|^2 \propto e^4 \propto \alpha_{\text{EM}}^2 \quad (2.2)$$

where \mathcal{M} is called the *matrix element*.

What we have not considered so far is that a photon can spontaneously oscillate into electron-positron pair as shown in Fig. 2.3. Since there are 4 vertices, such processes are suppressed by a factor α_{EM}^2 (see Eq. 2.2), but nevertheless contribute to the overall probability. Experimentally, it is not possible to distinguish between the processes shown in Figs. 2.2 and 2.3,

and as a result, the measured α'_{EM} will be a superposition of different powers of α_{EM} .

Calculating the amplitude for the sum of processes shown in Figs. 2.2 and 2.3 is tedious, but has been done by a number of authors (see, for example, [5]), with the following result for the *observed* coupling strength:

$$\alpha'_{\text{EM}} = \frac{e^2}{4\pi} \left[1 - \frac{\alpha_0}{3\pi} \ln \frac{\Lambda^2}{-q^2} \right] \quad (2.3)$$

where Λ has been introduced to cut off the infinities originating from the integration over momentum in the loop.

In principle, higher-order loop diagrams should also be taken into account. As the photon momentum is unchanged, these diagrams factor into $1 - x + x^2 - x^3 \dots$ which can be written as $1/(1+x)$. Eq. 2.3 then becomes

$$\alpha_{\text{EM}}(q^2) = \frac{\alpha_0}{1 + \frac{\alpha_0}{3\pi} \ln \left(\frac{\Lambda^2}{-q^2} \right)}. \quad (2.4)$$

One may notice that, in fact, the coupling constant is not constant but depends on the scale at which it is considered. For instance, let us assume that one can measure α_{EM} at some given scale $q^2 = -\mu^2$. Noting from Eq. 2.4 that $\frac{\alpha_0}{\alpha_\mu} = 1 + \frac{\alpha_0}{3\pi} \ln \frac{\Lambda^2}{\mu^2}$, for some arbitrary scale q^2 one can write

$$\alpha(q^2) = \frac{\alpha(\mu^2)}{1 + \frac{\alpha(\mu^2)}{3\pi} \ln \frac{\mu^2}{-q^2}} \quad (2.5)$$

which means that once the coupling constant α_{EM} is known at one scale μ^2 , its value can be calculated at any other scale q^2 .

Note that so far only e^+e^- loops have been considered. In general, fluctuations into heavier leptons or even $q\bar{q}$ pairs are also possible, if allowed by the energy scale, and therefore there is an additional factor next to the logarithm in the denominator of Eq. 2.5 which turns out to be

$$k = n_l + 3 \left(\frac{4}{9} \right) n_u + 3 \left(\frac{1}{9} \right) n_d \quad (2.6)$$

where n_l , n_u and n_d are the numbers, respectively, of leptons, up-type and down-type quarks available at the given energy scale.

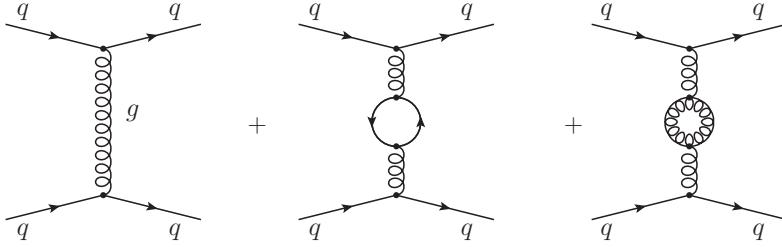


Figure 2.4: (Left) qq scattering via gluon exchange; (middle) qq scattering via gluon exchange with a $q\bar{q}$ loop; (right) qq scattering via gluon exchange with a gg loop.

2.3 The Coupling Constant in QCD

The scale dependence of the *strong* coupling constant $\alpha_s(q^2)$ can be derived in a similar manner to $\alpha_{\text{EM}}(q^2)$ with one notable difference: since gluons are colored objects, they can also couple to each other, and as a result there are two one-loop diagrams in QCD couplings that have to be considered, see Fig. 2.4. The virtual gluon loop essentially has a similar space-time structure as the virtual quark loop and just enters the amplitude calculations with a different scaling factor. Because gluons form a color-octet state, the contribution of their loops to the measured coupling strength is larger than that of the quark loop. However, most important is that this contribution is negative, meaning that α_s will *grow* with decreasing energy (increasing length) scales.

This can be understood in the context of the *antiscreening* effect. For example, let us consider a massive **blue** quark. This quark can spontaneously change its color to **green** by radiating a massless gluon, which in turn carries a color of **blue-antigreen** ($b\bar{g}$ for short). The gluon can then create a quark loop with a quark carrying **b** and antiquark carrying \bar{g} colors, as shown in Fig. 2.5(a). The color field between the \bar{g} anti-quark and **g** quark will have a negative contribution to the total color field strength, and the overall color field will be weakened. This effect is called *screening* and drives the α_s to smaller values at increasing distances. However, the effect is opposite in gluon loops, as illustrated in Fig. 2.5(b). If a gluon splits into two gluons, there will be a strong color field between the two.

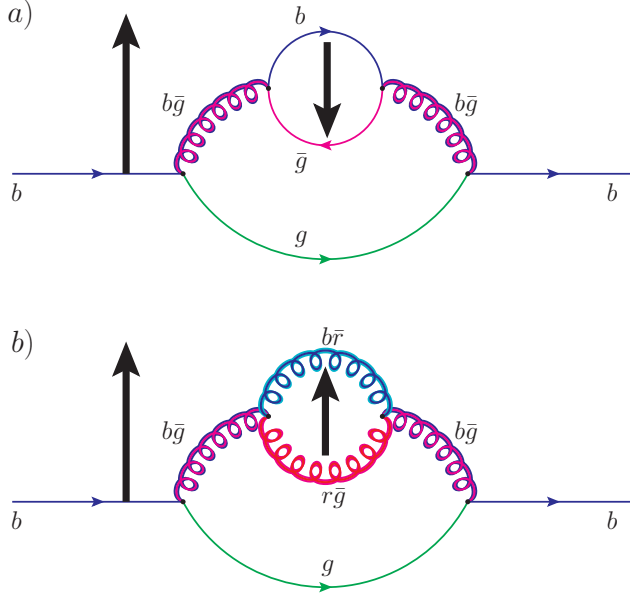


Figure 2.5: Virtual gluon radiation and reabsorption. Gluon has a $q\bar{q}$ loop (a) and gg loop (b). Thick black lines represent color field directions.

Moreover, its direction will be the same as that of the original field (created by the initial blue quark), thus making the total field stronger. This effect is called *antiscreening* and because of it, a colored particle that is far away from such a system will not see a color field originating from a single quark, but rather a much stronger field created by a quark and a cloud of gluons.

On the other hand, highly energetic partons (quarks and gluons) can penetrate the gluon cloud and therefore see *less* color charge concentrated at the origin. As a result, the strong coupling at large energies becomes weaker. Such a behavior is called *asymptotic freedom* and was proposed by Wilczek, Gross and Politzer in 1973 [6], who were awarded a Nobel Prize for their description of this phenomenon.

Taking into account all the diagrams shown in Fig. 2.4 and also counting higher-order loop diagrams, for the strong coupling constant α_s one

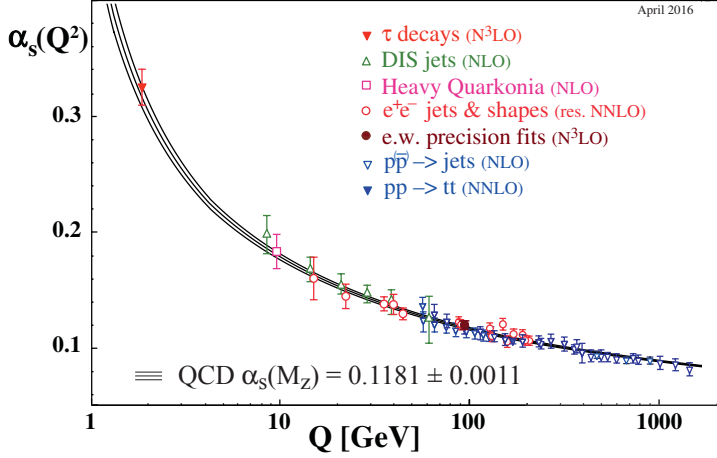


Figure 2.6: Strong coupling constant measured at different scales $Q = q$. Lines represent the scaling predicted by Eq. 2.7. Figure taken from [7].

can write [5]:

$$\alpha_s(q^2) = \frac{\alpha_s(\mu^2)}{1 + \frac{\alpha_s(\mu^2)}{12\pi} (33 - 2n_f) \ln\left(\frac{-q^2}{\mu^2}\right)} \quad (2.7)$$

where n_f is the number of flavors accessible at q^2 . As in the QED case, as long as α_s is known at some scale μ^2 , it can be calculated for any other scale. The strong coupling constant measured as a function of the scale q is shown in Fig. 2.6 [7] together with the scaling behavior predicted by Eq. 2.7.

From Eq. 2.7, one can see that at *low* energy scales, α_s becomes very large. In fact, at certain $q^2 = -\Lambda_{\text{QCD}}^2$, the denominator in Eq. 2.7 vanishes completely. Λ_{QCD} is called the *QCD scale* and can be found by solving

$$\alpha_s(\Lambda_{\text{QCD}}^2) = \frac{\alpha_s(\mu^2)}{1 + \frac{\alpha_s(\mu^2)}{12\pi} (33 - 2n_f) \ln\left(\frac{\Lambda_{\text{QCD}}^2}{\mu^2}\right)} \quad (2.8)$$

with $\alpha_s(\Lambda_{\text{QCD}}^2) = 1$. The current estimate for $\alpha_s(M_{Z^0}^2) \approx 0.11$ [7] (with M_{Z^0} being the Z^0 boson mass), which then gives the QCD scale $\Lambda_{\text{QCD}} \simeq 200$ MeV. Using this, Eq. 2.7 can also be simplified to

$$\alpha_s(q^2) = \frac{12\pi}{12\pi + (33 - 2n_f) \ln \left(\frac{-q^2}{\Lambda_{\text{QCD}}^2} \right)} \quad (2.9)$$

Physically, the magnitude of Λ_{QCD} is interpreted as a scale separating the domain of QCD where α_s is large from that where α_s is small. At scales $Q \gtrsim \Lambda_{\text{QCD}}$, $\alpha_s < 1$, color charges are approaching asymptotic freedom and strong interactions are studied by *perturbative* QCD. This regime is often called the *hard QCD* domain due to the large momentum transfers involved. On the other hand, at $Q \lesssim \Lambda_{\text{QCD}}$, $\alpha_s > 1$ and the strong force is very strong. This regime is often called *soft QCD* to reflect the low momentum transfers involved. In soft QCD, color charges are confined – an effect called *color confinement*, and analytic calculations are not possible due to the highly non-linear behavior of α_s . Instead, numerical methods are employed, as will be discussed next.

2.4 Lattice QCD

Quantum Chromodynamics at low energy scales can be studied on a lattice, where each point of the grid corresponds to a certain point in space-time; such an approach is called *lattice QCD* (LQCD) [8]. The discrete nature of the lattice introduces a momentum cut-off at $1/\xi$, where ξ is the lattice spacing. To obtain QCD continuum results, one has to take $\xi \rightarrow 0$. As a rule of thumb, this is done by extrapolating the calculations performed at different lattice spacings, but this is a highly non-trivial task.

Calculations in LQCD are carried out by numerical evaluation of path integrals and do not depend on perturbative expansions of the theory. In heavy-ion physics applications, LQCD is usually used to simulate how chiral symmetry is broken and quarks are deconfined at increasing temperatures and chemical potentials μ .

One of the topics one can study in LQCD is the binding of heavy quarks on the lattice as a function of temperature and separation distance. As seen in Fig. 2.7 [9], at $T = 0$ (cold hadronic matter) the potential between

two colored charges obtains a shape described by Coulomb-like and linear terms:

$$V_s(r) \approx -\frac{\alpha_s}{r} + \kappa r \quad (2.10)$$

with κ found to be around $\kappa \sim 1$ GeV/fm. At increasing temperatures, however, the linear part flattens out and becomes a constant, which in turn decreases further with T . This means that certain bound states of quarks, e.g. some charmonium states, are unable to form at high temperatures. In fact, this can be exploited to probe the hot medium in order to measure its temperature, as will be discussed in the next chapter.

The dependence of energy (ϵ) and pressure (p) density as a function of temperature in a QCD medium calculated on the lattice is shown in Fig. 2.8 [10]. A very sharp rise of ϵ/T^4 in the range $150 \lesssim T \lesssim 200$ (MeV) is seen, suggesting that the thermodynamical properties in this range change rapidly. Usually, this is associated with the growing number of degrees of freedom (NDF), which changes from the hadrons to the partonic NDF in a hot medium, resulting in a phase transition. It is also noteworthy that below this temperature, energy and pressure densities calculated on the lattice are in a very good agreement with the predictions for a hadronic resonance gas (HRG) model, which describes the evolution of an elastically scattering hadronic gas, see Fig. 2.9. This further suggests that the QCD medium undergoes a phase transition from hadronic matter to partonic, changing its thermodynamical properties completely.

A convenient way to illustrate different states of QCD matter is with a *phase diagram*, where different phases of the medium are plotted against its temperature T and net baryon density μ_B (often also called chemical potential), see Fig. 2.10.

At low μ_B and T values, QCD matter is composed of bound hadrons. If the chemical potential is increased under constant (low) temperatures, the nuclear wave functions of hadrons start to overlap. At some point, the overlap is so large that the quarks are no longer able to distinguish the nucleons they came from and can interact with quarks from other hadrons. The thermodynamical parameters of the system change dramatically, and the new state of medium – the quark–gluon plasma – is created. A detailed description of QGP will be provided in the next chapter. The transition between cold hadronic matter into QGP at low temperatures is a *first order* phase transition and occurs instantaneously.

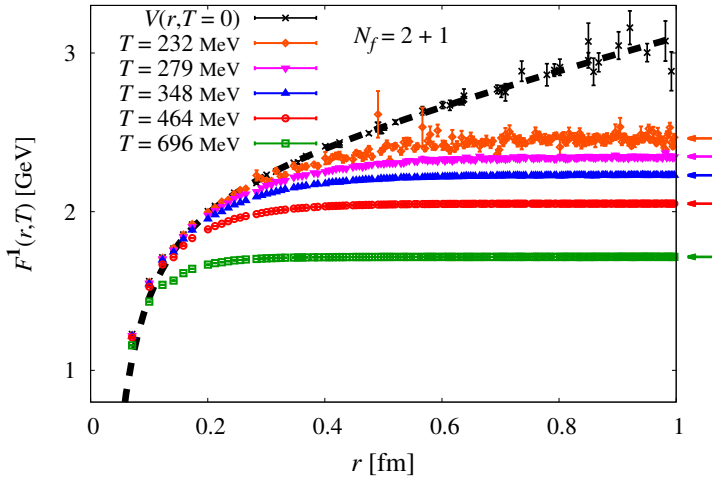


Figure 2.7: Strong potential between two quarks at zero temperature (black). The dashed line shows fit results of Eq. 2.10. Colored points represent quark free energy as a function of radius at different temperatures. Calculations were performed on lattice with 2+1 flavors [9].

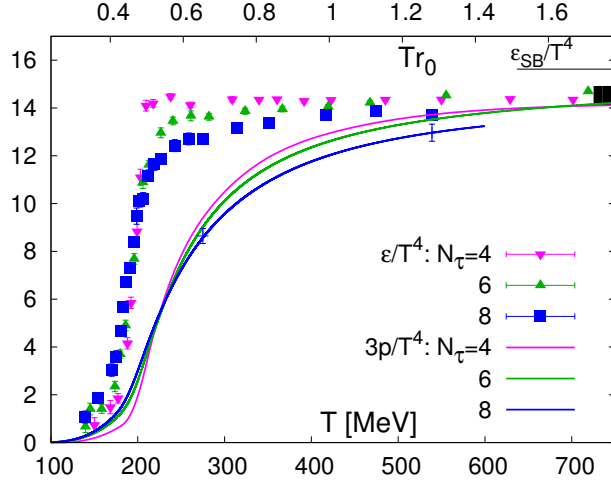


Figure 2.8: Energy (points) and pressure (lines) density of a QCD medium as a function of temperature. Different colors represent different lattice constants (spacing) [10].

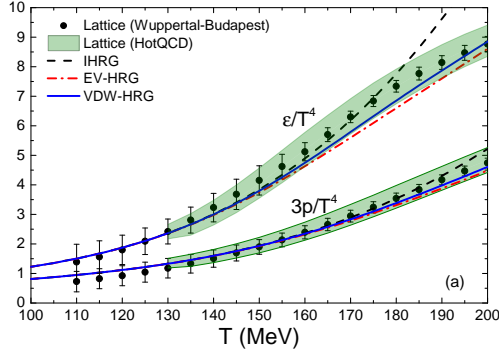


Figure 2.9: Energy and pressure density as a function of temperature calculated in LQCD with comparison to predictions from the Interacting Hadronic Resonance Gas model. Colored lines represent HRG with excluded volume and van der Waals corrections. Figure taken from [11]

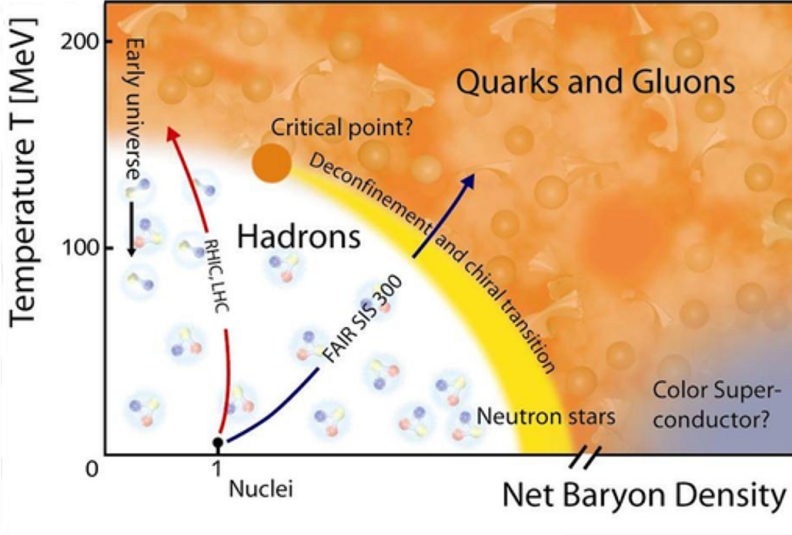


Figure 2.10: QCD phase diagram. Figure taken from [12]

On the other hand, under low μ_B , the hadronic matter can be turned into QGP by increasing its temperature, as is also shown in Fig. 2.10. In this case, the hadronic matter gradually crosses over into QGP with the thermodynamical properties changing continuously rather than abruptly. It should be mentioned that in our current understanding, this is the route the early universe took¹ when expanding, cooling and forming the hadronic matter.

Finally, due to the two different phase transition regions, it is expected that a critical point should exist. As it has been argued in [13], in the vicinity of the critical point one would expect the volume of the plasma produced to become very sensitive to the fluctuations of T or μ_B . This should then be reflected in enhanced fluctuations of certain QGP observables on an event-by-event basis. As of now, this critical point has not been found, although entire physics programs like the beam-energy scan at the Relativistic Heavy Ion Collider (RHIC) [14] are being conducted for this purpose.

¹But in opposite direction, i.e. from the QGP at high temperature to the hadronic matter at low temperature.

2.5 Color Deconfinement

In lattice QCD it has been observed that the potential of the strong force can be expressed by Eq. 2.10, where the first term represents a Coulomb-like potential and the second term is responsible for color confinement. Owing to a large number of colored quarks and gluons, the medium produced in heavy-ion collisions will screen potentials. The effect is called *Debye screening* and effectively turns the Coulomb-like potential into a Yukawa-like potential:

$$V_s(r) \propto -\frac{\alpha_s}{r} e^{-\frac{r}{r_D}} \quad (2.11)$$

where r_D is Debye screening length given by

$$r_D \propto \sqrt{\frac{T}{n}} \quad (2.12)$$

with n being the density of color charge carriers. In a very hot medium colored charges are produced thermally and therefore $n \propto T^3$. As a result, the screening length $r_D \propto T^{-1}$ and *decreases* with increasing temperature.

If one now considers a hadron in such a medium, at sufficiently large temperatures the screening length r_D will become smaller than the separation between the two quarks thus melting the hadron. As a result, the quarks become *unbound* and can strongly interact with other partons within the medium. Note that although in such case quarks are *effectively* free to move within the medium, the effect is not the same as asymptotic freedom because *the quarks are still strongly interacting*.

Chapter 3

Quark–Gluon Plasma in Large Systems

Lattice QCD predicts the strong force to exhibit unique features under extreme conditions. In particular, at very high temperatures hadrons melt down into deconfined quarks and gluons, forming a very hot and dense medium with drastically different thermodynamical properties. Such a state of matter is called the quark–gluon plasma and is created for instance in highly relativistic collisions of heavy ions (HI).

Because of very high pressure gradients, the QGP expands rapidly, cooling down along the way. As the temperature drops, color confinement binds the colored quarks into hadrons once again. The current estimate for the lifetime of the QGP phase is of order of $\sim 10^{-22}$ s, nevertheless, during this time the fireball will go through several stages, as illustrated in Fig. 3.1:

- Formation
- Hydrodynamical evolution
- Chemical freeze-out
- Kinetic freeze-out.

In the following chapter I will discuss each of these stages one by one. For each stage (where available), relevant experimental observables will be introduced.

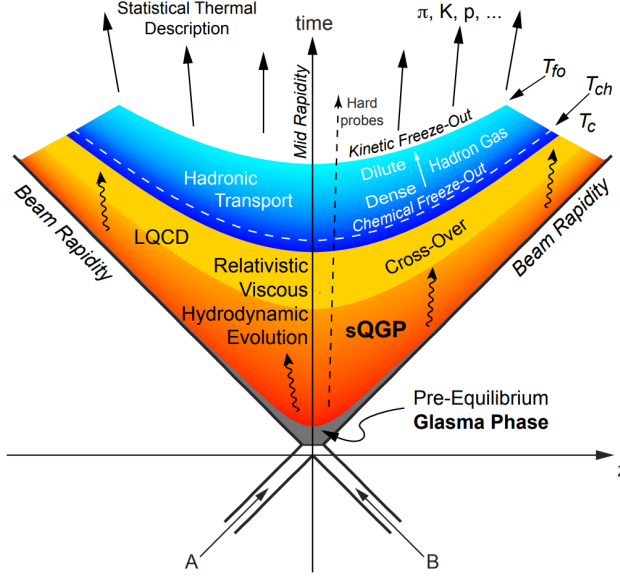


Figure 3.1: Evolution of the QGP created in a collision between nuclei A and B. Figure taken from [15].

3.1 Formation of QGP

The formation of quark–gluon plasma is the least-understood stage of relativistic heavy-ion collisions. In fact, most of the models in HI physics assume a pre-formed QGP and only consider its evolution. Currently, the proposed mechanism for the production of the QGP considers collisions of *color glass condensates* (CGC). The color glass condensate is inspired by the observations that the gluon density within a hadron grows rapidly with decreasing *Bjorken* x . The Bjorken x is defined as the fraction of the linear momentum of a hadron carried by a parton. At relativistic energies the occupancy number of low x gluons will saturate at some scale Q_s due to limited volume, forming very dense gluonic clouds. Because of the Lorentz contraction, these gluon fields will appear to be squeezed from the lab reference frame (and even more so from the target hadron). Because the low x gluons are packed tightly, the coupling between them is weak. Furthermore, the lifetimes of gluons are also subjected to time dilation,

making their evolution slow compared to the time scales involved. As a result, a hadron moving at relativistic energies has a built-in very high density, weakly coupled “wall of gluons”.

During the collision, the two walls of CGC pass each other, forming very strong electric and magnetic fields, conceptually similar to that in the string model. The medium of these strong fields, also called *glasma*, equilibrates by decaying into gluons with momenta given by the energy scale Q_s , thus forming the quark–gluon plasma.

The earliest probes of the QGP are the so called hard probes created in hard QCD scatterings. In the next two subsections I will give examples of the most studied hard probes.

3.1.1 Jet Quenching

Although the dominant mechanism in HI collisions is soft inelastic scatterings between CGCs, partonic interactions involving very high momentum transfers are also possible. Such scatterings result in high-energy partons moving in opposite directions in the transverse plane, ultimately forming collimated showers of hadrons called *jets*.

The production cross sections of jets in pp collisions are calculable by pQCD, and can be extrapolated to heavy-ions collisions considering the total number of nucleon-nucleon interactions, N_{coll} , see Section 5.2.1. While the fragmentation of jets in vacuum cannot be calculated perturbatively, it is successfully described by so-called parton showers. On the other hand, the evolution of partons traversing a colored medium is modified, and so far these effects are not well-understood. In [16, 17] it has been argued that the dominating mechanism of medium-induced modifications is the energy loss by elastic and radiative processes, and several methods to calculate the energy loss have been discussed in [18, 19, 20, 21].

Nevertheless, studies of jets in QGP have attracted much attention within the heavy-ion community. Due to their early formation times and very high energies, jets will traverse the QGP in its early phases. Any interactions with the medium will *quench* the jet, modifying its energy and thus making them very good probes of the quark–gluon plasma.

One can consider an event where a back-to-back jet is created close to the surface of the QGP, and one of the jets leaves the medium immediately. If the second jet is quenched by the medium, one expects to observe a

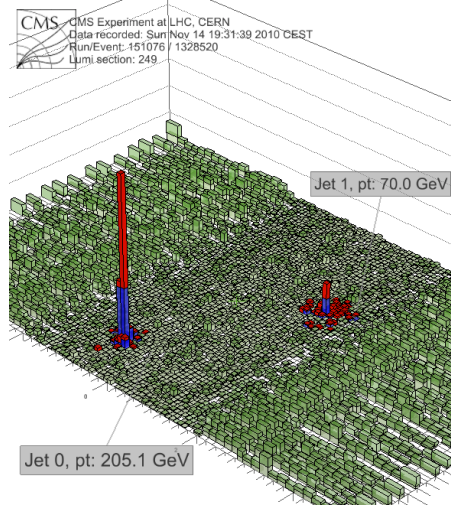


Figure 3.2: CMS event display for one Pb-Pb collision at $\sqrt{s_{\text{NN}}} = 2.76$ TeV. The two towers represent two jets. Figure taken [22]

large momentum imbalance between the two, as initially both had similar transverse momenta¹, p_{T} . In fact, this is exactly what one observes as shown in Fig. 3.2 [22].

As jet reconstruction in heavy-ion collisions is rather challenging due to large activity of the underlying events, high p_{T} hadrons are commonly used as proxies for jets. To quantify jet quenching, one typically constructs an observable called the *nuclear modification factor*, R_{AA} :

$$R_{\text{AA}}(p_{\text{T}}) = \frac{\frac{d^2 N_{\text{AA}}}{dy dp_{\text{T}}}(p_{\text{T}})}{N_{\text{coll}} \frac{d^2 N_{\text{pp}}}{dy dp_{\text{T}}}(p_{\text{T}})} \quad (3.1)$$

where the yields in the numerator and denominator are measured in Pb-Pb (or A-A in general) and pp collisions respectively. The scaling with N_{coll} is motivated by the small hard cross sections so that probabilities for hard interactions are expected to be linearly additive. Following are the values R_{AA} can obtain:

¹But opposite directions.

- $R_{AA} = 1$ – absence of medium effects; the collision is a superposition of N_{coll} hard pp scatterings
- $R_{AA} > 1$ – hadron production is systematically enhanced in AA
- $R_{AA} < 1$ – hadron production is systematically suppressed in AA.

The ALICE collaboration has measured the R_{AA} in Pb-Pb collisions at $\sqrt{s_{NN}} = 2.76$ TeV, see Fig. 3.3 [23]. It has been observed that the yield of high p_T particles is suppressed by a factor of ~ 5 in the most head-on Pb-Pb collisions where the volume of QGP produced is expected to be the largest. R_{AA} also appears to be increasing in a linear manner for $p_T \gtrsim 8$ GeV/ c , suggesting that suppression decreases at higher p_T .

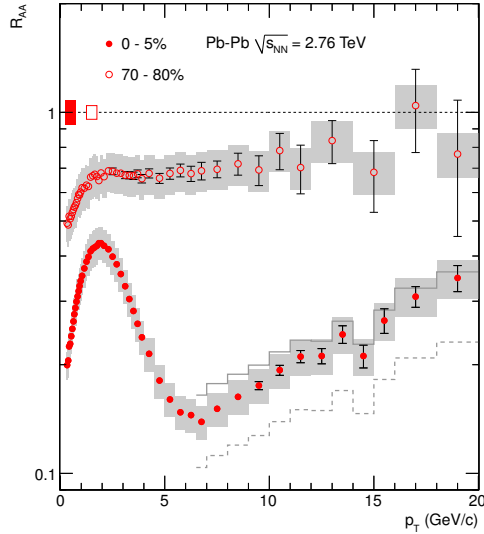


Figure 3.3: Nuclear modification factor R_{AA} of charged hadrons as a function of p_T measured in central and peripheral Pb-Pb collisions at $\sqrt{s_{NN}} = 2.76$ TeV by the ALICE collaboration. See Section 5.2.1 for the definition of centrality. Gray dashed line represents alternative pp references. Figure taken from [23].

3.1.2 Heavy Quarkonia Dissociation

From lattice QCD it has been seen that in a hot medium, the strong potential is screened beyond some separation radius R_C . Furthermore, with increasing temperature, the saturation value drops, and so does R_C , effectively reducing the binding energy of quarks. In this context, it is interesting to study the yields of certain bound states of $q\bar{q}$ systems. Of particular interest are the ground and excited states of quarkonia J/Ψ ($c\bar{c}$) and Υ ($b\bar{b}$), as these bound systems of heavy quarks have leptonic decay channels and are therefore easy to measure in the dense HI environments.

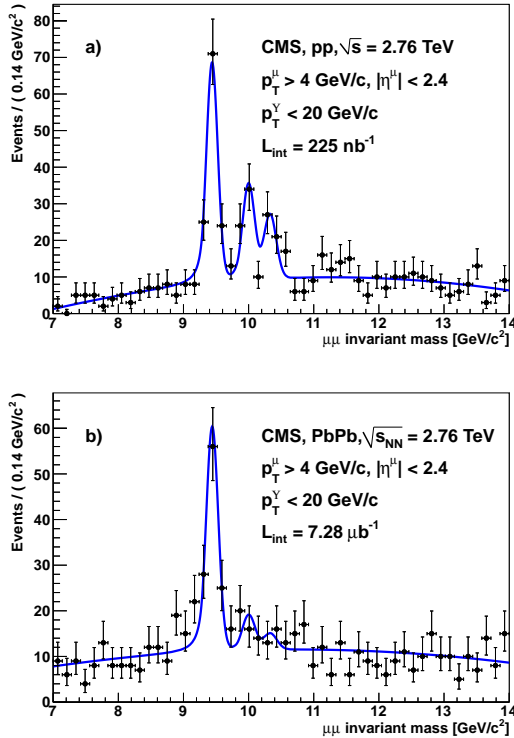


Figure 3.4: Dimuon invariant mass distributions around Υ mass from pp (a) and Pb-Pb (b) measured at $\sqrt{s_{NN}} = 2.76$ TeV. Excited states of Υ are suppressed in Pb-Pb collisions as compared to pp. Figure taken from [24].

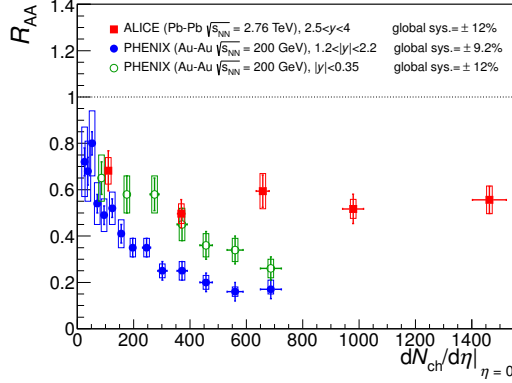


Figure 3.5: The nuclear modification factor R_{AA} of J/ψ meson as a function of charged-particle multiplicity measured in Pb-Pb collisions at $\sqrt{s_{NN}} = 2.76$ TeV and Au-Au collisions at $\sqrt{s_{NN}} = 200$ GeV. Figure taken from [25].

In heavy-ion collisions, measurements of ground and excited states of heavy quarkonium can serve as a probe for the QGP temperatures. These measurements are motivated by the idea that due to temperature-dependent reduction of binding energy, excited states of J/ψ and Υ would gradually dissociate and one would therefore observe disappearance of certain charmonium states in the invariant mass spectra.

Such measurements have been performed at the LHC, for example, by the CMS Collaboration and are shown in Fig. 3.4 [24]. A very large suppression of $\Upsilon(2S)$ and $\Upsilon(3S)$ is observed in Pb-Pb collisions measured at $\sqrt{s_{NN}} = 2.76$ TeV as compared to pp collisions at the same center-of-mass energy. Another interesting observation at LHC energies is that the dissociation of J/ψ in Pb-Pb collisions at $\sqrt{s_{NN}} = 2.76$ TeV is smaller than that measured at RHIC energies, see Fig. 3.5 [25]. This is understood as an effect of *regeneration*, where due to significantly larger cross sections at LHC than at RHIC, a pair of unbound charm quarks ($c\bar{c}$) can randomly recombine into another J/ψ meson. This suggests that charm quarks are indeed deconfined in the QGP.

3.2 Hydrodynamical Evolution

The evolution of locally thermalized QGP can be very well modelled by a hydrodynamical description of the system, suggesting that the medium created in heavy-ion collisions behaves like a strongly coupled liquid rather than a weakly interacting gas [26]. In hydrodynamical models, local conservation of energy and momentum is imposed, and the equation of state can be calculated from lattice QCD.

The inhomogeneities in the medium densities within the QGP give rise to pressure gradients, which drive the hydrodynamical expansion of the system. During the expansion, the system dilutes and cools down until the phase transition, after which a hadronic description of the system is needed. The expansion of the medium results in a *flow* of partons, inherited by the hadrons at later stages, and leading to a mass-dependent boost and spectral modifications of particles. These modifications are more pronounced in central Pb-Pb collisions, where “more” QGP is produced.

Features of the hydrodynamical evolution of the medium in heavy-ion collisions include orders of flow (discussed in the next section) and the modifications of the p_T -differential p/π ratio in central and peripheral collisions shown Fig. 3.6 [27]. Protons are of particular interest, since they are very sensitive to the flowing medium due to their large mass, and therefore the p/π ratio exhibits much stronger modifications than for example the K/π ratio, illustrated in Fig. 3.6. Also shown with the ratios are the predictions from the Krakow hydrodynamical model [28], together with several other models. However, recent studies suggest that p/π ratio modifications are not unique to the QGP and can have different origins in smaller systems, as will be discussed in Section 4.1.1.

3.2.1 Hydrodynamical Flow

In the azimuthally symmetric QGP, the density of the medium decreases from the center of the medium to its edges. In this case, the hydrodynamical evolution results in a uniform expansion throughout the whole azimuth, giving rise to *radial flow* and boosting the hadrons to higher transverse momenta in a mass-dependent way, as shown in Fig. 3.7 [29].

In practice, the density gradients in the QGP are never azimuthally symmetric. An important factor for the anisotropies of pressure gradients within QGP is the collision geometry. As shown in Fig. 3.8, in semi-central

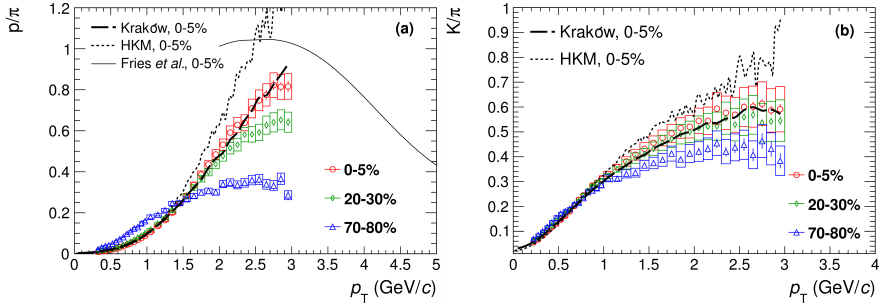


Figure 3.6: p_T -differential p/π (left) and K/π (right) ratios measured in Pb-Pb collisions at $\sqrt{s_{NN}} = 2.76$ TeV at different centralities in comparison to Krakow hydrodynamical model [28]. Figure taken from [27]

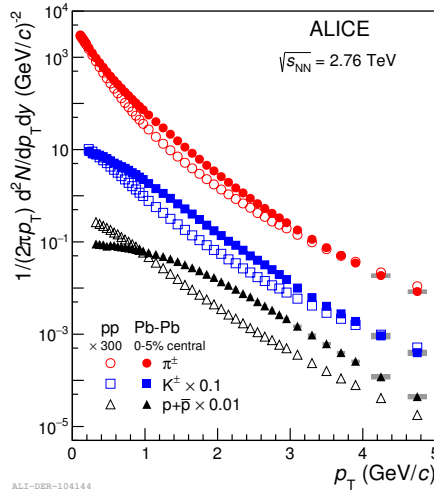


Figure 3.7: p_T -differential π , K and p spectra in most head-on Pb-Pb collisions at $\sqrt{s_{NN}} = 2.76$ TeV with comparison to the spectra measured in pp collisions. Hadrons in Pb-Pb collisions are boosted to higher p_T and the effect is more pronounced for heavier particles. Figure taken from [29].

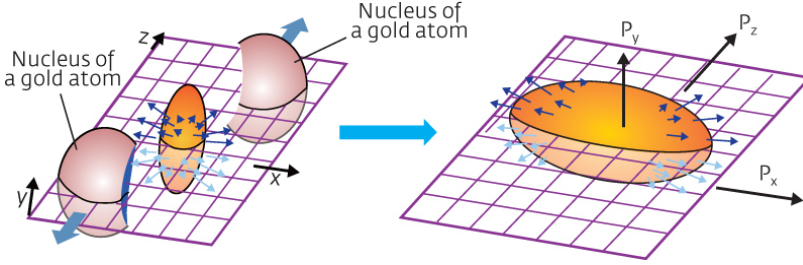


Figure 3.8: Collision geometry in a semi-central Au-Au collision.

heavy-ion collisions the overlap between two colliding nuclei results in an ellipsoid-shaped volume; the medium density gradient in the x direction is much steeper than along the y axis. The hydrodynamical evolution transfers this into momentum space anisotropy, so that matter receives a larger flow velocity in the event plane (xz) direction than perpendicular to it.

Moreover, distributions of nucleons within nuclei are stochastic, resulting in the so-called “hot regions” of QGP – areas with significantly larger densities. In a viscous fluid these fluctuations are smeared out, while in the perfect QGP liquid they give rise to phenomena such as triangular flow.

The angular anisotropies resulting from the QGP expansion are usually studied in terms of *flow* coefficients v_n . Each coefficient then corresponds to a different order of flow: *elliptic flow* (v_2), *triangular flow* (v_3) etc, as illustrated in Fig. 3.9. One of the most simplistic approaches to the topic that does not require the determination of the event plane is the Fourier decomposition of the two-particle correlation function, which can be expressed in terms of harmonics as:

$$\frac{dN^{\text{pair}}}{d\Delta\varphi} \propto C(\Delta\varphi) = 1 + \sum_{n=1}^{\infty} 2v_n(p_T^t)v_n(p_T^a) \cos(n\Delta\varphi) \quad (3.2)$$

The superscripts t and a represent *trigger* and *associated* particles respectively, n is the order of the harmonics and v_n is explicitly distinguished at different p_T . By fitting such function to the measured correlation, one can extract the amplitudes v_n for each harmonic, as is shown in Fig. 3.9 [30].

The elliptic and triangular flow coefficients of identified hadrons as a function of p_T in Pb-Pb collisions at $\sqrt{s_{\text{NN}}} = 5.02$ TeV are shown in

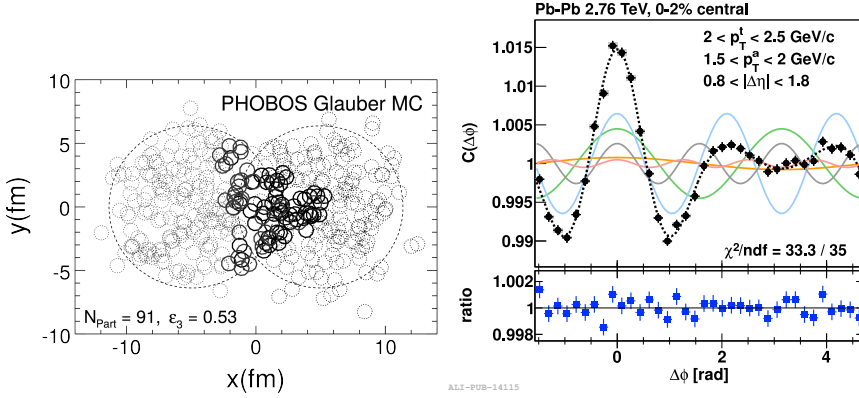


Figure 3.9: Participating nucleon distribution (left) [31] and Fourier decomposition of 2-particle correlations (right) [30]. By selecting the most central collisions one suppresses geometric flow (v_2 , green) and can study mainly the flow from fluctuations (v_3 , blue).

Fig. 3.10 for several centrality classes. The v_2 is measured to be larger for protons, which is also predicted by hydrodynamical modeling. Moreover, elliptic flow is stronger in semi-central collisions, where the geometrical shape of QGP is more ellipsoid-like.

Finally, if the nuclear overlap was smooth, the density gradients in the QGP would be symmetric with respect to the event plane, and odd- n harmonics would vanish. This is not the case owing to the observed non-zero v_3 also shown in Fig. 3.10 and is understood to originate from local density fluctuations [32, 33].

3.3 Chemical Freeze-out

As the QGP expands and cools down, it will undergo a transition to the hadronic phase at the critical temperature T_{crit} . The system will continue to interact via inelastic hadronic scatterings, which will supposedly maintain some form of chemical equilibrium. As the system expands further and cools down, inelastic scatterings will cease and the remaining hadrons will further scatter elastically. The transition between an inelastically scattering to an elastically scattering hadronic gas is called *chemical freeze-out*

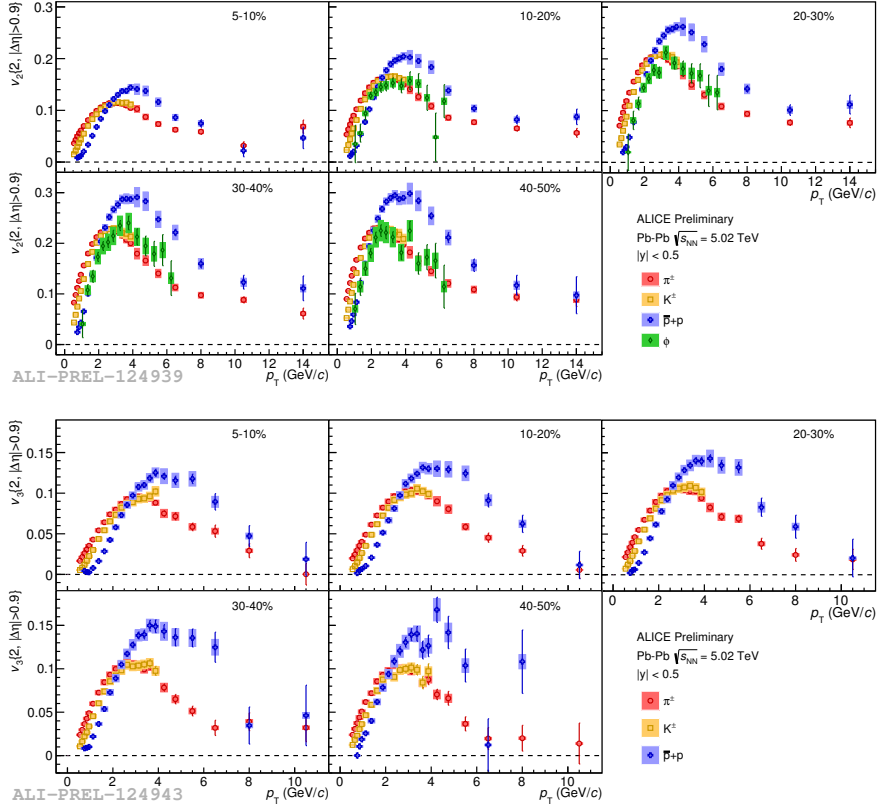


Figure 3.10: p_T -differential elliptic (v_2) and triangular (v_3) flow coefficients for π , K and p as a function of centrality in Pb-Pb collisions at $\sqrt{s_{NN}} = 5.02$ TeV.

and is characterized by a chemical freeze-out temperature T_{ch} . It has been argued in [34] that the chemical freeze-out occurs shortly after the QGP transition to the hadronic phase, so that $T_{\text{ch}} \approx T_{\text{crit}}$.

Assuming that hadrons form an ideal (chemically equilibrated) gas after the freeze-out, hadron production can be modeled in the context of thermodynamical laws. Such a system is then described by T_{ch} , its volume V and the chemical potentials of baryonic, charge and flavor quantum numbers. This will be discussed in detail in Chapter 4.

Thermal models proved to be very successful in predicting particle abundances measured at SPS [35] and RHIC, as shown in Fig. 3.11 [36], supporting the idea of a chemically equilibrated QGP. As the yields of thermally produced hadrons are trivially given by the parameters of the system, the chemical freeze-out temperature can be extracted by fitting a thermal model into the measured hadron abundances. The current estimate is $T_{\text{ch}} \sim 145 - 166$ MeV.

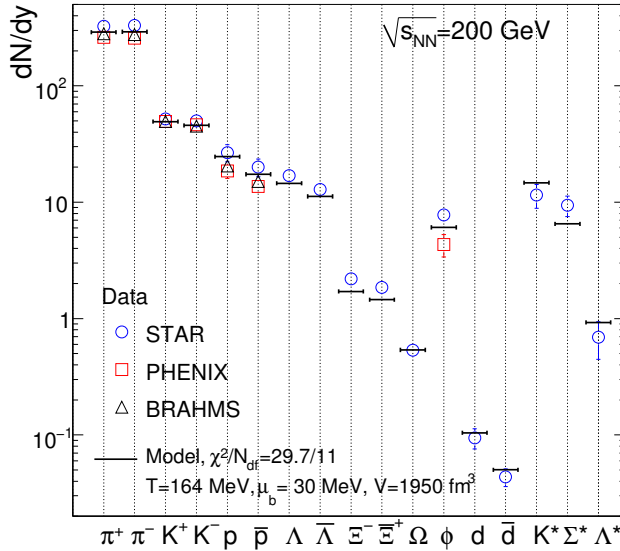


Figure 3.11: Thermal model fit to hadron yields measured in Au-Au collisions at $\sqrt{s_{\text{NN}}} = 200$ GeV. Figure taken from [36].

3.3.1 Strangeness Enhancement

In QCD vacuum, soft production of strange quarks is strongly suppressed due to its much larger (constituent) mass as compared to u and d quarks. In a QGP, however, quarks are unbound and their *current* masses are of importance. As a result, the production of $s\bar{s}$ pairs is expected to be enhanced by the medium and one would expect to measure larger abundances of (multi) strange hadrons in heavy-ion collisions as compared to pp. The effect was proposed in [37] as a signature for QGP formation and the phenomenon was later observed in [38].

The hyperon-to-pion ratios measured at LHC and RHIC as a function of number of participants², N_{part} , is shown in Fig. 3.12 [39]. The ratios show a clear evolution with N_{part} and appear to be more pronounced for hadrons with larger strangeness content.

In principle, one could argue that the observed enhancement is not related to the strangeness of the hadron, but rather to the baryonic number. If this was the case, however, one would also expect to see the enhancement in the p/π ratios. These have also been measured by BRAHMS, PHENIX and ALICE Collaborations, see Fig. 3.13. No such evolution in p/π is observed, suggesting that the strangeness production is indeed modified in the quark–gluon plasma.

Finally, one can note that at large N_{part} , hyperon-to-pion ratios seem to saturate. The solid and dashed lines shown in Fig. 3.12 represent thermodynamical predictions for the ratios reported in [40, 41]. Note that in some thermal models, the strangeness enhancement is seen as a canonical suppression in small systems, which is then gradually released with increasing system sizes. The saturation of experimentally measured ratios at values predicted by thermal models supports the picture of a thermalized QGP.

3.4 Kinetic Freeze-out

After the chemical freeze-out, the expansion and cooling of the system continues, with the constituents scattering only elastically and the heavy resonances decaying into stable or long-lived states. At some temperature T_{kin} , the time scale between two soft scatterings τ_{coll} becomes larger than the scale associated with the expansion, and elastic scatterings cease. A

² N_{part} can be used as a probe for the QGP size and will be defined in Section 5.2.1

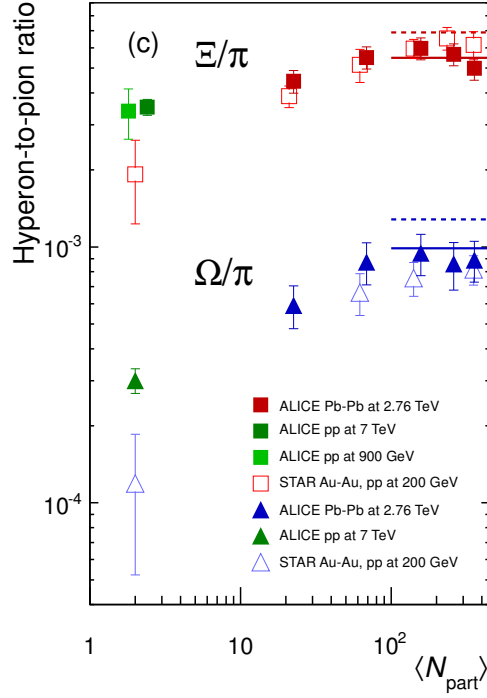


Figure 3.12: Hyperon-to-pion ratios as a function of N_{part} . Note that pp collisions correspond to $N_{\text{part}} = 2$. Figure taken from [39].

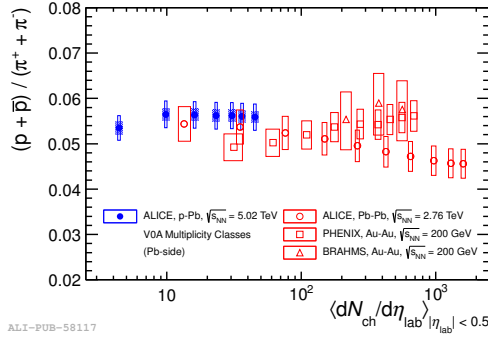


Figure 3.13: p/π ratios in Pb-Pb and p-Pb. Note that multiplicity $\langle dN_{ch}/d\eta \rangle$ scales with N_{part} . Figure taken from [42].

common approximation for this time is when the mean free path of a hadron is of the same order as the system size. After that, the p_T of hadrons are fixed, and thus T_{kin} is often called the *kinetic freeze-out* temperature. The evolution of the hadronic gas from the QGP phase transition at T_{crit} to the kinetic freeze-out at T_{kin} is well described by the ultrarelativistic quantum molecular dynamics (UrQMD) transport model [43], and after the chemical freeze-out behaves like hadron resonance gas described in Section 2.4.

As hadron kinematics are established at T_{kin} , both the freeze-out temperature and the expansion rate of the medium, $\langle \beta_T \rangle$, will be imprinted onto the spectral shapes of measured hadrons. A common tool to study these shapes is using Boltzmann–Gibbs blast wave (BW) model [44], which will be discussed in detail in Chapter 4. Let us mention here, however, that the blast wave model describes the p_T spectra of thermal hadrons boosted by the radial flow, where the boost can reflect the expansion of the QGP. Such a model is then fit to the measured transverse momenta or mass distributions in order to extract T_{kin} and $\langle \beta_T \rangle$. Usually, only the lightest hadrons (π , K and p) at low p_T ($\lesssim 3$ GeV/c) are considered in such analysis.

The extracted $\langle \beta_T \rangle$ and T_{kin} parameters from particle spectra measured in Pb-Pb collisions at $\sqrt{s_{NN}} = 2.76$ TeV and Au-Au collisions at $\sqrt{s_{NN}} = 200$ GeV are shown in Fig. 3.14 [27]. Note that the values of

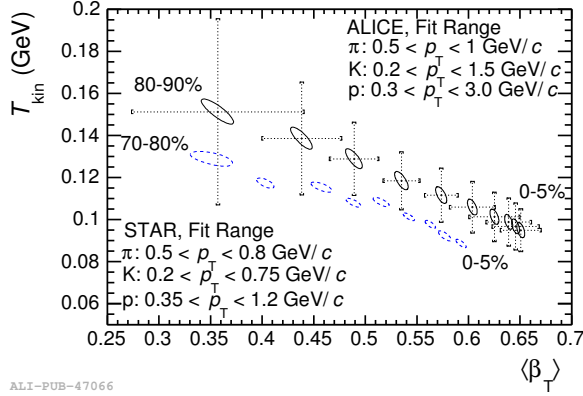


Figure 3.14: Correlation between average transverse expansion velocity $\langle\beta\rangle$ and kinetic freeze-out temperature T_{kin} measured in STAR (blue) and ALICE (black). Figure taken from [27]

T_{kin} and $\langle\beta_T\rangle$ are highly sensitive to the p_T ranges considered, and therefore STAR and ALICE results should not be compared directly. Nevertheless, such studies allow for some qualitative conclusions: in the most head-on collisions, one expects the QGP to be the most dense, leading to the strongest radial expansion. This is reflected by the incrementally larger $\langle\beta_T\rangle$ as the collisions become more central. On the other hand, the freeze-out temperature shows a decreasing trend, suggesting that larger QGP systems lead to lower kinetic freeze-out temperatures (longer lived systems).

Chapter 4

Microscopic and Macroscopic Models

Microscopic models usually involve perturbative description of hard QCD scatterings of quarks and gluons and are used to study small systems such as e^+e^- or pp collisions. Because of the stochastic nature of quantum physics, a single initial state can lead to a variety of final states, thus experimental measurements probe a superposition of the available (final) states weighted by their respective probabilities. Since there are many possible processes, one usually relies on Monte Carlo (MC) generators to simulate a number of collisions in order to make comparisons between theory and measurement.

Macroscopic models, on the other hand, do not consider each QCD process individually. Instead, they assume that a collision creates a medium which can be described by the equation of state, involving macroscopic parameters like temperature, density, etc.

In the following chapter I will cover the underlying assumptions of micro- and macroscopic models that give rise to collective-like behavior of particles and are relevant for the discussion of the results presented in this thesis. I will start with the Lund String model, employed in microscopic MC generators like PYTHIA 8 [45], also briefly discussing multi-partonic interactions (MPI) and color reconnection (CR). Afterwards, I will introduce a more advanced treatment of strings, known as color ropes. I will then move on to macroscopic models: hydrodynamical treatment of the medium in a blast wave model followed by the thermal particle production

model. I will finish the chapter with a discussion of core-corona (CC) models, which attempt to bridge the gap (“interpolate”) between microscopic and macroscopic descriptions. Note that I have not participated in the development of any of the models described in the following chapter.

4.1 Lund String Model

Let us consider the evolution of a meson in 1-dimensional space. If the quark and the antiquark have some kinetic energy and are moving away from each other, the binding potential in Eq. 2.10 is dominated by the linear term, $V(r) \propto \kappa r$. This potential can be seen as a string with tension κ connecting the $q\bar{q}$ dipole, and the evolution of the system is described by a *yo-yo* process [46] illustrated in Fig. 4.1. The important snapshots of the evolution are:

1. At a time $t = 0$ the kinetic energy of the system $E_{\text{kin}} = \sqrt{s}$ is shared between q and \bar{q} at $x = 0$. The potential energy of the system $E_{\text{p}} = 0$ and the quarks are moving away from each other.
2. As quarks move away from each other, kinetic energy is converted into potential energy stored in the string, $E_{\text{p}} = \kappa \Delta x$. At a time given by $t = \sqrt{s}/(2\kappa)$, kinetic energy $E_{\text{kin}} = 0$ and all the potential energy $E_{\text{p}} = \sqrt{s}$ is stored in the string. The quarks thus stop moving away from each other.
3. The force $F(r) = \kappa = \text{const.}$ pulls the quarks back together. At a time given by $t = \sqrt{s}/\kappa$, both q and \bar{q} are at $x = 0$. The kinetic energy $E_{\text{kin}} = \sqrt{s}$, potential energy $E_{\text{p}} = 0$ and quarks are moving in the directions opposite to those at $t = 0$.
4. At a time $t = 3\sqrt{s}/(2\kappa)$, $E_{\text{p}} = \sqrt{s}$ and $E_{\text{kin}} = 0$; quarks change their directions.
5. At a time $t = 2\sqrt{s}/\kappa$, $E_{\text{p}} = 0$ and $E_{\text{kin}} = \sqrt{s}$; quarks are at $x = 0$, the system is back to its initial state and the whole process repeats.

As the quarks move apart, the potential energy stored in the string increases, and at some point it might become energetically favorable for a

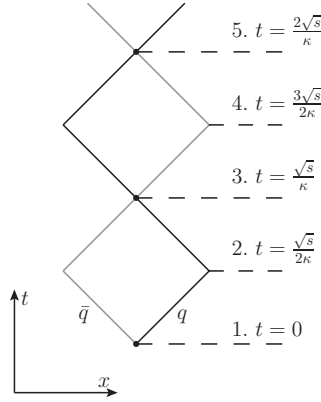


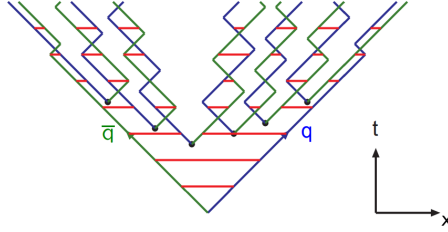
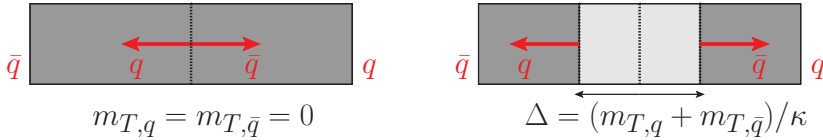
Figure 4.1: The yo-yo evolution of $q\bar{q}$ pair in their rest frame. 1) Beginning of the evolution; 2) 1/4 of full period, maximum tension in the string; 3) q and \bar{q} are back to their initial positions, but have their momenta swapped; 4) 3/4 of full period, maximum tension in the string; 5) full period, the system is back to its initial state.

$q\bar{q}$ pair to tunnel from vacuum. The string then breaks with a tunneling probability given by:

$$\frac{d\mathcal{P}}{dm_T} \propto \exp\left(-\frac{\pi m_{T,q}^2}{\kappa}\right) = \exp\left(-\frac{\pi p_{T,q}^2}{\kappa}\right) \exp\left(-\frac{\pi m_q^2}{\kappa}\right) \quad (4.1)$$

The prescription of the strong potential as a string which can hadronize is called the Lund String Model [47] and was proposed as an explanation for hadron abundances observed in e^+e^- collisions at PETRA. In electron-positron collisions, the initial $q\bar{q}$ pairs are created via Z/γ^* (Z boson or a photon), and then undergo multiple string breakings as shown in Fig. 4.2. Each breaking results in $1 \rightarrow 2$ particle splittings, with particles being more boosted the closer to the outskirts they are. In general, as each vertex is causally disconnected, the breaking can proceed in arbitrary order.

By popping $q\bar{q}$ pairs from the vacuum, the string fragments into mesons. Baryons are created in similar manner, but with diquark-antidiquark pairs. In order to create a $q\bar{q}$ with $m_{T,q}, m_{T,\bar{q}} \neq 0$, the potential energy required is $E_p = m_{T,q} + m_{T,\bar{q}} = \kappa\Delta$. As a result, $q\bar{q}$ is not produced at a vertex,

Figure 4.2: $q\bar{q}$ system in its rest frame with multiple string breakings.Figure 4.3: String breaking into massless (left) and massive (right) $q\bar{q}$ pair.

but with some displacement Δ , as shown in Fig. 4.3.

Finally, let us note that from Eq. 4.1, string breaking suppresses strange quark production relative to up- or down-type quarks by a factor

$$\rho = \exp\left(-\frac{\pi(m_s^2 - m_u^2)}{\kappa}\right) \quad (4.2)$$

Since it is not clear which quark masses should be used, this factor has to be tuned to the measurements. The current estimate using e^+e^- data from LEP [48] gives $\rho = 0.217$. One can also see that string fragmentation into even heavier quarks (e.g. c) is further suppressed to an extent where it becomes negligible compared to perturbative production.

4.1.1 Multi-Partonic Interactions and Color Reconnection

So far, only string fragmentation in e^+e^- collisions has been discussed. The prescription can be extended to pp, but one has to consider the following:

- After a hard scattering, partons from incoming protons are still connected to the beam remnants by color fields

- Multiple partons from each of the incoming protons can scatter, the effect called multi-partonic interactions.

The color field between a hard scattering parton and the beam remnants creates a long colored string, following the movement of partonic endpoints as illustrated in Fig. 4.4. For a parton scattered at midrapidity, the other end of the string is connected to a wounded nucleon moving along the beam axis. Such a string then fragments into low p_T hadrons, populating a large region of rapidity. If there are multiple independent partonic scatterings, each one of those creates such a string and gives rise to larger multiplicities, but the mean transverse momentum is not affected. As a result, one would measure a flat distribution of $\langle p_T \rangle$ as a function of N_{ch} .

On the other hand, results of the UA1 Collaboration showed trend of rising $\langle p_T \rangle$ with increasing charged-particle multiplicities [49]. This suggested that MPIs are not independent and color reconnection was proposed to explain such phenomenon [50].

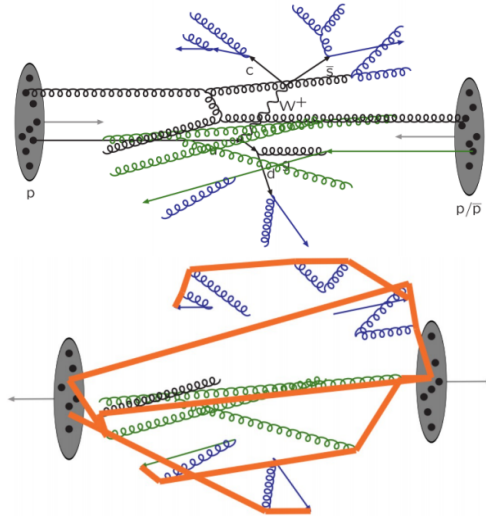


Figure 4.4: Sketch of multiple partons interacting in a pp collision (top). After the collision, the produced partons are color-connected to the beam remnants (bottom). Figures by T. Sjöstrand.

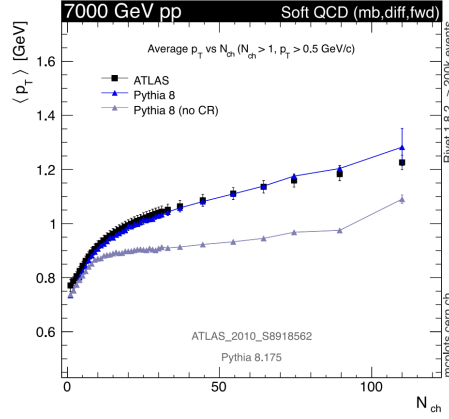


Figure 4.5: Average transverse momentum as a function of N_{ch} measured in pp collisions at $\sqrt{s} = 7$ TeV in comparison to PYTHIA 8 predictions with and without color reconnection. Figure taken from [51]

In CR, partons created in multiple (independent) hard scatterings are allowed to reconnect to each other. In this way, MPIs occur independently, however, their evolution is correlated. As a rule of thumb, the reconnection follows topology reducing the total string length [53] so that each MPI contributes less to the total multiplicity, but still provides an additional kick in p_T [51]. As shown in Fig. 4.5 [51], the Lund String model coupled with MPI and CR prescriptions is able to describe the measured $\langle p_T \rangle$ evolution over a large range of N_{ch} available at the LHC.

Finally, let us briefly discuss how particle production is affected by MPI and CR. As seen in Fig. 4.6 [52], p_T -differential p/π ratios have an emerging peak-like structure when MPIs (leading to large final state multiplicities) are considered. The peak also appears to be shifted towards larger p_T with increasing number of MPIs – which is a result of more pronounced CR effects – and disappears if CR is disabled. In fact, it has been argued in [52] that the Lund String model, coupled with multi-partonic interactions and color reconnection, produces final state effects similar to those expected from an expanding medium like QGP.

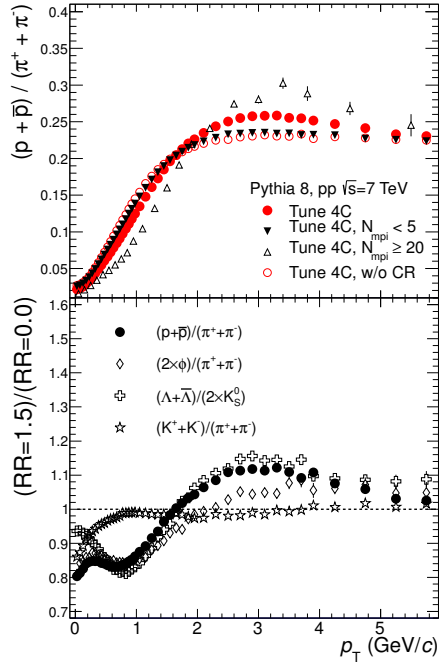


Figure 4.6: Top panel: p/π ratio in pp collisions at $\sqrt{s} = 7$ TeV as predicted by PYTHIA 8 with and without CR and considering different number of MPIs. Bottom panel: particle double ratios; ratio with CR divided by the ratio without CR. Figure taken from [52]

4.2 Color Ropes

The Lund String model prescribes color strings as 1-dimensional objects. A more sophisticated treatment of color fields is implemented in DIPSY [54, 55] and recent versions of PYTHIA 8, where strings are replaced by color flux tubes. If such tubes are overlapping, the field strength can also increase, leading to a larger effective string tension $\kappa \rightarrow \tilde{\kappa}$ in Eq. 2.10. Note that in the following section I will just introduce the idea behind the enhanced string tension, whereas a complete discussion is given in [56].

Let us consider two color flux tubes one lying atop the other and each connecting a color to an anticolor at the endpoints, $c_1 - \bar{c}_1$ and $c_2 - \bar{c}_2$ as shown in Fig. 4.7. The two distinct cases are (a) $c_1 \neq c_2$ and (b) $c_1 = c_2$. In case (a), the two colored states make an anti-color, e.g. $|r \oplus b\rangle = |\bar{g}\rangle$ and the superposition of two fields results in a color field equivalent to that of a single dipole, but with color flowing the opposite direction, see Fig. 4.7a.

In case (b), two colors are the same and the total field strength is enhanced as seen in Fig. 4.7b. Such an enhanced field flux tube is called a *color rope*, and its tension $\tilde{\kappa}$ with respect to that of a single string is given by [56]

$$\frac{\tilde{\kappa}}{\kappa} = \frac{1}{4} (p^2 + q^2 + pq + 3(p + q)) \quad (4.3)$$

where p and q are the quantum numbers defining the multiplet. In the case shown in Fig. 4.7, c_1 and c_2 are triplets, so $p = 2$, $q = 0$ and the rope tension $\tilde{\kappa}/\kappa = 5/2$. The rope then breaks one string at a time. After the first breaking, the rope tension becomes $\tilde{\kappa}/\kappa (p = 1) = 1$, so that the first rope breaks with effective tension $3\kappa/2$, while the second one – with κ .

The larger effective string tension can modify the particle production rates via string breaking. Recalling the strangeness suppression factor derived for the Lund String model in Eq. 4.2, for color ropes one can write:

$$\tilde{\rho} = \exp\left(-\frac{\pi(m_s^2 - m_u^2)}{\tilde{\kappa} \frac{\kappa}{\kappa}}\right) = \left[\exp\left(-\frac{\pi(m_s^2 - m_u^2)}{\kappa}\right)\right]^{\frac{\kappa}{\tilde{\kappa}}} = \rho^{\frac{\kappa}{\tilde{\kappa}}} \quad (4.4)$$

In collisions with a large number of MPIs, more color flux tubes are created, increasing the probability of overlap and thus resulting in larger effective rope tension κ . As seen in Eq. 4.4, larger tension leads to an enhanced production of strange particles and as $\tilde{\kappa} \rightarrow \infty$, $\tilde{\rho} \rightarrow 1$ and strange quarks

are produced at the same rate as u and d . The gradual enhancement of strange particle production is also a feature of QGP, although the origins are supposedly very different.

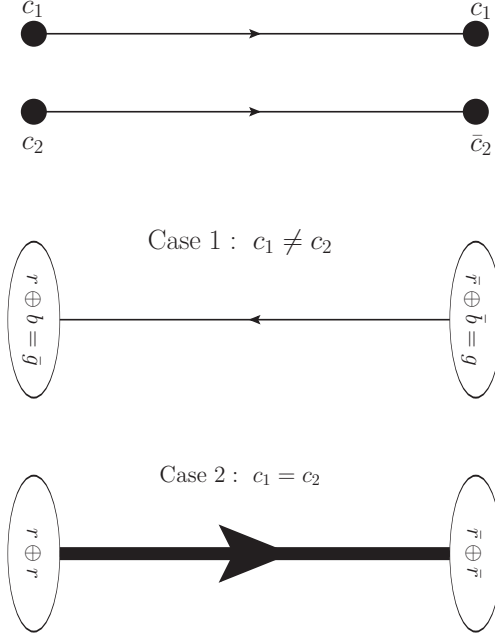


Figure 4.7: Two color dipoles $c_1\bar{c}_1$ and $c_2\bar{c}_2$ on top of each other with $c_1 \neq c_2$ (case 1) and $c_1 = c_2$ (case 2).

4.3 Boltzmann–Gibbs Blast Wave Model

One of the outcomes from studies performed at the Super Proton Synchrotron (SPS) at CERN was a phenomenological description for the transverse mass m_T and rapidity distribution dN/dy of π , p , K_s^0 , Λ and $\bar{\Lambda}$ [57, 58] measured in $^{32}\text{S} + ^{32}\text{S}$ at $\sqrt{s_{NN}} = 19.4$ GeV by the NA35 Collaboration. The model is called the blast wave model and it assumes particle production by a thermalized source, boosted in longitudinal and transverse directions. In the following section I will go step-by-step through the underlying assumptions within the model and discuss the observables that

can be extracted from BW-based studies. Note that this section and all its derivations is based on [44].

4.3.1 Thermal Source Spectra

The invariant momentum spectrum of particles radiated by a thermal source can be described as

$$E \frac{d^3N}{dp^3} = \frac{d^3N}{dy m_T dm_T d\varphi} = \frac{gV}{(2\pi)^3} E e^{-(E-\mu)/T} \quad (4.5)$$

where g is the degeneracy factor for particle species considered and μ is the chemical potential of the relevant quantum numbers. Considering that $E = m_T \cosh y$, for the m_T -differential yield of particles one can write

$$\begin{aligned} \frac{dN}{m_T dm_T} &= \frac{gV}{(2\pi)^3} \int_{-\infty}^{\infty} dy \int_0^{2\pi} d\varphi m_T \cosh y e^{-(m_T \cosh y - \mu)/T} \\ &= \frac{gV}{2\pi^2} e^{\mu/T} m_T \int_0^{\infty} dy \cosh y e^{-(m_T \cosh y)/T} = \frac{gV}{2\pi^2} e^{\mu/T} m_T K_1\left(\frac{m_T}{T}\right) \end{aligned} \quad (4.6)$$

where $K_1(x) = \int_0^{\infty} dy \cosh y e^{-x \cosh y}$ and azimuthal angular symmetry is assumed. At sufficiently large transverse momenta or for heavy hadrons, Eq. 4.6 simplifies to

$$\frac{dN}{m_T dm_T} \xrightarrow{m_T \gg T} V' \sqrt{m_T} e^{-m_T/T}. \quad (4.7)$$

One may notice that the overall particle yields are governed by the volume V' , which also includes a suppression factor $e^{\mu/T}$. On the other hand, spectral shapes are driven by the *kinetic freeze-out* temperature, which enters the expression in an exponent $e^{-m_T/T}$ and can be extracted by fitting the data. An attempt to fit a π spectrum is shown in Fig. 4.8. One sees that Eq. 4.7 provides a satisfactory description of the data in the low m_T region, but predicts a steeper slope than that observed at higher m_T . Note that in this section the spectral shapes are of interest and not the overall yields, thus the overall normalization will be treated as a free parameter and I will come back to particle yields in the next section.

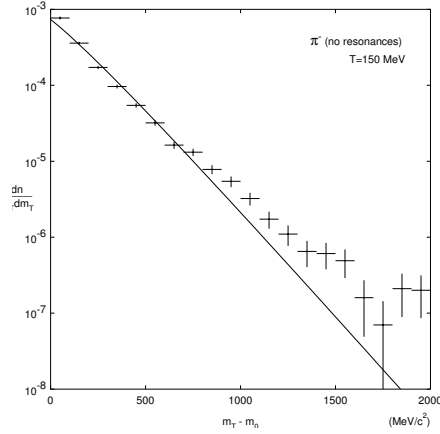


Figure 4.8: Transverse mass spectrum of π^- measured in S-S collisions at $\sqrt{s_{\text{NN}}} = 19.4$ GeV [57] with a thermal spectrum fit (solid line) given by Eq. 4.7. Figure taken from [44].

4.3.2 Feed-down from Resonance Decays

Studies reported in [59, 60] suggest that a significant fraction of light-flavor particle abundances originate from resonance hadron decays. The very short lifetimes characteristic of strong decays (10^{-23} s) make their identification extremely challenging and, as a rule of thumb, the products of strong decays are treated as primary particles by experimentalists. On the other hand, Eq. 4.7 predicts the yields of primordial hadrons only, and therefore the feed-down of the resonance decays has to be taken into account.

In the blast wave model, this enters as an additional term in particle yields:

$$\frac{d^2 N}{m_T dy dm_T} = \frac{d^2 N_{\text{primordial}}}{m_T dy dm_T} + \frac{d^2 N_{\text{FD}}}{m_T dy dm_T}. \quad (4.8)$$

The feed-down contribution can then be estimated as

$$\begin{aligned} \frac{d^2 N_{\text{FD}}}{m_T dy dm_T} &= \int_{W^{2(-)}}^{W^{2(+)}} dW^2 \int_{y_R^{(-)}}^{y_R^{(+)}} dy_R \int_{m_{T,R}^{2(-)}}^{m_{T,R}^{2(+)}} dm_{T,R}^2 \\ &\times f(W, p_R, p) \frac{d^2 N_R}{m_{T,R} dy_R dm_{T,R}} \end{aligned} \quad (4.9)$$

where the factor $f(W, p_R, p)$ represents the phase space of the resonance R decay. In this thesis, very low transverse momenta regions (populated by resonance decay products) will not be considered in the blast wave analysis.

4.3.3 Longitudinal Flow

To obtain the rapidity distribution of thermally produced particles, one can integrate Eq. 4.5 over the transverse components:

$$\begin{aligned} \frac{d^3 N}{m_T dy dm_T d\varphi} &= \frac{gV}{(2\pi)^3} E e^{-(E-\mu)/T} \\ \Rightarrow \frac{dN}{dy} &\propto \int_m^\infty m_T E e^{-E/T} dm_T \end{aligned} \quad (4.10)$$

and performing the integration yields

$$\begin{aligned} &\int_m^\infty m_T E e^{-E/T} dm_T \\ &= \frac{T^3}{\cosh^2 y} \int \frac{m_T^2}{T^2} \cosh^2 y e^{-\frac{m_T}{T} \cosh y} d\left(\frac{m_T}{T} \cosh y\right) \\ &= T^3 e^{-\frac{m}{T} \cosh y} \left[\frac{m^2}{T^2} + \frac{2m}{T \cosh y} + \frac{2}{\cosh^2 y} \right] \end{aligned} \quad (4.11)$$

where the identity $\int x^2 e^{-x} dx = -e^{-x}(x^2 + 2x + 2)$ was used. The rapidity distribution of π^- measured in S-S collisions at $\sqrt{s_{\text{NN}}} = 19.4$ GeV is shown in Fig. 4.9 together with a comparison against predictions for a purely thermal source [44]. It is clear that such source alone cannot produce the

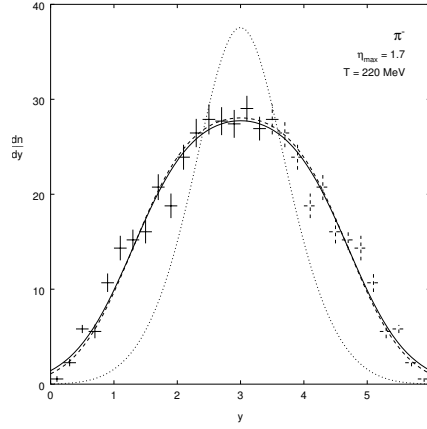


Figure 4.9: dN/dy distributions from a purely thermal source (dotted line), with longitudinal flow (dashed line) and longitudinal + resonances (solid line). Figure taken from [44].

plateau of the rapidity distributions observed in the data. To account for this, one can use the boost-invariant longitudinal expansion model postulated by Bjorken in [61], where multiple rescatterings ultimately lead to a boost-invariant longitudinal flow of the medium with locally thermalized sources. The hadron yields are then a superposition of spectra produced by these sources distributed in flow angle η . The angle is limited by the beam energy, and considering the limiting angles $\eta_{\min}, \eta_{\max} = -\eta_{\min}$, the dN/dy can be calculated as

$$\frac{dN}{dy}(y) = \int_{\eta_{\min}}^{\eta_{\max}} d\eta \frac{dN_{\text{thermal}}}{dy}(y - \eta). \quad (4.12)$$

As seen in Fig. 4.9, the measured dN/dy is well reproduced by the BW model if longitudinal expansion is considered.

For the remainder of the thesis, I will focus on particle spectra measured at central rapidities and will not study the y -dependence; any modifications originating from longitudinal flow will therefore be included in the normalization.

4.3.4 Transverse Flow

Although the blast wave model was sufficient for describing the existing data at the time of the development (light pions), it did not contain any transverse flow, which had been observed already in [62]. In a simplified case, the pressure is symmetric in the azimuthal direction and the boost of particles are studied in terms of radial flow. In practice, the asymmetries result in higher orders of flow, but for the BW model, higher orders will not be considered.

The (azimuthal symmetric) transverse boost of thermally produced particles in the BW model is implemented considering an average transverse velocity profile

$$\beta_r(r) = \beta_s \left(\frac{r}{R} \right)^n \quad (4.13)$$

where β_s is the maximum velocity at the surface of the fireball. The functional form of the profile can then be varied with n and in practice is one of the fit parameters. As in the case of longitudinal flow, one can define transverse boost angle $\rho = \tanh^{-1} \beta_r$. The isotropic velocity field in the transverse plane can then be generated as

$$u^\nu = (\cosh \rho, \cos \varphi \sinh \rho, \sin \varphi \sinh \rho, 0) \quad (4.14)$$

and the invariant momentum spectra for particles in the Boltzmann approximation is given by

$$E \frac{d^3 N}{dp^3} \approx \frac{g}{(2\pi)^3} \int e^{-(u^\nu p_\nu - \mu)/T} p^\lambda d\sigma_\lambda. \quad (4.15)$$

In the absence of transverse flow, the integration over volume in cylindrical coordinates simplifies to $p^\lambda d\sigma_\lambda = r dr d\phi dz$. For the term in the exponent one has

$$u^\nu p_\nu = m_T \cosh y \cosh \rho - p_T \sinh \rho \cos(\phi - \varphi) \quad (4.16)$$

Substituting this into Eq. 4.15, for invariant yields one has

$$\begin{aligned}
 \frac{d^3 N}{m_T dy d\varphi dm_T} &= \frac{ge^{\frac{\mu}{T}}}{(2\pi)^3} \int dz \int_0^{2\pi} d\phi \int_0^R r dr m_T \cosh y \\
 &\quad \times \exp \left[-\frac{m_T \cosh y \cosh \rho}{T} \right] \exp \left[-\frac{p_T \sinh \rho \cos(\phi - \varphi)}{T} \right] \\
 &= A \int dz \int_0^R r dr m_T \cosh y \exp \left[-\frac{m_T \cosh y \cosh \rho}{T} \right] \\
 &\quad \times I_0 \left(\frac{p_T \sinh \rho}{T} \right)
 \end{aligned} \tag{4.17}$$

where the last equality was obtained noting the azimuthal symmetry and using the modified Bessel function of the first kind:

$$I_0(z) = \frac{1}{2\pi} \int_0^{2\pi} e^{z \cos \phi} d\phi \tag{4.18}$$

Note that in Eq. 4.17, integration over z gives a constant, which can be absorbed into the normalization. To get the spectral shape, the yields are integrated over y and φ :

$$\begin{aligned}
 \frac{dN}{m_T dm_T} &= A \int dz \int_0^{2\pi} d\varphi \int_0^R r dr I_0 \left(\frac{p_T \sinh \rho}{T} \right) \\
 &\quad \times \int_{-\infty}^{\infty} dy m_T \cosh y \exp \left[-\frac{m_T \cosh y \cosh \rho}{T} \right] \\
 &= V m_T \int_0^R r dr I_0 \left(\frac{p_T \sinh \rho}{T} \right) K_1 \left(\frac{m_T \cosh \rho}{T} \right)
 \end{aligned} \tag{4.19}$$

where the modified Bessel function of the second kind K_1 was used to perform the integration over the rapidity and the azimuthal integration was done considering isotropic particle spectra. The remaining dr corresponds to the integration over the volume of the fireball, where the velocity at

each r is given by Eq. 4.13 and the expansion stops at the kinetic freeze-out surface at R . As the velocity profile depends on $\xi = r/R$, it is convenient to replace $rdr = R^2\xi d\xi$ in Eq. 4.19. The term R^2 is then absorbed into the normalization, leaving four free parameters: surface velocity β_s , its profile given by n , the freeze-out temperature T and overall normalization V . The first three parameters are characteristic of the medium and are the same for all particle species in a given collision system. Normalization, on the other hand, contains overall particle yields (among other factors) which are different for each species.

In this thesis, I will fit the BW model to π , K and p spectra simultaneously to extract the dynamical parameters of the medium. The overall normalization of the spectra will be treated as free parameters without any interpretation and a more sophisticated modeling of particle yields will be used, as discussed in the next section.

4.4 Thermal Model

Statistical (thermal) hadronization models (SHM) have successfully described hadron abundances measured in heavy-ion collisions over a wide range of energies [63, 64, 65]. Such models usually employ a grand-canonical (GC) ensemble, which requires a system size of $VT^3 > 1$ for the approach to hold. On the other hand, small systems like e^+e^- require explicit conservation of quantum numbers and are therefore described with canonical ensembles. In practice, as each of the charges in SHM is conserved separately, it is possible to have a situation where for example a large number of non-strange final state hadrons follow the grand-canonical description, while the canonical approach is required for strangeness production.

In this work, measured hadron abundances will be studied in the context of the strangeness-canonical ensemble implemented in the THERMUS code [66]. Yields of strange particles in this framework are assumed to be small and therefore strangeness conservation is explicitly imposed, while non-strange hadrons are produced in bulk and are described by the grand-canonical ensemble. The following section covers the physics implemented in THERMUS with the derivations of equations based on [66].

4.4.1 The Grand-Canonical Ensemble

In the grand-canonical ensemble, energy and quantum numbers are conserved on average in the system considered. In strong interactions, the conserved charges are baryon number B , charge number Q and strangeness number S . The partition function for a GC ensemble can be written as

$$\ln \mathcal{Z}^{\text{GC}}(T, V, \mu_h) = \sum_h \frac{g_h V}{(2\pi)^3} \int d^3p \ln \left[1 \pm e^{-\frac{(E_h - \mu_h)}{T}} \right]^{\pm 1} \quad (4.20)$$

where the sum is over all hadron species considered: $h = \pi, K, p, \dots$. Fermions follow Fermi–Dirac distribution, resulting in a (+) sign in Eq. 4.20 while a (−) sign is used for bosons. The degeneracy of the h hadron is denoted as g_h and the chemical potential is given by

$$\mu_h = B_h \mu_B + Q_h \mu_Q + S_h \mu_S. \quad (4.21)$$

Integrating over the momentum space, Eq. 4.20 becomes

$$\begin{aligned} \ln \mathcal{Z}^{\text{GC}} &= \sum_h \frac{VT g_h}{2\pi^2} \sum_{k=1}^{\infty} \frac{(\pm 1)^{k+1}}{k^2} \lambda_h^k m_h^2 K_2 \left(\frac{km_h}{T} \right) \\ &= \sum_h \sum_{k=1}^{\infty} \frac{1}{k} z_h^k \lambda_h^k \end{aligned} \quad (4.22)$$

where K_2 is the modified Bessel function of second kind and

$$\lambda_h = e^{\frac{B_h \mu_B + Q_h \mu_Q + S_h \mu_S}{T}}. \quad (4.23)$$

is *fugacity* – a quantity relating the pressure of ideal gas to the effective pressure of real gas. For $k = 1$, Eq. 4.22 becomes the Boltzmann approximation for a single-particle h partition function given by

$$z_h^1 = \frac{TV g_h}{2\pi^2} m_h^2 K_2 \left(\frac{m_h}{T} \right) \quad (4.24)$$

which has been shown to be a valid approximation for all the particles but pions [66]. The multiplicity of a hadron h is

$$N_h = T \frac{\partial}{\partial \mu_h} \ln \mathcal{Z}^{\text{GC}} = \sum_{k=1}^{\infty} z_h^k \lambda_h^k \approx z_h^1 \lambda_h \quad (4.25)$$

where the last approximation is valid in the Boltzmann limit. Note that in this prescription, any additional conserved charges enter the partition function via fugacity in Eq. 4.23.

4.4.2 The Strangeness-Canonical Ensemble

Due to low abundances of strange hadrons, strangeness in small systems has to be treated canonically. To couple the canonical prescription of strangeness conservation with grand-canonically treated charges B and Q , the partition function can be written as

$$Z_S = \frac{1}{2\pi} \int d\xi_S e^{-iS\xi_S} \times \exp \left\{ \sum_h \frac{g_h V}{(2\pi)^3} \int d^3p \ln \left[1 \pm e^{-\beta E_h} e^{\beta \mu_h} e^{iS_h \xi_S} \right]^{\pm 1} \right\}. \quad (4.26)$$

To extract the multiplicity of particle t , the exponent in the logarithm of Eq. 4.26 corresponding to the t hadron is multiplied by a fictitious fugacity $\Lambda_t = e^{\beta \mu_S}$ with $\mu_S = 0$ so that $\Lambda_t = 1$. Noting that $\beta T = 1$ and

$$\frac{d}{d\mu_s} \Lambda_t = \beta \Lambda_T \quad (4.27)$$

particle multiplicity can be calculated as

$$N_t^S = T \frac{\partial \ln Z_S}{\partial \mu_S} = \frac{1}{Z_S} \frac{\partial Z_S}{\partial \Lambda_t} = \frac{1}{2\pi Z_S} \int d\xi_S e^{-iS\xi_S} \times \exp \left\{ \sum_h \frac{g_h V}{(2\pi)^3} \int d^3p \ln \left[1 \pm e^{-\beta E_h} e^{\beta \mu_h} e^{iS_h \xi_S} \right]^{\pm 1} \right\} \times \frac{g_t V}{(2\pi)^3} \int d^3p \frac{e^{-\beta E_t} e^{\beta \mu_t} e^{iS_t \xi_S}}{1 \pm e^{-\beta E_t} e^{\beta \mu_t} e^{iS_t \xi_S}} \quad (4.28)$$

where the last term can be expressed as

$$\begin{aligned}
& \frac{g_t V}{(2\pi)^3} \int d^3 p \frac{e^{-\beta E_t} e^{\beta \mu_t} e^{i S_t \xi_S}}{1 \pm e^{-\beta E_t} e^{\beta \mu_t} e^{i S_t \xi_S}} \\
&= \sum_{k=1}^{\infty} \frac{g_t V}{(2\pi)^3} \int d^3 p (\mp 1)^{k+1} e^{-k\beta E_t} e^{k\beta \mu_t} e^{ik S_t \xi_S} \\
&= \sum_{k=1}^{\infty} \frac{TV g_t}{2\pi^2} \frac{(\mp 1)^{k+1}}{k} m_t^2 K_2 \left(\frac{k m_t}{T} \right) e^{k\mu_t} e^{ik S_t \xi_S} \\
&= \sum_{k=1}^{\infty} z_t^k e^{k\beta \mu_t} e^{ik S_t \xi_S}
\end{aligned} \tag{4.29}$$

and the last equality was obtained considering the particle partition function in GC ensemble given in Eq. 4.22. Substituting the result into Eq. 4.28 yields

$$\begin{aligned}
N_t^S &= \frac{1}{2\pi Z_S} \int d\xi_S e^{-i S \xi_S} \dots \times \sum_{k=1}^{\infty} z_t^k e^{k\beta \mu_t} e^{ik S_t \xi_S} \\
&= \sum_{k=1}^{\infty} \frac{1}{2\pi Z_S} \int d\xi_S e^{-i(S-kS_t)\xi_S} \dots \times z_t^k e^{k\beta \mu_t} = \\
&= \left(\frac{Z_{S-S_t}}{Z_S} \right) N_t^{\text{GC}}|_{\mu_S=0}
\end{aligned} \tag{4.30}$$

and strange hadron yields turn out to be the same as in the GC ensemble with the strangeness chemical potential set to $\mu_S = 0$ and suppressed by a factor Z_{S-S_t}/Z_S . Moreover, in the large volume limit at high temperatures,

$$\lim_{V \rightarrow \infty} \left(\frac{Z_{S-S_t}}{Z_S} \right) = e^{\beta S_t \mu_S} \tag{4.31}$$

and the multiplicities approach the grand-canonical limit.

4.4.3 Excluded Volume Corrections

At high energies, the medium created in nucleus-nucleus collisions cannot be treated as an ideal gas and a van der Waals volume correction [67, 68, 69]

has to be taken into account. The volume corrections enter the model in the partition function by substitution

$$V \rightarrow V - \sum_h v_h N_h \quad (4.32)$$

where h runs over all particle species considered and $v_h = 4/3 \cdot \pi r_h^3$ is the volume of h hadron. This corresponds to particles being extended objects, so that the total gas volume is reduced by the volume of hadrons created. A commonly used value for the hadronic volume is given by the hard cross section of a proton, $r_h = 0.3$ fm [70]. In general, for a given T and μ , all thermodynamical properties of a hadron gas are reduced compared to those of an ideal gas, and the differences become more significant with increasing volume.

The exclusion of hadronic volume results in a shift of chemical potentials, which can be found by solving the set of equations

$$\begin{cases} P(T, \{\mu\}) = \sum_h P_h^{\text{ideal}}(T, \tilde{\mu}_h) \\ \tilde{\mu}_h = \mu_h - v_h P(T, \{\mu\}) \end{cases} \quad (4.33)$$

The particle partition function (for simplicity in the Boltzmann approximation) then becomes

$$\begin{aligned} z_t^1 \left(V \rightarrow V - \sum_h v_h N_h \right) &= \frac{T g_h}{2\pi^2} m_h^2 K_2 \left(\frac{m_h}{T} \right) \left(V - \sum_h v_h N_h \right) \\ &= z_t^1 - z_t^1 \sum_h \frac{v_h N_h}{V} = \frac{z_t^1}{1 + \sum_h v_h n_h} \end{aligned} \quad (4.34)$$

where $n_h = N_h/V$ is particle multiplicity density. Then, accounting for excluded volume, particle t multiplicity density in the system can be estimated as

$$n_t(T, \{\mu\}) = \frac{T}{V} \frac{\partial}{\partial \mu_t} \ln Z(T, \tilde{\mu}) = \frac{n_t^{\text{ideal}}(T, \tilde{\mu}_t)}{1 + \sum_h v_h n_h^{\text{ideal}}(T, \tilde{\mu}_h)} \quad (4.35)$$

where n^{ideal} is calculated for ideal gas, but with a modified chemical potential. The following results in two suppression factors: the shifted potential $\tilde{\mu}$ and the denominator $1 + \sum v n$. Note, however, that while $\tilde{\mu}$ effects are species-dependent, the denominator is constant for all the hadrons considered and therefore cancels in particle ratios.

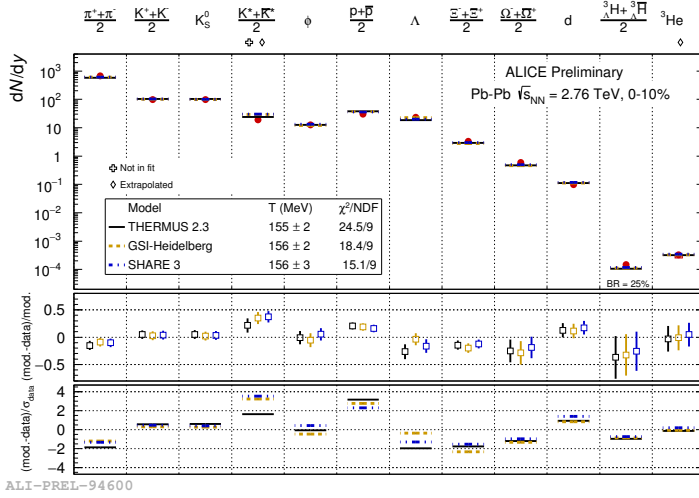


Figure 4.10: Integrated particle yields in 0–10% centrality Pb-Pb collisions at $\sqrt{s_{\text{NN}}} = 2.76$ TeV measured by ALICE in comparison with thermal model predictions. The parameters for the model (T and r) were extracted by fitting the measured yields with the model.

4.4.4 Model Predictions and the Data

Thermal model predictions for hadron yields in comparison with those measured in 0–10% centrality (see Section 5.2.1 for the definition) Pb-Pb collisions at $\sqrt{s_{\text{NN}}} = 2.76$ TeV are shown in Fig. 4.10. The temperature T and radius r were obtained by fitting the data with the model. The obtained chemical freeze-out temperature $T = 155 \pm 2$ MeV is similar to that previously observed in RHIC [71, 72]. The model is found to describe the data within 2σ for most of the hadrons and is slightly worse for protons. A good agreement between the model and the data suggests that in Pb-Pb collisions hadrons are produced in a chemically equilibrated QGP.

As the Ω hyperon has the largest number of strange quarks, it is the most affected by strangeness modification mechanisms. The measured $(\Omega^- + \bar{\Omega}^+)/(\pi^- + \pi^+)$ ratios in Pb-Pb collisions at $\sqrt{s_{\text{NN}}} = 2.76$ TeV saturate as shown in Fig. 4.11, suggesting that no strangeness suppression is present at these multiplicities. This means that the system in this region is fully equilibrated and therefore particle production in the thermal model

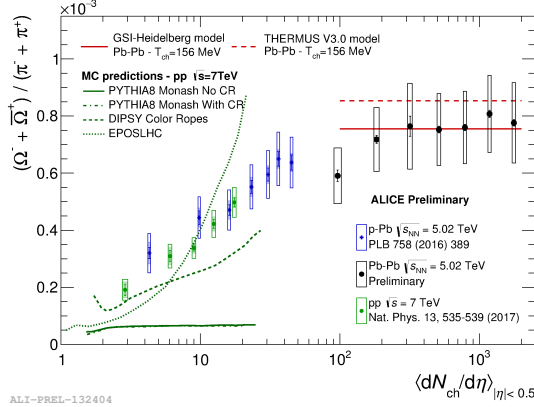


Figure 4.11: Integrated $(\Omega^- + \bar{\Omega}^+)/(\pi^- + \pi^+)$ ratios as a function of multiplicity in pp collisions at $\sqrt{s} = 7$ TeV, p-Pb collisions at $\sqrt{s_{NN}} = 5.02$ TeV and Pb-Pb collisions at $\sqrt{s_{NN}} = 2.76$ TeV measured by ALICE.

approaches the grand-canonical limit.

In smaller systems like p-Pb collisions at $\sqrt{s_{NN}} = 5.02$ TeV, Ω yields are suppressed in a multiplicity-dependent manner. As there is no mechanism facilitating the observed suppression in GC model, the strangeness-canonical (SC) approach is a natural choice. The current implementation of THERMUS code considers two effective volumes in the strangeness-canonical approach: fireball freeze-out volume $V_f \propto r^3$ and correlation volume $V_c \propto r_c^3$. The freeze-out volume governs the conservation of B and Q in the grand-canonical way, providing an overall normalization for hadron multiplicities, while strangeness is conserved in the V_c . In previous studies [73, 74] it has been suggested that $V_c < V_f$ is required to explain the observed strangeness suppression. A comparison between the particle yields measured in 20–40% centrality p-Pb collisions at $\sqrt{s_{NN}} = 5.02$ TeV and model predictions for grand-canonical and strangeness-canonical ensembles is shown in Fig. 4.12. All the predictions were fit to the data to extract the relevant parameters: T and r for GC; T , r and r_c for SC.

An alternative way to modify the strange hadron production is by allowing the strangeness to be produced out of equilibrium. This is done by multiplying Boltzmann factors by a factor γ_s^n , where $n = |S_h|$ is the total number of strange (and anti-strange) valence quarks in a hadron. By

setting $\gamma_s < 1$, the production of strange hadrons is suppressed and the effect is more pronounced for particles with a larger strangeness content. Note that in such cases, both ϕ and Ξ are suppressed by γ_s^2 . In addition, setting $\gamma_s > 1$ results in enhancement, whereas $\gamma_s = 1$ in fully equilibrated strangeness production.

Comparison between the measured yields and thermal model predictions using the GC ensemble and γ_s suppression is also shown in Fig. 4.12. Under each assumption, the model agrees with the data within 2–3 standard deviations for most of the hadrons. This suggests that if particle production takes place in the medium, the medium is chemically and thermally equilibrated. Note, however, that the agreement between the model and the data does not *imply* particle production by an equilibrated medium. In fact, it has been shown in [75] that hadron abundances are well described by thermal models even in e^+e^- collisions, which might indicate that the agreement between the statistical hadronization and the perturbative particle production has a different origin.

It is also worth mentioning that although using $r_c \neq r_f$ or $\gamma_s < 1$ has become a norm in thermal model analyses, there is little argumentation from the physical point of view for any of the choices apart from a better agreement with the data.

4.5 Core-Corona Model

In the thermal hadronization model, the underlying assumption is that the medium comes to a thermal equilibrium stretching throughout the whole system and the geometry does not play a role. It has been argued in [76] that this is not necessarily the case: nucleons that are on the surface of the fireball exhibit far less rescatterings than those at the core of the fireball, and therefore will not equilibrate with the environment. This leads to two competing mechanisms for particle production: thermal production inside the medium (core) and the conventional¹ pp-like collisions on the surface of the medium (corona). The model addressing particle yields as a superposition of the two components is called the core-corona model.

The contributions of core and corona to the number of final state

¹By “conventional” it is meant that no collective-like effects are assumed to be present in pp collisions.

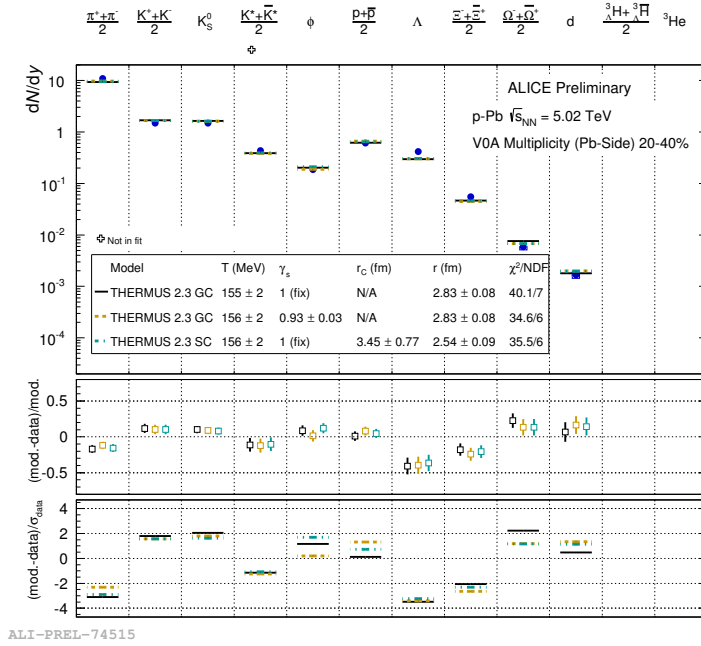


Figure 4.12: Thermal model predictions using grand-canonical, grand-canonical with γ_s and strangeness-canonical approaches for 20–40% centrality p-Pb collisions at $\sqrt{s_{NN}} = 5.02$ TeV with comparison to the measured particle yields. In each case, the parameters were fit to the data in order to get the best description.

particles is dependent on the centrality². In particular, as the fireball grows in size, the relative number of surface nucleons decreases, and head-on heavy-ion collisions are dominated by the core production. On the other hand, pp collisions where no medium is created can serve as the baseline for the corona production, as no core is present.

Defining the relative contribution of the core to the final state yields as f_{core} implies $f_{\text{corona}} = 1 - f_{\text{core}}$. In practice, these fractions can be extracted, for example, using Glauber Monte Carlo simulations. The multiplicity at given centrality is

$$\begin{aligned} \frac{dN}{dy}(N_{\text{part}}) = & N_{\text{part}} [f_{\text{core}}(N_{\text{part}}) M_{\text{core}} \\ & + (1 - f_{\text{core}}(N_{\text{part}})) M_{\text{corona}}] \end{aligned} \quad (4.36)$$

where M_{core} and M_{corona} are the core and corona multiplicities per colliding nucleon (participant). Nucleons with only one binary collision give M_{corona} and the core multiplicity is calculated by solving Eq. 4.36 for M_{core} . Note that although only the total yields of hadrons have been considered, the same can be done for transverse momentum spectra. In such case, the same technique applies, but particle multiplicities are replaced by the p_T spectra:

$$M = \frac{1}{N_{\text{part}}} \frac{dN}{dy} \Rightarrow M'(p_T) = \frac{1}{N_{\text{part}}} \frac{d^2N}{dy dp_T}(p_T). \quad (4.37)$$

Implementation in EPOS MC

One of the MC generators that will be used in comparison with the results presented in this thesis is EPOS LHC [77], which employs the core-corona prescription similar to that described above, but the initial state is treated in a different manner.

In EPOS, partonic scatterings create color fields, often called flux tubes [78]. If many partonic interactions are involved, volumes with high and low density tubes are formed as shown in Fig. 4.13 [79] for Pb-Pb, but conceptually similar in pp. The volume with high density of tubes is then regarded as the core and subjected to full hydrodynamical evolution, while in the low density volume (corona) tubes are allowed to fragment in a similar manner as Lund Strings described in Section 4.1.

²This will be discussed in Section 5.2.1

Throughout this thesis, a particular adaptation of the model, EPOS LHC, will be used. This adaptation does not include a full hydrodynamical treatment of the core, but instead includes a parametrization of flow as described in [77]. The particle production in the core is treated not by string fragmentation, but using a statistical hadronization model described by the grand-canonical ensemble as described in Section 4.4.1.

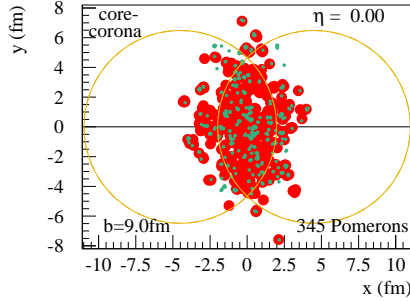


Figure 4.13: Color flux tube distribution in Pb-Pb collisions, but also similar in pp. Core is represented in red, corona in green [79]

Generalizing Core-Corona to pp Collisions

In this study, I will use the core-corona model to describe p_T -integrated particle yield ratios. Assuming f to be a core fraction for a given multiplicity (centrality) from a Glauber MC, the hadron a to hadron b ratio can be written as

$$\begin{aligned}
 R &= \frac{M^a}{M^b} = \frac{f M_{\text{core}}^a + (1-f) M_{\text{corona}}^a}{f M_{\text{core}}^b + (1-f) M_{\text{corona}}^b} \\
 &= \frac{f R_{\text{core}}}{f + (1-f) \frac{M_{\text{corona}}^b}{M_{\text{core}}^b}} + \frac{(1-f) R_{\text{corona}}}{f \frac{M_{\text{core}}^b}{M_{\text{corona}}^b} + 1-f}.
 \end{aligned} \tag{4.38}$$

Redefining the core fraction as

$$f' = \frac{f}{f + (1-f) \frac{M_{\text{corona}}^b}{M_{\text{core}}^b}} \tag{4.39}$$

one can calculate

$$1 - f' = \frac{1 - f}{f \frac{M_{\text{corona}}^b}{M_{\text{core}}^b} + (1 - f)} \quad (4.40)$$

so that Eq. 4.38 becomes

$$R = f' R_{\text{core}} + (1 - f') R_{\text{corona}} \quad (4.41)$$

but the core fraction for the ratio has slightly different shape than the one for the yields. Considering that the yield of π 's in central Pb-Pb collisions at $\sqrt{s_{\text{NN}}} = 2.76$ TeV is larger than the one measured in pp collisions at $\sqrt{s} = 7$ TeV by several orders of magnitude, in the extreme limits of pure core (corona) production $f' \rightarrow 1(0)$. Moreover, in order to remove model dependence, in the following chapters I will distance myself from using Glauber MC to estimate f and instead extract it in a data-driven way as will be described in Section 9.2.

Chapter 5

The ALICE Detector

5.1 A Large Ion Collider Experiment

A Large Ion Collider Experiment, *ALICE* [80], is a heavy-ion optimized experiment at the Large Hadron Collider at the European Organization for Nuclear Research, CERN. It has excellent particle identification (PID) capabilities in a wide transverse momentum range ($0.15 \lesssim p_T \lesssim 20 \text{ GeV}/c$) and even higher reach ($p_T \lesssim 100 \text{ GeV}/c$) for unidentified charged hadrons¹. ALICE is designed to operate in very high multiplicity environment, which in Pb-Pb collisions can be as large as $dN_{\text{ch}}/d\eta \sim 1600$ [81]. The set-up of the detector is illustrated in Fig. 5.1.

The two main parts of the ALICE detector system are the central barrel and the muon arm. In addition, there are forward detectors used for multiplicity measurements and triggering: the Forward Multiplicity Detector (FMD), the Photon Multiplicity Detector (PMD), the timing and trigger detector T0, the multiplicity estimator VZERO and the Zero-Degree Calorimeter (ZDC). The central barrel provides full azimuthal coverage in the pseudorapidity region $|\eta| < 0.9$. It is situated inside the solenoid magnet L3, which creates a $B = 0.5 \text{ T}$ magnetic field parallel to the beam axis in the central region. The L3 magnet plays two important roles: it bends the trajectory of charged particles in the transverse plane so that their momenta can be estimated; also, it suppresses the diffusion of secondary electrons in the time-projection chamber as will be discussed later. The

¹The limit is set by the momentum resolution.

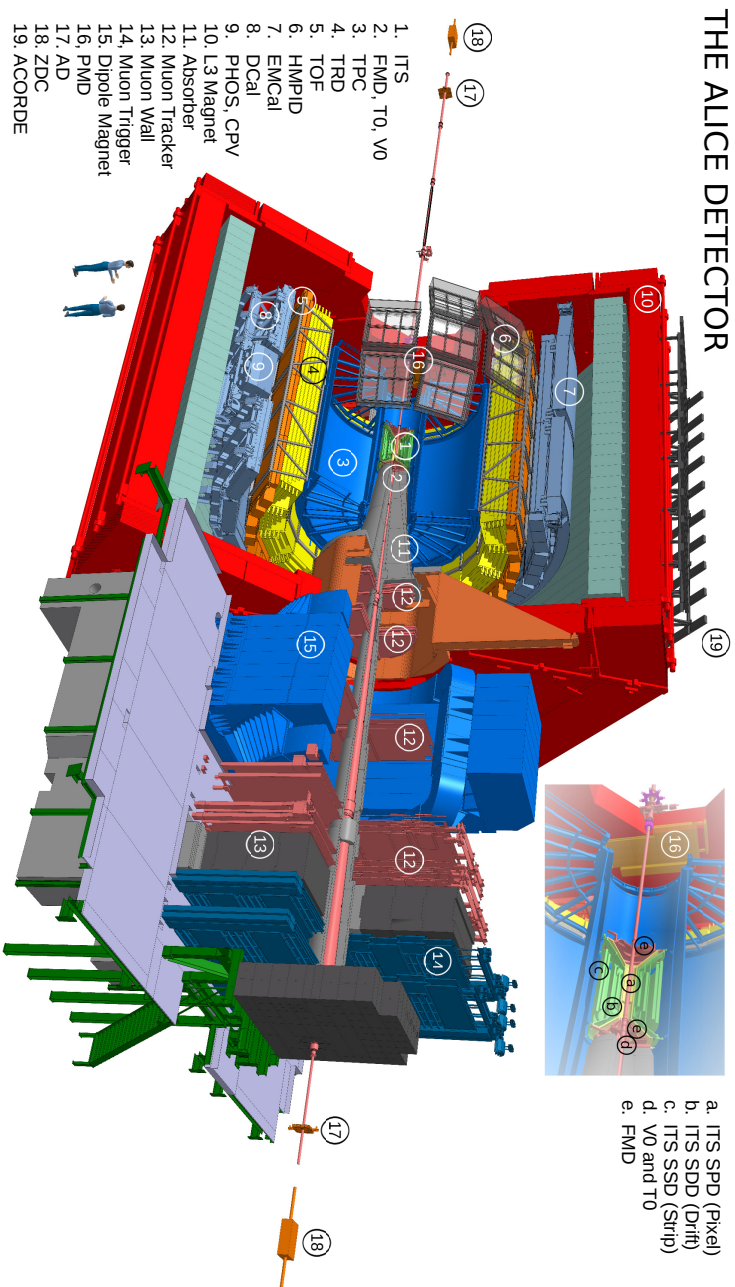


Figure 5.1: Sketch of the ALICE detector. Figure taken from [82].

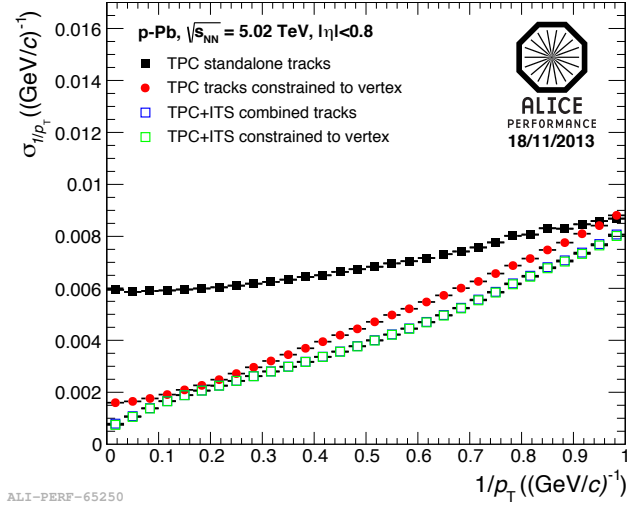


Figure 5.2: p_T -inverse resolution of reconstructed tracks as a function of $1/p_T$ for TPC standalone and combined TPC-ITS tracks, measured in p-Pb collisions at $\sqrt{s_{NN}} = 5.02$ TeV. Figure taken from [83].

relatively low B -field is optimized for heavy-ion collisions where the focus is on low and intermediate hadron momenta; the compromise is on performance at very high p_T . The inverse- p_T resolution σ_{1/p_T} as a function of $1/p_T$ measured in p-Pb collisions at $\sqrt{s_{NN}} = 5.02$ TeV in ALICE is shown in Fig. 5.2 [83]. The σ_{1/p_T} is related to the p_T resolution σ_{p_T} as

$$\frac{\sigma_{p_T}}{p_T} = p_T \sigma_{1/p_T} \quad (5.1)$$

The cartesian coordinate system in ALICE with $(x, y, z) = (0, 0, 0)$ coinciding with the center at the central barrel is defined as: the z -axis points along the beam-line away from the muon arm, the x -axis points towards the center of the LHC ring, and the y -axis points upwards, orthogonal to the xz plane.

The detectors in the central barrel are used for particle tracking, identification and triggering and consist of the following subsystems:

- The Inner Tracking System (ITS), which consists of Silicon Pixel

Detector (SPD), Silicon Drift Detector (SDD) and Silicon Strip Detector (SSD)

- The Time–Projection Chamber (TPC)
- The Transition Radiation Detector (TRD)
- The Time-of-Flight detector (TOF)
- The High-Momentum Particle Identification Detector (HMPID)
- The Photon Spectrometer (PHOS)
- The Electromagnetic Calorimeter (EMCAL).

In the following chapter, I will focus on the detectors used for the PID analysis presented in this thesis and the VZERO used for triggering and multiplicity estimation.

5.1.1 The Inner Tracking System

The ITS [80, 84] is the closest detector to the interaction point and consists of three subsystems: the SPD, SDD and SSD as shown in Fig. 5.3. Each one of the subsystems contains two concentric layers of silicon detectors, a summary of their positions and resolution is given in Table 5.1. Overall, the ITS serves the following purposes:

- Tracking at midrapidity $|\eta| < 0.9$
- Primary and secondary vertex finder with resolution $\sim 100 \mu\text{m}$ in $r\varphi$ and z directions
- Low p_{T} ($\lesssim 1 \text{ GeV}/c$) PID via (non-relativistic) energy energy loss in SDD and SSD (particles not entering the TPC)
- Triggering (SPD).

The **SPD** consists of 60 staves positioned in two layers around the beam axis, with the inner (outer) layer containing 20 (40) staves and covering $|\eta| < 1.98$ (1.31) regions respectively. A single staff is formed by four ladders, containing five readout chips each. An individual chip is $200 \mu\text{m}$ thick and has 256×32 pn -type diode cells, with each cell covering $50 \times$

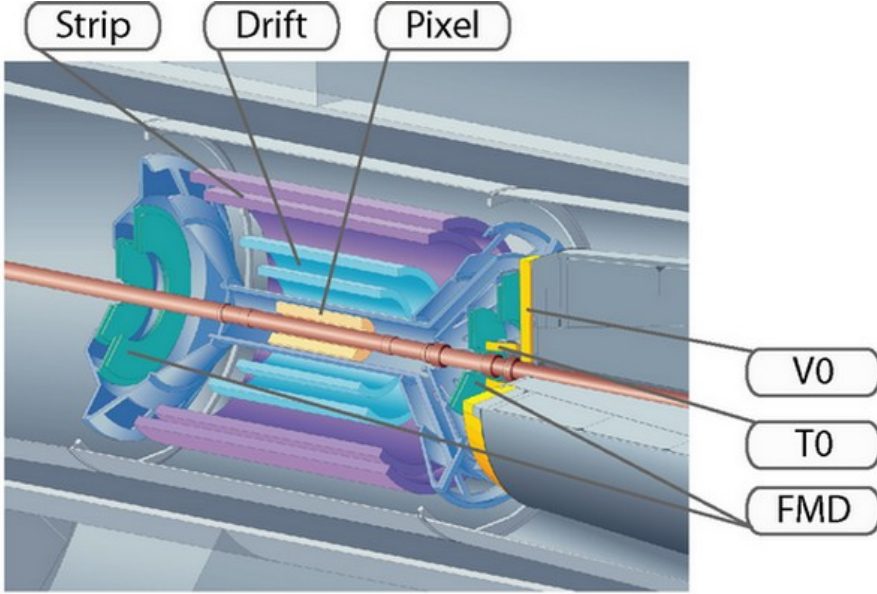


Figure 5.3: Schematic layout of the ITS. FMD, T0 and V0 also shown. Figure taken from [85].

Table 5.1: Spatial positions and resolution of different parts of the ITS detector. Values taken from [86]

	SPD	SDD	SSD
Radius r (cm)	3.9 and 7.6	15.0 and 23.9	38.0 and 43.0
Length z (cm)	24.5	44.4 and 59.4	86.2 and 97.8
Spatial resolution $r\varphi$ (μm)	12	35	20
Spatial resolution z (μm)	100	25	830

425 (μm) in the $r\varphi$ and z directions respectively. The signal in each SPD cell is compared to a preset threshold value, and the response is a logical 0 or 1.

Overall, the SPD consists of ~ 9.8 million cells that are read out by 1200 chips and has a total surface area of 0.24 m^2 . Due to such fine granularity, the SPD is able to operate in very dense charged-particle environment ($\lesssim 80 \text{ cm}^{-2}$) and can also reconstruct secondary vertices originating from heavy flavor decays.

The **SDD** equips the two middle layers of ITS and consists of two dimensional sensors providing high resolution coordinates. The inner (outer) layer of the SDD comprises 14 (22) ladders, each of them supporting six (eight) sensors with $7.02 \times 7.53 \text{ cm}^2$ active area. The sensor area is divided into two drift regions of 35 mm, each equipped with 256 anode wires. Electrons created by a particle traversing the $300 - \mu$ -thick sensor drift in the 500 V/m E -field towards the anodes, and by measuring the drift time, one can calculate the distance between the electrode and the ionization point. For electrons drifting the maximum distance of 35 mm with the speed $v_e \approx 6.6 \mu\text{m/ns}$, the maximum drift time is $t_{\text{max}} \approx 5.3 \text{ ns}$ [87]. The second coordinate can be obtained from the centroid of the charge collected by neighboring electrodes. Such a design requires fewer readout channels (since the information is also spread out in the time domain) and also lower power consumption compared to, for example, pixel detectors, while still offering good spatial resolution.

The **SSD** occupies the two outermost layers of the ITS. Layer 5 (6) consists of 34 (38) ladders, with every ladder supporting 22 (25) sensor modules. Each module is a $300 - \mu$ -thick silicon wafer with an active area of $73 \times 40 \text{ mm}^2$ and 768 parallel strips on each side. The angle between N- and P-side strips is 35 mrad and each P-strip crosses 15 N-strips. In order to reconstruct the ionization points, consecutive fired strips on each side are grouped together. If groups of strips from opposite sides cross, the spatial coordinates of the ionization point are calculated as a mean value of strip coordinates, weighted by the signal strength in each of the strips. The charge associated with the space point is calculated as the mean value on P- and N-strips², and in the case where a group of strips on one side is crossed by several groups on the other side, only one side is used for

²Note that electrons and holes have different gain factors, and therefore charges collected in P- and N-sides need to be normalized.

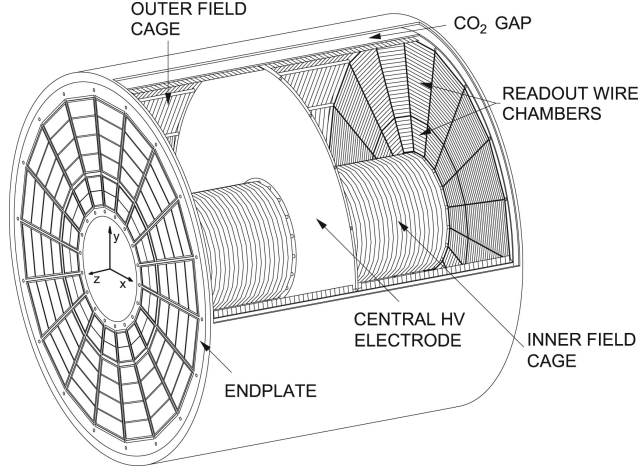


Figure 5.4: Schematic view of the TPC. Figure taken from [88].

charge estimation. Such a scenario is only important in Pb-Pb collisions, since the track density in pp collisions is very low.

5.1.2 The Time-Projection Chamber

The time-projection chamber is one of the main detectors of ALICE, offering both tracking and PID capabilities. It is made of a large 5 meter long hollow cylinder with inner and outer radii of 85 and 250 cm respectively. The schematic view of the TPC is shown in Fig. 5.4.

There are two main parts of the TPC: the field cage and the readout chambers. In the middle of the field cage ($z = 0$), there is a central electrode, splitting the whole volume into two 2.5 meter long parts. The central electrode is biased at -100 kV, creating a 400 V/m strength electric field, perpendicular to the cathode pads in the readout chambers. In the vicinity of the inner/outer TPC walls, the homogeneity of the electric field is obtained using matching potential strips biased by a voltage divider.

The whole TPC volume is filled with a mixture of Ne, Ar and CO_2 gas, varying the composition for optimization. CO_2 is a non-organic quencher with good aging properties, while Ne has a faster ion drift and Ar induces greater ionization, which requires lower amplification voltage and results in better detector stability. A charged particle traversing the volume will

ionize the gas along its curved trajectory. The electrons will drift towards the readout chambers and collide with other gas constituents, so that their average drift velocity is given by

$$v_e = \mu_e E \quad (5.2)$$

where E is the electric field and $\mu_e = e\tau/m_e$ is the electron mobility in the given gas and τ is the average time between the collisions. The ions will drift towards the central electrode, but at lower speeds due to their much larger mass.

Because multiple collisions occur, the drifting electron cloud, which initially is assumed to be point-like, will diffuse in all directions. After time t the electron cloud shows a gaussian density distribution ρ in the transverse plane xy given by [89]:

$$\rho(xy) \propto \frac{1}{D_{xy}t} \exp\left(-\frac{x^2 + y^2}{4D_{xy}t}\right) \quad (5.3)$$

where D_{xy} is the diffusion coefficient in the transverse plane. The L3 magnetic field parallel to the electric field will suppress the transverse diffusion by a factor

$$\frac{D_{xy}(\omega)}{D_{xy}(0)} = \frac{1}{1 + \omega^2\tau^2} \quad (5.4)$$

where $\omega = eB/m_e$ is the cyclotron frequency. This is a small effect in ALICE since the magnetic field is not very strong.

The readout chambers of TPC are Multi Wire Chamber working in Proportional mode (MWPC), illustrated in Fig. 5.5, which consists of gating, cathode, anode wire planes and the cathode pad plane. The gating grid can be biased to alternating positive and negative voltage or on a fixed negative potential; in the former case the grid is said to be closed while in the latter it is open. In the former case, electrons arriving at the readout chamber are collected at the grid and do not enter the MWPC. When the gating grid is open, the electrons enter the readout chamber and drift towards the anode wires, which are biased to +1500 V. The decision whether the grid should be opened or closed is made by an external trigger (e.g. SPD or VZERO).

In the vicinity of the anode wires, the electric field grows as $1/r$ and electrons start an avalanche. Because the chamber is working in the pro-

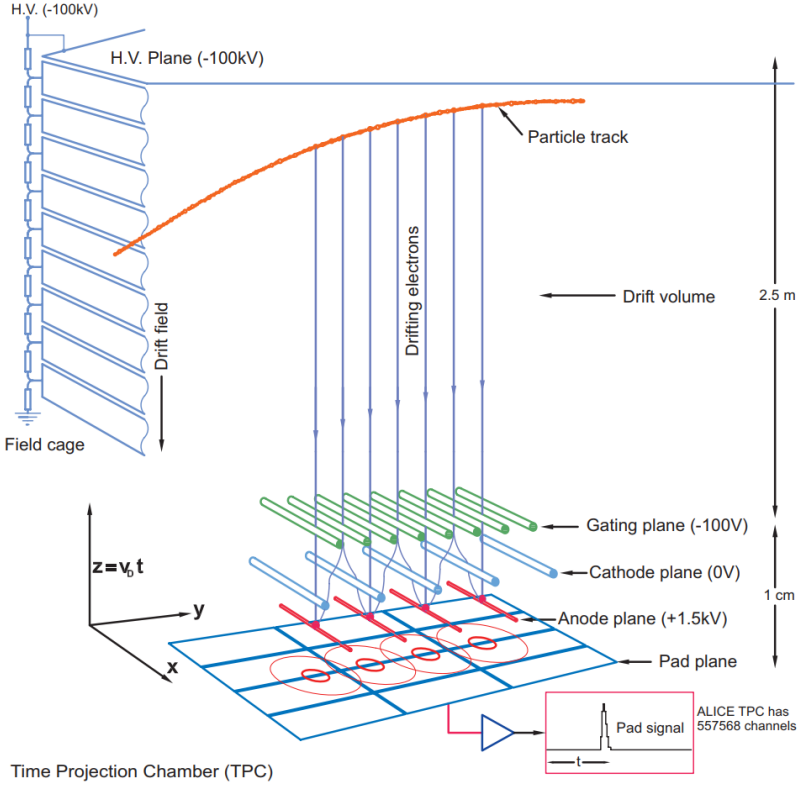


Figure 5.5: An illustration of an ionizing particle in the TPC. The gating grid is opened, electrons drift to the readout chambers and start an avalanche. The holes from the avalanche are collected at the pad rows. Figure taken from [90]

portional mode, the number of secondary electrons and ions created during the avalanche will be proportional to the number of ionizations by the primary track, and therefore will carry the information on the energy lost by the incident particle per unit length, dE/dx .

The secondary ions created during the avalanche induce a signal on the cathode pad rows. In each readout chamber there are 159 pad rows distributed in the radial direction. The 2D coordinates (in the xy plane) of the ionization point can be calculated as weighted centroids from the charge collected on the pads, while the z coordinate can be calculated measuring the drift time. Note that both the 3D position and the charge are read out on the cathode pads. The shaping time of the electronics (160 ns) allows signal integration matched to the time evolution of the avalanche.

During the avalanche near the anode wires, a number of photons are also produced. If these photons escape the avalanche regions, they can ionize more gas molecules or reach the electronics, ultimately leading to an avalanche breakdown (c.f. Geiger mode) and damage to the detector. In the ALICE TPC, this effect is quenched by the CO_2 gas, which has a large photoabsorption cross section and minimizes the number of escaping photons.

Typically, the grid is opened for around $\sim 90 \mu\text{s}$ – this is the time required for the electrons to drift from the middle of the field cage to the readout chambers. Afterwards, the grid closes, which in turn also prevents the vast majority of the ions created during the avalanche from drifting back into the field cage. This is very important, as the ions escaping into the main volume would distort the E -field and the TPC tracking capabilities would degrade. Overall, it takes $\sim 190 \mu\text{s}$ to clear the readout chambers from the secondary ions, which results in the highest allowed TPC event rate of $\sim 3.6 \text{ kHz}$ (compared to $\sim 1 \text{ kHz}$ allowed by the data readout).

5.1.3 The Time-Of-Flight Detector

The ALICE Time-Of-Flight detector is a set of 1593 Multigap Resistive Plate Chambers (MRPCs) combined into 87 gas-tight modules and distributed on a surface of 141 m^2 with an inner radius of 3.7 m and pseudorapidity coverage $|\eta| < 1$. The whole TOF structure is divided into 18 supermodules in azimuthal angle, each of which is 9 meter long and con-

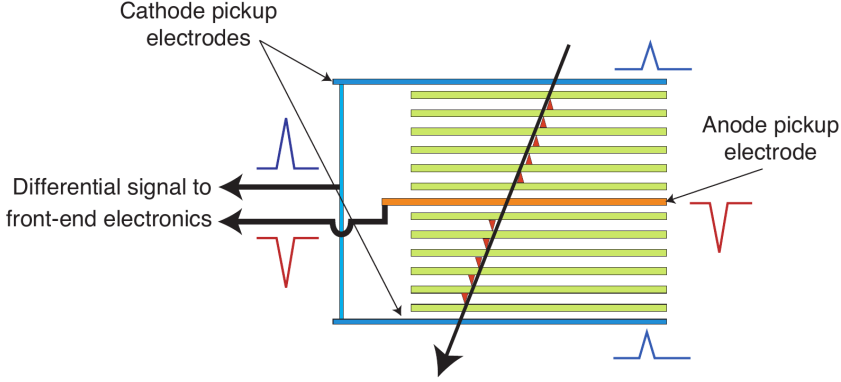


Figure 5.6: Schematic view of a single MRPC module with a traversing particle. Figure taken from [92].

tains five modules, except for the three supermodules that contain three modules to reduce the material budget for PHOS.

Each MRPC contains two stacks of high volume resistivity glass plates ($\sim 10^{13} \Omega \text{cm}$) operating like parallel-plate avalanche detectors. The stacks are separated by a pickup anode and the external surfaces are covered with cathodes as shown in Fig. 5.6. In each stack, there are six 0.4 mm thick glass plates separated by $250 \mu\text{m}$ wide gaps, filled with $\text{C}_2\text{H}_2\text{F}_4$ (93%) and SF_6 (7%) [91]. The role of the resistive glass plates is to quench the avalanche, while still being transparent to the fast signals induced on the pickup electrodes. Such MRPC can operate under very high electric fields ($\sim 100 \text{ kV/cm}$) and have time resolution $< 100 \text{ ps}$. The output signal of the MRPC is the sum of the signals from each of the gaps and the efficiency increases with the number of gaps. However, another important factor to consider is that the time jitter in each of the gaps will worsen the time resolution, and therefore the width of the gaps should be kept small.

In general, the TOF detector only measures the arrival time of particles and the position. In order to get the time-of-flight of the particle, one has to measure the time when the collision happened. For time-of-flight measurements, this is done in two ways:

- With the T0 detector
- Calculating the collision time using TOF arrival time of several particles

and their tracking information

The T0 detector is essentially two cylindrical arrays of 12 Cherenkov quartz counters. The arrays cover pseudorapidity regions $4.6 \leq \eta \leq 5$ (T0A) and $-3.2 \leq \eta \leq -2.9$ (T0C) and measure the collision time with a resolution of ~ 35 ps. The drawback of T0 start time estimation is that due to low pseudorapidity coverage, especially in low-multiplicity pp collisions, the T0 might not trigger.

Alternatively, the collision time t_{ev} can be estimated combinatorially using the measured TOF arrival time and using tracking information. For a track j , one calculates the χ^2 as

$$\chi^2 = \sum_{n \neq j} \frac{((t_{n,\text{TOF}} - t_{\text{ev}}) - t_{n,\text{exp}}(m_i))^2}{\sigma_{\text{TOF}}^2 + \sigma_{\text{exp}}^2} \quad (5.5)$$

where the sum loops over all the tracks except j ; $t_{n,\text{TOF}}$ is the measured TOF arrival time of the n -track; and $t_{n,\text{exp}}(m_i)$ is the *expected flight time* for a particle under mass hypothesis m_i ($i = \pi, K, p$). The global minimization attempts to determine the event time that will make all tracks deviate the least from a mass hypothesis, varying the mass hypothesis for each track. Such estimation is only applicable in events with at least three tracks that have an associated TOF signal.

In general, the start times of events are obtained by combining the start time estimates from T0 and TOF and weighting them by respective resolutions. In case neither T0 nor TOF estimates exist, the run-average t_{ev} is used but with much worse resolution [91].

5.1.4 VZERO Multiplicity Estimator

The ALICE VZERO detector (often called just V0) is comprised of two plastic scintillator hodoscopes positioned at $2.8 < \eta < 5.1$ (V0A) and $-3.7 < \eta < -1.7$ (V0C). Each hodoscope is divided into four rings in the radial direction, and each ring is segmented into eight sections with every section connected to a photomultiplier tube (PMT).

A charged particle traversing the detector loses energy in the scintillator material exciting the molecules. The de-excitation emits light, which is guided to the PMTs. A photon reaching the cathode of a PMT can kick out a photoelectron, which will then be accelerated in the tube and produce

more electrons each time it hits a dynode on its way, ultimately resulting in a measurable signal on the anode of the PMT.

The advantages of plastic scintillators are their short relaxation times (typically $2 - 4$ ns) and large light output. Most of the particles entering the VZERO scintillators will be highly relativistic ($\beta \rightarrow 1$) and deposit similar amounts of energy in the material. As a result, the response of each of the VZERO segment, to a good approximation, will be proportional to the number of particles that passed the sensitive part of the segment (despite their mass or momenta). The sum of the amplitudes measured in all VZERO segments is therefore correlated to the total number of particles reaching the detector and can serve as a probe for the total charged-particle multiplicity.

Due to its excellent timing characteristics, VZERO is also used as a trigger for both Pb-Pb and pp collisions. In addition, it can separate the beam-gas interactions during the pp runs, serve as luminosity monitor and is essential when dealing with the pileup during high luminosity runs as will be discussed in Section 6.1.1.

5.2 Multiplicity and Centrality Estimation

The multiplicity of an event can be estimated in several ways. One such method is measuring the charged tracks in the forward region (*V0 estimator*), as described in the previous section; alternatively, one can calculate the number of charged tracks in, for example, the TPC (*midrapidity estimator*). In Pb-Pb collisions at $\sqrt{s_{\text{NN}}} = 2.76$ TeV, the VZERO amplitude (*V0M*) is strongly correlated to the number of tracks measured in the TPC, see [23]. Because of high multiplicities in Pb-Pb collisions, the events selected using the V0 and the midrapidity estimators show similar multiplicity density distributions $dN_{\text{ch}}/d\eta$ as a function of η (see Fig. 5.7).

However, the situation is different in pp collisions. As a rule of thumb, in the field of heavy-ion physics one is interested in the events where high multiplicities are generated by the bulk and therefore have a flat distribution of $dN_{\text{ch}}/d\eta$ over several units pseudorapidity (*underlying event*). In pp collisions, high multiplicities can also originate from jets, which appear as “bumps” in $dN_{\text{ch}}/d\eta$. If the analysis (spectra measurement) region is overlapping with the multiplicity estimation region, the event selection is biased by these bumps. On the other hand, using forward detectors de-

couples the $dN_{\text{ch}}/d\eta$ measurement region from the analysis region, thus removing the autocorrelation biases. A comparison of $dN_{\text{ch}}/d\eta$ distributions as a function of η in different multiplicity classes selected using different multiplicity estimators in pp collisions at $\sqrt{s} = 7$ TeV is also shown in Fig. 5.7.

5.2.1 Collision Centrality and Glauber MC

At speeds close to that of light, ions are Lorentz contracted into “pancakes”. If the distance between their geometrical centers in the transverse plane – the *impact parameter* b – is non-zero, the nuclei overlap only partly as illustrated in Fig. 5.8. The quantity describing the overlap between two ions is called the *centrality*. In head-on collisions ($b = 0$), centrality is said to be zero (most central events), while at large b where ions barely overlap, the collisions are regarded as peripheral.

In the collisions where the overlap between the two ions is only partial, only a fraction of nucleons will interact. These nucleons are called *participants*. The remnants of the wounded nuclei that do not participate in the collision are called *spectators*³. In Pb-Pb collisions, the maximum number of participants, $N_{\text{part}} = 416$. However, a participant nucleon from the projectile can interact with multiple nucleons from the target. The number of participant-participant interactions is called the *number of binary collisions*, N_{coll} .

In general, centrality is directly related to the impact parameter b . In practice, b cannot be measured experimentally and instead the centrality is estimated from the multiplicity assuming that $dN_{\text{ch}}/d\eta$ is monotonically increasing with N_{part} (i.e. as the collision becomes more central). The highest centrality events then also yield the highest multiplicities.

In order to extract parameters like N_{part} and N_{coll} , one usually depends on a *Glauber Monte Carlo* simulation [95]. In Glauber MC, nucleons populate a nucleus of radius R and skin thickness a following the Fermi distribution [96]. Two such nuclei are then displaced by an impact parameter b and projected on a plane. A nucleon in the projectile nuclei is assumed to interact with all target nucleons within $d = \sqrt{\sigma_{\text{INEL}}/\pi}$ (where σ_{INEL} is the inelastic cross section measured in pp collisions) and vice versa for

³After the collision, spectators might form smaller nuclei.

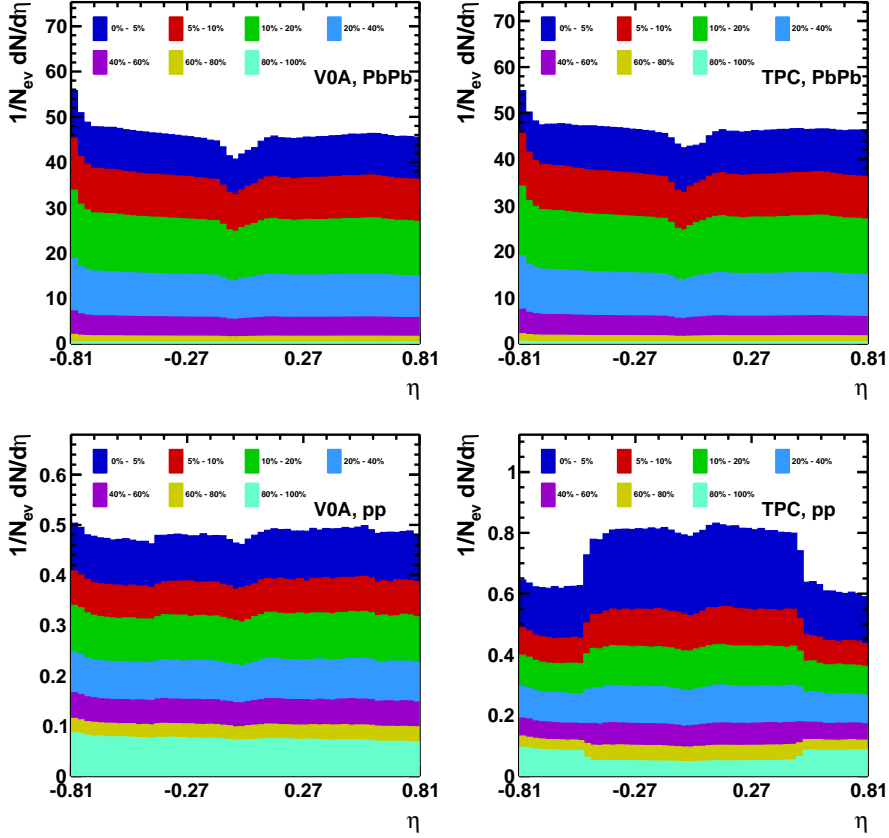


Figure 5.7: Charged particle pseudorapidity density as a function of pseudorapidity in Pb-Pb collisions at $\sqrt{s_{\text{NN}}} = 2.76$ TeV (top) and pp collisions at $\sqrt{s} = 7$ TeV (bottom) in different multiplicity classes. The multiplicities were estimated by using V0A estimator (left) and counting charged tracks in $|\eta| < 0.5$ (right). The figure was produced by the author as part of the CERN Summer Student project.

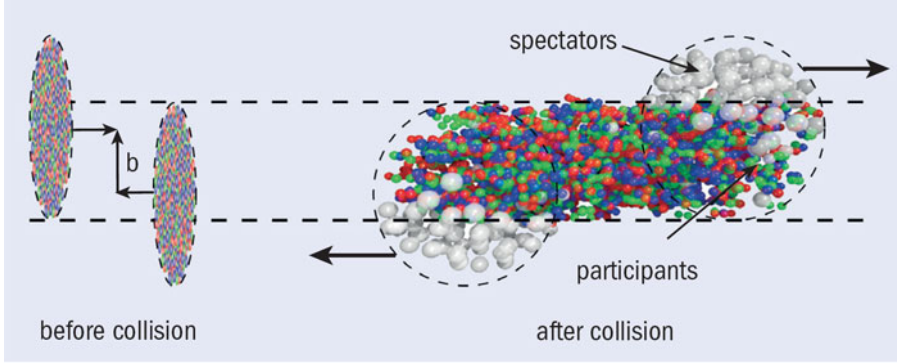
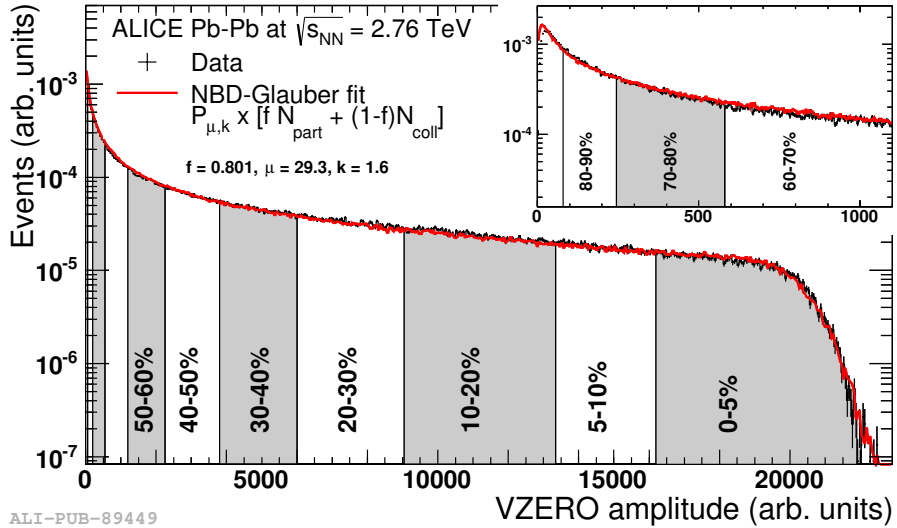


Figure 5.8: Illustration of semi-central heavy-ion collision. Figure taken from [93]



ALI-PUB-89449

Figure 5.9: Glauber MC fit to the VZERO amplitude distribution measured in Pb-Pb collisions at $\sqrt{s_{NN}} = 2.76$ TeV. Figure taken from [94].

target nucleons. Each nucleon-nucleon interaction is one binary collision, and nucleons that collide at least once are participants.

The Glauber MC can then be fit to the measured multiplicity distribution to extract N_{coll} and N_{part} as shown in Fig. 5.9 [94]. To obtain a similar shape as for the experimental multiplicity, fluctuations are modeled using Negative Binomial Distributions (NBD), which was shown to describe the $d\sigma/dN_{\text{ch}}$ well in pp collisions [97], and one should note that in general, the multiplicity in Glauber MC receives contributions from both N_{part} and N_{coll} .

5.3 Track Reconstruction

Before the tracking starts, signals from neighboring channels are clustered together for each of the relevant detectors individually in order to obtain hit coordinates. Examples of clustering can be combining signals in adjacent pads in the TPC, several neighboring (fired) strips in the SSD, etc. The purpose of the clustering is to convert the raw data measured by each of the detectors into 3D coordinates (and associated timing information) of hits – points where the incident particles interacted with the detector material. From the clusters in SPD, a preliminary position of the primary vertex can be established.

The tracking algorithm then starts at the two outermost pad rows of the TPC. Clusters from the two pad rows are combined under different hypothesis in order to look for potential track candidates. Such sets of clusters are called *seeds*. Once all the seeds are found, the tracks are propagated inwards to the interaction point, adding more clusters at each step as illustrated in Fig. 5.10. The propagation is carried out using the Kalman algorithm [99], which allows updating the track parameters each time new information (additional cluster) is added and estimates the effect of energy loss in the material on the track parameters. Once the inner wall is reached, the track is extrapolated to the ITS and the same procedure is followed all the way to the preliminary primary vertex.

Once the inward tracking is finished, the same procedure is repeated, but this time the propagation starts in the ITS and goes outwards. Tracks found in the previous step are used as seeds in addition to the unused ITS clusters, which are combined combinatorially to form new seeds. Tracks are then propagated throughout ITS, TPC and TRD updating the track

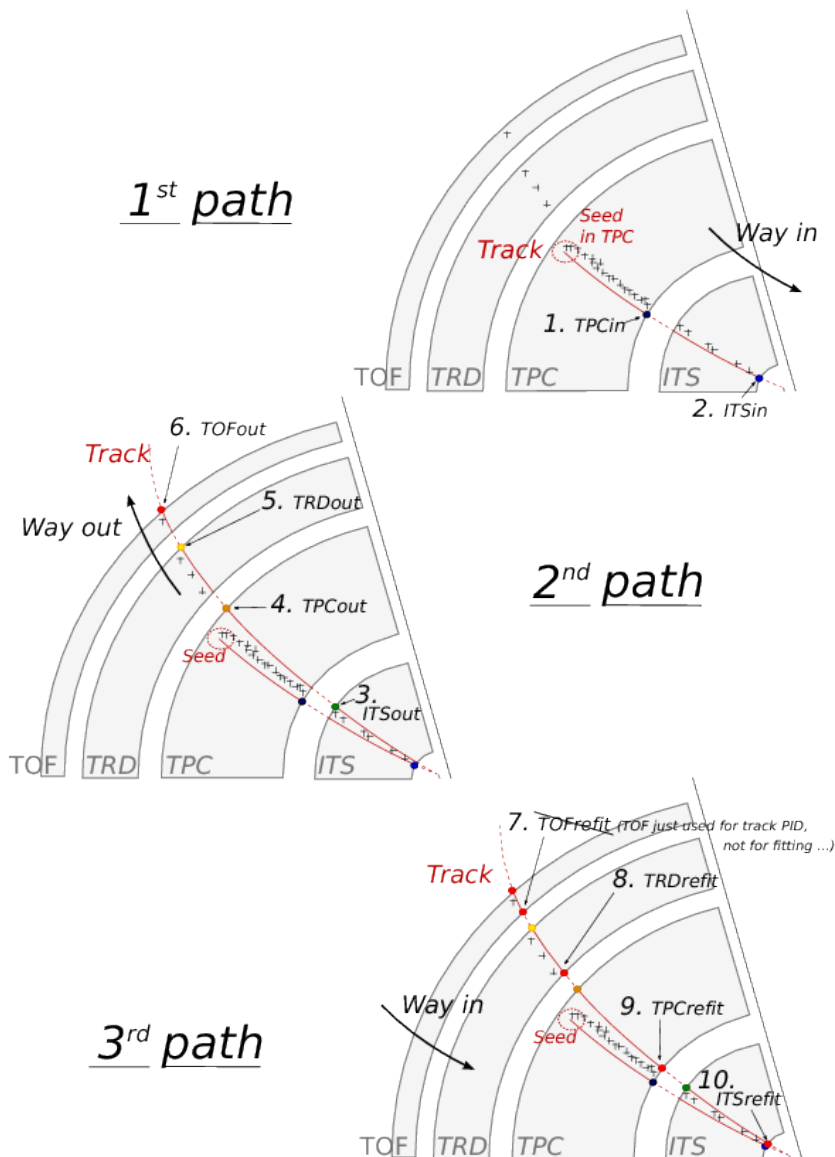


Figure 5.10: Tracking in ALICE. See text for explanation. Figure taken from [98]

parameters whenever a new cluster is added, and in addition to TOF, HMPID, EMCal and PHOS if any clusters compatible with the track can be found. Such tracks are called *global tracks*.

The final step of the tracking procedure is to refit the global tracks into the associated clusters in TRD, TPC and ITS in order to obtain the best quality track parameters at the primary vertex. If the refit is successful, the tracks are extrapolated to the interaction point and the position of the primary vertex can be recalculated to higher accuracy.

Note that the parameters obtained using the Kalman algorithm are calculated at the *interaction point and not where the clusters were found*.

Chapter 6

Event, Vertex, Track Selection and Transverse Spherocity

The data sets used for the presented analysis were recorded with the ALICE detector in years 2010 ($\sqrt{s} = 7$ TeV) and 2016 ($\sqrt{s} = 13$ TeV). As the detector was operating under different configurations during these periods, there are some minor differences in the selection criteria used to choose events of interest. In the following chapter, I will describe the official prescriptions for event, vertex and track selection used by the ALICE collaboration (and also in this thesis) for multiplicity-related spectral analysis. I will then discuss the event shape observables with a focus on the *transverse spherocity* S_0 and describe how events are selected based on this observable.

6.1 Event Selection Criteria

Minimum bias events from the $\sqrt{s} = 7$ and 13 TeV data sets were selected by requiring trigger inputs from VZERO-A and/or VZERO-C counters or the SPD. In the analysis of 7 TeV dataset, only one out of three was required (VZERO-A, VZERO-C or a hit in SPD), while for the 13 TeV dataset, a more strict trigger was used, requiring signal inputs from VZERO-A and VZERO-C in coincidence.

Background rejection was done considering the correlation between SPD clusters and the number of tracklets. Namely, the event was considered as background, if the number of SPD clusters $N_{\text{SPD Cls}}$ and the number of tracklets N_{tr} fulfilled the condition $N_{\text{SPD Cls}} \leq 65 + 4N_{\text{tr}}$.

Events were considered as **pileup** if a second primary vertex could be reconstructed within 0.8 cm along the beam axis. The second vertex was also required to have at least three tracklets associated with it, if the total number of tracklets $N_{\text{tr}} < 20$; at least four tracklets if $20 \leq N_{\text{tr}} < 50$; or at least five tracklets if $50 \leq N_{\text{tr}}$.

Events with **incomplete DAQ readout** were rejected.

Only events with at least one **inelastic scattering** were used for the analysis. This was ensured by requesting at least one tracklet with $p_{\text{T}} > 150 \text{ MeV}/c$ in pseudorapidity region $|\eta| < 1$. A class of events that have at least one inelastic scattering is usually called $\text{INEL} > 0$. Note that this class only corresponds to the visible cross-section, as a fraction of events will be lost due to detector inefficiency and the limited acceptance.

6.1.1 Out-of-Bunch Pileup

The spacing between proton bunches in the beams during the operational periods of LHC in the year 2016 was 25 ns – a much smaller spacing compared to previous runs. This resulted in an increased rate of collisions and gave rise to an additional contribution to the pile up. Also known as out-of-bunch pileup, this effect was first noticed in the study of K_s^0 production as a function of multiplicity, where the observed yields of the meson between the data sets recorded at the same $\sqrt{s} = 13 \text{ TeV}$ throughout years 2015 and 2016 differed by (up to) a factor of 7.

In order to understand the origins of this effect, the readout time of the SPD detector has to be considered. Once the trigger is issued, the SPD buffer is read out for three clock cycles: one cycle before the trigger is fired, one cycle when trigger is fired and one cycle after the trigger is fired. With the internal SPD clock running at a frequency of 10 MHz, this amounts to a 300 ns readout window. On the other hand, at the interaction point the bunches are crossing at a rate of 40 MHz, which means that during the SPD readout there are 12 crossings overall, any of which can result in a collision. Consequently, if during the SPD readout there is another hard scattering, it will bias the hadronic yields.

To eliminate the out-of-bunch pileup, triggers that are within 250 ns of one another are rejected. This is done using the V0 detector, which features excellent timing characteristics (order of nanoseconds) and is able to recover between LHC clock cycles. The event selection is done offline, making sure that for each SPD trigger at time t_0 , there are no additional V0 triggers in the time range $t_0 - 10 < t < t_0 + 10$ (ns).

Note that the TOF detector has a time resolution of approximately 10 – 100 ps and therefore is not affected by the out-of-bunch pileup. On the other hand, the TPC is a much slower detector where tracks from a number of events are accumulated. As sphericity is estimated from the TPC tracks, its sensitivity to the out-of-bunch pileup has to be studied.

6.2 Vertex Selection

For the event to be considered, it must have at least one reconstructed vertex fulfilling the following criteria:

- A vertex is reconstructed in SPD (SPD vertex) or from the tracks (track vertex), or both
- The SPD vertex (if reconstructed) resolution along the beam axis is better than $|z_{\text{vtx}}^{\text{SPD}}| < 0.25$ cm and the dispersion is less than 0.04
- If both the SPD and track vertices exist, the displacement between them must be $|z_{\text{vtx}}^{\text{track}} - z_{\text{vtx}}^{\text{SPD}}| < 0.5$ cm
- The reconstructed vertex along the beam line must be $|z_{\text{vtx}}| < 10$ cm.

6.3 Track Selection for Spectral Analysis

Tracks in the following analysis were selected by requiring each track to have:

- The minimum number of crossed rows in TPC $N_{\text{CR}} \geq 70$
- The ratio of crossed rows to findable clusters¹, $N_{\text{CR}}/N_{\text{CLS}} > 0.8$

¹Some clusters might not be findable if e.g. a track crosses the boundary between two readout chambers or leaves the η acceptance region.

- Kalman fit to the findable TPC clusters has quality better than $\chi_{max}^2/N_{CLS} = 4$
- The displacement of the track with respect to the primary vertex can be calculated
- The distance of closest approach (DCA) of the reconstructed track to the vertex in z -direction is $|DCA_z| < 2 \text{ cm}$
- Track reconstructed in TPC after Kalman filter refits back to the vertex (see Section 5.3)
- Track reconstructed in ITS after Kalman filter refits back to the vertex
- Kalman fit to the available ITS clusters has quality better than $\chi_{max}^2/N_{ITS} = 36$.

Particles that are not created during the collision, but are products of weak decays or particle-material interactions, have a reconstructed vertex displaced with respect to the primary vertex. In order to filter out the tracks *not* corresponding to primary particles, an additional p_T -dependent cut on the transverse component of DCA is applied:

$$|DCA_{xy}| < 0.0105 + \frac{0.0350}{[p_T \text{ (GeV}/c)]^{1.1}} \quad (6.1)$$

which corresponds to 7σ in DCA_{xy} and is a compromise between removing a large fraction of secondary hadrons and having minimum effect on the primary particles (see Fig. 6.1).

To further reduce the number of secondary hadrons in the sample, tracks reconstructed in the TPC and constrained to the primary vertex can be compared to the global tracks. Such selection is done with a cut $\chi_{CvsG}^2 < 36$ (CvsG – “constrained vs. global”) and the fraction of primary hadrons in the sample before and after the cut is shown in Fig. 6.2a. While at first glance one would consider this as the optimal configuration of the track cuts, there is an issue introduced by this cut that has not been discussed yet.

The contamination by secondary hadrons in the signal region given by Eq. 6.1 is still not negligible even after the χ_{CvsG}^2 ; the removal of this

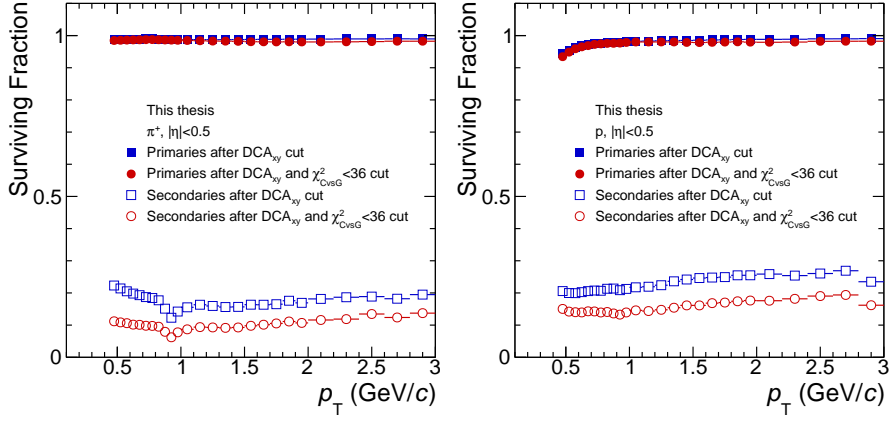


Figure 6.1: Fraction of primary (solid markers) and secondary (empty markers) hadrons after the 7σ DCA_{xy} cut (blue squares) and $\chi^2_{CvsG} < 36$ cut (red circles).

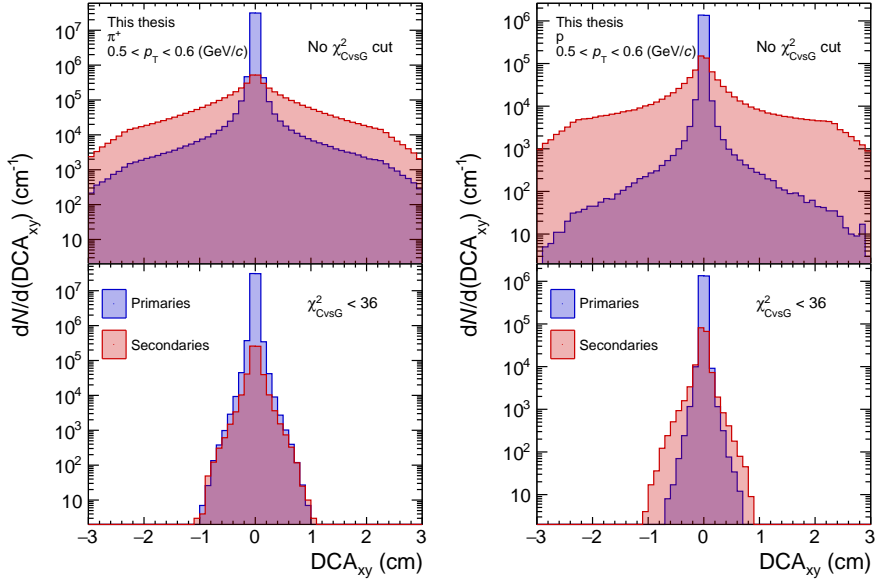


Figure 6.2: Comparison of DCA_{xy} distributions of primary (blue) and secondary (red) π^+ (left) and p (right) without (top panels) and with (bottom panels) $\chi^2_{CvsG} < 36$ cut.

contribution is described in Section 7.4 and depends on the differences in DCA_{xy} shapes. As shown in Fig. 6.2b, the large fraction of hadrons removed with $\chi^2_{\text{CvsG}} < 36$ cut lie on the tails of the DCA_{xy} distributions. Rejecting these tracks modifies the shapes of the secondary hadron DCA_{xy} distributions, making them very similar to those of the primary hadrons. As a result, the statistical unfolding of the measured DCA_{xy} distributions becomes impossible, which means that the estimated primary hadron yields might still have a significant contamination by other particles. Therefore, to get the best estimate of primary particle yields, the $\chi^2_{\text{CvsG}} < 36$ cut will not be used and the contamination will be removed using different methods.

6.4 Transverse Spherocity

In hadron-hadron collisions, one of the most dominant effects of final state kinematics are low momentum transfer (Q^2) scatterings between incoming partons. To many, these are of little interest and usually seen as background that needs to be removed in searches for new physics. Perturbative QCD provides a solid baseline for understanding particle production at large momentum transfers in the form of jets, where most of the physics beyond the Standard Model are expected to reside. Unfortunately, these calculations do not extend to low Q^2 due to the increasing complexity of the theory, and instead one usually resorts to phenomenological models in Monte Carlo event generators to simulate the evolution of the partons.

Thus far, event shape observables have been explored as a means to separate one or several hard scatterings from underlying events, which are to a large extent dominated by soft QCD, but in general might also contain hard processes. Recently, signatures of collective-like phenomena were observed in multiplicity-dependent hadron yields in pp collisions that qualitatively were reminiscent of those observed in p-Pb and Pb-Pb [42]. The effect of the collectivity usually manifests itself in the soft QCD sector, making event shape observables an appealing tool to better distinguish the underlying physics behind the pp collisions.

While there are a number of ways to construct different event shape observables [100], they all aim at describing the distribution of the (transverse) energy in the final state of the collision. Due to multiple low Q^2 scatterings, underlying events usually exhibit a flat azimuthal angular

distribution of final state hadrons, as opposed to highly collimated jets. Experimentally, this means that events dominated by small momentum transfers exhibit isotropic angular distributions and abundance of low- p_T particles, while events dominated by a single hard scattering have most hadrons collimated around a single axis (back-to-back jet structure) and harder p_T spectra.

In the sections to follow, event shapes are characterized using *transverse sphericity* S_O , given by

$$S_O = \frac{\pi^2}{4} \left(\frac{\sum_i |\vec{p}_{T,i} \times \hat{\mathbf{n}}|}{\sum_i p_{T,i}} \right)^2 \quad (6.2)$$

where $\hat{\mathbf{n}}$ is a two-dimensional unit vector in the transverse plane, chosen in a way so that S_O is minimized. In practice, this vector coincides with one of the transverse momentum vectors p_T [100] and by construction has two limits:

$$S_O = \begin{cases} 0 & \text{"jetty" limit} \\ 1 & \text{"isotropic" limit} \end{cases}$$

where it is expected that the jetty (isotropic) events are dominated by the hard (soft) QCD processes.

6.4.1 Sphericity Selection Track Cuts

In an internal ALICE study on detector response to sphericity selection, it has been shown that the calculated sphericity can vary by up to 5% when the multiplicity of an event is at least ten tracks. Note, however, that this is an extreme case where 25% of the tracks in an isotropic event have been lost. The variation is smaller ($< 3\%$) in the jetty events and reduces further to fractions of a percent with increasing multiplicity. Therefore, in order to minimize sensitivity to particle loss, only events with at least ten tracks are considered for the sphericity-related analysis.

To study the effects of track selection in sphericity calculation, I start with generic quality cuts for TPC tracking². The selected track is required to be reconstructed from at least 50 clusters in the TPC with the reconstruction quality per TPC cluster, $\chi^2/N_{\text{Cls}} < 4$ and the distance of closest approach to the reconstructed primary vertex to be less than 3.2(2.4) cm in

²This was suggested in an internal ALICE study.

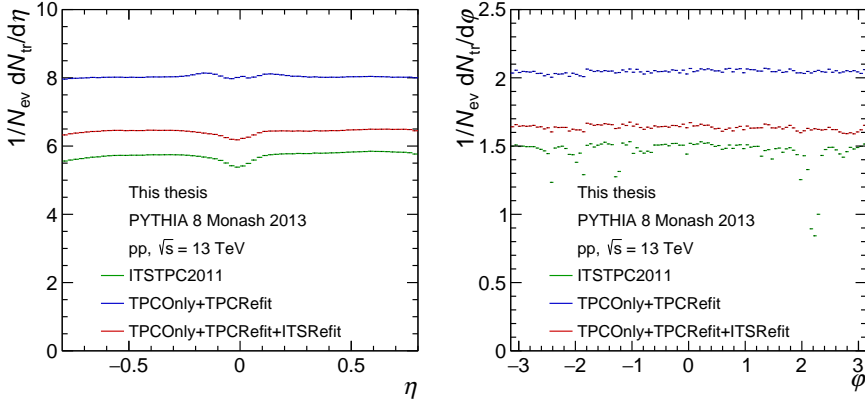


Figure 6.3: $dN_{\text{tr}}/d\eta$ (left) and $dN_{\text{tr}}/d\phi$ (right) distributions under three different track selection criteria: standard cuts used for PID analysis (ITSTPC2011), tracks reconstructed in the TPC (TPCOnly+TPCRefit) and tracks reconstructed both in the TPC and the ITS (TPCOnly+TPCRefit+ITSRefit).

the longitudinal (transverse) directions. In addition, after reconstructing the track in the Kalman filter (ITS \rightarrow TPC \rightarrow TRD), the track is required to refit the TPC clusters. The observed $dN_{\text{tr}}/d\eta$ and $dN_{\text{tr}}/d\phi$ distributions are flat, as shown in Fig. 6.3 (TPCOnly + TPCRefit). It is important to note that a flat azimuthal angular acceptance is essential for a viable estimation of the sphericity, as any ϕ -dependent detector inefficiencies will introduce a bias in the observed event shapes.

With the following track selection criteria, an abundance of $S_0 \rightarrow 0$ events were observed in the data and MC samples (see Fig. 6.4). Most of these events were found to contain at least one unexpectedly high p_T track ($p_T \gtrsim 100 \text{ GeV}/c$) and therefore required further investigation. A Monte Carlo study of the correlation between the measured and real p_T of tracks revealed an issue in the reconstruction, which manifested in some tracks having a significantly larger measured transverse momentum, $p_T^{\text{Rec}} \gg p_T^{\text{True}}$ (see Fig. 6.5). To solve the issue, reconstruction performance with an additional sets of cuts has been studied. It was concluded that an additional requirement of the tracklet to be refit to the ITS clusters removes the poorly reconstructed tracks as well as the abundance of $S_0 \rightarrow 0$ events

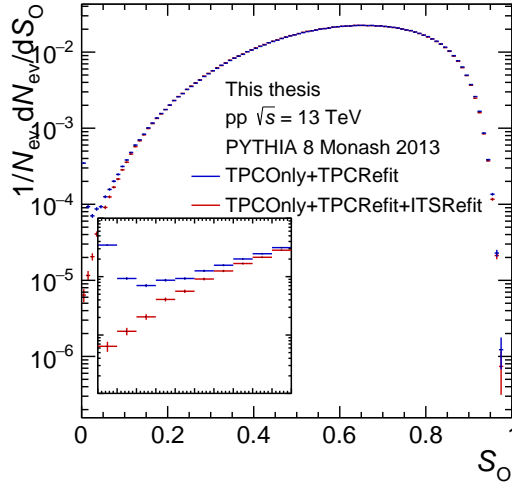


Figure 6.4: Spherocity distribution calculated from the TPC-only and the TPC-ITS tracks. The small plot shows spherocity distribution in range $0 < S_0 < 0.1$.

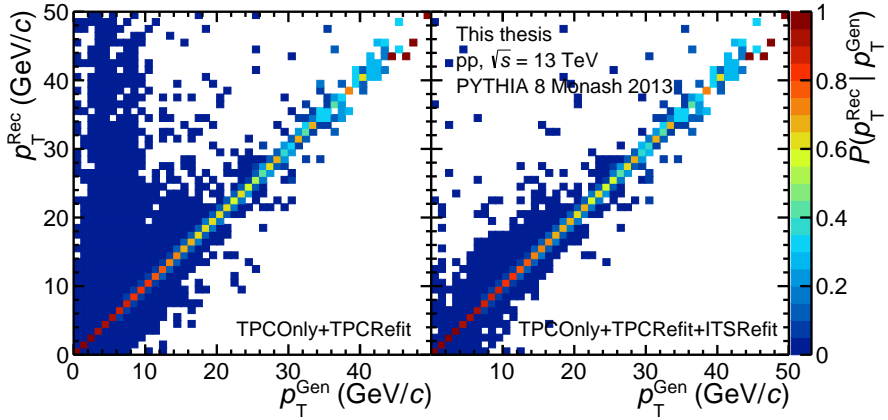


Figure 6.5: Correlation between the true p_T^{Gen} measured on a generated particle level and p_T^{Rec} after the track reconstruction for tracks reconstructed in the TPC (left) and TPC-ITS (right).

while retaining the flat azimuthal angular acceptance, although with lower track statistics, see Fig. 6.5 and Fig. 6.3 (TPCOnly + TPCRefit + ITSRefit).

For completeness, I have also studied the sphericity selection using the standard track cuts for π , K and p analysis, ITSTPC2011. These are tight quality cuts optimized to reject a large fraction of secondary tracks, see Section 6.3 for a more detailed description. As seen in Fig. 6.3, the track statistics suffer further and, more importantly, the $dN_{\text{tr}}/d\varphi$ distribution is no longer flat. The inhomogenities in the detector acceptance render the ITSTPC2011 track cuts unviable and therefore should not be considered.

Finally, the kinematic cuts on track selection should also be considered. Very low p_{T} hadrons will suffer from the nuclear stopping power, making the reconstruction of the tracks impossible. This puts a limit on the lowest p_{T} measurable by the detector, which in case of ALICE is $p_{\text{T}}^{\text{min}} = 150 \text{ MeV}/c$. Moreover, as LHC is a colliding-beam experiment, the pseudorapidity coverage is also limited. The main tracking detector of ALICE, the TPC, has an acceptance of $|\eta| < 1$, but one should note that the reconstruction performance drops down close to the vicinity of the TPC end planes. The commonly used analysis region with a flat η -acceptance is therefore $|\eta| < 0.8$.

To summarize, the tracks for sphericity calculation are selected using the following criteria:

- TPCOnly + TPCRefit + ITSRefit
- $p_{\text{T}} > 0.15 \text{ GeV}/c$
- $|\eta| < 0.8$.

6.4.2 Detector Response to Sphericity Selection

In order to study the detector response to the transverse sphericity selection, a Monte Carlo sample was used to calculate the true (generated) sphericity $S_{\text{O,G}}$ and compare to the measured (reconstructed) sphericity $S_{\text{O,R}}$. The $S_{\text{O,R}}-S_{\text{O,G}}$ correlation in 10% highest multiplicity events selected by the V0M estimator is shown in Fig. 6.6. Note that the matrix is

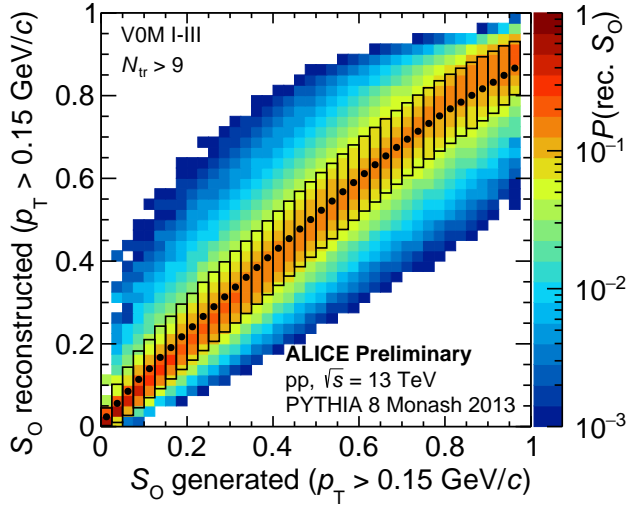


Figure 6.6: True-measured spherocity correlation matrix in 0–10% VOM events. Normalization done column-wise.

normalized in a way so that

$$\int_0^1 \frac{d^2 P(S_{O,G}, S_{O,R})}{dS_{O,G} dS_{O,R}} dS'_{O,G} = 1 \quad (6.3)$$

From the correlation matrix, the following events were selected:

- 20% highest *generated* spherocity events, $S_{O,G}^{\text{high}}$
- 20% highest *reconstructed* spherocity events, $S_{O,R}^{\text{high}}$
- 20% lowest *generated* spherocity events, $S_{O,G}^{\text{low}}$
- 20% lowest *reconstructed* spherocity events, $S_{O,R}^{\text{low}}$.

As discussed in the preamble of this chapter, the identified hadron spectra is expected to be harder (softer) in jetty (isotropic) events as compared to the spherocity-inclusive spectra. Moreover, one would naively anticipate no differences between the spectra measured using the two estimators³. In

³The two estimators are $S_{O,G}$ and $S_{O,R}$.

practice this is not the case: the *generated spectra* of identified hadrons selected with $S_{O,G}$ exhibits larger modifications than that selected with $S_{O,R}$. On the other hand, the *reconstructed spectra* measured in the events selected by the two estimators show a very good agreement, as is illustrated in Fig. 6.7.

To understand the origins of the observed differences, the composition of isotropic and jetty events have to be considered in the context of detector efficiency. Isotropic events exhibit an abundance of low- p_T hadrons, while in the jetty limit, most of the transverse energy is shared between one or more tracks. If some of these tracks are not included in the sphericity calculation, jetty events can be reconstructed as isotropic and vice versa. Since the spectral modifications introduced by losing a high- p_T track are more significant than those in low- p_T case, the effect is more pronounced for initially jetty events.

The π , K and p reconstruction efficiencies for $S_{O,G}$ and $S_{O,R}$ selected events are shown in Fig. 6.8. The efficiencies in events selected by $S_{O,G}$ are consistent with those in MB events, indicating that the evolution of efficiency observed in $S_{O,R}$ -selected events is an autocorrelation. This autocorrelation can be eliminated using the minimum bias efficiency. Combining this with the good agreement of *reconstructed spectra* between the two sphericity estimators shown in Fig. 6.7, it is found that *selecting events with measured sphericity $S_{O,R}$ and correcting them with the MB efficiency is similar to selecting events with true sphericity $S_{O,G}$.*

Finally, the technical definition of the sphericity class has to be considered. Ideally, one would like to use very narrow $\Delta S_{O,R}$ ranges in limits $S_{O,R} \rightarrow 0(1)$ for jetty (isotropic) event selection to achieve high purity sample. On the other hand, the available statistics diminish rapidly for small $\Delta S_{O,R}$ ranges. As a compromise between distinct event shapes and available statistics, 20% of highest (lowest) sphericity events from the multiplicity class are selected as isotropic (jetty). This amounts to $\sim 2\%$ of all the events in the MB sample, if the sphericity selection is done on the 10% highest multiplicity pp events.

As the events tend to be on average more jetty-like after the reconstruction, the sphericity selection based on the number of events result in different shapes between $S_{O,G}$ and $S_{O,R}$ estimators: for 20% highest sphericity events one would measure $\langle S_{O,R} \rangle < \langle S_{O,G} \rangle$. In order to estimate the magnitude of this effect, we calculate the $S_{O,R}^{\text{Cutoff}}$ values used to

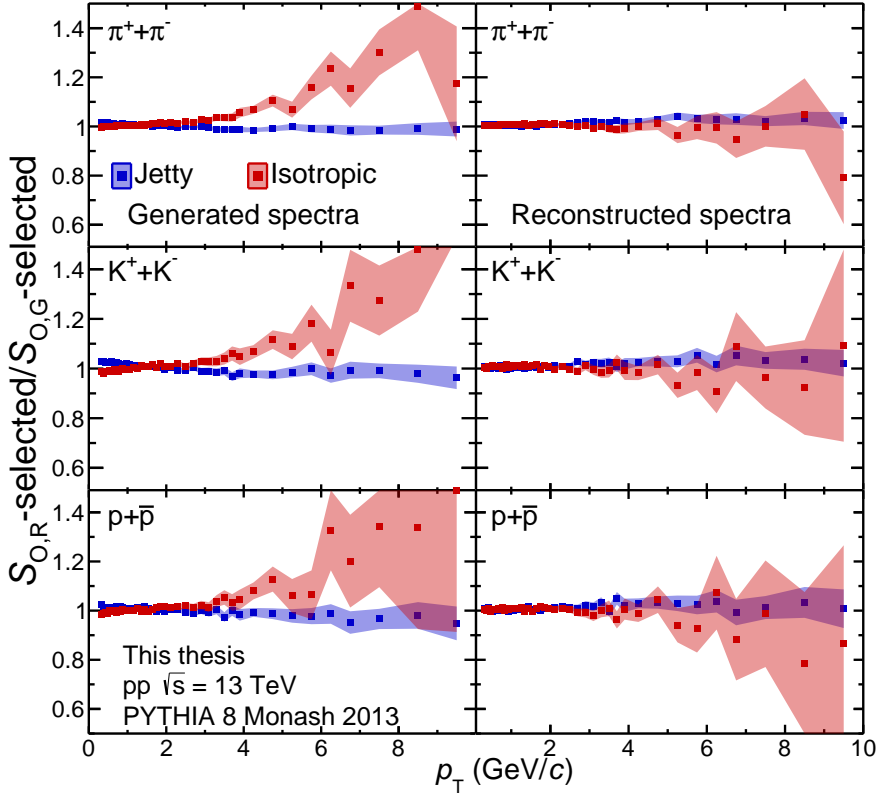


Figure 6.7: Comparison of the generated (left) and reconstructed (right) spectra for different hadron species. To calculate the ratios, spectra from the events selected using the reconstructed sphericity $S_{O,R}$ were divided by spectra from the events selected using the generated sphericity $S_{O,G}$.

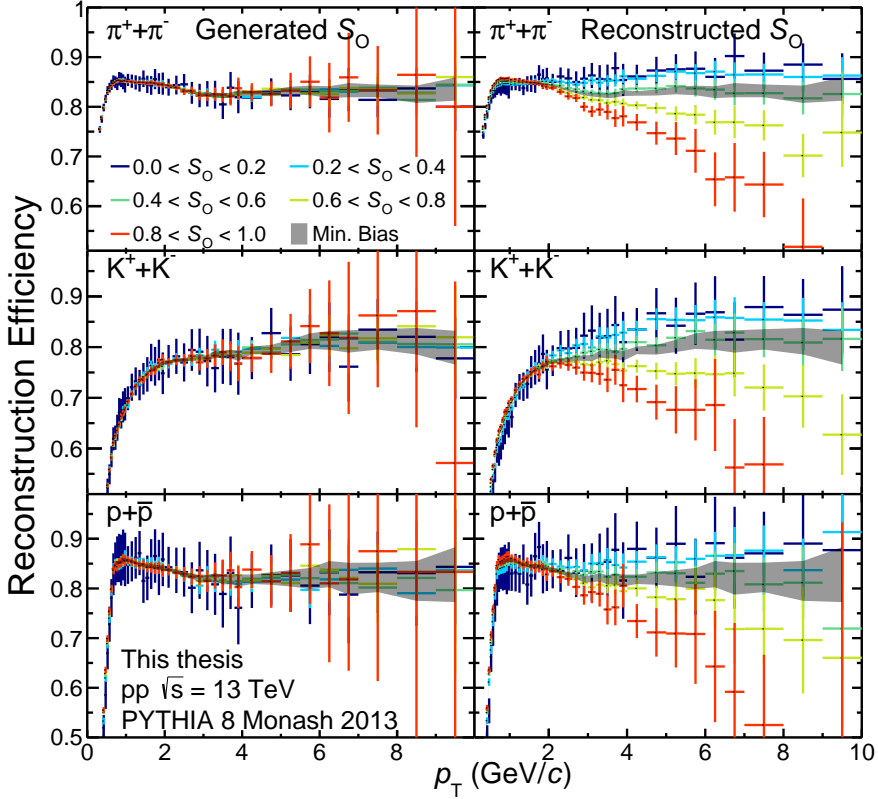


Figure 6.8: Track reconstruction efficiency as a function of p_T in different sphericity classes for different hadron species. Events were selected using generated sphericity $S_{O,G}$ (left) and reconstructed sphericity $S_{O,R}$ (right).

select the sphericity classes from reconstructed tracks, apply these cuts to $S_{O,G}$ and study the spectral modifications. Note that with these cuts, the isotropic (jetty) $S_{O,G}$ class contains more (less) than 20% of the events available in the high-multiplicity sample. The summary of the study is given in Fig. 6.9, where the reconstructed spectra are corrected by the MB efficiency as discussed above. We find that the uncertainties introduced by using the minimum bias efficiency and not unfolding the spectra in sphericity are $< 1\%$ in the p_T region considered. This uncertainty is

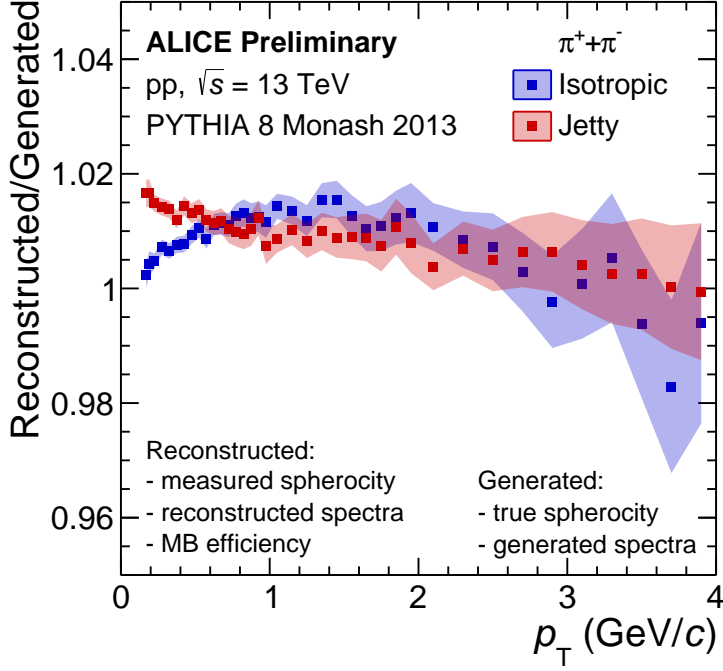


Figure 6.9: Comparison between the generated and reconstructed π spectra using different sphericity estimators. See text for more info.

also correlated among different particle species and vanishes in the ratios. The proposed recipe to use in the sphericity-related analysis is therefore as follows:

- Use minimum-bias efficiency to correct the raw spectra
- Do not unfold the spectra
- Apply a 1% uncertainty, correlated among particle species.

Chapter 7

Particle Identification

For the measurement of charged π , K and p spectra, data recorded by the TPC and TOF detectors was analyzed and combined in order to obtain identified hadron spectra in range $0.3 < p_T < 3 \text{ (GeV/c)}$. A summary of analysis regions and p_T ranges used to obtain the identified hadron spectra by each detector is given in Table 7.1.

Table 7.1: Overview of p_T ranges and analysis regions used in different PID techniques.

Analysis Technique	p_T Range (GeV/c)			Analysis Region
	π	K	p	
TPC $n\sigma$ fits	0.3–0.5	0.3–0.6	0.4–0.8	$ y < 0.5$
TOF β fits	0.5–3	0.6–3	0.8–3	$ \eta < 0.4$

7.1 Particle Identification with the TOF Detector

In order to perform particle identification, the TOF detector measures the arrival time of a particle T_{meas} . The time-of-flight can then be calculated as $T_{\text{TOF}} = T_{\text{meas}} - T_{\text{ev}}$, where event time T_{ev} is measured by the T0 detector or estimated from the TOF tracks as described in Section 5.1.3. The total length of particle trajectory before reaching the TOF detector, L_{TOF} , is

obtained using tracking information. In the conventional method, one then calculates the *expected* TOF time for a given particle hypothesis i :

$$T_{\text{TOF}}^{i,\text{exp}} = \frac{L_{\text{TOF}}}{\beta_{i,\text{exp}}} = \frac{L_{\text{TOF}} \sqrt{p^2 + m_i^2}}{p} \quad (7.1)$$

where p is estimated by TPC and ITS. If the time resolution σ is known, one can perform a variable transformation

$$n_{\sigma,i} = \frac{T_{\text{TOF}} - T_{\text{TOF}}^{i,\text{exp}}}{\sigma_i} \quad (7.2)$$

to get a distribution $d^3N_i/dydp_Tdn_{\sigma,i}^i$. To extract the p_T -differential raw yield of i -particle, one then performs integration:

$$\frac{d^2N_i}{dydp_T} = \int_{-3}^3 \frac{d^3N_i}{dydp_Tdn_{\sigma,i}} dn_{\sigma,i}' \quad (7.3)$$

There are few things to consider with such technique:

- For a perfectly gaussian shape, an integral within $|n_{\sigma}| < 3$ contains 99.7% of given species yield. In reality, the distribution has an exponential tail with the shape of $f(t) \propto \exp(-t)$ instead of $f(t) \propto \exp(-t^2)$ and falls off more gradually than a normal gaussian. Therefore, the integral in $|n_{\sigma}| < 3$ would underestimate the total yield.
- As the track is considered under a certain hypothesis of particle i , it is convenient to apply a rapidity cut $|y| < 0.5 (\Rightarrow \Delta y = 1)$ in order to simplify the normalization to phase space. However, such a cut introduces a smearing in p for a given p_T , reducing the resolution one can achieve. On the other hand, a particle created at central rapidity will leave a shorter track in TOF than the one created at forward rapidity and therefore will be measured with lower accuracy.
- For a hadron i , one would expect the distribution $dN_i/dn_{\sigma,i}$ to be centered at $\mu = 0$ with RMS = 1. Due to internal miscalibrations, this is not always true. While for one species this could be fixed by recentering the distribution, it is ambiguous how other species are affected.

Moreover, the $dN_{\text{tr}}/dn_{\sigma}$ distributions for pions and kaons (protons) start overlapping at around $p_{\text{T}} \approx 1.2$ (2) GeV/ c , rendering the method unviable above those values.

An alternative technique to extend the p_{T} range of TOF PID capabilities is to fit the signal with predefined functions. If the shapes and positions of the functions are understood and fixed, hadron yields can be extracted even in the regions that exhibit a heavy overlapping of different species' signals, as will be shown in the following sections.

7.1.1 Track Cuts Specific to TOF Analysis

In addition to the common track cuts described in Section 6.3, the following track cuts specific only to TOF analysis were applied:

- the track has an associated hit in TOF with measured time
- the length of the track is > 350 cm
- the track in TOF is matched with $\Delta x < 10$ cm and $\Delta z < 10$ cm
- $|\eta| < 0.2$ and $0.2 < |\eta| < 0.4$, samples analyzed separately¹

7.1.2 Raw Yield Extraction

Raw yields of hadrons are extracted from $d^3N_{\text{tr}}(\eta, p, \beta)/d\eta dp d\beta$ distributions shown in Fig. 7.1, which are measured in narrow pseudorapidity windows $|\eta| < 0.2$ and $0.2 < |\eta| < 0.4$ to minimize the resolution dependency on η while maintaining reasonable track statistics. The distributions are fit with four gaussian functions with exponential tails to describe pions, kaons, protons and the mismatched tracks.

The form of one gaussian with a tail is prescribed as:

$$f_i(\beta) = \frac{d^3N_i}{d\eta dp d\beta}(\beta|\eta, p) = \frac{d^2N_i}{d\eta dp}(\eta, p) \cdot \frac{1}{\sqrt{2\pi\sigma_i^2}} \cdot \begin{cases} e^{-\frac{(\beta - \langle\beta_i\rangle)^2}{2\sigma_i^2}} & \beta > t_i \\ e^{-\frac{(t_i - \langle\beta_i\rangle)^2}{2\sigma_i^2}} \cdot e^{-s_i(t_i - \beta)} & \beta < t_i \end{cases} \quad (7.4)$$

¹Narrow $\Delta\eta$ regions are convenient for the $p \rightarrow p_{\text{T}}$ transformation, see Section 7.1.4.

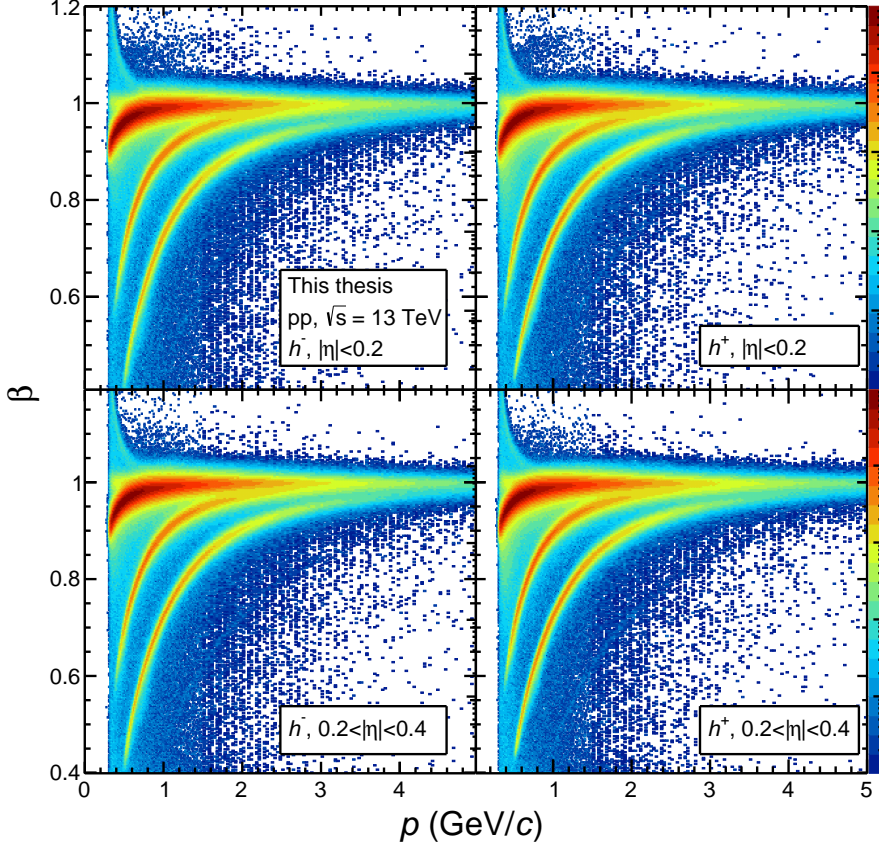


Figure 7.1: $\frac{d^3 N_{\text{tr}}}{d\eta dp_{\text{TD}} d\beta}$ distributions for negative (left) and positive (right) hadrons measured in pseudorapidity regions $|\eta| < 0.2$ (top) and $0.2 < |\eta| < 0.4$ (bottom) in pp collisions at $\sqrt{s} = 13$ TeV.

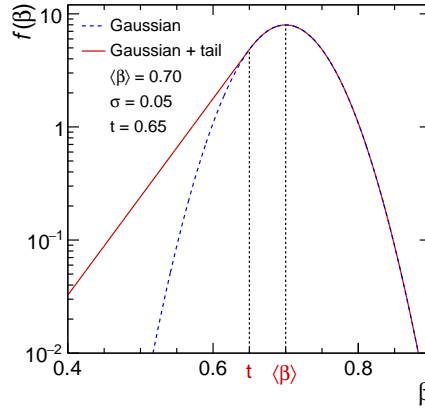


Figure 7.2: An illustration of a single gaussian distribution with a tail.

where $\langle\beta_i\rangle$ is the mean value of each distribution, t_i, s_i are tail cut-off and slope values respectively and $i = \pi, K, p$ and mismatched tracks. An illustration of a single gaussian distribution with a tail is shown in Fig. 7.2.

Mean β

The advantage of performing signal fits in p space, as opposed to p_T , is that one can directly relate the mean value of the distribution for a given particle with mass m . In the following analysis, $\langle\beta_i\rangle$ is defined as

$$\langle\beta_i\rangle(p) = \frac{p}{\sqrt{p^2 + m_i^2}} + \Delta\beta \quad (7.5)$$

where the first term is the expected β for a particle with mass m_i and momentum p and $\Delta\beta$ is a free parameter limited to small values ($|\Delta\beta| < 0.02$) to account for any shifts in the mean. There are several possible sources for the shift:

- Miscalibration in the TOF time measurement, which can result in offset in the measured particle arrival time.
- Uncertainties in the TOF time measurement. The time-of-flight of the track is measured as the difference between the time the track

exits the TOF detector and the collision time. Deviations in any of these times will also be propagated to the measured β .

- Uncertainties in the measured momentum p . Due to the detector material, a traversing particle is subjected to multiple scatterings, losing a fraction of its energy and giving rise to the uncertainty on the measured p . An additional uncertainty comes from a finite momentum bin size in which tracks are measured. Both of these uncertainties are propagated in the β calculation and might result in an offset of the measured $\langle\beta\rangle$ with respect to the expected value.

Tail Parametrization

At first glance, the exponential tail in Eq. 7.4 contains two parameters: s being the slope of the tail and t the cutoff, that is the transition between quadratic and linear behavior of the exponent. However, the transition between the gaussian and the exponential tail must be smooth, implying the following system of equations at the point $\beta = t$:

$$\left\{ \begin{array}{l} C \exp \left[-\frac{(\beta - \langle\beta\rangle)^2}{2\sigma^2} \right] \equiv C \exp \left[-\frac{(t - \langle\beta\rangle)^2}{2\sigma^2} \right] \exp [-s(t - \beta)] \\ \frac{\partial}{\partial \beta} \left(-\frac{(\beta - \langle\beta\rangle)^2}{2\sigma^2} \right) \equiv \frac{\partial}{\partial \beta} (-s(t - \beta)) \end{array} \right. \quad (7.6a)$$

where Eq. 7.6a is always true for $\beta = t$ and Eq. 7.6b was obtained by taking logarithm of Eq. 7.6a. Solving Eq. 7.6b for the tail slope s yields:

$$s = \frac{\langle\beta\rangle - t}{\sigma^2} \quad (7.7)$$

which can then be substituted into Eq. 7.4 to eliminate one of the fit parameters. As a result, the tail is described by a single parameter t .

Resolution

The TOF time of arrival resolution consists of the following components:

- An intrinsic time resolution of Multigap Resistive Plate Chamber, $\sigma_{\text{MRPC}} \sim 30 \text{ ps}$

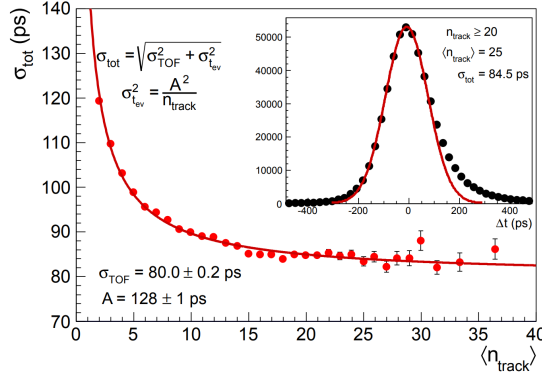


Figure 7.3: Full TOF resolution as a function of N_{ch} . Solid line represents a fit to the data. Figure taken from [91].

- Time jitter of the amplification electronics, $\sigma_{\text{el}} \sim 20 \text{ ps}$
- Uncertainties arising from the LHC digital clock distribution to the experiments, $\sigma_{\text{clock}} \sim 15 \text{ ps}$
- TOF time calibration uncertainties: global offset (common to all channels), channel-by-channel offset and time-slewing correction at time level. The total contribution $\sigma_{\text{calib}} \sim 60 \text{ ps}$

An additional uncertainty originates from the event time measurement. The time resolution of the T0 detector is estimated to be $\sigma_{\text{T0}} \sim 35 \text{ ps}$ [101], while that estimated by TOF (see Section 5.1.3) is in general dependent on the number of tracks (N_{tr}) reaching the detector. The full time-resolution of TOF as a function of N_{tr} is shown in Fig. 7.3. Propagating this uncertainty to the resolution of β gives:

$$\sigma_{\beta} = \sqrt{\left(\sigma_{\text{full}} \frac{\partial}{\partial T_{\text{TOF}}} \frac{L_{\text{TOF}}}{T_{\text{TOF}}} \right)^2} = \beta \cdot \frac{\sigma_{\text{full}}}{T_{\text{TOF}}} \quad (7.8)$$

which becomes constant for $\beta \rightarrow 1$ and should become smaller at lower β values.

In practice, owing to multiple rescatterings in the material, the momentum of a particle is smeared, which also increases the spread of the

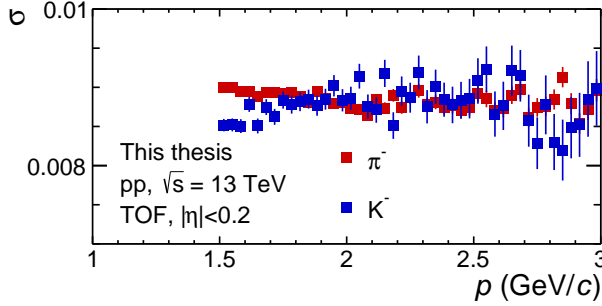


Figure 7.4: TOF β resolution as a function of p in $|\eta| < 0.2$ for π^- and K^- .

signal. This effect competes with the one described by Eq. 7.8, and is more pronounced for particles at low momenta.

In the analysis presented here, we have experimentally observed that σ for π and K becomes constant at $p \gtrsim 1.5 \text{ GeV}/c$ (see Fig. 7.4), while the proton resolution improves in the momentum range considered.

7.1.3 Mismatched Tracks

A fraction of the tracks measured by the TPC are matched to an incorrect track in the TOF detector. Mismatched tracks contaminate the TOF response and their contribution has to be identified to precisely determine the signals of π , K and p . The distribution of mismatched tracks takes a gaussian shape with an exponential tail, although with much larger spread and smaller tail slope as compared to π , K or p responses.

An important consideration when identifying mismatches is how they originate from tracks corresponding to different particles, which can also be of different species. Therefore, it makes little sense to attempt to calculate the $\langle\beta\rangle$ for such a distribution and instead it has to be measured experimentally. However, it is well known that the most abundant particles created in hadron-hadron collisions are pions, which in turn should have the largest contribution to the mismatched tracks.

Several examples of TOF signal fits following the parametrization described above are shown in Fig. 7.5.

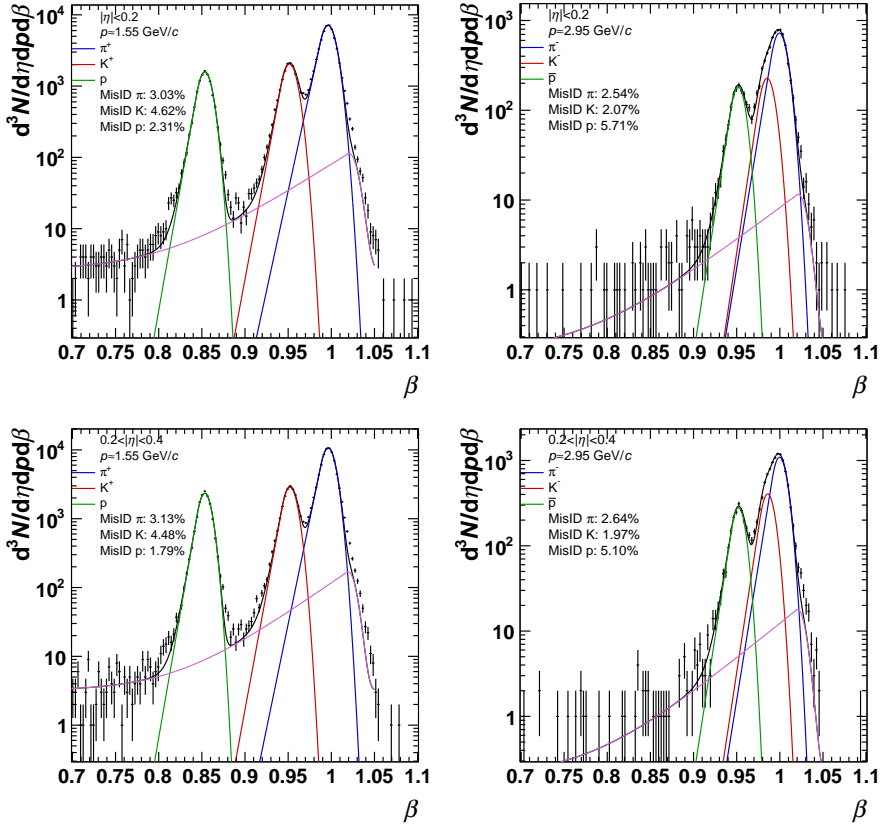


Figure 7.5: TOF PID performance for positive and negative charged hadrons at different p_T values and measured at different pseudorapidity windows.

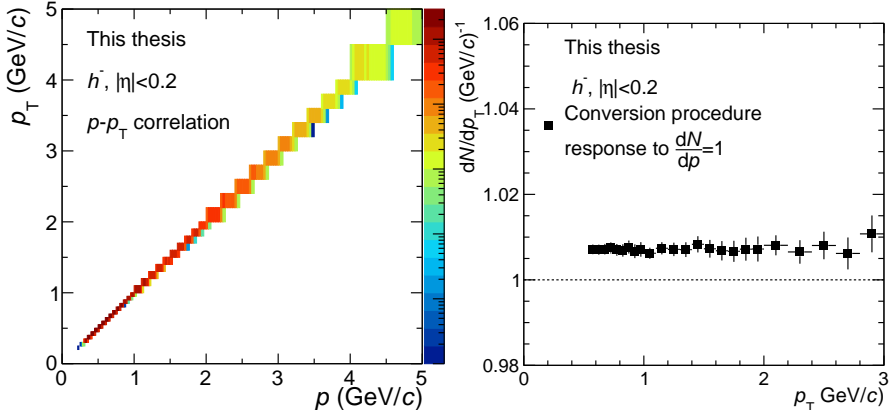


Figure 7.6: Left: double-differential distribution $d^2N_{\text{ch}}/(dp dp_T)$ of all charged particles measured in $|\eta| < 0.2$. Right: response of transformation procedure, $dN/dp_T(p_T)$, to a flat signal $dN/dp(p) = 1$ in $|\eta| < 0.2$.

7.1.4 From p to p_T

As discussed in previous sections, particle identification with TOF in the analysis presented is done in the momentum space. In order to obtain the p_T -differential hadron yields, one must transform the spectra, $dN/dp \rightarrow dN/dp_T$. To perform the transformation, we measure the double-differential distribution $d^2N_{\text{ch}}/(dp dp_T)$ in pseudorapidity regions $|\eta| < 0.2$ and $0.2 < |\eta| < 0.4$, see Fig. 7.6. The normalization constants $C_i(p)$ are then calculated so that

$$C_i(p) \cdot \int_0^\infty dp_T \frac{d^2N_{\text{ch}}}{dp dp_T}(p, p_T) = \frac{dN_i}{dp}(p) \quad (7.9)$$

where the term on the right-hand side of Eq. 7.9 is the p -differential raw yield of i hadron obtained from the signal fits. The yields in p_T -space are then obtained by integrating

$$\frac{dN_i}{dp_T}(p_T) = \int_0^\infty dp C_i(p) \frac{d^2N_{\text{ch}}}{dp dp_T}(p, p_T) \quad (7.10)$$

Note that such a transformation is sensitive to the chosen binning in $dp \rightarrow \Delta p$ and $dp_T \rightarrow \Delta p_T$. In particular, when measuring $d^2N_{\text{ch}}/(dp dp_T)$

one has to make sure that $\Delta p \ll \Delta p_T$. To study the uncertainties originating from this transformation, we measure the response to a (hypothetical) flat p distribution, $dN/dp(p) = 1$. Note that in a symmetric pseudorapidity window, $|\eta| < 0.2$, the mean pseudorapidity $\langle \eta \rangle = 0$ and $p_T \approx p$. We therefore expect the response to be $dN/dp_T(p_T) = 1$ and any deviations from unity would give rise to uncertainties. As shown in Fig. 7.6, the deviations from unity are $< 1\%$.

7.1.5 Normalization to Rapidity

In the analysis presented here, the raw spectra of identified hadrons were measured in narrow windows of $|\eta|$. The pseudorapidity is not a Lorentz-invariant quantity, and the approximation $\eta \sim y$, where y is the rapidity², holds only at sufficiently high p_T . In order to obtain the invariant yield $d^2N_i/dydp_T$ from $d^2N_i/d\eta dp_T$, the spectra need to be renormalized to Δy . For a given hadron i with mass m_i , transverse momentum $p_{T,i}$ and pseudorapidity η_i , rapidity can be calculated as

$$y(m_i, p_{T,i}, \eta_i) = \log \left\{ \frac{\sqrt{m_i^2 + p_{T,i}^2} \cosh^2 \eta_i + p_{T,i} \sinh \eta_i}{\sqrt{m_i^2 + p_{T,i}^2}} \right\} \quad (7.11)$$

The rapidity window Δy corresponding to the measured $\eta_{\min} < |\eta| < \eta_{\max}$ can then be calculated as

$$\Delta y(m_i, p_{T,i}) = 2 \cdot (y(m_i, p_T, \eta_{\max}) - y(m_i, p_T, \eta_{\min})) \quad (7.12)$$

where the additional factor of 2 comes from a symmetric η selection.

²Which is additive under a Lorentz transformation along the z axis

7.2 Particle Identification with Time–Projection Chamber

Particle identification with the TPC is done by measuring the specific energy loss dE/dx within its barrel. For a track with a maximum number of clusters, $N_{\max} = 159$, the TPC yields dE/dx resolution of $\sim 5\%$ [88]. The measurement is compared with the expected energy loss $\langle dE/dx \rangle_{exp}$, calculated using the so-called ALEPH parametrization [102]:

$$f(\beta\gamma) = \frac{P_1}{\beta^{P_4}} \left(P_2 - \beta^{P_4} - \ln \left(P_3 + \frac{1}{(\beta\gamma)^{P_5}} \right) \right) \quad (7.13)$$

with $\beta\gamma$ for a particle with mass hypothesis m_i and momentum p given by

$$\beta\gamma = \frac{p}{m_i} \quad (7.14)$$

where material parameters $P_{1..5}$ are obtained from fitting the TPC response to a known ionizing particle. If the spread of the signal σ_i is known, the separation of track in terms of σ_i can be calculated as

$$n_{\sigma,i}^{TPC} = \frac{dE/dx - \langle dE/dx \rangle_{exp}}{\sigma_i} \quad (7.15)$$

The distributions $dN_i/dn_{\sigma,i}$ are then integrated in the range $|n_{\sigma}| < 3$ to estimate the raw yields of hadrons.

The specific energy loss dE/dx as a function of p measured in pp collisions at $\sqrt{s} = 13$ TeV is shown in Fig. 7.7. Up to $p \approx 600$ MeV/ c , the TPC provides a good separation between π and K bands, while the proton signal can be resolved up to $p \approx 800$ MeV/ c .

7.2.1 Raw Yield Extraction

Under a given particle mass hypothesis i , the measured $d^2N_i/dp_T dn_{\sigma,i}$ distribution receives two contributions:

$$\frac{d^2N_i}{dp_T dn_{\sigma,i}} = \left(\frac{d^2N_i}{dp_T dn_{\sigma,i}} \right)_{true} + \left(\frac{d^2N_i}{dp_T dn_{\sigma,i}} \right)_{BG} \quad (7.16)$$

where *true* denotes the signal created by true hadrons of species i and *BG* is the (background) contribution from the rest of the tracks. In the

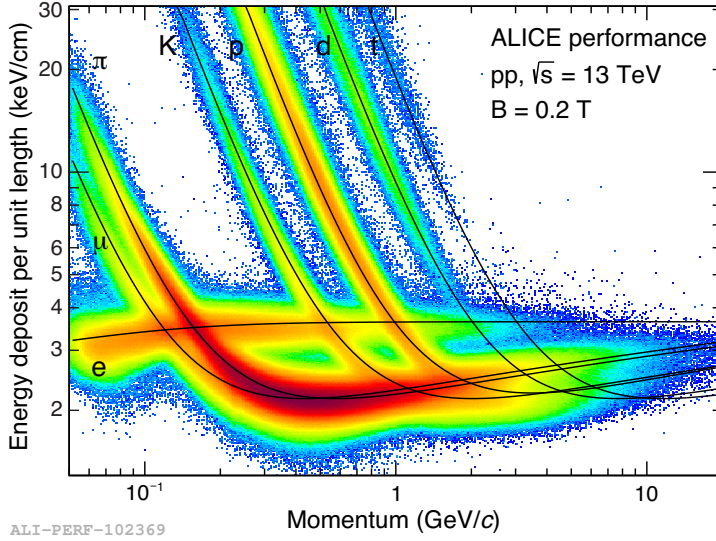


Figure 7.7: Energy deposit per unit length as a function of momentum in the TPC. Figure taken from [7].

regions where the true hadron signal is well separated from the background, $|n_{\sigma,i}| < 3$ integration is performed to extract the raw yields. One should note however that this method is very sensitive to the overlapping of the different particle bands shown in Fig. 7.7.

In order to extend the TPC PID range, statistical unfolding of the measured $d^2N_i/dp_T dn_{\sigma,i}$ is performed. Contrary to the TOF PID analysis, here each hadron is analyzed separately. Ideally, if one considers the true signal term in Eq. 7.16, by construction one would expect it to follow a gaussian distribution with the mean value $\mu = 0$ and the spread $\sigma' = 1$. In practice, there are uncertainties both on the mean value and the spread³, and therefore one should avoid approximating the distribution with a function if possible.

In the following analysis, each species was treated differently to obtain optimal accuracy for the raw yields. In order to simplify the normalization to phase space, only tracks within the rapidity region $|y| < 0.5$ under each

³A gaussian function with $\mu = 0$ and $\sigma = 1$ does not describe the distribution perfectly.

hypothesis were considered. A pure $|n_{\sigma,i}| < 3$ integration of $d^2N_i/dp_T dn_{\sigma,i}$ distributions was performed where the separation between signals was large, namely in ranges $0.4 < p_T < 0.5$ (GeV/c) for π , $p_T < 0.45$ (GeV/c) for K and $p_T < 0.6$ (GeV/c) for protons. In the regions of overlap, the following strategies were used:

Pions

In the $p_T < 0.4$ GeV/c, two gaussians would be fit in the range $1 < n_{\sigma,i} < 10$. The first gaussian would have a mean value in range $|\mu_\pi| < 0.5$ and $0.1 < \sigma_\pi < 1.1$ to describe the positive n_σ tail of the π signal. The second gaussian was fit to describe the contamination by electrons, with $4 < \mu_e < 10$ and $0.5 < \sigma_e < 2$. With this configuration the fit was found to describe the observed $d^2N_{dp_T dn_{\sigma,i}}$ distribution the best. The raw pion yield is then calculated as

$$\frac{dN_i}{dp_T} = \int_{-3}^3 \frac{d^2N_i}{dp_T dn_{\sigma,i}} dn'_{\sigma,i} - \int_{-3}^3 f(n_{\sigma,i}) dn'_{\sigma,i} \quad (7.17)$$

where the first term is an integral of the measured (full) distribution and the second term is the gaussian function describing the electron contribution.

Kaons

The kaon signal may have significant contamination from both electrons and pions. As the statistical unfolding of the electron signal is not viable for certain p_T ranges, we first extract the raw yield of both K and e . The electron contribution to the signal is removed later as feed-down, described in section 7.4. The contamination from π is removed by fitting two gaussians in range $-6 < n_{\sigma,i} < 1$. The first gaussian has constraints of mean $|\mu_{K+e}| < 0.5$, spread $0.1 < \sigma_{K+e}$ and describes the negative tail of the signal from K and e . The second gaussian is constrained to have mean $-10 < \mu_\pi < 6$ and spread $0.8 < \sigma_\pi < 2$ and parametrizes the tail part of pion signal which overlaps with K and e . Note that one could in principle attempt to remove the electrons from the sample with statistical means where the separation allows it. However, that would eventually introduce larger uncertainties.

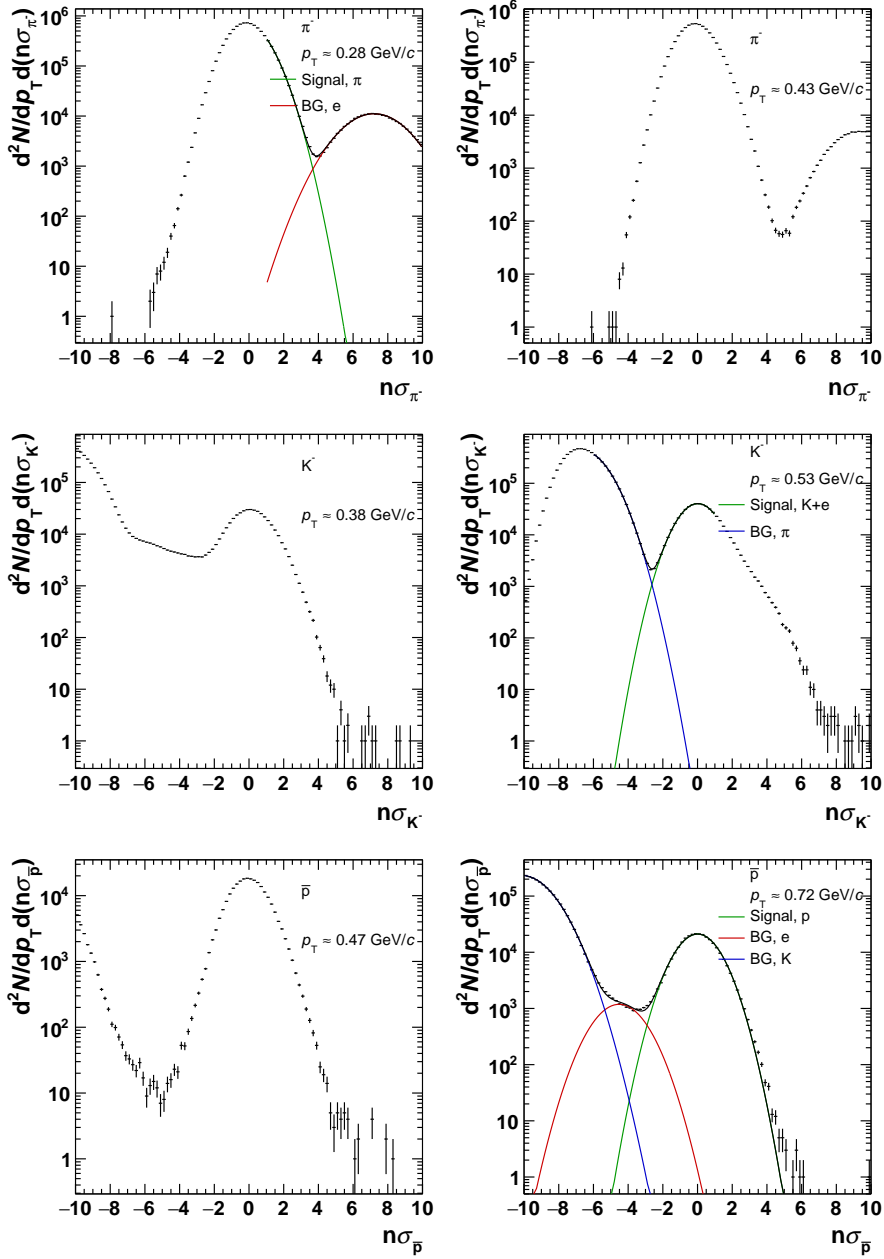


Figure 7.8: Illustration of different raw yield extraction techniques used for the TPC PID analysis.

Protons

The proton signal in the range $0.6 < p_T < 0.8$ (GeV/c) is significantly contaminated by e . Moreover, in this range, it is not trivial to resolve electrons from π and K bands. Therefore, to extract the raw yield of protons, three gaussians are fit in the range $|n_{\sigma,i}| < 6$:

- $|\mu_p| < 0.5$, $0.7 < \sigma_p < 1.2$ to describe the proton signal
- $-6 < \mu_e < -2.6$, $0.45 < \sigma_e < 1.3$ to describe the electron signal
- $-12 < \mu_{\pi+K} < -8$, $0.8 < \sigma_{\pi+K} < 3$ to describe the high- $n_{\sigma,i}$ tail of π and K contribution to electron signal.

The raw yield of protons is then estimated by integrating the proton fit function.

The different approaches of extracting π , K and p yields are illustrated in Fig. 7.8.

7.3 Efficiency Corrections

Due to limited detector acceptance, only a fraction of the particles created in the collision will be detected. Moreover, because of the stochastic nature of particle interactions in the material, not all the particles create signals in the detectors that can be reconstructed into tracks and survive the number of cuts applied for the PID analysis. The loss of particles due to acceptance and reconstruction can be as large as 80% and in general is dependent on the particle species, charge, p_T and particle direction. The estimation of particle loss is performed by simulating the detector response to different particles at different p_T , and is limited by how well the detector is understood.

To calculate the detector efficiency, a large sample of pp collisions at $\sqrt{s} = 13$ TeV is simulated using the PYTHIA 8 Monash 2013 tune. The generated particles are then propagated through a replica of the ALICE detector, which is simulated with the GEANT3 particle transport generator. Afterwards, the propagated tracks are selected, applying the same cuts as for PID analyses and the detector efficiency can be calculated as the ratio of reconstructed *primary* tracks surviving the cuts N_{rec} to the number of generated particles N_{gen} :

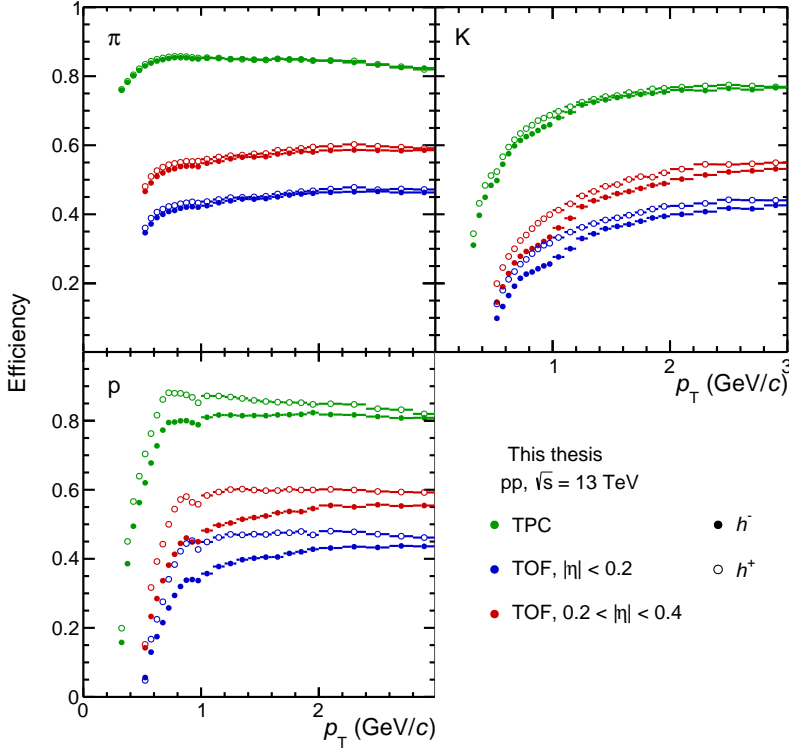


Figure 7.9: Particle identification efficiency in the TPC (green) and TOF in two pseudorapidity ranges (blue and red). Solid (empty) markers show the efficiencies for negative (positive) hadrons.

$$\epsilon_{\text{TPC}} = \frac{N_{\text{rec}}}{N_{\text{gen}}} \quad (7.18)$$

As the TPC PID is done by integrating the $d^2N/dp_T dn_{\sigma,i}$ distributions in $|n_{\sigma,i}| < 3$ for all but protons and antiprotons in range $0.6 < p_T < 0.8$ (GeV/c), the track selection for N_{rec} is done with the same cut. Technically, this is just an approximation for proton yields extracted by fit integrals; however, the introduced uncertainty is only $\sim 0.3\%$.

As discussed in the previous sections, a reconstructed track in the TOF detector has to be matched to a track in the TPC, giving rise to a TOF

matching efficiency ϵ_{ma} . This implies that the track has to be first measured in the TPC with a *tracking* efficiency ϵ_{tr} , which is very similar to the efficiency described in Eq. 7.18. The differences between ϵ_{tr} and the TPC PID efficiency are the following:

- The ϵ_{tr} values are calculated in the (pseudo-) rapidity regions used for the TOF analysis
- For ϵ_{tr} , TPC PID response ($|n_{\sigma,i}| < 3$) is not required.

The PID efficiency of the TOF detector is then a convolution of the two efficiencies:

$$\epsilon_{\text{TOF}} = \epsilon_{\text{tr}} \cdot \epsilon_{\text{ma}} = \frac{N_{\text{tr}}}{N_{\text{gen}}} \cdot \frac{N_{\text{ma}}}{N_{\text{tr}}} = \frac{N_{\text{ma}}}{N_{\text{gen}}} \quad (7.19)$$

Note that due to the statistical extraction of hadron yields, no cuts are applied to the TOF PID response. The TPC and TOF PID efficiencies for different hadrons estimated in MB pp collisions at $\sqrt{s} = 13$ TeV are shown in Fig. 7.9.

7.4 Feed-down

Both π and p yields estimated by techniques described in the previous sections are contaminated by the products of strange and multistrange baryon weak decays⁴. Moreover, the proton signal receives a significant contribution from the material budget and kaons identified in the TPC have a large contamination from electrons. The extraction of primary particle fractions in the sample is made possible due to different shapes of DCA_{xy} distributions of primaries, material conversion and weak decay products. These shapes, also called templates, can be obtained from MC studies. A summary of different sources contributing to the feed-down in different detectors is given in Table 7.2. Noting that the measured DCA_{xy} distribution is essentially a superposition of templates with different weights, one can perform a fit to the data to extract these weights. In practice it is done by minimizing the χ^2 for a given p_T

⁴Dominated by the Λ decay.

Table 7.2: List of templates used to estimate the primary fraction of π , K and p in TPC and TOF.

Specie	MC Templates Used	
	TPC	TOF
π^\pm	Primaries, weak decays	Primaries, weak decays
K	Kaons, electrons	No fits
p (\bar{p})	Primaries, Λ , Σ decays, material (protons only)	

$$\chi^2 = \sum_i \frac{\left[\frac{dN_{\text{meas}}}{d(\text{DCA}_{xy})}(x_i) - \sum_j w_j \frac{dN_j}{d(\text{DCA}_{xy})}(x_i) \right]^2}{\sigma^2(x_i)} \quad (7.20)$$

where x_i runs through the DCA_{xy} range considered (-3 cm to 3 cm), w_j is the weight of j template (primary, weak decay, material) and σ is the statistical uncertainty on the total number of particles in each x_i bin. The measured DCA_{xy} distributions for h hadron were obtained by selecting tracks with $|\sigma_h^{\text{TPC/TOF}}| < 2$. With the weights obtained from the fitting, the fraction of primary particles in the sample can be calculated as

$$\frac{N_{\text{prim}}}{N_{\text{all}}} = \frac{\int_{x_{\min}}^{x_{\max}} dx \left[w_{\text{prim}} \frac{dN_{\text{prim}}}{d(\text{DCA}_{xy})}(x) \right]}{\int_{x_{\min}}^{x_{\max}} dx \left[\sum_j w_j \frac{dN_j}{d(\text{DCA}_{xy})}(x) \right]} \quad (7.21)$$

where the numerator integrates only the primary particle distribution and the denominator sums over all the templates to ensure the unitarity. Note that the DCA_{xy} cut imposed in the track selection has to be taken into account, hence the integration is done only in the region $x_{\min, \max}$ given by Eq. 6.1.

The obtained fractions of primary particles in the sample as a function of p_T for TPC and different pseudorapidity regions of TOF are shown in Fig. 7.10. Note there is a dip in the kaon feed-down at $p_T \approx 400 \text{ MeV}/c$ in TPC due to the electron and kaon dE/dx band crossing. On the other hand, there is no need for feed-down corrections for kaons measured in TOF due to the lack of weak decays $X \rightarrow K^\pm$.

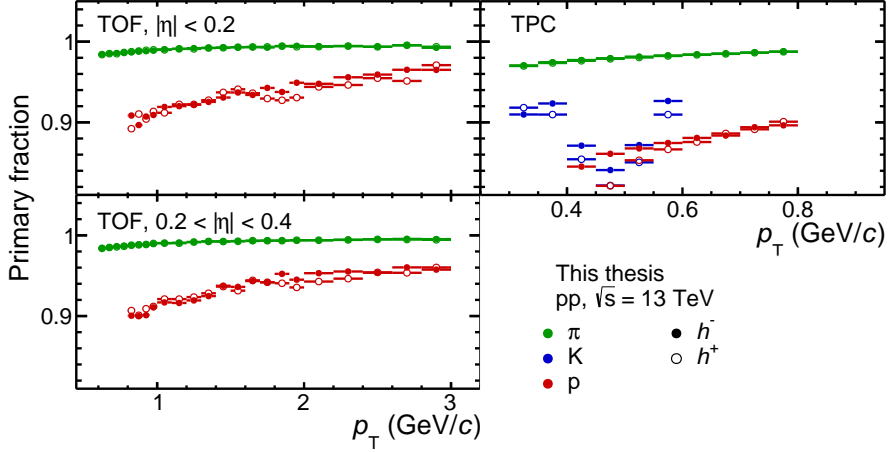


Figure 7.10: Feed-down as a function of p_T for TPC (right) and TOF (left) in pseudorapidity regions $|\eta| < 0.2$ (top) and $0.2 < |\eta| < 0.4$ (bottom). Note that K^\pm measured in TOF are not contaminated, therefore feed-down is not calculated.

7.5 Geant3, Geant4 and Fluka Corrections

The detector response to positively and negatively charged hadrons is not the same. As a result, the measured raw yields of positive and negative particles are different, even though we expect that both charges are created at the same rates. As the efficiency of the detector is calculated exclusively for hadrons of different charges, the discrepancies between particles and antiparticles are eliminated after correcting the raw yields by the efficiencies. At the end, the invariant yields of positive and negative charged hadrons should be the same at the LHC energies within the relevant systematic uncertainties.

By now it is well known that the particle transport generator used to simulate the ALICE detector, GEANT3, overestimates the absorption cross-section of the negative kaons and antiprotons [103]. Consequently, the tracking (TPC, TOF) and matching (TOF) efficiencies are not estimated correctly from the MC sample. If these efficiencies are applied to correct the raw yields, a systematic deviation is introduced into the positive-to-negative hadron ratios.

In order to eliminate this issue, tracking and matching efficiencies of K

and \bar{p} have to be corrected. Although the most straightforward way to do this would be to generate new MC samples using the transport generators where the cross-section issue is resolved, this is not an optimal solution due to the time and effort required. Alternatively, one can generate a smaller sample of collisions and use different detector simulations for particle transport. Since the effect we seek only depends on the hadron-material interaction cross-section, it is sufficient to generate a few MC samples – one for each transport generator – with the same detector configuration. Then, corrections to the efficiencies calculated from, for example, MC samples with pp collisions at $\sqrt{s} = 7$ TeV, can also be applied to the efficiencies for $\sqrt{s} = 13$ TeV collisions.

Corrections k to the tracking and matching efficiencies used in the following analysis were calculated internally in the ALICE collaboration and are shown in Fig. 7.11. The efficiencies applied to correct the raw yields are then

$$\epsilon_{\text{Corrected}} = \epsilon_{\text{Uncorrected}} \cdot k \quad (7.22)$$

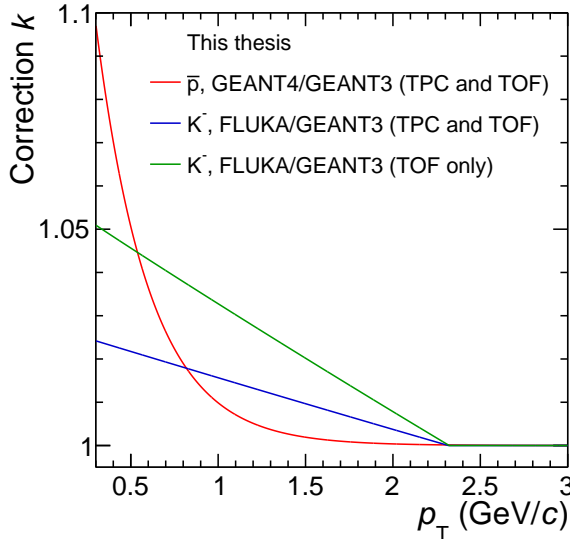


Figure 7.11: Corrections to tracking and matching efficiencies of K^- and \bar{p} in TPC and TOF detectors.

Chapter 8

Results

In the following chapter, p_T -differential spectra of charged pions, kaons and protons measured in proton-proton collisions at $\sqrt{s} = 7$ TeV and $\sqrt{s} = 13$ TeV as a function of multiplicity and sphericity are presented. Note that the analysis of pp collisions at $\sqrt{s} = 7$ TeV was performed together with other measurements (done by other people) and therefore also include strange and multistrange baryons, K_s^0 and ϕ meson results, which are important for a complete picture. Strange hadron production as a function of multiplicity was reported in [104] while a more detailed study, including the full set of light flavor hadrons, is being prepared for publication. The sphericity analysis is performed on the 13 TeV data set for charged pions, kaons and protons and was completed solely by the author.

In the analysis presented in this thesis, two multiplicities are used. The analysis is done in the slices of the charged-particle multiplicity measured by the VZERO detector. This multiplicity is called the *VOM multiplicity* and is only a relative measure. In order to relate the multiplicities in different VOM classes to different collision systems and center-of-mass energies, the mean charged-particle multiplicity density $\langle dN_{\text{ch}}/d\eta \rangle$ is measured in the pseudorapidity region $|\eta| < 0.5$. This multiplicity is called *mean* or *average multiplicity*.

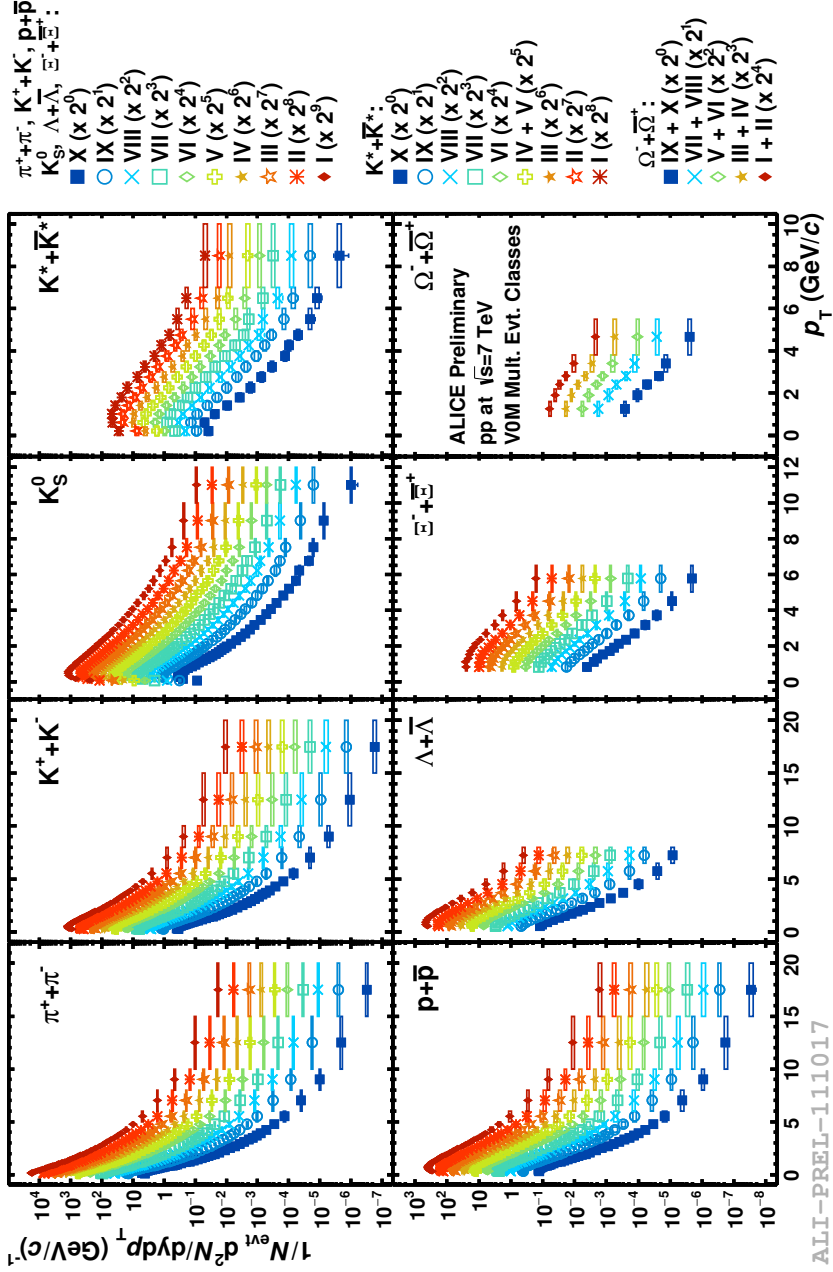
Table 8.1: V0M multiplicity classes, corresponding $\sigma/\sigma_{\text{INEL}>0}$ and $\langle dN_{\text{ch}}/d\eta \rangle$ measured in $|\eta| < 0.5$. The uncertainties quoted correspond to the quadratic sum of statistical and systematic contributions.

Class	I	II	III	IV
$\sigma/\sigma_{\text{INEL}>0}$	0–0.95%	0.95–4.7%	4.7–9.5%	9.5–14%
$\langle dN_{\text{ch}}/d\eta \rangle$	21.3 ± 0.6	16.5 ± 0.5	13.5 ± 0.4	11.5 ± 0.3
Class	V	VI	VII	VIII
$\sigma/\sigma_{\text{INEL}>0}$	14–19%	19–28%	28–38%	38–48%
$\langle dN_{\text{ch}}/d\eta \rangle$	10.1 ± 0.3	8.45 ± 0.25	6.42 ± 0.21	5.40 ± 0.17
Class	IX	X		
$\sigma/\sigma_{\text{INEL}>0}$	48–68%	68–100%		
$\langle dN_{\text{ch}}/d\eta \rangle$	3.90 ± 0.14	2.26 ± 0.12		

8.1 Proton-Proton Collisions at $\sqrt{s} = 7$ TeV

The p_{T} -differential spectra of π^{\pm} , K^{\pm} , $p(\bar{p})$, K_{S}^0 , $K^{*}(\bar{K}^{*})$, $\Lambda(\bar{\Lambda})$, $\Xi^{-}(\bar{\Xi}^{+})$ and $\Omega^{-}(\bar{\Omega})^{+}$ in different V0M multiplicity classes is shown in Fig. 8.1. The relation between the V0M class, the corresponding fraction to the total number of inelastic events and the mean charged-particle multiplicity density measured in the class is summarized in Table 8.1 [104]. We observe that the spectra become harder with increasing multiplicity and the hardening to be more pronounced for heavier hadrons, which is qualitatively similar to findings in larger systems like Pb-Pb.

Comparisons of p_{T} -differential K/π and p/π ratios at high and low multiplicities measured in pp, p-Pb and Pb-Pb collisions are shown in Fig. 8.2. In all three systems the observed p/π ratios suggest that protons are shifted towards higher p_{T} values at higher multiplicities, while K/π ratios exhibit no significant modifications with multiplicity or colliding systems. Note that the proton shift is much stronger in Pb-Pb collisions, which can be understood considering that larger systems have longer life times allowing stronger flow to build up.

Figure 8.1: p_T -differential spectra of identified hadrons in different V0M classes in pp collisions at $\sqrt{s} = 7$ TeV.

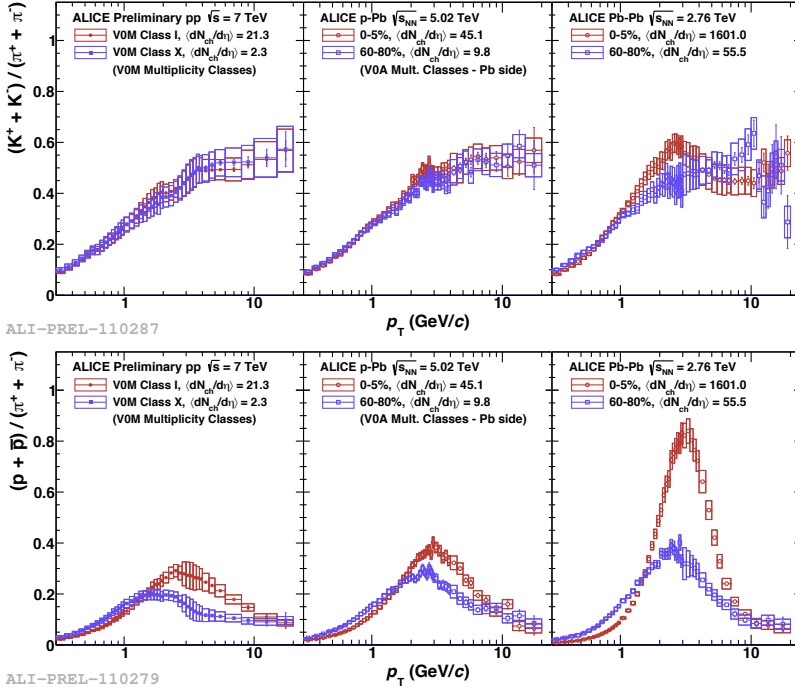


Figure 8.2: p_T -differential K/π (top) and p/π (bottom) ratios for high and low multiplicities measured in pp ($\sqrt{s} = 7$ TeV), p-Pb ($\sqrt{s_{NN}} = 5.02$ TeV) and Pb-Pb ($\sqrt{s_{NN}} = 2.76$ TeV) collisions.

8.2 Proton-Proton Collisions at $\sqrt{s} = 13$ TeV

The p_T -differential spectra of π , K and p as a function of V0M multiplicity in pp collisions at $\sqrt{s} = 13$ TeV are shown in Fig. 8.3 together with the minimum bias (MB) spectra. The mean multiplicities for each of the V0M classes considered have been measured¹ by the ALICE collaboration and are summarized in Table 8.2. Similar to the measurements at $\sqrt{s} = 7$ TeV, spectra become harder with increasing multiplicity, which is well-illustrated by the V0M-to-MB spectral ratios. Note that the error boxes shown on the spectra in Fig. 8.3 represent full systematics, a large fraction of which is correlated among multiplicities and therefore cancel in the ratios.

To study the performance of particle identification techniques used in this thesis, π , K and p spectra measured in minimum bias pp collisions at $\sqrt{s} = 13$ TeV is compared with the ALICE preliminary results, see Fig. 8.4. Spectra are found to agree within systematic uncertainties in the p_T ranges considered.

The p_T -differential K/ π and p/ π ratios are shown in Fig. 8.5 for several V0M multiplicity classes along with the MB case. We find no strong modifications of K/ π ratios in the multiplicity ranges considered, a result compatible with previous observations shown in Fig. 8.2. On the other hand, p/ π ratios in high-multiplicity (HM) pp collisions show a characteristic depletion at low p_T values, followed by an enhancement at intermediate transverse momenta. This observation is consistent with the presence of an expanding medium, suggesting that particle dynamics in pp collisions are similar to those in larger systems.

Identified Particle Production as a Function of Transverse Sphericity in High-Multiplicity Proton-Proton Collisions at $\sqrt{s} = 13$ TeV

In order to study π , K and p production as a function of transverse sphericity in pp collisions at $\sqrt{s} = 13$ TeV, only the 10% highest V0M multiplicity events are considered. The high V0M multiplicity cut ensures that most of the events have *at least ten charged tracks* required for the sphericity estimation, see Section 6.4.1 for details. In the 10% highest V0M

¹Not yet published.

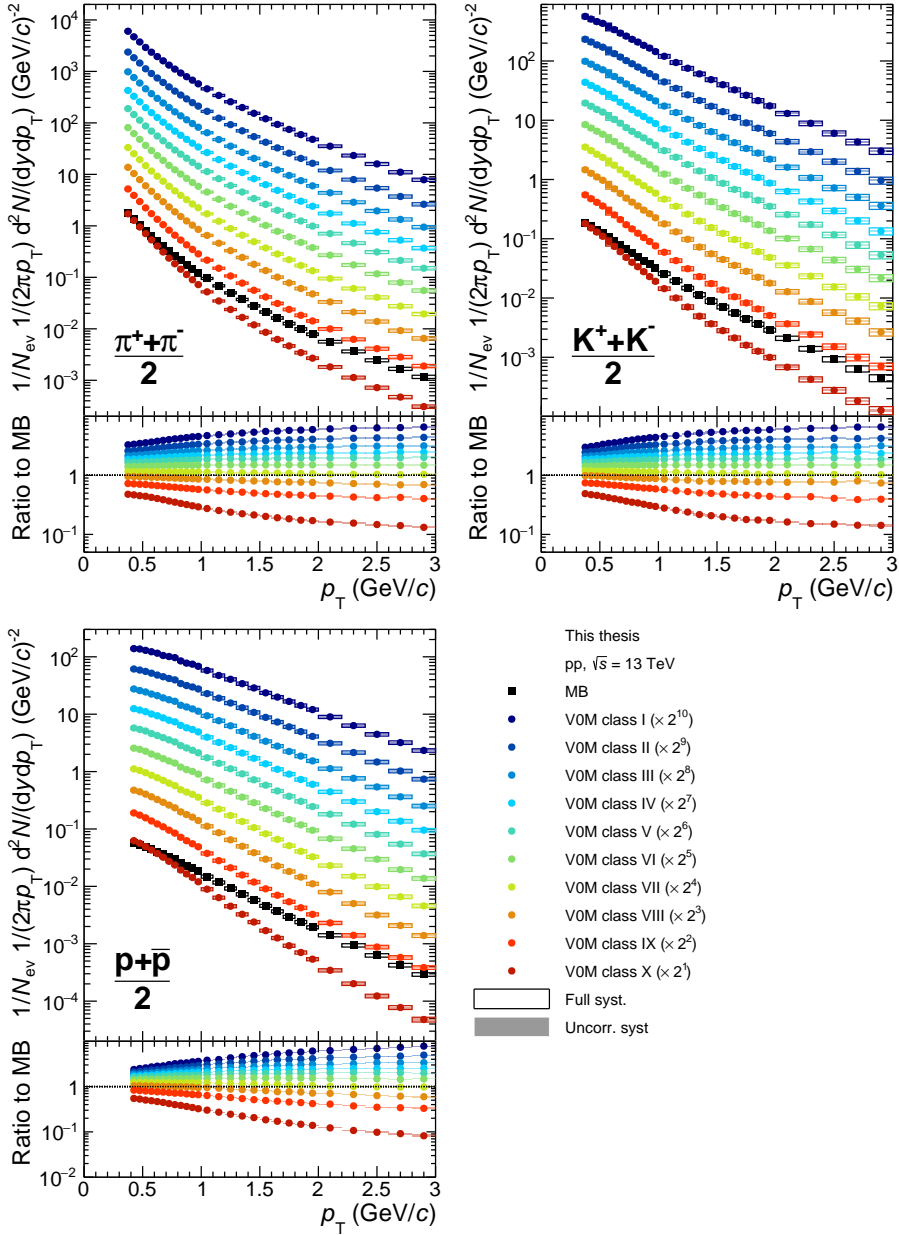


Figure 8.3: Invariant π , K and p yields as a function of V0M multiplicity in pp collisions at $\sqrt{s} = 13$ TeV.

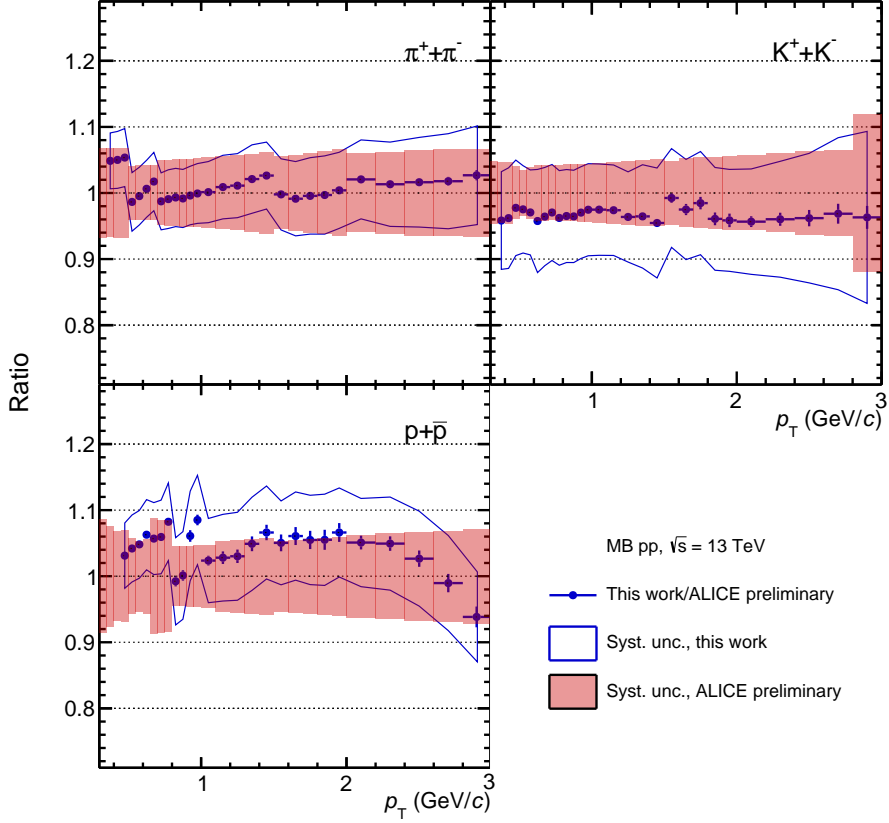


Figure 8.4: Comparison of minimum bias π , K and p spectra measured in pp collisions at $\sqrt{s} = 13$ TeV. The ratios are of spectra measured in this work to the ALICE preliminary spectra. Blue error contours represent systematic uncertainties calculated in this work and the red shaded boxes show systematic uncertainties of the ALICE preliminary spectra.

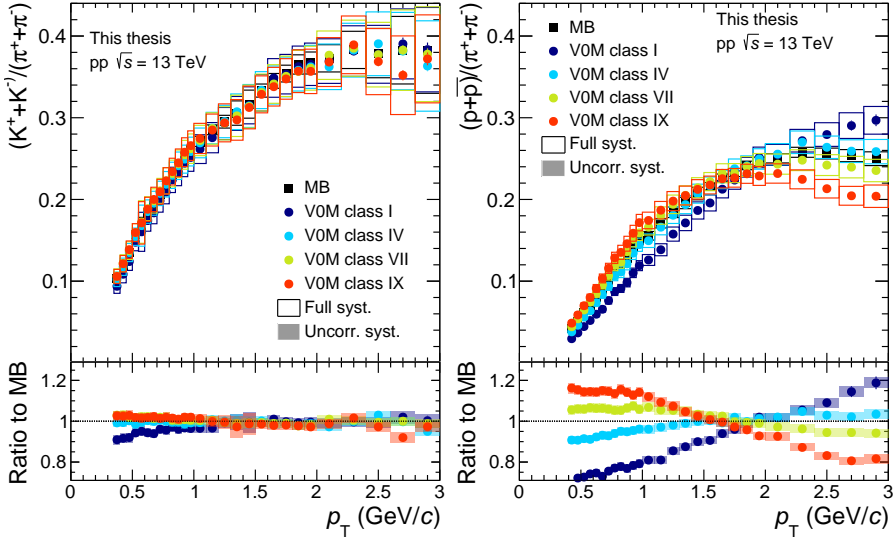


Figure 8.5: p_T -differential K/π (left) and p/π (right) ratios in several V0M multiplicity classes measured in pp collisions at $\sqrt{s} = 13$ TeV.

Table 8.2: V0M multiplicity classes and corresponding $\langle dN_{\text{ch}}/d\eta \rangle$ measured in $|\eta| < 0.5$ at $\sqrt{s} = 13$ TeV. The reported errors are not final and the relation to $\sigma/\sigma_{\text{INEL}>0}$ is approximate

Class	I	II	III	IV
$\sigma/\sigma_{\text{INEL}>0}$	0–1%	1–5%	5–10%	10–15%
$\langle dN_{\text{ch}}/d\eta \rangle$	26.18 ± 0.55	20.16 ± 0.41	16.40 ± 0.34	14.00 ± 0.29
Class	V	VI	VII	VIII
$\sigma/\sigma_{\text{INEL}>0}$	15–20%	20–30%	30–40%	40–50%
$\langle dN_{\text{ch}}/d\eta \rangle$	12.28 ± 0.25	10.31 ± 0.21	8.24 ± 0.17	6.62 ± 0.13
Class	IX	X		
$\sigma/\sigma_{\text{INEL}>0}$	50–70%	70–100%		
$\langle dN_{\text{ch}}/d\eta \rangle$	4.77 ± 0.09	2.26 ± 0.05		

multiplicity sample, we find that 97% of events match this requirement. The sphericity distribution in this multiplicity class is shown in Fig. 8.6. To select different final state shapes, 20% of events with the *highest* measured S_O were considered as *isotropic* and 20% of events with the *lowest* S_O – as *jetty*. The selection resulted in following S_O cut-off values:

$$\begin{aligned} 0 < S_O < 0.46 & \quad \text{for jetty events} \\ 0.76 < S_O < 1 & \quad \text{for isotropic events} \end{aligned}$$

To estimate charged-particle multiplicities in the event classes used for the sphericity-selected analysis, we first measure the correlation between the $\langle dN_{\text{ch}}/d\eta \rangle$ given in Table 8.2 and the mean number of charged tracks $\langle N_{\text{ch}} \rangle$ in $|\eta| < 0.8$. The correlation function can then be interpolated to extract the $\langle dN_{\text{ch}}/d\eta \rangle$ in 10% V0M, jetty and isotropic event classes. The measured $\langle dN_{\text{ch}}/d\eta \rangle$ as a function $N_{\text{ch}}(|\eta| < 0.8)$ is shown in Fig. 8.7 and the interpolated $\langle dN_{\text{ch}}/d\eta \rangle$ are summarized in Table 8.3.

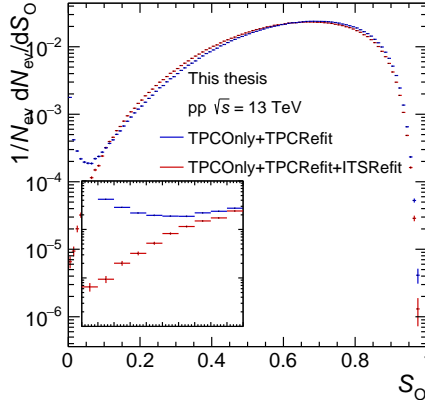


Figure 8.6: Sphericity distribution measured in 0–10% (V0M class I–III) in pp collisions at $\sqrt{s} = 13$ TeV. The small figure shows the sphericity distribution in range $0 < S_O < 0.1$. The excess of very low S_O events discussed in Section 6.4.1 is also present in the data and can be removed by requiring the tracks to be reconstructed in the ITS.

The comparison of p_T -differential π , K and p yields measured in jetty and isotropic collisions are shown in Fig. 8.8 together with sphericity un-

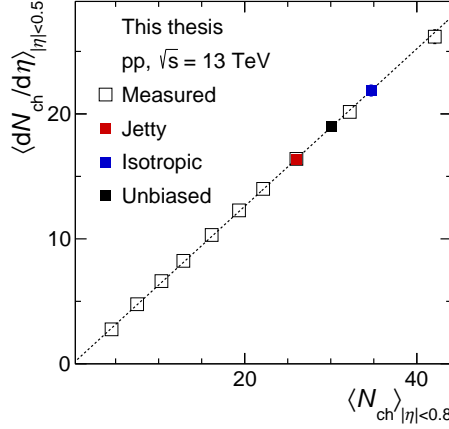


Figure 8.7: Correlation between mean charged-particle multiplicity measured in one unit of pseudorapidity and the number of charged particles in pseudorapidity region $|\eta| < 0.8$. Empty squares represent $\langle dN_{\text{ch}}/d\eta \rangle$ measured in V0M multiplicity classes in pp collisions at $\sqrt{s} = 13$ TeV, the dashed line shows a linear fit to the data points and the solid squares show the interpolated values for different sphericity classes.

biased yields. The spectra in isotropic events exhibit an enhanced hadron production at low transverse momenta as compared to S_{O} -unbiased collisions, followed by a suppression for transverse momenta above 2 – 2.5 GeV/ c for π and K. The spectra of protons in isotropic events appears to be enhanced in the whole p_{T} range considered and crosses the S_{O} -unbiased spectra at $p_{\text{T}} \sim 3$ GeV/ c . Particle production in jetty events shows the opposite behavior: spectra are suppressed at low transverse momenta and enhanced at intermediate p_{T} .

Table 8.3: Mean charged-particle multiplicity in one unit of pseudorapidity and different sphericity classes in 0–10% highest V0M multiplicity pp collisions at $\sqrt{s} = 13$ TeV.

Event class	S_{O} -unbiased	Jetty, $S_{\text{O}} < 0.47$	Isotropic, $S_{\text{O}} > 0.76$
$\langle dN_{\text{ch}}/d\eta \rangle_{ \eta <0.5}$	18.97 ± 0.38	16.38 ± 0.33	21.67 ± 0.44

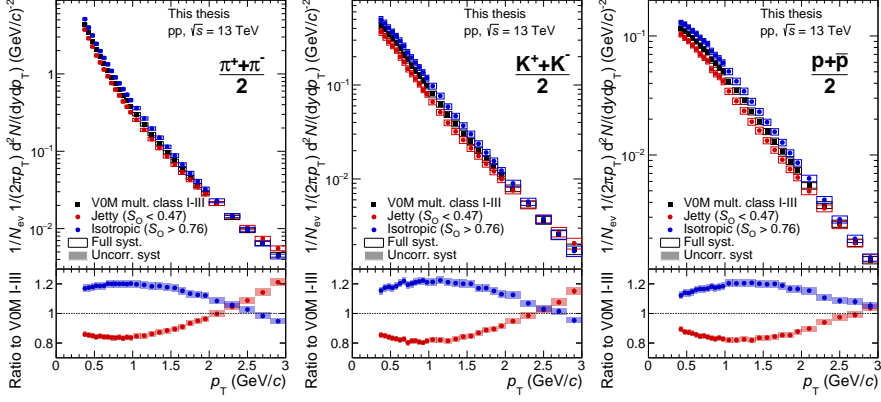


Figure 8.8: Invariant π , K and p yields measured in jetty, isotropic and sphericity unbiased (V0M class I–III) pp collisions at $\sqrt{s} = 13$ TeV.

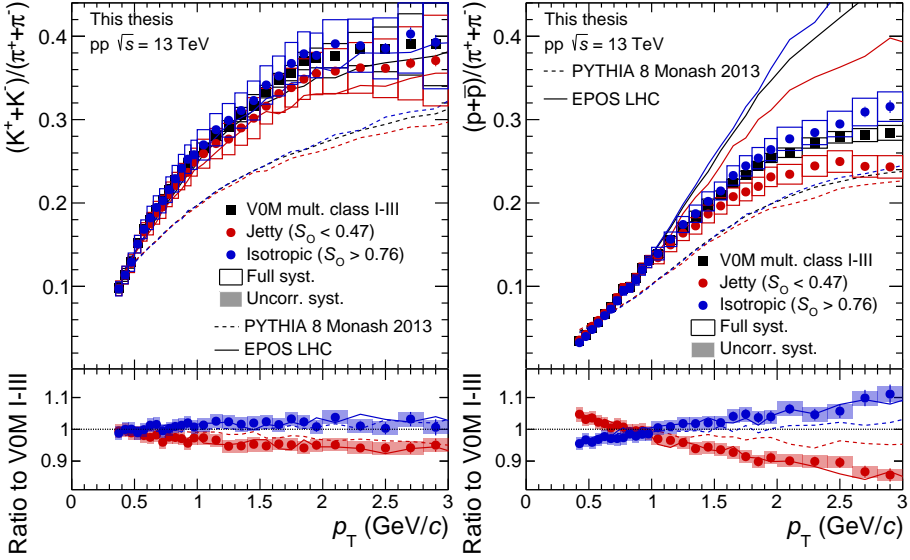


Figure 8.9: Top: p_T -differential K/π (left) and p/π (right) ratios measured in jetty, isotropic and sphericity-unbiased (V0M class I–III) pp collisions at $\sqrt{s} = 13$ TeV. Bottom: double ratios of jetty (isotropic) to sphericity-unbiased class. Solid and dashed lines show EPOS LHC and PYTHIA 8 predictions respectively.

The p_T -differential K/π and p/π ratios measured in jetty, isotropic and spherocity-unbiased high-multiplicity pp collisions at $\sqrt{s} = 13$ TeV are shown in Fig. 8.9. We find that the K/π ratio in isotropic events is consistent with those measured in the spherocity-unbiased case, while the jetty events show signatures of a suppression. The latter can be understood considering that hadron production via jet fragmentation is modified by the transverse momentum of the jet in a species-dependent manner [105], which will be discussed in detail later.

Alternatively, the p/π ratios in isotropic collisions appear to be shifted in p_T with respect to the ratios measured in spherocity-unbiased collisions. The effect is qualitatively similar to the multiplicity dependent modifications of p/π ratio observed in Pb-Pb, suggesting that QGP-like effects can be further enhanced in pp collisions using S_O . The jetty events show a suppression of p/π ratio with respect to the S_O -unbiased case, which can be attributed to the production mechanisms of protons in jets.

8.3 Systematic Uncertainties

Systematic uncertainties of identified hadron spectra and their ratios were estimated by varying the track selection criteria and the parameters specific to each PID technique. For each variation, fully corrected spectra were recalculated following the steps described in Chapter 7 and their differences from the default spectra were taken as systematic uncertainties. The multiplicity uncorrelated uncertainties were taken as differences between spectral ratios (V0M class to minimum bias) before and after the parameter variation. The spherocity-uncorrelated uncertainties were calculated in a similar manner, but using spherocity-unbiased spectra instead of minimum bias. The same was also done for all the particle ratios presented in this work. In cases where a parameter was varied several times (e.g. TOF resolution), the largest uncertainty was used. Uncertainties originating from different sources were assumed to be uncorrelated and summed in quadrature to obtain full systematic errors.

Tracking Uncertainties

The global tracking uncertainty was calculated by varying the track selection parameters as summarized in Table 8.4. The following parameters

Table 8.4: Different sets of track cuts used to estimate systematic uncertainties on track selection.

Parameter	Lower	Higher	Standard
Min. crossed rows in TPC	60	80	70
Max. χ^2 per TPC cluster	-	5	4
Max. DCA _z (cm)	1	3	2

were varied:

- Minimum number of crossed rows in the TPC; fewer crossed rows result in lower tracking resolution and potentially more V0 daughter particles in the sample. On the other hand, more crossed rows lead to tracks with better tracking resolution, but also a larger number of primary tracks are rejected.
- Maximum allowed χ^2 per TPC cluster, which regulates the quality of track reconstruction with Kalman filter.
- Cut on the maximum DCA_z value, which regulates track extrapolation to the primary vertex quality.

Uncertainties calculated by varying different track selection parameters are summed in quadrature to calculate the total tracking uncertainty, shown in Fig. 8.10 (separate contributions to tracking uncertainties are shown in Appendix B). Note that this is a standard procedure for global tracking uncertainty estimation used by the ALICE collaboration for all π , K and p analyses.

In addition, the following systematic uncertainties were previously estimated internally by the ALICE collaboration and used in this analysis:

- p_T -dependent (1%–6%) ITS-TPC matching uncertainty, multiplicity-correlated
- p_T -independent TOF matching efficiency (3%, 6% and 4% for π , K and p), multiplicity-correlated [106]
- p_T -independent efficiency uncertainty (2.1% for all species), uncorrelated among multiplicity classes.

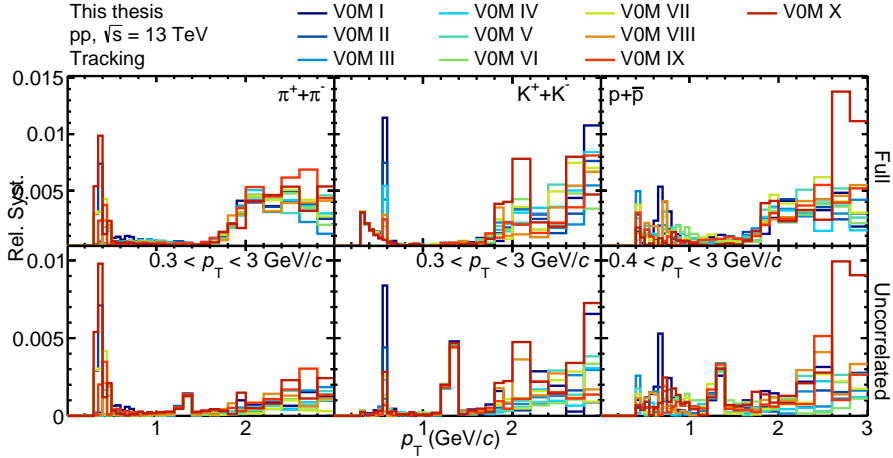


Figure 8.10: Global tracking uncertainty, full (top panels) and multiplicity uncorrelated (bottom panels) for π , K and p in different VOM multiplicity classes.

PID Uncertainties

The systematic uncertainties on particle spectra in the TPC were estimated by integrating the $d^2N_i/dp_T dn_{\sigma,i}$ distributions in $-2.5 < n_{\sigma,i} < 2.5$ and $-3.5 < n_{\sigma,i} < 3.5$ ranges. Note that an integral of a gaussian distribution in range $|n_{\sigma,i}| < 2.5$ (3.5) corresponds to 98.7% (99.9%) of the total area, and therefore the yields estimated in this way have to be renormalized respectively. The uncertainties are found to be below 1%, 5% and 2% for π , K and p, with a large fraction of it being correlated among multiplicity classes. The uncorrelated systematic uncertainty originating from different $n_{\sigma,i}$ integration regions was found to be $< 0.5\%$ for π and p, and $< 2\%$ for K in all the multiplicity classes considered, see Fig. 8.11.

To estimate the systematic uncertainties on particle spectra measured with TOF below $p_T < 1.5$ GeV/c, $|n_{\sigma,i}| < 3$ integration was done. Note that such method does not remove mismatched tracks and cuts off a part of the TOF tail, see Section 7.1. Moreover, this technique is unviable above $p_T > 1.5$ GeV/c due to the overlap of π and K signals. The uncertainties calculated using $n_{\sigma,i}$ integration are shown in Fig. 8.12.

At higher transverse momentum, the following approaches were taken:

- Varying the TOF resolution for each of the species

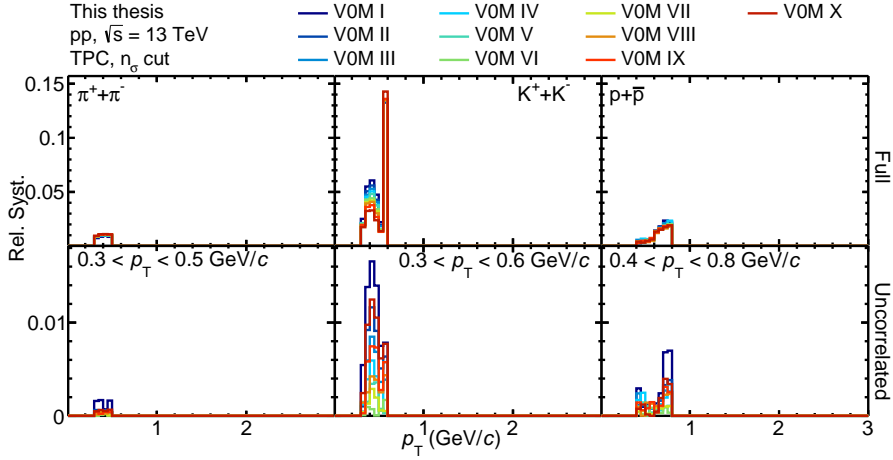


Figure 8.11: TPC PID uncertainty, full (top panels) and multiplicity uncorrelated (bottom panels) for π , K and p in different VOM multiplicity classes.

- Varying the tail cut-off parameter for each of the species
- Setting the β offset, $\Delta\beta = 0$.

The resolution of TOF for π and K was found to be constant above $p_T > 1.5 \text{ GeV}/c$. To calculate the uncertainty of the resolution, $\sigma_{\text{TOF}}/\langle\sigma_{\text{TOF}}\rangle - 1$ distribution was fit with a gaussian function, with σ_{TOF} being π and K resolution obtained from fits at each p bin and $\langle\sigma_{\text{TOF}}\rangle$ – averaged over $1.5 < p < 3 \text{ GeV}/c$ range. The distribution with the fit function is shown in Fig. 8.13. The uncertainty on TOF resolution is found to be roughly 2%. In order to estimate the effect of this uncertainty on the identified hadron spectra, TOF PID procedures were repeated with 98% and 102% of nominal resolution values. The resulting full and multiplicity uncorrelated uncertainties on particle spectra are shown in Fig. 8.14. The uncertainties were found to be below 1%, 1.5% and 1% for π , K and p, with the multiplicity uncorrelated parts being below 0.1%, 0.5% and 0.5% respectively.

A similar procedure was repeated to estimate the uncertainty on the tail cut-off parameter t , also illustrated in Fig. 8.13. The uncertainties on the hadron spectra and ratios were obtained by fixing the tail parameter to 96% and 104% of its nominal values; the obtained uncertainties are shown in Fig. 8.15. The full (and multiplicity uncorrelated) uncertainties from

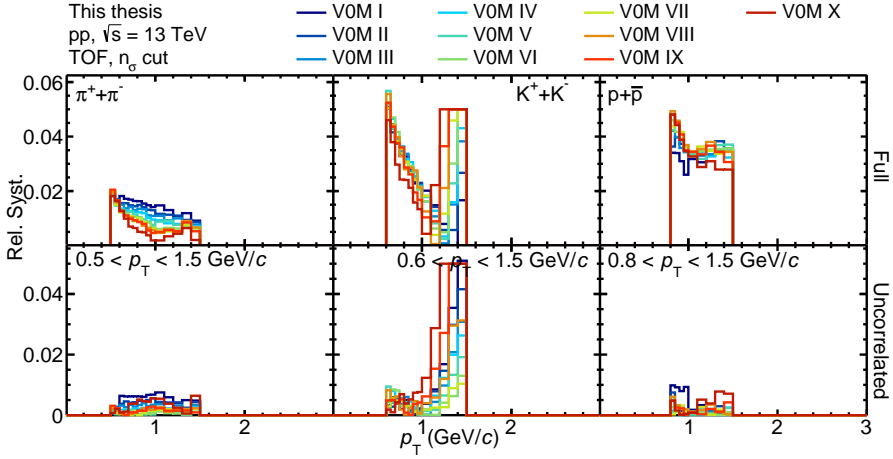


Figure 8.12: TOF PID performance for $p_T < 1.5 \text{ GeV}/c$ π , K and p, estimated as an integral of $dN/dn_{\sigma,i}$ in $|n_{\sigma,i}| < 3$ range in different VOM classes. Full and multiplicity uncorrelated uncertainties are shown in top and bottom panels respectively.

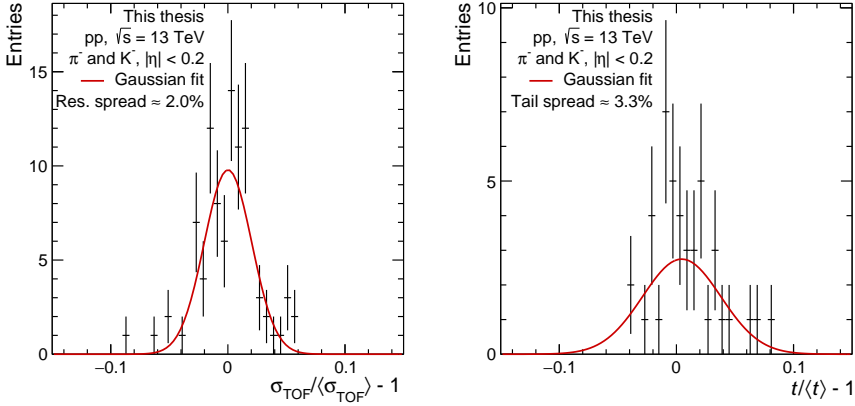


Figure 8.13: Spread of TOF resolution (left) and tail cut-off parameter (right) with gaussian fits.

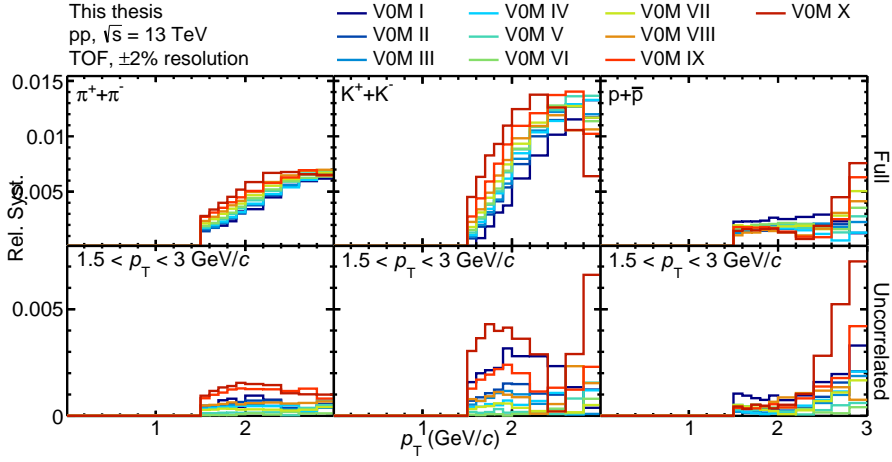


Figure 8.14: Full (top panels) and multiplicity uncorrelated (bottom panels) systematic uncertainties from TOF resolution as a function of p_T for π , K and p as a function of VOM multiplicity.

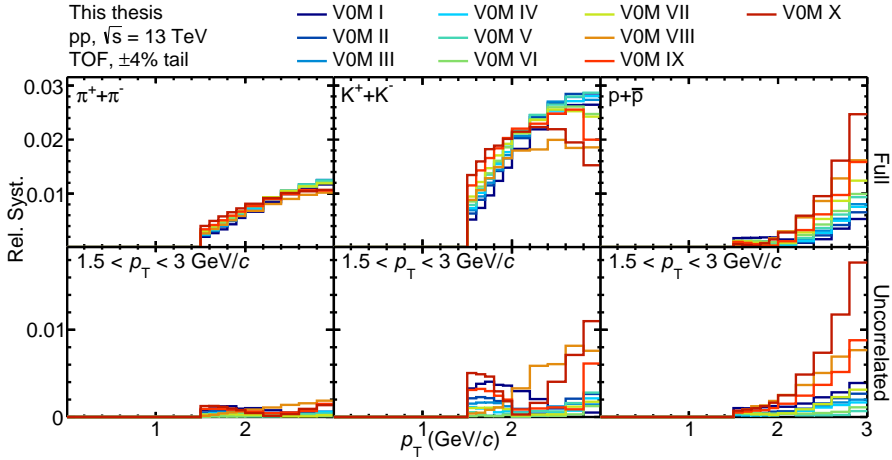


Figure 8.15: Full (top panels) and multiplicity uncorrelated (bottom panels) systematic uncertainties from tail parametrization in TOF as a function of p_T for π , K and p as a function of VOM multiplicity.

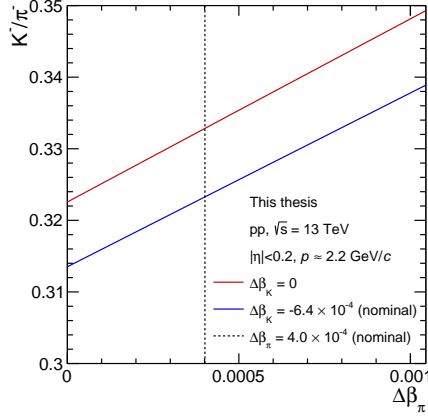


Figure 8.16: K^-/π^- raw yields ratios measured in $|\eta| < 0.2$ at $p_T \approx 2.2 \text{ GeV}/c$ as a function of $\Delta\beta_\pi$. Red line shows the ratio obtained from fits with $\Delta\beta_K = 0$ (internal TOF calibration) and blue lines represent fits with $\Delta\beta_K = -6.4 \cdot 10^{-4}$ (value obtained in this work). The dashed line shows the $\Delta\beta_\pi$ calculated in this thesis.

TOF tail parametrization are below 1% (0.2%), 3% (1%) and 3% (1%) for π , K and p respectively.

In order to estimate the uncertainties originating from the TOF miscalibration, the offset of β for each species is set to $\Delta\beta = 0$. In the momentum regions where the TOF responses for different species are overlapping (e.g. π and K at $p \gtrsim 1.5 \text{ GeV}/c$), this is the dominant source of uncertainties. As shown in Fig. 8.16, for K^-/π^- ratio at $p \approx 3 \text{ GeV}/c$, a $\Delta\beta_\pi = 10^{-3}$ (which corresponds to $\sim 0.1\%$ in β_π) can have a $\sim 10\%$ effect. Protons, on the other hand, are well separated from kaons and pions in the momentum range considered and are therefore less sensitive to this effect. The uncertainties on hadron spectra originating from the TOF miscalibration are shown in Fig. 8.17 with typical values of 3%, 10% and 2% for π , K and p at $p_T \approx 3 \text{ GeV}/c$. It is also worth noting that a large fraction of the uncertainties is correlated among multiplicity classes, and thus the multiplicity uncorrelated part is much smaller.

All the systematic uncertainties originating from the particle identification techniques in each V0M class are shown Appendix C.

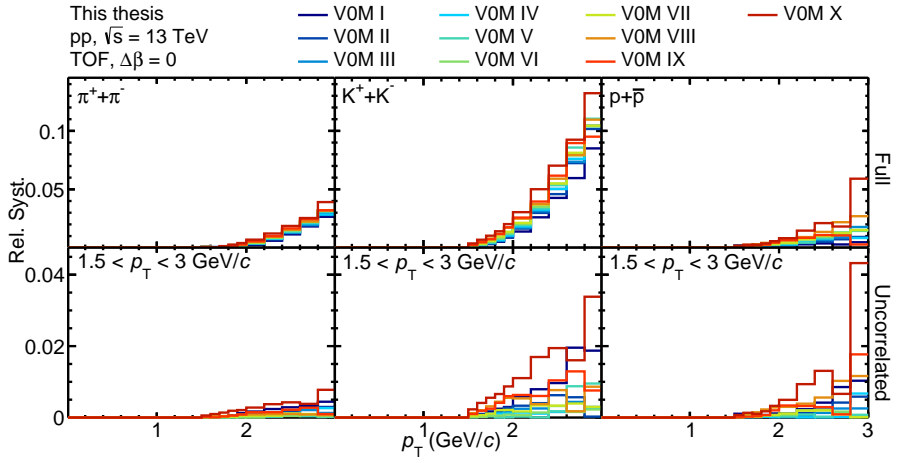


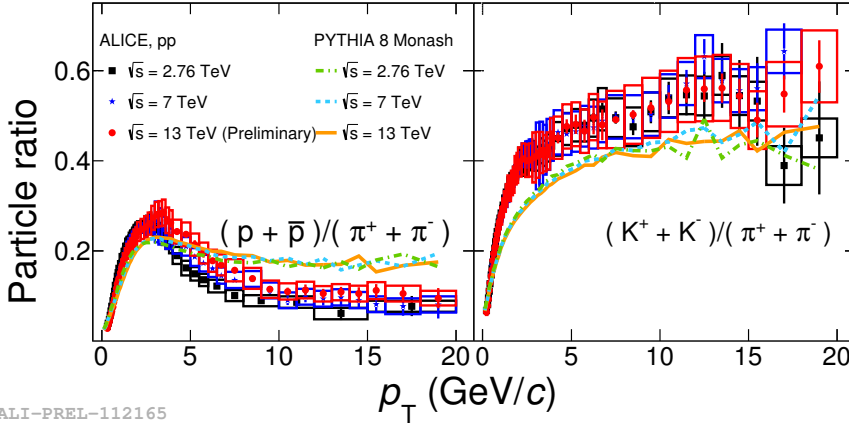
Figure 8.17: Full (top panels) and multiplicity uncorrelated (bottom panels) systematic uncertainties from TOF miscalibration as a function of p_T for π , K and p as a function of VOM multiplicity.

Chapter 9

Discussion

One of the key signatures of QGP in heavy-ion collisions is the mass-dependent boost of hadrons, which results in a characteristic shift of p_T -differential hadron-to-pion ratios in central collisions with respect to peripheral, as was discussed in Section 3.2. The p_T -differential K/π ratios measured in high and low-multiplicity pp, p-Pb and Pb-Pb collisions shown in Fig. 8.2 exhibit no strong multiplicity dependence. On the other hand, protons appear to be shifted towards larger transverse momenta at high multiplicities in all three systems, and the shift gets stronger with increasing system size. Similar behavior is also found in pp collisions at $\sqrt{s} = 13$ TeV as shown in Fig. 8.5, where the modifications of p/π ratios are more pronounced at higher multiplicities and, in fact, a small shift of protons is already seen in MB pp collisions at different center-of-mass energies (see Fig. 9.1 [107]).

The qualitatively similar trends observed in pp, p-Pb and Pb-Pb collisions suggest that particle dynamics in small and large systems are governed by the same physics, which means that the QGP created in Pb-Pb collisions might also be present in pp. To study if this is true, this chapter will explore how perturbative QCD models describing small systems extend to Pb-Pb and how the macroscopic prescription of large systems extend to pp. I will then discuss if the pQCD and QGP-like effects in pp collisions can be isolated using event shape techniques and examine the physics under the two domains.



ALI-PREL-112165

Figure 9.1: p_T -differential p/π and K/π ratios measured in minimum-bias pp collisions at different center center-of-mass energies.

9.1 Spectral Shapes

The evolution of the p/π ratio with $dN_{\text{ch}}/d\eta$ in Pb-Pb collisions is usually understood in terms of quark coalescence [108] or radial flow [109] which was discussed in Section 3.2 and might require a fireball in a local thermodynamic equilibrium. On the other hand, in pp collisions certain QCD effects like color reconnection (see Section 4.1) or rope hadronization (see Section 4.2) can mimic the collective behavior without hydrodynamical considerations. In Fig. 9.2 we show the p/π ratio as a function of $dN_{\text{ch}}/d\eta$ at a fixed (low and intermediate) p_T in pp collisions at $\sqrt{s} = 7$ TeV together with predictions from several MC generators.

We find that PYTHIA 8 [45] is able to reproduce the observed trends qualitatively, provided that color reconnection is considered. It is particularly interesting to see that both PYTHIA 8 without CR and HERWIG7 [110] predict almost no evolution of the ratios with multiplicity, indicating that the observed effects cannot be explained solely in terms of pQCD. DIPSY [54, 55], featuring a more advanced treatment of colored strings leading to a larger effective string tension, is able to reproduce the observed trends well, although the absolute values of p/π ratios at low p_T are highly overestimated. Finally, EPOS LHC [77], which has a

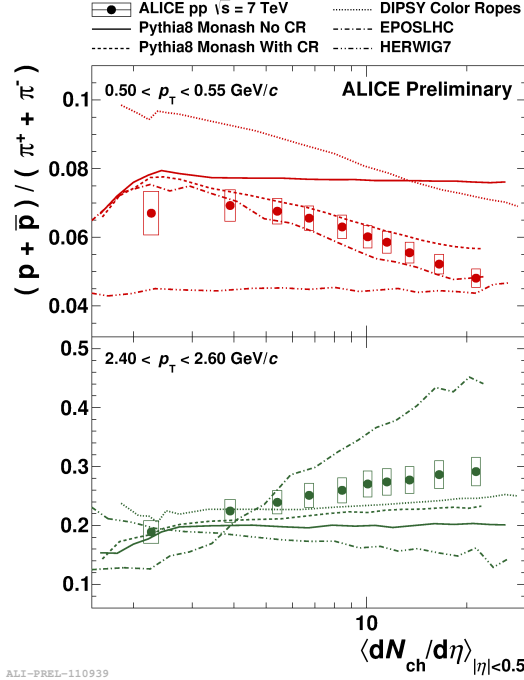


Figure 9.2: Evolution of p/π ratio at low (top) and intermediate (bottom) p_T with $\langle dN_{ch}/d\eta \rangle$ in comparison to PYTHIA8, EPOS LHC and DIPSY predictions.

built-in flow parametrization, predicts the falling (rising) behavior at low (intermediate) p_T , but the predicted hydrodynamical effects are too strong. Overall, it appears that the dynamics of the p/π ratios can be described by several mechanisms and more systematic studies are required to check their validity.

Comparison to the Blast Wave Model

One of the biggest open questions in the heavy-ion field is whether the dynamics observed in pp and Pb-Pb collisions share the same origins. We have already discussed how the dynamics in pp collisions can be described by perturbative models. However, similar dynamics seen in heavy-ion collisions have been successfully explained by macroscopic models that include hydrodynamical elements, such as the blast wave model. It is therefore

worth examining how the BW model can describe p_T spectra measured in pp collisions.

As described in Section 4.3, the underlying assumption of the BW model is that hadrons are produced thermally and are then boosted in the transverse plane by some velocity with a profile given by Eq. 4.13. The boost originates from the expansion of the system, which terminates at kinetic freeze-out temperature T_{kin} . The average transverse velocity $\langle\beta_T\rangle$ and T_{kin} can be extracted by simultaneously fitting the hadron spectra. For our discussion, we will consider BW fits to π , K and p spectra and then extrapolate the results for other hadrons. As the thermal production of particles is expected to be the dominant mechanism in HI collisions, we will only consider low p_T hadrons. However, as π abundances receive a significant contribution from resonance hadron decays, $p_T < 500 \text{ MeV}/c$ pions are excluded from the fits. For consistency, the p_T ranges of particles used for BW fitting in pp collisions at $\sqrt{s} = 7 \text{ TeV}$ are the same as those used for similar studies in p-Pb and Pb-Pb studies by the ALICE collaboration

$$\begin{aligned}\pi &: 0.5 < p_T < 1 \text{ GeV}/c \\ \text{K} &: 0.2 < p_T < 1.5 \text{ GeV}/c \\ \text{p} &: 0.3 < p_T < 3 \text{ GeV}/c\end{aligned}$$

The performance of BW model fitting in 0–5% highest multiplicity pp collisions at $\sqrt{s} = 7 \text{ TeV}$ is shown in Fig. 9.3. The solid lines show the fit result, while the dashed lines show the predictions for other particle species. We find that in restricted p_T regions, all hadrons except resonances are affected by the same velocity field. These regions are observed to be larger for heavier hadrons, which in the hydrodynamical picture is a feature of radial flow (a change in hadron velocity, $\Delta\beta$, results in a larger Δp_T for heavier hadrons). The poor description of resonance spectra could be understood considering their low elastic cross sections and life-times [79]. Due to its short life-time ($1.39 \cdot 10^{-23} \text{ s}$) [7], K^* can decay in the hadronic phase and its daughters are subjected to stronger rescatterings due to the larger elastic cross section.

Due to limited p_T range of hadron spectra in the 13 TeV analysis, it was not possible to perform the BW fitting in the same range as used in ALICE for other systems and center-of-mass energies. Instead, for the

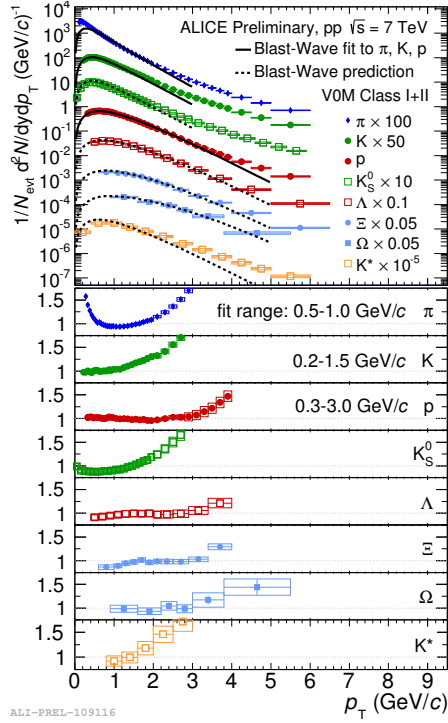


Figure 9.3: Comparison of p_T -differential spectra to blast wave model fits (solid lines) and predictions (dashed lines) in V0M class I–II in pp collisions at $\sqrt{s} = 7$ TeV. The model was fit to π , K and p spectra and then used to estimate the spectral shapes of (multi) strange hadrons.

$\sqrt{s} = 13$ TeV analysis presented here the following ranges were considered

$$\begin{aligned} \pi : & \quad 0.5 < p_T < 1 \text{ GeV}/c \\ K : & \quad 0.3 < p_T < 1.5 \text{ GeV}/c \\ p : & \quad 0.4 < p_T < 3 \text{ GeV}/c \end{aligned}$$

For cross checks, the BW fits were performed using this range on the hadron spectra measured in pp collisions at $\sqrt{s} = 7$ TeV. We find that the effects of using a narrower fitting range are very small, as shown in Fig. 9.4. The performance of blast wave fits in the highest and lowest multiplicity pp collisions at two center-of-mass energies is shown in Fig. 9.5, and for other multiplicity classes see Appendix D and Appendix E. We find that

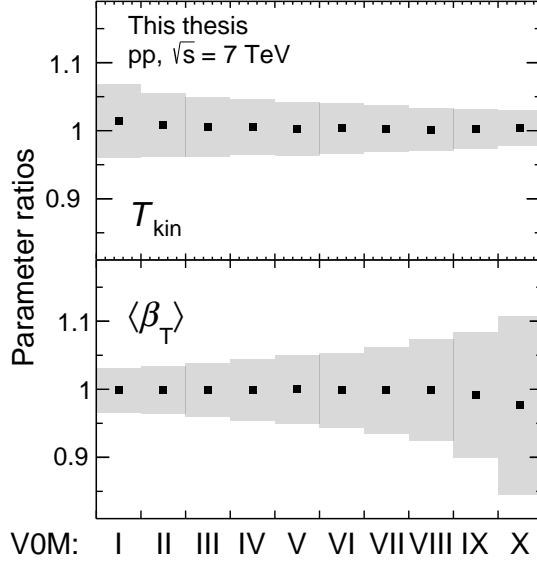


Figure 9.4: Comparison of T_{kin} and $\langle\beta_T\rangle$ extracted from pp collisions at $\sqrt{s} = 7$ TeV using different blast wave fitting ranges. Ratios were calculated dividing the parameters extracted using wider p_T ranges (used in previous analyses) by those extracted using narrower p_T ranges (available in this thesis). Shaded boxes represent the uncertainties of the parameters extracted using wider p_T ranges.

proton spectra are well described by the BW model at both high and low multiplicities under the two center-of-mass energies considered, while the description of π and K becomes worse at lower multiplicities. On the other hand, protons are the most sensitive to the expanding medium as discussed in Section 3.2, and the very good agreement between the model and the data suggests the presence of transverse flow in small systems for the multiplicities considered.

The BW parameters $\langle\beta_T\rangle$ and T_{kin} extracted from pp collisions measured at $\sqrt{s} = 7$ and 13 TeV in different multiplicity classes are shown in Fig. 9.6 together with those extracted from p-Pb and Pb-Pb analyses. We observe the following:

- In all systems, $\langle\beta_T\rangle$ increases with charged-particle multiplicity, sug-

gesting that the expansion is increasingly stronger at larger $\langle dN_{\text{ch}}/d\eta \rangle$

- The freeze-out temperature in pp collisions at $\sqrt{s} = 13$ TeV is systematically lower than that measured at 7 TeV and at large multiplicities compares better to p-Pb data. This suggests that the decoupling of the medium occurs at later times as the center-of-mass energy increases
- Pb-Pb collisions show a significantly lower T_{kin} as compared to pp or p-Pb in the whole multiplicity range considered, indicating that thermal freeze-out might be affected by the size of the colliding system.

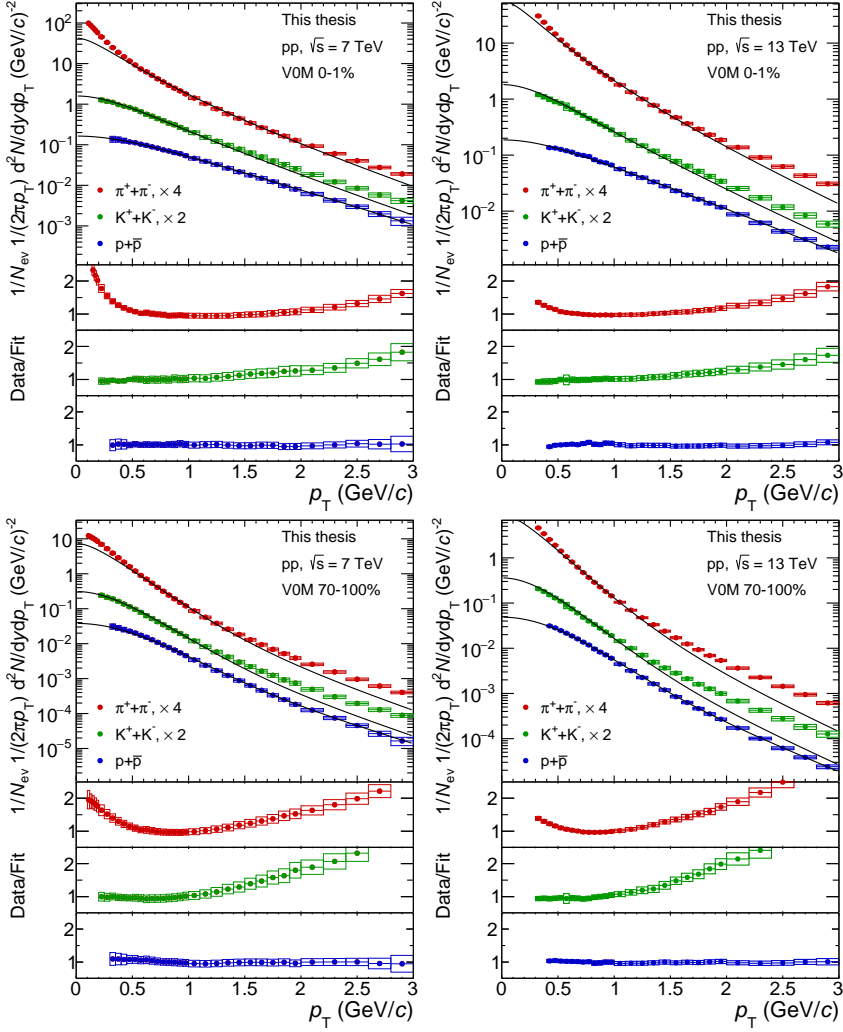


Figure 9.5: Blast wave fit performance in high (top) and low (bottom) multiplicity pp collisions at $\sqrt{s} = 7$ (left) and 13 TeV (right). Identical fitting ranges were used in both center-of-mass energies.

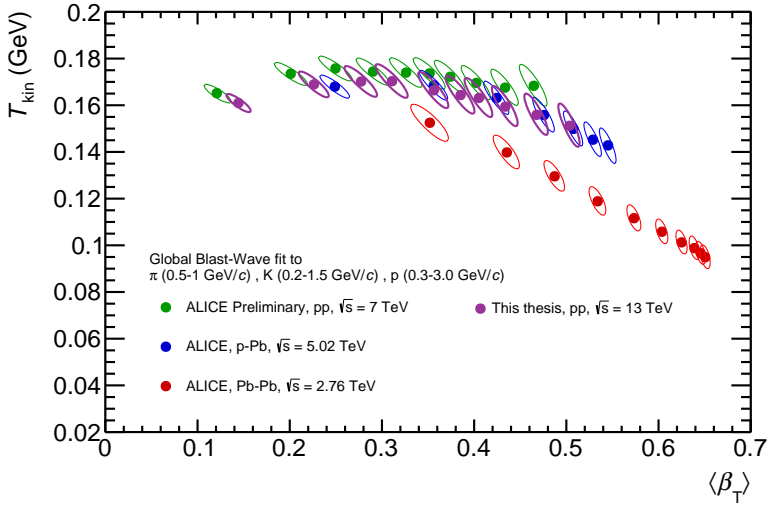


Figure 9.6: $\langle\beta_T\rangle$ and T_{kin} extracted from blast wave model fits in different colliding systems and center-of-mass energies. Note that different p_T ranges were considered for the analysis of pp collisions at $\sqrt{s} = 13$ TeV (see text). The contours around data points represent an uncertainty equal to one standard deviation.

9.2 Integrated Hadron Yields

The spectral modifications originating from the hydrodynamical expansion of the medium in Pb-Pb collisions indicate the presence of a fireball in thermal equilibrium. Consequently, thermal equilibrium might require a chemically equilibrated system, and it is therefore interesting to study the hadrochemistry of particles.

The p_T -integrated hadron abundances were obtained by integrating the measured transverse momentum distributions for all hadrons. In the p_T ranges where spectra were not covered by the measurements, yields were

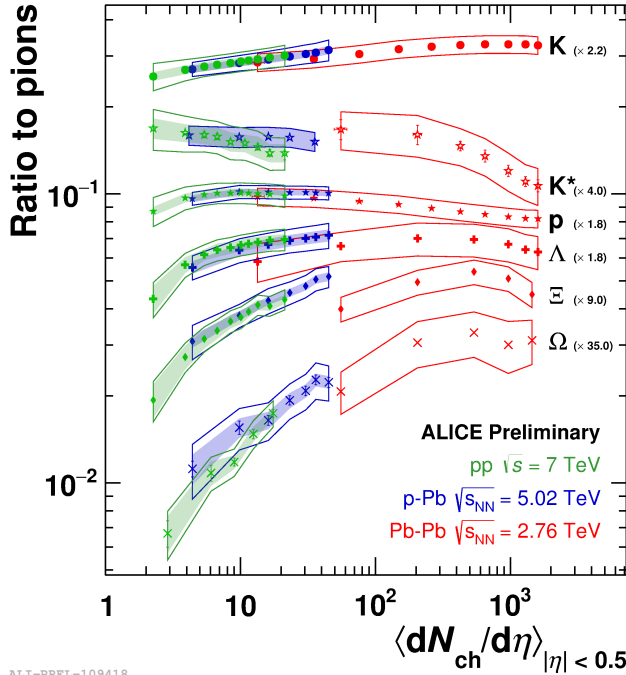


Figure 9.7: p_T -integrated hadron-to-pion ratios as a function of $\langle dN_{ch}/d\eta \rangle$ in three different systems.

extrapolated using the Levy–Tsallis parametrization [111]:

$$\frac{d^2N}{dp_T dy} = p_T \frac{dN}{dy} \frac{(n-1)(n-2)}{nC(nC + m(n-2))} \left(1 + \frac{\sqrt{m^2 + p_T} - m}{nC} \right)^{-n} \quad (9.1)$$

The systematic uncertainties were propagated by shifting each data point up and down by the associated systematic error and repeating the fitting procedure. The extrapolation errors were obtained by changing the functional form of the fit to Bose–Einstein, Fermi–Dirac and p_T -exponential distributions. In the 13 TeV analysis, the largest contribution of systematic uncertainty was found to originate from the low- p_T extrapolation.

The integrated hadron-to-pion ratios for a comprehensive set of light-flavored particles are shown in Fig. 9.7. We find that the ratios exhibit a smooth evolution with $\langle dN_{\text{ch}}/d\eta \rangle$ from pp to p-Pb and then to Pb-Pb collisions. This remarkable observation suggests that hadrochemistry is dominantly driven by charged-particle multiplicity and not the colliding system. What is even more interesting is that the modification of strange quark production, previously observed in heavy-ion collisions, is now seen in both p-Pb and pp systems. This effect is better illustrated in Fig. 9.8, where only the strange and multistrange hadron-to-pion ratios are shown. Not only do we find that hyperons exhibit stronger enhancement, but also that the modifications are more pronounced for hadrons with a larger strangeness content. These observations have very important implications for our understanding of small and large systems, and in particular they indicate that *soft particle production in pp collisions is similar to that in p-Pb and Pb-Pb collisions*.

We have already discussed that some pQCD inspired effects can (qualitatively) capture the trends seen in particle dynamics. It is therefore very important to consider how the evolution of hadrochemistry is described by these models. In Fig. 9.8 we also show the predictions of the hadron-to-pion ratios by several MC generators. We observe the following:

- PYTHIA 8 predicts no evolution of hadron-to-pion ratios. This is understood considering that hadronization in PYTHIA is done via string fragmentation. Each string has the same probability to fragment into a particular hadron and this probability is not modified by the total number of strings in the system (see Section 4.1 for details).

- EPOS LHC predicts a very large increase in the rates of hyperons, in fact much larger than the observed ones. The increase of the hyperon-to-pion ratio with multiplicity in EPOS LHC originates from the increasing core fraction (see Section 4.5), which has larger strange hadron yields than the corona. This could suggest that, for example, the core-corona parametrization in the generator is not optimal or that it breaks down.
- DIPSY appears to describe the measured ratios best, although the relative Ω yields are significantly underestimated. Strangeness enhancement in DIPSY originates from the multiple overlapping color strings forming color ropes with a larger effective string tension (see Section 4.2 for details), and the effect is more pronounced at larger multiplicities.

It is clear that the evolution of measured ratios is best captured by DIPSY, where the overlapping color strings form color ropes that enhance both the strangeness and baryon production. The latter, however, also leads to a large overestimation of the p/π ratio, as shown in Fig. 9.9. As a result, *none of the MC generators considered are able to describe the observed hadron yield ratios consistently.*

Thermal Model and Core-Corona predictions

We have seen that many attempts to consistently describe the dynamics and hadrochemistry evolution with MC models do not achieve a satisfactory agreement with data. On the other hand, blast wave studies of spectral shapes in pp collisions at $\sqrt{s} = 7$ and 13 TeV indicated the presence of an expanding medium. The observed scaling of hadron abundances further suggested that the particle production mechanism in small systems is similar to that of chemically equilibrated QGP in Pb-Pb. It is therefore important to study the particle yields in small systems with thermal models.

The measured integrated particle yield ratios as a function of pion yield, dN_π/dy , are shown in Fig. 9.10 and compared with the thermal model predictions, described in Section 4.4. The predictions were calculated with baryon (μ_B) and electric charge (μ_C) chemical potentials set to zero and strangeness saturation parameter set to $\gamma_S = 1$. The yields of hadrons

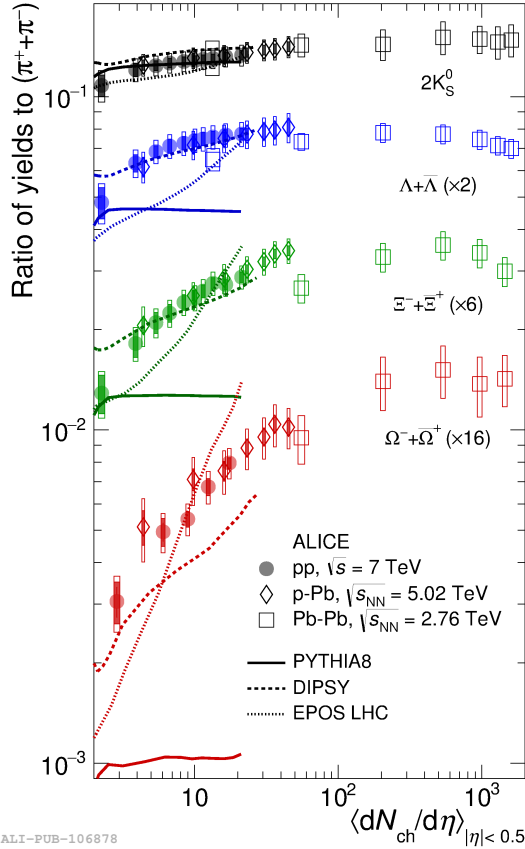


Figure 9.8: p_T -integrated (multi) strange hadron-to-pion ratios as a function of $dN_{ch}/d\eta$ measured in pp collisions at $\sqrt{s} = 7$ TeV in comparison to several MC model predictions. Figure published in [104].

were then obtained by varying the radius of a fireball R under three different chemical freeze-out temperatures $T_{ch} = 146, 156$ and 166 MeV. The strangeness correlation volume was fixed to the total volume of a fireball ($R_S = R$) at all times. All the ratios except K^* were normalized to the ratios measured at 0–60% most central Pb-Pb collisions in order to isolate the volume dependence. Because of the short life-time, K^* decays in the hadronic phase and its daughters are strongly affected by hadronic rescat-

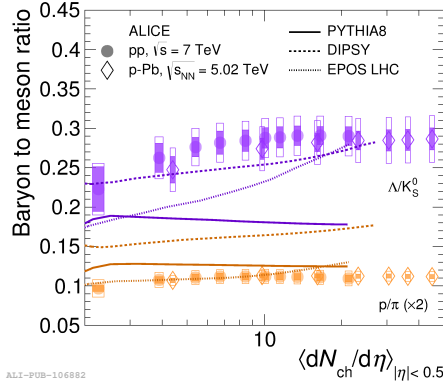


Figure 9.9: p_T -integrated baryon-to-meson ratios as a function of $dN_{ch}/d\eta$ measured in pp $\sqrt{s} = 7$ TeV and p-Pb ($\sqrt{s_{NN}} = 5.02$ TeV) collisions with comparison to several MC model predictions. Figure published in [104].

terings; in order to minimize this effect, the most peripheral Pb-Pb bin was used for K^* normalization. This is not an issue for the ϕ meson, as its life-time is much longer than that of K^* .

Note that the measurement of dN_π/dy only considers the rapidity region $|y| < 0.5$, while in the thermal model, no rapidity cuts are considered and the predictions are done for the full phase space. To account for this, the size of the fireball was not fixed to reproduce the exact measured dN_π/dy , but instead one that is k -times larger than the measured one. Effectively, this corresponds to a k -times larger measurement rapidity region, provided dN_π/dy is a flat distribution. Since all ratios are studied as a function of pion multiplicity, the same k factor was used for all particles. In practice, k is just a constant scaling factor of the x -axis in Fig. 9.10 for the functions describing the double ratios.

In order to determine the value of k , the functional forms of double ratios generated by the thermal model were fit simultaneously to the experimental data of all the hadrons, with k being the only free parameter. To estimate the systematic uncertainties on the scaling factor, the same procedure was repeated using different normalization for the double ratios: the data was normalized to the highest centrality bin in Pb-Pb instead of the 0–60% bins. The value obtained is $k = 1.35 \pm 0.28$ indicating that strangeness can be effectively equilibrated over ~ 1.35 units of rapidity.

This observation is meaningful from a physical point of view, considering the rapidity distributions measured at the LHC¹ [112] and could be measured experimentally. Similar values can also be obtained from pure theoretical considerations on causality constraints [113].

The agreement between the experimental data and the model predictions of K, p, Λ , Ξ , Ω and K^* double ratios is found to be within 1–2 standard deviations, indicating that particle production rates can be well described in the framework of strangeness canonical suppression. The larger deviation observed in the K^*/π double ratio in the most central Pb-Pb collisions can be attributed to the hadronic rescatterings. However, while the model predicts a flat evolution of the ϕ/π ratio with dN_π/dy , a different behavior is observed in the experimental data. Note that ϕ is also not described by the common blast wave fits to the identified particle spectra in peripheral Pb-Pb collisions [114], suggesting that the strangeness-neutral meson might be produced out of equilibrium.

In addition to thermal model calculations, Fig. 9.10 also shows comparisons of hadron-to-pion double ratios calculated using the core-corona framework described in Section 4.5. For core ratios we have used those measured in 0–60% Pb-Pb collisions. Such an approximation is meaningful in a physical way considering that the ratios appear to be flat at these multiplicities. The initial values for corona ratios were assumed to be given by the lowest multiplicity pp collisions. In practice, this is not necessarily true and will be addressed later.

In general, one would then calculate the core fraction f from a Glauber MC, see Sections 4.5 and 5.2.1. Here however we want to minimize model dependence, and therefore take a different approach to calculating the core fractions. For a given double ratio R_n in multiplicity bin n , one can calculate f_n as:

$$f_n = \frac{R_n - R_{pp}}{R_{Pb-Pb} - R_{pp}} \quad (9.2)$$

where R_{pp} and R_{Pb-Pb} are the corona and core double ratios respectively. The calculated f values are then fit with a function²

$$f(x) = 1 - \frac{a}{x - b} \quad (9.3)$$

¹Typically with plateau extending to 2–4 units of rapidity, depending on the system.

²This function was found to describe the calculated f values best.

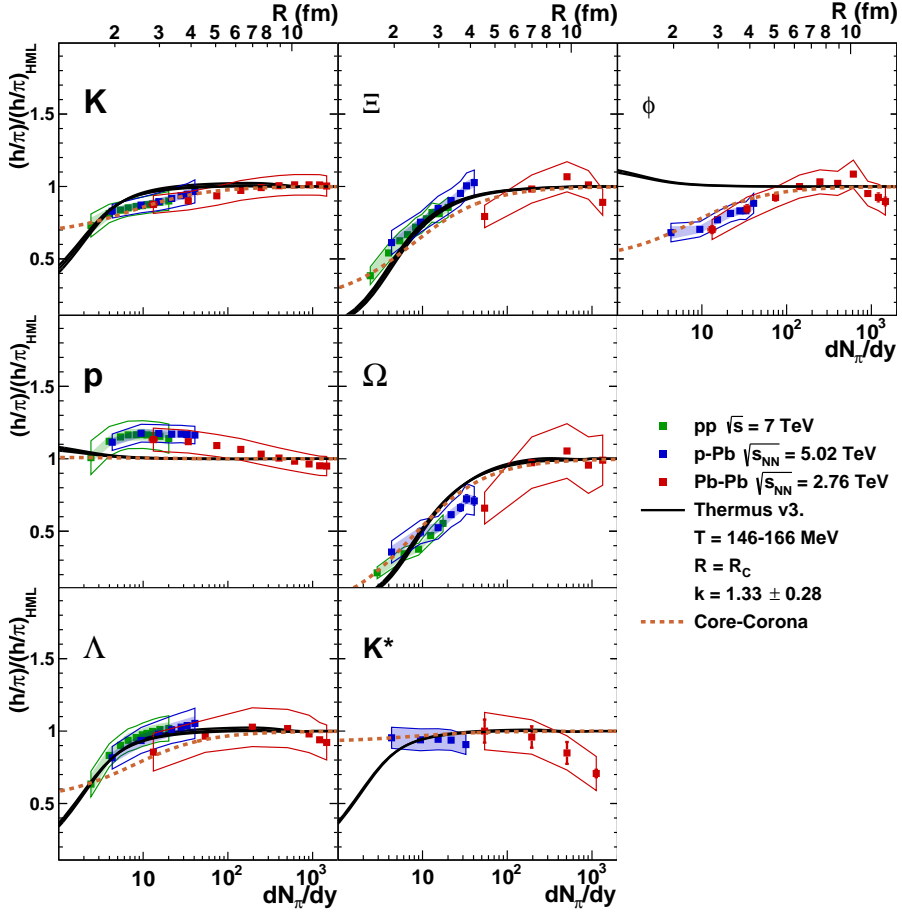


Figure 9.10: p_T -integrated hadron-to-pion ratios, normalized to the high-multiplicity ratios, as a function of pion yield. Black lines: thermal model predictions at $T = 146, 156$ and 166 MeV. Dashed line: core-corona predictions.

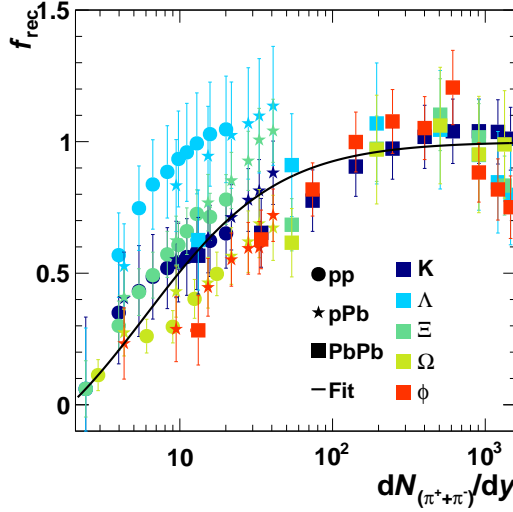


Figure 9.11: Core fraction, calculated (markers) and fit (line). Only (multi) strange hadrons in three different colliding systems were considered for the fit.

Only strange hadrons are considered in this procedure, since non-strange particles do not show any strong evolution with dN_π/dy .

As the double ratios measured at the lowest available multiplicities might still have a contribution from the core, corona values are recalculated by solving Eq. 9.2 for R_{pp} , explicitly ensuring that the experimental data is correctly predicted for both the lowest and the highest pion multiplicities measured. The calculated core fractions f , together with the fit function, are shown in Fig. 9.11.

We find that core-corona predictions are in good agreement with the experimental data. The deviations from the measured double ratios are below 2σ and are similar to the predictions from the thermal model. Note however, that the CC model presented here has been explicitly tuned to reproduce the double ratios exactly at both high and low multiplicities. Moreover, it does not consider any particular mechanism for particle production and only describes the relative scaling from low to high multiplicities. Because the yields in Fig. 9.10 are described by a single core function f which is only dependent on the multiplicity, CC suggests that all hadron abundances scale the same way, but for a conclusive comparison a more

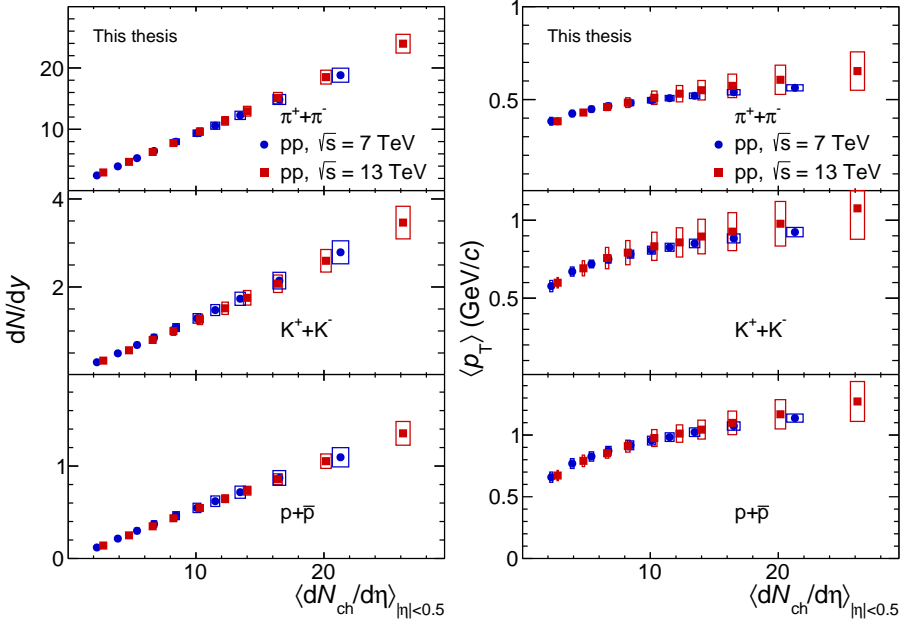


Figure 9.12: p_T -integrated hadron yields (left) and average transverse momenta (right) as a function of multiplicity, measured in pp collisions at $\sqrt{s} = 7$ and 13 TeV.

comprehensive study coupled to a specific particle production mechanism is required.

9.3 Center-of-Mass Energy Scaling

In the previous section it has been shown that hadron abundances scale well with particle multiplicity, and the scaling extends across three different colliding systems, each at a different center-of-mass energy. If the observed scaling is not coincidental, it should hold for any given system at different \sqrt{s} .

To study the validity of $\langle dN_{ch}/d\eta \rangle$ scaling at different center-of-mass energies, the integrated hadron yields in pp collisions at $\sqrt{s} = 7$ and 13 TeV are compared in Fig. 9.12. The yields of π , K and p follow the same patterns under two different \sqrt{s} and are comparable at similar $\langle dN_{ch}/d\eta \rangle$.

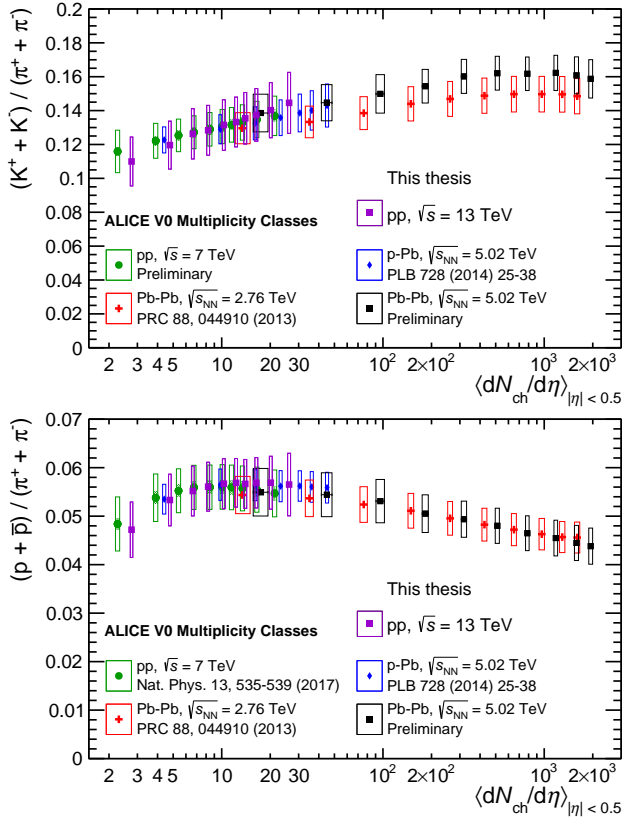


Figure 9.13: p_T -integrated K/π (top) and p/π yields as a function of multiplicity measured in pp collisions at $\sqrt{s} = 7$ and 13 TeV in comparison to those measured in different colliding systems.

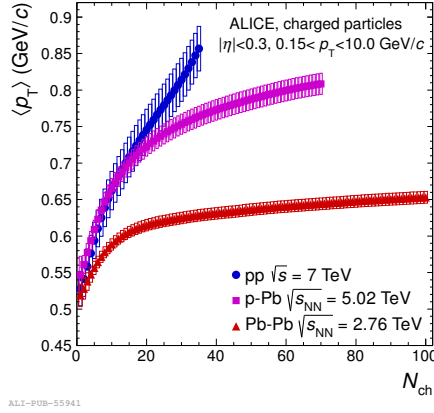


Figure 9.14: Average transverse momenta of charged hadrons as a function of charged-particle multiplicity measured in Pb-Pb, p-Pb and pp collisions at $\sqrt{s_{NN}} = 2.76, 5.02$ and 7 TeV respectively. Note that N_{ch} shown here has been measured in the pseudorapidity region $|\eta| < 0.3$. Figure taken from [115].

The p_T -integrated K/π and p/π ratios in pp collisions at the two different center-of-mass energies are compared to those measured in different systems, see Fig. 9.13. The ratios are found to follow the same trends as in p-Pb and Pb-Pb collisions, suggesting that *hadrochemistry is dominantly driven by the charged-particle multiplicity and not center-of-mass energy or colliding system*. Similar trends are also observed for (multi) strange hadrons, as reported in [107].

Another interesting observable to study is the average transverse momentum $\langle p_T \rangle$ as a function of multiplicity, \sqrt{s} and the colliding system. The $\langle p_T \rangle$ evolution with charged-particle multiplicity in Pb-Pb, p-Pb and pp collisions measured at $\sqrt{s_{NN}} = 2.76, 5.02$ and 7 TeV respectively is shown in Fig. 9.14 [115]. We see that the average transverse momenta in three different colliding systems are very different. In particular, Pb-Pb shows a moderate increase of $\langle p_T \rangle$ at above $N_{ch} \gtrsim 10$, while pp exhibits a steep rise in the whole multiplicity range considered; p-Pb appears to follow the trends seen in pp collisions up to $N_{ch} \sim 20$ and then becomes more Pb-Pb like. The large differences between $\langle p_T \rangle$ evolution in small and large systems have been understood as different mechanisms driving the particle dynamics. In Pb-Pb collisions, the slow increase of $\langle p_T \rangle$ originates from

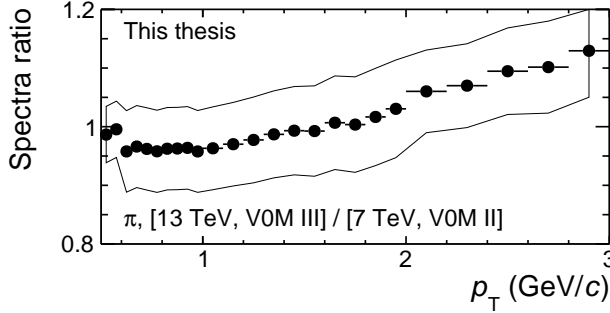


Figure 9.15: Ratio of π spectra measured in pp collisions at $\sqrt{s} = 7$ and 13 TeV and similar $\langle dN_{ch}/d\eta \rangle$.

the hydrodynamic behavior of the expanding medium and is thus associated with collective flow [27]. In pp collisions, the high multiplicities could originate from multi-partonic interactions and color reconnection, which in turn would enhance $\langle p_T \rangle$ (see Section 4.1.1). We also note that the differences between pp, p-Pb and Pb-Pb cannot be explained by different center-of-mass energies, as the \sqrt{s} dependence was previously observed to be weak[115].

In Fig. 9.12 we have also shown $\langle p_T \rangle$ for π , K and p as a function of $\langle dN_{ch}/d\eta \rangle$ in pp collisions at $\sqrt{s} = 7$ and 13 TeV. The mean transverse momenta were obtained by integrating the spectra in p_T regions available, and using Levy–Tsallis fits to extrapolate to the regions where it has not been measured, similarly to dN/dy calculations. For systematic uncertainties, the data points were shifted to the edges of p_T bins in order to make the hardest/softest spectra. The largest contribution to the systematic uncertainties in 13 TeV analysis is found to originate from the extrapolation of the spectra to $p_T = 0$ and a large fraction of this error can be reduced by measuring the yields at lower transverse momenta.

The measured $\langle p_T \rangle$ for π , K and p are numerically larger at higher \sqrt{s} and comparable $\langle dN_{ch}/d\eta \rangle$. Similar trends are also observed for (multi) strange hadrons [107] and for all charged hadrons at lower center-of-mass energies [115]. To study this further, π spectra measured in pp collisions at $\sqrt{s} = 7$ and 13 TeV and similar multiplicities (VOM class III in pp collisions at $\sqrt{s} = 13$ TeV; VOM class II at $\sqrt{s} = 7$ TeV) are compared in Fig. 9.15. The ratio of spectra shows an increase, which clearly indicates that $\langle p_T \rangle$

scaling with $\langle dN_{\text{ch}}/d\eta \rangle$ is not valid across different colliding systems or \sqrt{s} and suggests that the mechanisms driving particle dynamics might be different in pp and Pb-Pb collisions.

9.4 Event Shape Studies

So far we have found the following:

- p_{T} -differential p/π ratios in pp collisions are modified in a multiplicity dependent way, similar to that observed in Pb-Pb collisions
- The integrated hadron yields show a remarkable scaling with charged-particle multiplicity, extending across different \sqrt{s} and colliding systems
- $\langle p_{\text{T}} \rangle$ in the same colliding system at similar N_{ch} grows with the center-of-mass energy
- Current tunes of MC generators are not able to provide a satisfactory description of the observables
- Macroscopic models used in Pb-Pb collisions can also describe dynamics and hadrochemistry in pp collisions.

We have also discussed that $\langle p_{\text{T}} \rangle$ evolution in small and large systems has different origins: MPI and CR in pp collisions and expansion of thermalized medium governed by soft QCD processes in Pb-Pb. In Section 6.4 we have argued that using event shape observables one can differentiate between the two domains of QCD, and in the following discussion we will focus on sphericity-differential observables.

Unidentified Charged Hadrons

In Fig. 9.16 we show the unidentified hadron $\langle p_{\text{T}} \rangle$ evolution with N_{ch} in jetty, isotropic and sphericity-unbiased events. Note that in this particular case, only two tracks were required to calculate sphericity. We see that jetty events exhibit a steeper rise and systematically larger $\langle p_{\text{T}} \rangle$ as compared to the S_{O} -unbiased case, which is a behavior one would expect

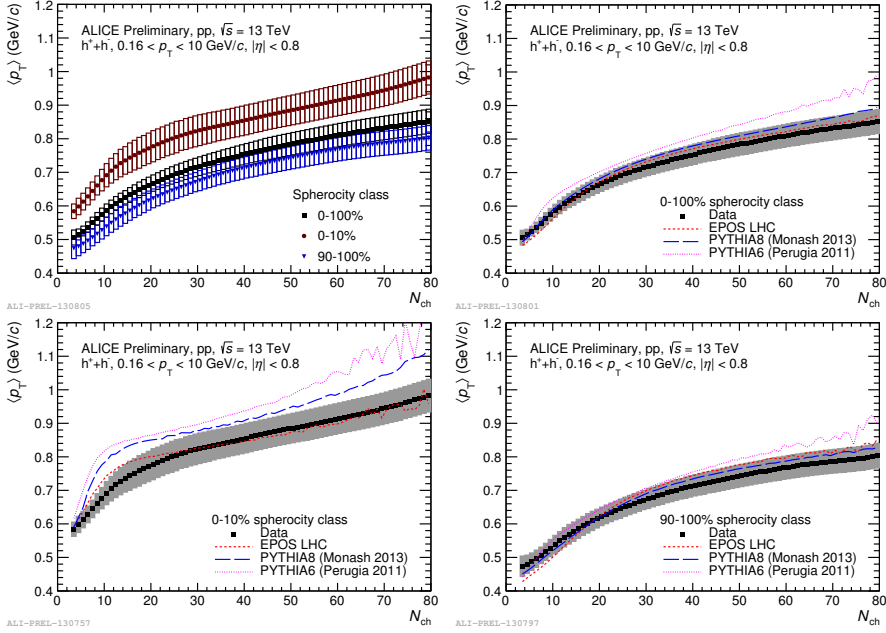


Figure 9.16: Average transverse momentum as a function of charged-particle multiplicity and transverse sphericity in comparison to MC predictions. N_{ch} is measured in $|\eta| < 0.8$.

from jet production. On the other hand, $\langle p_T \rangle$ in isotropic events is systematically below that measured in the S_O -unbiased case and appears to be more like p-Pb results shown in Fig. 9.14.

Shown in Fig. 9.16 are comparisons of the average transverse momenta in each sphericity class compared with those predicted by MC generators. We see that in both isotropic and S_O -unbiased cases, PYTHIA and EPOS LHC describe the $\langle p_T \rangle$ evolution moderately well with some minor deviations for EPOS at very low N_{ch} . Most interesting observations however are obtained from the jetty event class. While EPOS LHC appears to overestimate the rise of $\langle p_T \rangle$ at low multiplicities, it agrees very well with the data at above $N_{ch} \gtrsim 15$. On the other hand, both PYTHIA tunes significantly overestimate the measured average transverse momenta in the whole N_{ch} range considered. Such observation suggests that the contribution of underlying event in PYTHIA is significantly underestimated.

Spectral Shapes and Hydrodynamics

Identified hadron spectra measured in high-multiplicity pp collisions at $\sqrt{s} = 13$ TeV are found to be harder in jetty collisions and softer in isotropic as was shown in Fig. 8.3. Note that sphericity selection introduces a multiplicity bias, and as a result the $\langle dN_{\text{ch}}/d\eta \rangle$ measured for the jetty event class is smaller than that in isotropic events, as was summarized in Table 8.3. However, from multiplicity-dependent studies one would expect the hardening of the spectra with *increasing* multiplicity, which is the opposite of what is observed. This indicates that the spectral modifications are indeed resulting from event shape selection, and not a multiplicity bias. It is also worth noting that the crossing between spectra measured in jetty and isotropic collisions occurs at increasingly larger p_T for heavier particles, suggesting that *spectral modifications introduced by sphericity selection are mass-dependent*.

The K/π and p/π ratios in jetty collisions, shown in Fig. 8.5, appear to be smaller than those measured in the S_O -unbiased case. Jet fragmentation to charged hadrons has been studied in [105], where it was found that in higher transverse momentum jets, the ratios are shifted to larger p_T (see Fig. 9.17). Effectively, this means that particles produced in a jet along the jet axis are shifted in p_T and the shift is stronger at larger jet transverse momenta. Consequently, protons and kaons produced in jetty events are shifted towards higher p_T values, resulting in lower K/π and p/π ratios as compared to S_O -unbiased events.

In isotropic collisions, we observe no strong K/π evolution, just as in p-Pb collisions. There is, however, a significant increase to the p/π ratio. This effect is reminiscent of the modifications seen in multiplicity-dependent pp studies, and more importantly, the hydrodynamical evolution in large systems.

To study the origins of spectral modifications with S_O , we want to compare how different MC generators respond to event shape selection. The hadron-to-pion double ratios in jetty and isotropic events, normalized to S_O -unbiased class, are shown in Fig. 9.18 together with the predictions from PYTHIA 8 and EPOS LHC. We see that the K/π double ratios are well-described by both generators, which comes as no surprise considering that K/π is not expected to exhibit any evolution other than that originating from jet fragmentation, which is well-controlled in pQCD models.

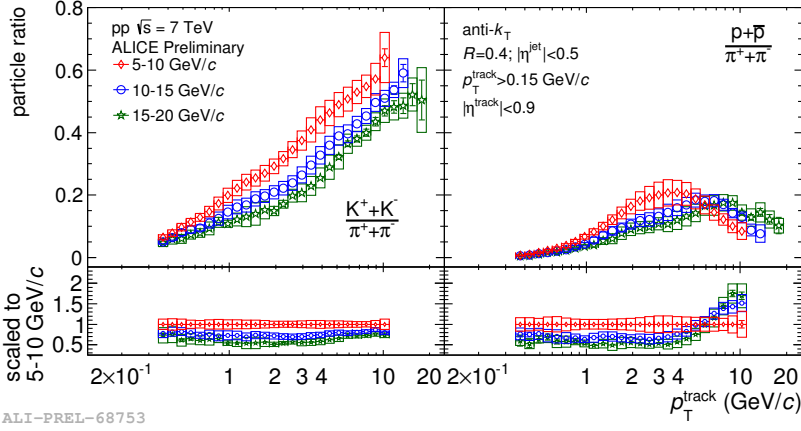


Figure 9.17: p_T -differential K/π and p/π ratios measured at different energy jets in pp collisions at $\sqrt{s} = 7$ TeV.

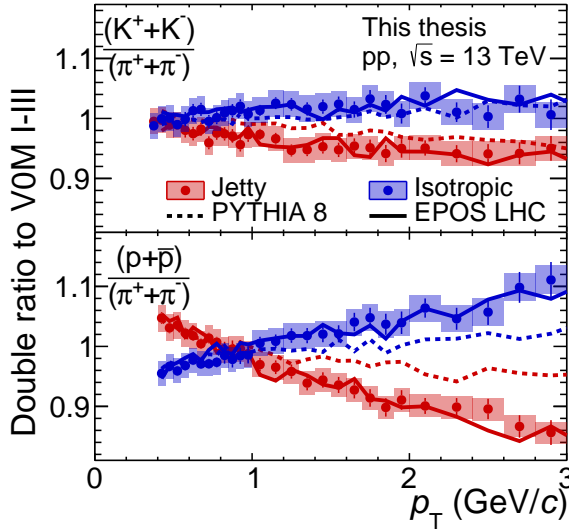


Figure 9.18: p_T -differential K/π (top) and p/π (bottom) double ratios in jetty and isotropic collisions, normalized to the ratios measured in sphericity unbiased sample. Values are compared to PYTHIA 8 (dashed lines) and EPOS LHC (solid lines) predictions.

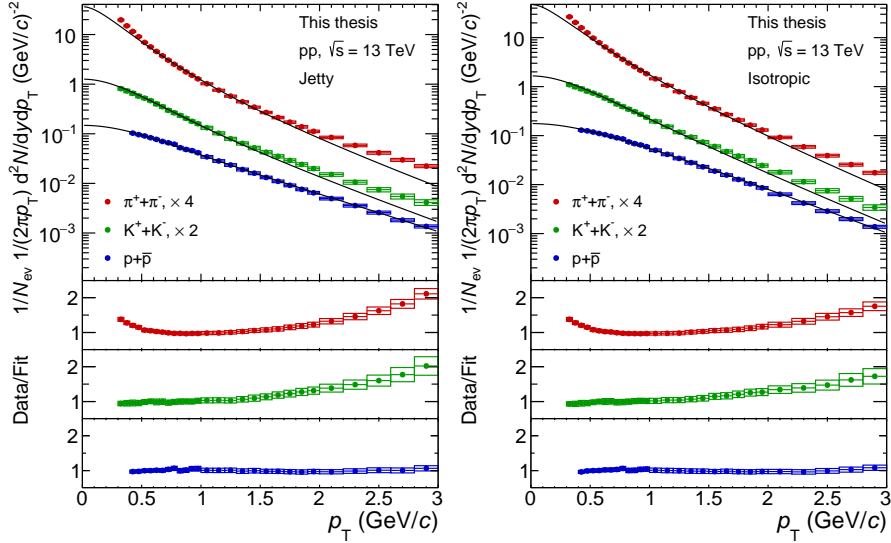


Figure 9.19: Blast wave fit performance in jetty and isotropic event classes.

A more interesting conclusion can be drawn from the p/π double ratios. We see that PYTHIA predicts the observed rising/falling trends, however, it also significantly underestimates the magnitude of the modification. This indicates that there is something missing in PYTHIA, and, considering the $\langle p_T \rangle$ evolution shown in Fig. 9.16, one could speculate this deviation to originate from, for example, underestimated underlying event.

The high-multiplicity pp collisions in EPOS are assumed to produce a small volume of high density, thermalized medium, which expands hydrodynamically. As seen in Fig. 9.18, it is clear that such an interpretation is at least consistent with the observations. Naturally, it does not imply the presence of QGP in small systems, although so far the data tends to favor such models.

Identified particle spectra measured as a function of sphericity was also studied with the BW model. The performance of the fits in jetty and isotropic events are shown in Fig. 9.19. While protons are well described by the model in the full p_T range considered, we find the fit quality to be slightly better in isotropic collisions.

The extracted $\langle \beta_T \rangle$ and T_{kin} parameters in jetty and isotropic events

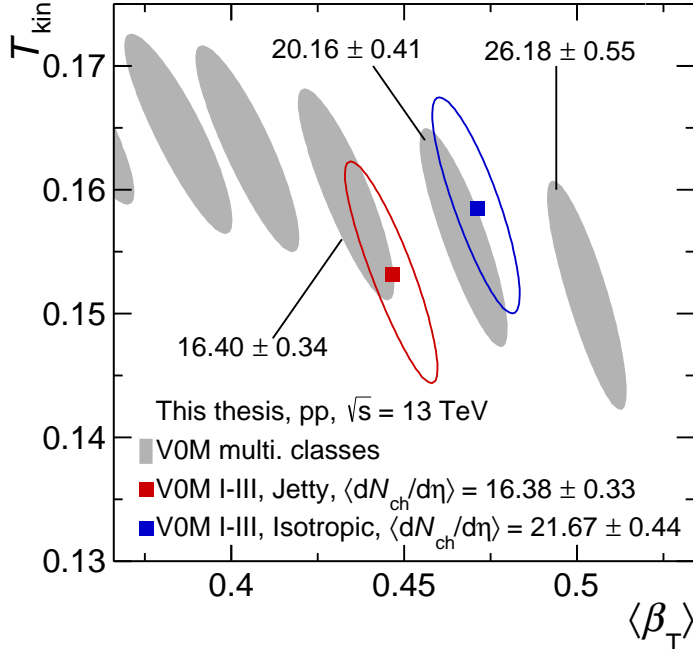


Figure 9.20: Thermal freeze-out temperature T_{kin} and common average velocity $\langle\beta_T\rangle$ extracted from BW fits to particle spectra in jetty and isotropic events in pp collisions at $\sqrt{s} = 13$ TeV. Shaded areas represent the parameters extracted from sphericity-unbiased studies. Numbers indicate the mean multiplicities measured in the corresponding VOM classes.

are shown in Fig. 9.20, in comparison to those measured from multiplicity-dependent studies in pp collisions at $\sqrt{s} = 13$ TeV. We find that hadrons move with a larger common average velocity $\langle\beta_T\rangle$ in isotropic collisions, which suggests a stronger radial flow component. In general, the $\langle dN_{ch}/d\eta \rangle$ measured in the isotropic events is similar to that measured in the VOM 1–5% event class, and therefore the extracted $\langle\beta_T\rangle$ is also similar. One can argue that the kinetic freeze-out temperature measured in the isotropic collisions does not seem to follow the decreasing trend seen in sphericity-unbiased studies; such an increase could be understood considering the enhanced p/π ratios, although the significance of such observation is not clear with the current uncertainties.

The situation is more complex in the jetty collisions: $\langle dN_{\text{ch}}/d\eta \rangle$ in jet-like events is very similar to that measured in a spherocity-unbiased V0M 5–10% multiplicity class, but there seems to be an offset in both $\langle \beta_{\text{T}} \rangle$ and T_{kin} . The lower freeze-out temperature in jetty events could be explained by the p/π imbalance originating from the jet fragmentation. The increase in $\langle \beta_{\text{T}} \rangle$, on the other hand, originates from events where very large multiplicities are generated by a superposition of underlying event (thus increasing $\langle \beta_{\text{T}} \rangle$) and a hard jet (so that overall the event appears to be jetty). To isolate events that have this underlying contribution further suppressed or enhanced, one should tighten the spherocity cuts, which unfortunately was not possible in this thesis due to the limited statistics available.

Integrated Yields and $\langle p_{\text{T}} \rangle$

The integrated yields and the $\langle p_{\text{T}} \rangle$ in jetty and isotropic events are extracted the same way as previously described for the 7 and 13 TeV analysis. For completeness, we also consider spherocity-unbiased events, corresponding to V0M 0–10% multiplicity class. The extracted dN/dy and $\langle p_{\text{T}} \rangle$ are shown in Fig. 9.21 in comparison to those extracted from 13 TeV multiplicity-related studies.

We do not find any significant deviations of hadron yields in jetty or isotropic events from the $\langle dN_{\text{ch}}/d\eta \rangle$ scaling seen earlier. However, in Fig. 9.7 we have seen that p_{T} -integrated K/π and p/π in very low multiplicity pp collisions (pQCD-like) and highest multiplicity Pb-Pb collisions (QGP-like) are very similar, so there is no reason to expect to see any deviations from the $\langle dN_{\text{ch}}/d\eta \rangle$ scaling in jetty or isotropic events. On the other hand, it would be very interesting to study Ξ and Ω yields as a function of multiplicity. If the strangeness modification shown in Fig. 9.8 indeed originates from bulk particle production, jetty and isotropic events should exhibit very different multistrange baryon yields at similar $\langle dN_{\text{ch}}/d\eta \rangle$. In particular, hyperon-to-pion ratios should be constant at different multiplicities and well described by pQCD, while isotropic events should follow the strangeness enhancement patterns.

The average transverse momenta, on the other hand, appears to be systematically larger in jetty events. Note that large systematic uncertainties in jetty collisions originate from extrapolation and can be significantly re-

duced by measuring the spectra for lower p_T values. The increase of $\langle p_T \rangle$ in jetty collisions originates from boosted particle production within the jet and trend is consistent with that observed in $\langle p_T \rangle$ of all charged hadrons shown in Fig. 9.16. The isotropic events show hints of lower average transverse momenta, which would also follow the trends of all charged hadrons, however, the current systematic uncertainties are too large to draw rigid conclusions.

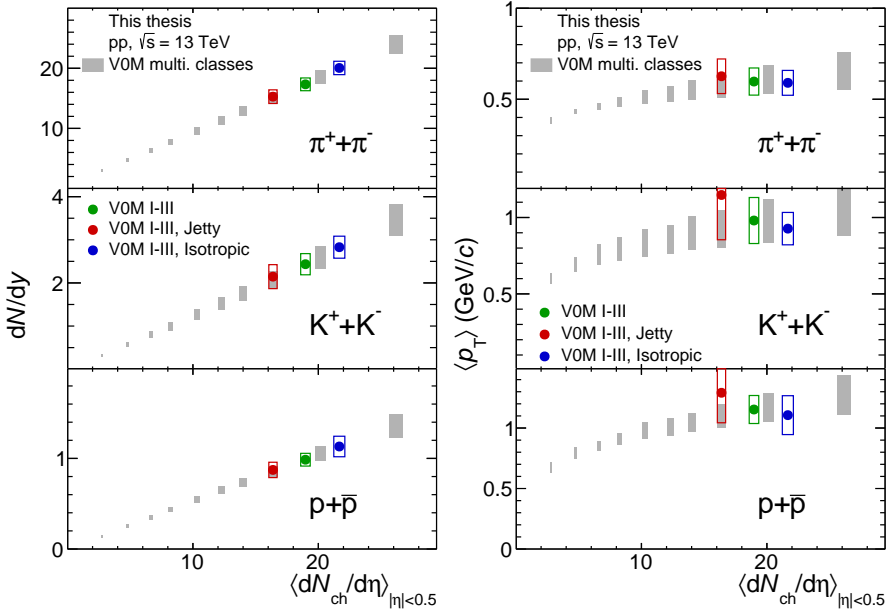


Figure 9.21: p_T -integrated hadron yields (left) and average transverse momenta (right) in jetty and isotropic events as a function of charged-particle multiplicity in pp collisions at $\sqrt{s} = 13$ TeV. Shaded areas represent dN/dy and $\langle p_T \rangle$ extracted from sphericity-unbiased studies.

Chapter 10

Conclusions

This work reports on the production of π , K and p as a function of multiplicity and transverse sphericity in pp collisions. In order to isolate the impact of center-of-mass energy to the final state observables, spectra were measured at $\sqrt{s} = 7$ and 13 TeV. In addition, event shape studies were performed in high-multiplicity pp collisions at $\sqrt{s} = 13$ TeV.

Integrated Hadron Yields and Average p_T

The integrated hadron yields show a strongly correlated scaling with event multiplicity, which holds at different center-of-mass energies and extends to different colliding systems, such as p-Pb and Pb-Pb. This suggests that particle hadrochemistry is dominantly driven by event activity and not \sqrt{s} . On the other hand, the average transverse momenta show hints of an increase in pp collisions at $\sqrt{s} = 13$ TeV as compared to 7 TeV, which indicates that the dynamics of particle production might be different at different energies.

The integrated hadron-to-pion ratios as a function of $\langle dN_{\text{ch}}/d\eta \rangle$ measured in pp collisions at $\sqrt{s} = 7$ TeV show larger yields of (multi) strange hadron production at higher multiplicities. This effect is stronger for hadrons with more strange quarks and is not seen in, for example, the p/π ratio, indicating that the enhancement is related to the strangeness content, and not baryonic number.

A comparison of measured hadron-to-pion ratios to different models show that rope hadronization predicts strangeness enhancement qualitatively.

ively well, although the rates of, for example, Ω production are underestimated by several orders of magnitude. The enhancement of hyperon production is also predicted by EPOS LHC, but the evolution is much stronger than that measured. Finally, PYTHIA 8 with color reconnection does not predict any modification of the integrated ratios with multiplicity. On the other hand, the measured ratios are well-described by macroscopic models such as thermal hadronization or core-corona, which are often used in heavy-ion studies.

Spectral Shapes in pp Collisions at $\sqrt{s} = 7$ and 13 TeV

Identified hadron spectra measured in pp collisions at $\sqrt{s} = 7$ and 13 TeV become harder at increasing multiplicities with the effect being more pronounced for heavier hadrons. The p_T -differential K/π ratios under the two different center-of-mass energies show no strong evolution with $\langle dN_{ch}/d\eta \rangle$, while p/π ratios show a blueshift in high-multiplicity pp collisions as compared to low multiplicities. Similar observations were previously reported from studies on larger systems, where such effects would be associated with stronger radial flow.

Comparisons of the measured p_T -differential hadron-to-pion ratios with several MC generators suggest that the observed p/π evolution with the multiplicity can be qualitatively explained by QCD phenomenology, like color reconnection or rope hadronization. Alternatively, spectral analysis using a blast wave model shows that in restricted p_T ranges, hadrons move in a common velocity field, which might indicate a presence of an expanding medium.

The average expansion velocity extracted from the BW analysis increases with multiplicity in all the colliding systems at different center-of-mass energies, indicating that the expansion is stronger at higher $\langle dN_{ch}/d\eta \rangle$. The kinetic freeze-out temperature in pp collisions at $\sqrt{s} = 13$ TeV is lower than that in 7 TeV and suggests that the medium decouples at later stages as \sqrt{s} increases.

Event Shape Studies

In order to disentangle the soft and hard modes of QCD in pp collisions at $\sqrt{s} = 13$ TeV, transverse sphericity was used to select high-multiplicity events with isotropic and jetty final states. π , K and p spectra in isotropic

events are found to be softer than that in jetty, and spectral modifications appear to be stronger for heavier particles. This indicates that isotropic states indeed originate from soft-QCD events, while jetty events have a more pronounced hard-QCD component.

The p_T -differential K/π ratios in isotropic collisions show no significant deviations from the sphericity-unbiased case, while a small shift in p_T is seen in the jetty events. This shift is understood to originate from particle production in jets. On the other hand, significant evolution with sphericity is seen in the p/π spectral ratios: in the p_T ranges considered, the isotropic events exhibit an enhanced ratio compared to the sphericity-unbiased case, while in jetty events, the ratio appears to be depleted. This observation suggests that the amount of flow-like effects in the sample can be controlled with the sphericity observable.

Studying p_T -differential K/π and p/π ratios with MC generators, it is found that PYTHIA 8 provides only qualitative description of the spectral modifications introduced by the sphericity selection. Furthermore, comparison of the measured $\langle p_T \rangle$ as a function of multiplicity to the MC predictions in isotropic events suggest that in high-multiplicity events, the hard QCD component is overestimated or the underlying event is underestimated. However, EPOS LHC describes the relative spectral ratio modifications with sphericity very well. Considering that EPOS LHC employs a core-corona model for particle production along with a built-in flow parametrization, this suggests that an expanding medium is created in pp collisions.

The BW model is found to describe the proton spectra in both jetty and isotropic events well, which might indicate the presence of an expanding medium in both cases. The average expansion velocity $\langle \beta_T \rangle$ in isotropic events is larger than that in jetty events, suggesting a more “explosive” medium. The lower kinetic freeze-out temperature in jetty events can be interpreted as a signature for a longer-lived system, but might also be a bias originating from the imbalance in p/π ratios.

The integrated hadron yields and $\langle p_T \rangle$ in jetty and isotropic events are compared to those measured in the multiplicity-differential study. Hadron yields in different sphericity classes are comparable to those measured in sphericity-unbiased events at similar $\langle dN_{\text{ch}}/d\eta \rangle$ and therefore follow the same scaling. On the other hand, $\langle p_T \rangle$ in jetty (isotropic) events appear to be numerically larger (smaller) than those in the sphericity-unbiased

events, hinting at different dynamics in the two cases. To understand the significance of such a result, however, systematic uncertainties have to be reduced.

Summarizing, it has been shown that the identified hadron production as a function of multiplicity in pp collisions at $\sqrt{s} = 7$ and 13 TeV exhibits similar patterns to those found in Pb-Pb collisions and usually associated with the presence of the QGP. The heavy-ion models provide a better description of the data than the pQCD-inspired models often used for pp collisions. In addition, the QGP-like effects can be further enhanced by using event shape observables like transverse sphericity.

Bibliography

- [1] https://en.wikipedia.org/wiki/Standard_Model.
- [2] B. Pontecorvo. Neutrino Experiments and the Problem of Conservation of Leptonic Charge. *Sov. Phys. JETP*, 26:984–988, 1968. [Zh. Eksp. Teor. Fiz.53,1717(1967)].
- [3] V. N. Gribov and B. Pontecorvo. Neutrino astronomy and lepton charge. *Phys. Lett.*, 28B:493, 1969.
- [4] Steven Weinberg. A Model of Leptons. *Phys. Rev. Lett.*, 19:1264–1266, 1967.
- [5] Gordon L. Kane. *MODERN ELEMENTARY PARTICLE PHYSICS*. Cambridge University Press, 2017.
- [6] David J. Gross and Frank Wilczek. Ultraviolet Behavior of Nonabelian Gauge Theories. *Phys. Rev. Lett.*, 30:1343–1346, 1973.
- [7] C. Patrignani et al. Review of Particle Physics. *Chin. Phys.*, C40(10):100001, 2016.
- [8] Kenneth G. Wilson. Confinement of quarks. *Phys. Rev. D*, 10:2445–2459, Oct 1974.
- [9] Yu Maezawa, Takashi Umeda, Sinya Aoki, Shinji Ejiri, Tetsuo Hatsuda, Kazuyuki Kanaya, and Hiroshi Ohno. Application of fixed scale approach to static quark free energies in quenched and 2+1 flavor lattice QCD with improved Wilson quark action. *Prog. Theor. Phys.*, 128:955–970, 2012.

- [10] A. Bazavov et al. Equation of state and QCD transition at finite temperature. *Phys. Rev.*, D80:014504, 2009.
- [11] Volodymyr Vovchenko, Mark I. Gorenstein, and Horst Stoecker. van der Waals Interactions in Hadron Resonance Gas: From Nuclear Matter to Lattice QCD. *Phys. Rev. Lett.*, 118(18):182301, 2017.
- [12] <http://www.gauss-centre.eu/ gauss-centre/EN/Projects/ElementaryParticlePhysics/2015/philipsen.PDNM.html>.
- [13] Misha A. Stephanov, K. Rajagopal, and Edward V. Shuryak. Event-by-event fluctuations in heavy ion collisions and the QCD critical point. *Phys. Rev.*, D60:114028, 1999.
- [14] Grazyna Odyniec. The RHIC Beam Energy Scan program in STAR and what's next ... *J. Phys. Conf. Ser.*, 455:012037, 2013.
- [15] Nuclear Physics European Collaboration Committee. NuPECC Long Range Plan 2017: Perspectives of Nuclear Physics. <http://www.nupecc.org/index.php?display=lrp2016/main>.
- [16] Miklos Gyulassy and Michael Plumer. Jet Quenching in Dense Matter. *Phys. Lett.*, B243:432–438, 1990.
- [17] Xin-Nian Wang and Miklos Gyulassy. Gluon shadowing and jet quenching in A + A collisions at $\sqrt{s} = 200$ GeV. *Phys. Rev. Lett.*, 68:1480–1483, 1992.
- [18] Roy A. Lacey, N. N. Ajitanand, J. M. Alexander, X. Gong, J. Jia, A. Taranenko, and Rui Wei. Scaling patterns of jet suppression in Au+Au collisions at $\sqrt{s_{NN}} = 200$ GeV: Links to the transport properties of the QGP. *Phys. Rev.*, C80:051901, 2009.
- [19] Roy A. Lacey, N. N. Ajitanand, J. M. Alexander, J. Jia, and A. Taranenko. Scaling patterns for the suppression of charged hadron yields in Pb+Pb collisions at $\sqrt{s} = 2.76$ TeV: Constraints on transport coefficients. 2012.
- [20] Roy A. Lacey, N. N. Ajitanand, J. M. Alexander, J. Jia, and A. Taranenko. Scaling patterns for azimuthal anisotropy in Pb+Pb collisions at $\sqrt{s} = 2.76$ TeV: Further constraints on transport coefficients. 2012.

- [21] Peter Christiansen, Konrad Tywoniuk, and Vytautas Viskavicius. Universal scaling dependence of QCD energy loss from data driven studies. *Phys. Rev.*, C89(3):034912, 2014.
- [22] CMS Collaboration. <http://cds.cern.ch/record/1309898>.
- [23] K. Aamodt et al. Suppression of Charged Particle Production at Large Transverse Momentum in Central Pb-Pb Collisions at $\sqrt{s_{NN}} = 2.76$ TeV. *Phys. Lett.*, B696:30–39, 2011.
- [24] Serguei Chatrchyan et al. Indications of suppression of excited Υ states in PbPb collisions at $\sqrt{s_{NN}} = 2.76$ TeV. *Phys. Rev. Lett.*, 107:052302, 2011.
- [25] Betty Abelev et al. J/ψ suppression at forward rapidity in Pb-Pb collisions at $\sqrt{s_{NN}} = 2.76$ TeV. *Phys. Rev. Lett.*, 109:072301, 2012.
- [26] I. Arsene et al. Quark gluon plasma and color glass condensate at RHIC? The Perspective from the BRAHMS experiment. *Nucl. Phys.*, A757:1–27, 2005.
- [27] Betty Abelev et al. Centrality dependence of π , K, p production in Pb-Pb collisions at $\sqrt{s_{NN}} = 2.76$ TeV. *Phys. Rev.*, C88:044910, 2013.
- [28] Piotr Bozek and Iwona Wyskiel-Piekarska. Particle spectra in Pb-Pb collisions at $\sqrt{s_{NN}} = 2.76$ TeV. *Phys. Rev.*, C85:064915, 2012.
- [29] Betty Bezverkhny Abelev et al. Production of charged pions, kaons and protons at large transverse momenta in pp and Pb-Pb collisions at $\sqrt{s_{NN}} = 2.76$ TeV. *Phys. Lett.*, B736:196–207, 2014.
- [30] K. Aamodt et al. Harmonic decomposition of two-particle angular correlations in Pb-Pb collisions at $\sqrt{s_{NN}} = 2.76$ TeV. *Phys. Lett.*, B708:249–264, 2012.
- [31] B. Alver and G. Roland. Collision geometry fluctuations and triangular flow in heavy-ion collisions. *Phys. Rev.*, C81:054905, 2010. [Erratum: *Phys. Rev.* C82,039903(2010)].

- [32] K. Aamodt et al. Higher harmonic anisotropic flow measurements of charged particles in Pb-Pb collisions at $\sqrt{s_{NN}}=2.76$ TeV. *Phys. Rev. Lett.*, 107:032301, 2011.
- [33] A. Adare et al. Measurements of Higher-Order Flow Harmonics in Au+Au Collisions at $\sqrt{s_{NN}} = 200$ GeV. *Phys. Rev. Lett.*, 107:252301, 2011.
- [34] P. Braun-Munzinger, J. Stachel, and Christof Wetterich. Chemical freezeout and the QCD phase transition temperature. *Phys. Lett.*, B596:61–69, 2004.
- [35] P. Braun-Munzinger, J. Stachel, J. P. Wessels, and N. Xu. Thermal and hadrochemical equilibration in nucleus-nucleus collisions at the SPS. *Phys. Lett.*, B365:1–6, 1996.
- [36] A. Andronic, P. Braun-Munzinger, and J. Stachel. Thermal hadron production in relativistic nuclear collisions. *Acta Phys. Polon.*, B40:1005–1012, 2009.
- [37] Johann Rafelski and Berndt Muller. Strangeness Production in the Quark - Gluon Plasma. *Phys. Rev. Lett.*, 48:1066, 1982. [Erratum: *Phys. Rev. Lett.* 56,2334(1986)].
- [38] E. Andersen et al. Enhancement of central Lambda, Xi and Omega yields in Pb - Pb collisions at 158 A-GeV/c. *Phys. Lett.*, B433:209–216, 1998.
- [39] Betty Bezverkhny Abelev et al. Multi-strange baryon production at mid-rapidity in Pb-Pb collisions at $\sqrt{s_{NN}} = 2.76$ TeV. *Phys. Lett.*, B728:216–227, 2014. [Erratum: *Phys. Lett.* B734,409(2014)].
- [40] A. Andronic, P. Braun-Munzinger, and J. Stachel. Thermal hadron production in relativistic nuclear collisions: The Hadron mass spectrum, the horn, and the QCD phase transition. *Phys. Lett.*, B673:142–145, 2009. [Erratum: *Phys. Lett.* B678,516(2009)].
- [41] J. Cleymans, I. Kraus, H. Oeschler, K. Redlich, and S. Wheaton. Statistical model predictions for particle ratios at $\sqrt{s_{NN}} = 5.5$ TeV. *Phys. Rev.*, C74:034903, 2006.

- [42] Betty Bezverkhny Abelev et al. Multiplicity Dependence of Pion, Kaon, Proton and Lambda Production in p-Pb Collisions at $\sqrt{s_{NN}} = 5.02$ TeV. *Phys. Lett.*, B728:25–38, 2014.
- [43] M. Bleicher et al. Relativistic hadron hadron collisions in the ultrarelativistic quantum molecular dynamics model. *J. Phys.*, G25:1859–1896, 1999.
- [44] Ekkard Schnedermann, Josef Sollfrank, and Ulrich W. Heinz. Thermal phenomenology of hadrons from 200-A/GeV S+S collisions. *Phys. Rev.*, C48:2462–2475, 1993.
- [45] Torbjorn Sjostrand, Stephen Mrenna, and Peter Z. Skands. A Brief Introduction to PYTHIA 8.1. *Comput. Phys. Commun.*, 178:852–867, 2008.
- [46] Xavier Artru. Classical String Phenomenology. 1. How Strings Work. *Phys. Rept.*, 97:147, 1983.
- [47] Bo Andersson, G. Gustafson, G. Ingelman, and T. Sjostrand. Parton Fragmentation and String Dynamics. *Phys. Rept.*, 97:31–145, 1983.
- [48] Peter Skands, Stefano Carrazza, and Juan Rojo. Tuning PYTHIA 8.1: the Monash 2013 Tune. *Eur. Phys. J.*, C74(8):3024, 2014.
- [49] C. Albajar et al. A Study of the General Characteristics of $p\bar{p}$ Collisions at $\sqrt{s} = 0.2$ -TeV to 0.9-TeV. *Nucl. Phys.*, B335:261–287, 1990.
- [50] Torbjorn Sjostrand and Maria van Zijl. A Multiple Interaction Model for the Event Structure in Hadron Collisions. *Phys. Rev.*, D36:2019, 1987.
- [51] Torbjörn Sjöstrand. Colour reconnection and its effects on precise measurements at the LHC [arxiv:1310.8073 [hep-ph]]. 2013.
- [52] Antonio Ortiz Velasquez, Peter Christiansen, Eleazar Cuaute Flores, Ivonne Maldonado Cervantes, and Guy Paić. Color Reconnection and Flowlike Patterns in pp Collisions. *Phys. Rev. Lett.*, 111(4):042001, 2013.

- [53] Bo Andersson, G. Gustafson, and B. Soderberg. A Probability Measure on Parton and String States. *Nucl. Phys.*, B264:29, 1986. [,145(1985)].
- [54] Christoffer Flensburg, Gosta Gustafson, and Leif Lonnblad. Inclusive and Exclusive Observables from Dipoles in High Energy Collisions. *JHEP*, 08:103, 2011.
- [55] Christian Bierlich and Jesper Roy Christiansen. Effects of color reconnection on hadron flavor observables. *Phys. Rev.*, D92(9):094010, 2015.
- [56] Christian Bierlich. *Rope Hadronization, Geometry and Particle Production in pp and pA Collisions*. PhD thesis, Lund University, 2016.
- [57] J. Baechler et al. Charged particle spectra in central S + S collisions at 200-GeV/c per nucleon. *Phys. Rev. Lett.*, 72:1419–1422, 1994.
- [58] J. Bartke et al. Neutral strange particle production in sulphur sulphur and proton sulphur collisions at 200-GeV/nucleon. *Z. Phys.*, C48:191–200, 1990.
- [59] Josef Sollfrank, Peter Koch, and Ulrich W. Heinz. The Influence of resonance decays on the P(t) spectra from heavy ion collisions. *Phys. Lett.*, B252:256–264, 1990.
- [60] Josef Sollfrank, Peter Koch, and Ulrich W. Heinz. Is there a low p(T) ‘anomaly’ in the pion momentum spectra from relativistic nuclear collisions? *Z. Phys.*, C52:593–610, 1991.
- [61] J. D. Bjorken. Highly Relativistic Nucleus-Nucleus Collisions: The Central Rapidity Region. *Phys. Rev.*, D27:140–151, 1983.
- [62] H. A. Gustafsson et al. Collective Flow Observed in Relativistic Nuclear Collisions. *Phys. Rev. Lett.*, 52:1590–1593, 1984.
- [63] A. Andronic, P. Braun-Munzinger, and J. Stachel. Hadron production in central nucleus-nucleus collisions at chemical freeze-out. *Nucl. Phys.*, A772:167–199, 2006.

- [64] J. Cleymans and K. Redlich. Unified description of freezeout parameters in relativistic heavy ion collisions. *Phys. Rev. Lett.*, 81:5284–5286, 1998.
- [65] A. Andronic, P. Braun-Munzinger, K. Redlich, and J. Stachel. The thermal model on the verge of the ultimate test: particle production in Pb-Pb collisions at the LHC. *J. Phys.*, G38:124081, 2011.
- [66] S. Wheaton and J. Cleymans. THERMUS: A Thermal model package for ROOT. *Comput. Phys. Commun.*, 180:84–106, 2009.
- [67] Granddon D. Yen, Mark I. Gorenstein, Walter Greiner, and Shin-Nan Yang. Excluded volume hadron gas model for particle number ratios in A+A collisions. *Phys. Rev.*, C56:2210–2218, 1997.
- [68] Dirk H. Rischke, Mark I. Gorenstein, Horst Stoecker, and Walter Greiner. Excluded volume effect for the nuclear matter equation of state. *Z. Phys.*, C51:485–490, 1991.
- [69] J. Cleymans, Mark I. Gorenstein, J. Stalnacke, and E. Suhonen. Excluded volume effect and the quark - hadron phase transition. *Phys. Scripta*, 48:277–280, 1993.
- [70] P. Braun-Munzinger, I. Heppe, and J. Stachel. Chemical equilibration in Pb + Pb collisions at the SPS. *Phys. Lett.*, B465:15–20, 1999.
- [71] Masashi Kaneta and Nu Xu. Centrality dependence of chemical freeze-out in Au+Au collisions at RHIC. In *Ultra-relativistic nucleus-nucleus collisions. Proceedings, 17th International Conference, Quark Matter 2004, Oakland, USA, January 11-17, 2004*, 2004.
- [72] J. Cleymans, Burkhard Kampfer, M. Kaneta, S. Wheaton, and N. Xu. Centrality dependence of thermal parameters deduced from hadron multiplicities in Au + Au collisions at $\sqrt{s_{NN}} = 130$ GeV. *Phys. Rev.*, C71:054901, 2005.
- [73] Jean Cleymans, Helmut Oeschler, and Krzysztof Redlich. Influence of impact parameter on thermal description of relativistic heavy ion collisions at (1-2) A-GeV. *Phys. Rev.*, C59:1663, 1999.

- [74] J. Cleymans, H. Oeschler, and K. Redlich. Statistical model description of K^+ and K^- production between 1-GeV/A to 10-GeV/A. *Phys. Lett.*, B485:27–31, 2000.
- [75] Francesco Becattini. A Thermodynamical approach to hadron production in $e^+ e^-$ collisions. *Z. Phys.*, C69(3):485–492, 1996.
- [76] Klaus Werner. Core-corona separation in ultra-relativistic heavy ion collisions. *Phys. Rev. Lett.*, 98:152301, 2007.
- [77] T. Pierog, Iu. Karpenko, J. M. Katzy, E. Yatsenko, and K. Werner. EPOS LHC: Test of collective hadronization with data measured at the CERN Large Hadron Collider. *Phys. Rev.*, C92(3):034906, 2015.
- [78] K. Werner, Iu. Karpenko, T. Pierog, M. Bleicher, and K. Mikhailov. Event-by-Event Simulation of the Three-Dimensional Hydrodynamic Evolution from Flux Tube Initial Conditions in Ultrarelativistic Heavy Ion Collisions. *Phys. Rev.*, C82:044904, 2010.
- [79] A. G. Knospe, C. Markert, K. Werner, J. Steinheimer, and M. Bleicher. Hadronic resonance production and interaction in partonic and hadronic matter in the EPOS3 model with and without the hadronic afterburner UrQMD. *Phys. Rev.*, C93(1):014911, 2016.
- [80] K. Aamodt et al. The ALICE experiment at the CERN LHC. *JINST*, 3:S08002, 2008.
- [81] Kenneth Aamodt et al. Centrality dependence of the charged-particle multiplicity density at mid-rapidity in Pb-Pb collisions at $\sqrt{s_{NN}} = 2.76$ TeV. *Phys. Rev. Lett.*, 106:032301, 2011.
- [82] Arturo Tauro. ALICE Schematics as during RUN2, 2017. <https://cds.cern.ch/record/2263642>.
- [83] Betty Bezverkhny Abelev et al. Performance of the ALICE Experiment at the CERN LHC. *Int. J. Mod. Phys.*, A29:1430044, 2014.
- [84] *ALICE Inner Tracking System (ITS): Technical Design Report*. Technical Design Report ALICE. CERN, Geneva, 1999.
- [85] http://alicematters.web.cern.ch/?q=ALICE_currentITS.

- [86] Marek Chojnacki, R J M Snellings, G J L Nooren, R Kamermans, and M van Leeuwen. *Measurement of pions, kaons and protons with the ALICE detector in pp collisions at the LHC*. PhD thesis, 2012. Presented 03 May 2012.
- [87] Davide Falchieri. Status and performance of the ALICE Silicon Drift Detector in pp and Pb-Pb collisions. *Nucl. Instrum. Meth.*, A730:24–27, 2013.
- [88] J. Alme et al. The ALICE TPC, a large 3-dimensional tracking device with fast readout for ultra-high multiplicity events. *Nucl. Instrum. Meth.*, A622:316–367, 2010.
- [89] Walter Blum, Luigi Rolandi, and Werner Riegler. *Particle detection with drift chambers*. Particle Acceleration and Detection. 2008.
- [90] Alexander Kalweit. *Production of light flavor hadrons and anti-nuclei at the LHC*. PhD thesis, 2012.
- [91] D. De Gruttola. Particle IDentification with the ALICE Time-Of-Flight detector at the LHC. *JINST*, 9(10):C10019, 2014.
- [92] http://aliceinfo.cern.ch/Public/en/Chapter2/Chap2_TOF.html.
- [93] Participants and spectators at the heavy-ion fireball. *CERN Cour.*, 53N4:31–33, 2013.
- [94] Betty Abelev et al. Centrality determination of Pb-Pb collisions at $\sqrt{s_{NN}} = 2.76$ TeV with ALICE. *Phys. Rev.*, C88(4):044909, 2013.
- [95] Michael L. Miller, Klaus Reygers, Stephen J. Sanders, and Peter Steinberg. Glauber modeling in high energy nuclear collisions. *Ann. Rev. Nucl. Part. Sci.*, 57:205–243, 2007.
- [96] B. Alver, M. Baker, C. Loizides, and P. Steinberg. The PHOBOS Glauber Monte Carlo. 2008.
- [97] K. Aamodt et al. Charged-particle multiplicity measurement in proton-proton collisions at $\sqrt{s} = 0.9$ and 2.36 TeV with ALICE at LHC. *Eur. Phys. J.*, C68:89–108, 2010.

- [98] Antonin Maire and Christian Kuhn. *Production des baryons multi-étranges au LHC dans les collisions proton-proton avec l'expérience ALICE*. PhD thesis, 2011. Presented 13 Oct 2011.
- [99] Rudolf Kalman. A new approach to linear filtering and prediction problems. 82:35–45, 01 1960.
- [100] Andrea Banfi, Gavin P. Salam, and Giulia Zanderighi. Phenomenology of event shapes at hadron colliders. *JHEP*, 06:038, 2010.
- [101] M. Bondila et al. ALICE T0 detector. *IEEE Trans. Nucl. Sci.*, 52:1705–1711, 2005.
- [102] W. Blum and L. Rolandi. *Particle Detection with Drift Chambers*. 1998.
- [103] K. Aamodt et al. Midrapidity antiproton-to-proton ratio in pp collisions at $\sqrt{s} = 0.9$ and 7 TeV measured by the ALICE experiment. *Phys. Rev. Lett.*, 105:072002, 2010.
- [104] Jaroslav Adam et al. Enhanced production of multi-strange hadrons in high-multiplicity proton-proton collisions. *Nature Phys.*, 13:535–539, 2017.
- [105] Xianguo Lu. Measurement of hadron composition in charged jets from pp collisions with the ALICE experiment. *Nucl. Phys.*, A931:428–432, 2014.
- [106] Jaroslav Adam et al. Measurement of pion, kaon and proton production in proton-proton collisions at $\sqrt{s} = 7$ TeV. *Eur. Phys. J.*, C75(5):226, 2015.
- [107] Vytautas Vislavicius. Multiplicity dependence of identified particle production in proton-proton collisions with ALICE. *Nucl. Phys.*, A967:337–340, 2017.
- [108] Rainer J. Fries, Vincenzo Greco, and Paul Sorensen. Coalescence Models For Hadron Formation From Quark Gluon Plasma. *Ann. Rev. Nucl. Part. Sci.*, 58:177–205, 2008.
- [109] K. Werner. Lambda-to-Kaon Ratio Enhancement in Heavy Ion Collisions at Several TeV. *Phys. Rev. Lett.*, 109:102301, 2012.

- [110] Johannes Bellm et al. Herwig 7.0/Herwig++ 3.0 release note. *Eur. Phys. J.*, C76(4):196, 2016.
- [111] B. I. Abelev et al. Strange particle production in p+p collisions at $\sqrt{s}(1/2) = 200$ -GeV. *Phys. Rev.*, C75:064901, 2007.
- [112] Jaroslav Adam et al. Charged-particle multiplicities in proton–proton collisions at $\sqrt{s} = 0.9$ to 8 TeV. *Eur. Phys. J.*, C77(1):33, 2017.
- [113] P. Castorina and H. Satz. Causality Constraints on Hadron Production In High Energy Collisions. *Int. J. Mod. Phys.*, E23(4):1450019, 2014.
- [114] Betty Bezverkhny Abelev et al. $K^*(892)^0$ and $\phi(1020)$ production in Pb-Pb collisions at $\sqrt{s_{NN}} = 2.76$ TeV. *Phys. Rev.*, C91:024609, 2015.
- [115] Betty Bezverkhny Abelev et al. Multiplicity dependence of the average transverse momentum in pp, p-Pb, and Pb-Pb collisions at the LHC. *Phys. Lett.*, B727:371–380, 2013.

Appendix A

List of Acronyms

ALICE – A Large Ion Collider Experiment
BW – Blast Wave
CERN – European Organization for Nuclear Research
CGC – Color Glass Condensate
CR – Color Reconnection
DCA – Distance of Closest Approach
GC – Grand-Canonical
HI – Heavy-Ions
HM – High-Multiplicity
HRG – Hadronic Resonance Gas
ITS – Inner Tracking System
LHC – Large Hadron Collider
LQCD – Lattice Quantum Chromodynamics
MB – Minimum Bias
MC – Monte Carlo
MPI – Multi-Partonic Interactions
MRPC – Multigap Resistive Plate Chambers
MWPC – Multi-Wire Proportional Chamber
PID – Particle Identification
PMT – Photo Multiplier Tube
pQCD – Perturbative Quantum Chromodynamics
QCD – Quantum Chromodynamics
QED – Quantum Electrodynamics
QGP – Quark–Gluon Plasma

RHIC – Relativistic Heavy-Ion Collider

SC – Strangeness-Canonical

SDD – Silicon Drift Detector

SHM – Statistical Hadronization Model

SM – Standard Model

SPD – Silicon Pixel Detector

SPS – Super Proton Synchrotron

SDD – Silicon Drift Detector

TOF – Time-Of-Flight

TPC – Time-Projection Chamber

UrQMD – Ultrarelativistic Quantum Molecular Dynamics

Appendix B

Different Sources of Tracking Uncertainties

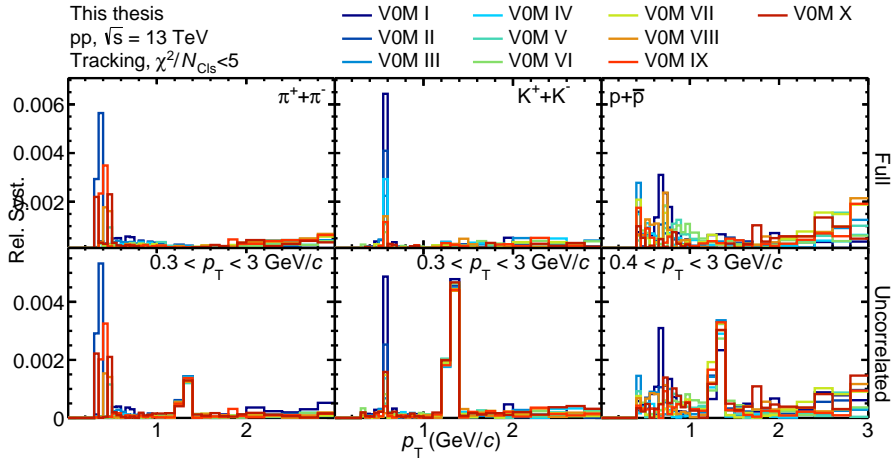


Figure B.1: Full (top panels) and multiplicity uncorrelated (bottom panels) tracking uncertainties obtained by varying the maximum allowed χ^2 per TPC cluster. Uncertainties shown for π , K and p spectra in different VOM multiplicity classes.

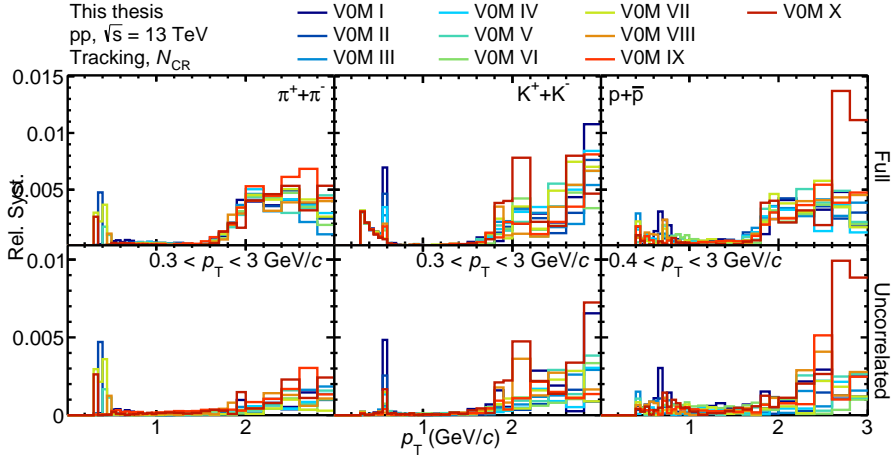


Figure B.2: Full (top panels) and multiplicity uncorrelated (bottom panels) tracking uncertainties obtained by varying the minimum number of crossed rows in the TPC. Uncertainties shown for π , K and p spectra in different VOM multiplicity classes.

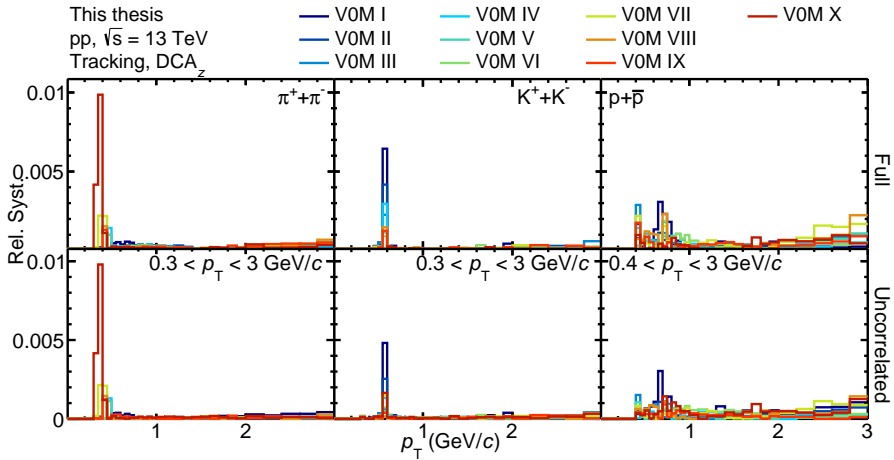


Figure B.3: Full (top panels) and multiplicity uncorrelated (bottom panels) tracking uncertainties obtained by varying the maximum allowed DCA in z direction. Uncertainties shown for π , K and p spectra in different VOM multiplicity classes.

Appendix C

Systematic Uncertainties on Particle Spectra

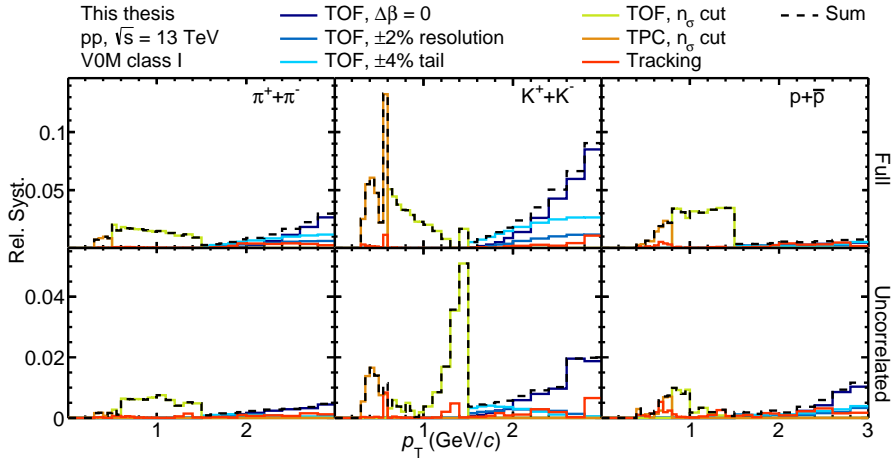


Figure C.1: Full (top panels) and multiplicity uncorrelated (bottom panels) systematic uncertainties for π , K and p in V0M multiplicity class I.

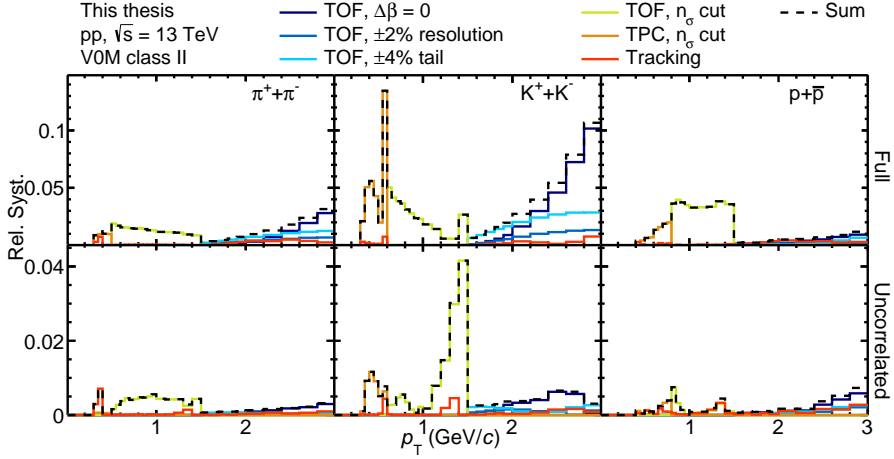


Figure C.2: Full (top panels) and multiplicity uncorrelated (bottom panels) systematic uncertainties for π , K and p in V0M multiplicity class II.

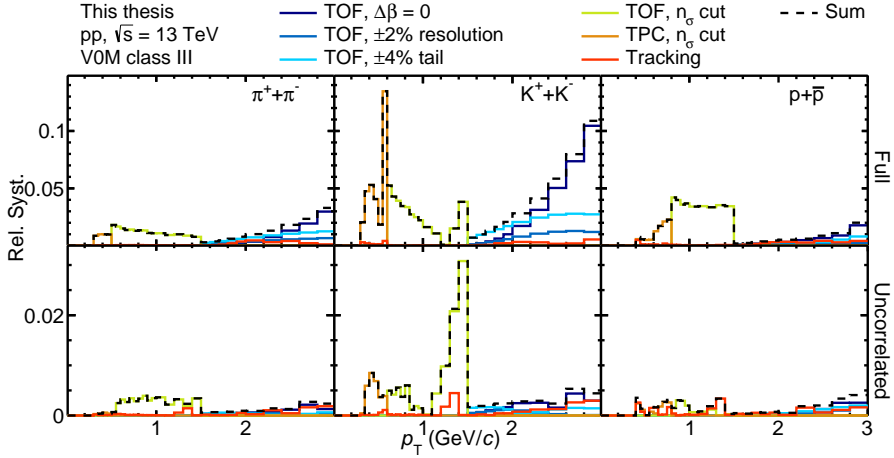


Figure C.3: Full (top panels) and multiplicity uncorrelated (bottom panels) systematic uncertainties for π , K and p in V0M multiplicity class III.

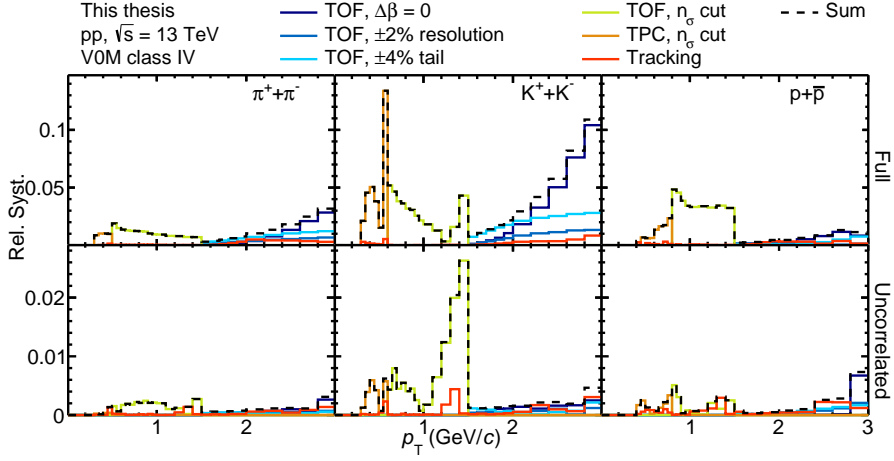


Figure C.4: Full (top panels) and multiplicity uncorrelated (bottom panels) systematic uncertainties for π , K and p in V0M multiplicity class IV.

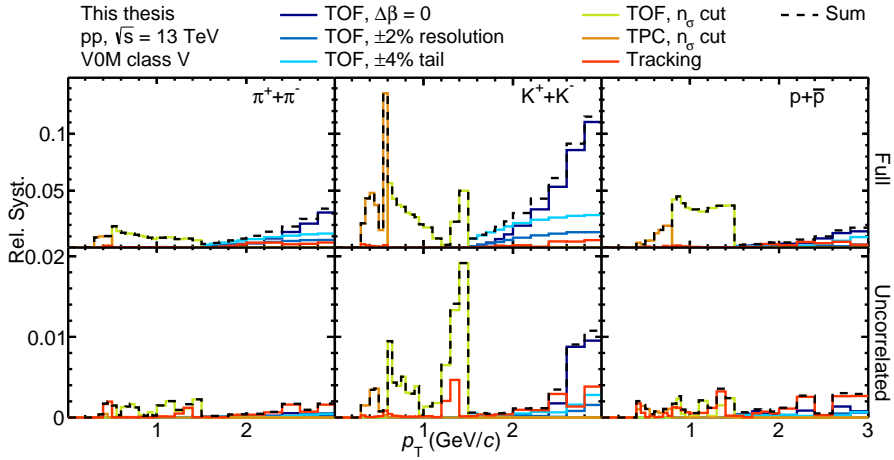


Figure C.5: Full (top panels) and multiplicity uncorrelated (bottom panels) systematic uncertainties for π , K and p in V0M multiplicity class V.

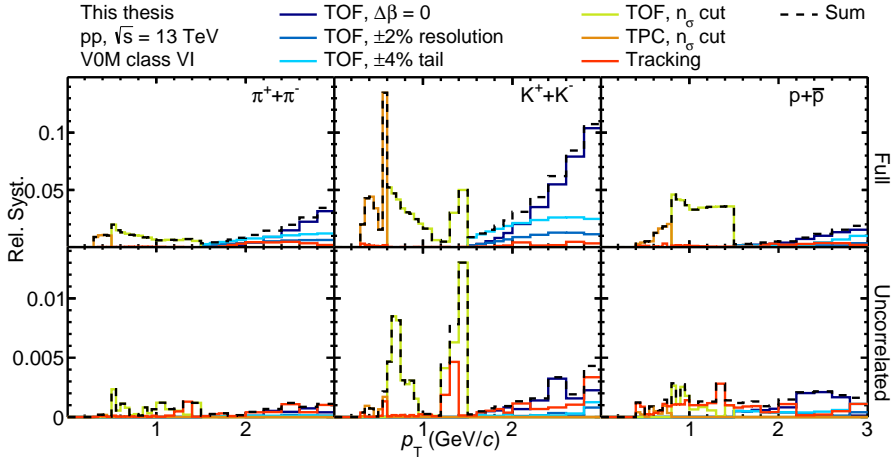


Figure C.6: Full (top panels) and multiplicity uncorrelated (bottom panels) systematic uncertainties for π , K and p in V0M multiplicity class VI.

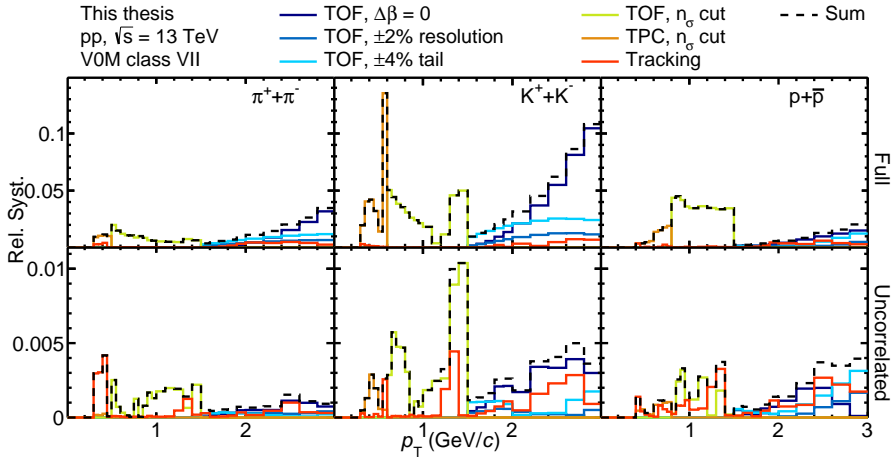


Figure C.7: Full (top panels) and multiplicity uncorrelated (bottom panels) systematic uncertainties for π , K and p in V0M multiplicity class VII.

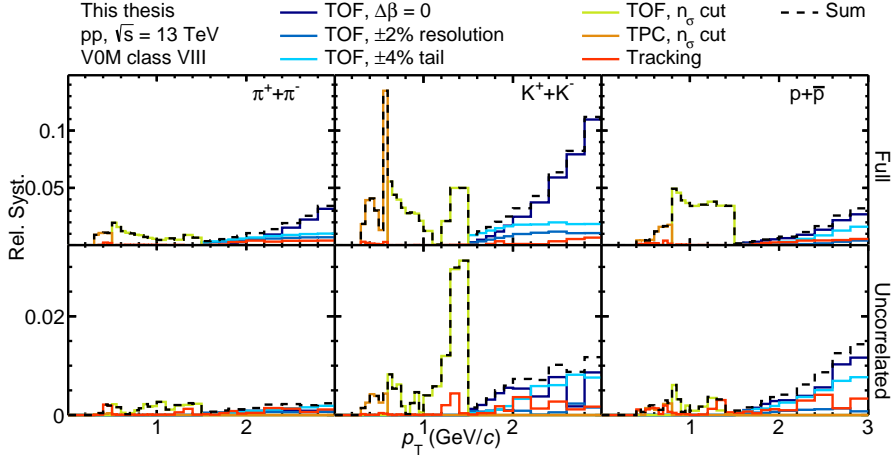


Figure C.8: Full (top panels) and multiplicity uncorrelated (bottom panels) systematic uncertainties for π , K and p in V0M multiplicity class VIII.

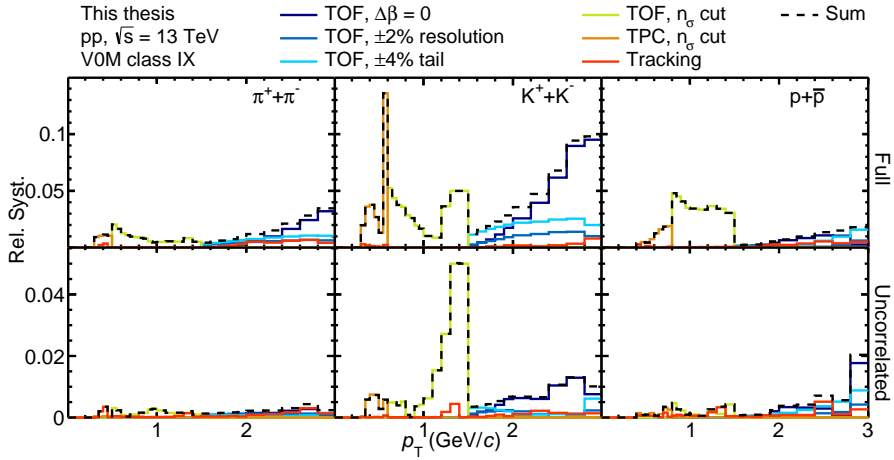


Figure C.9: Full (top panels) and multiplicity uncorrelated (bottom panels) systematic uncertainties for π , K and p in V0M multiplicity class IX.

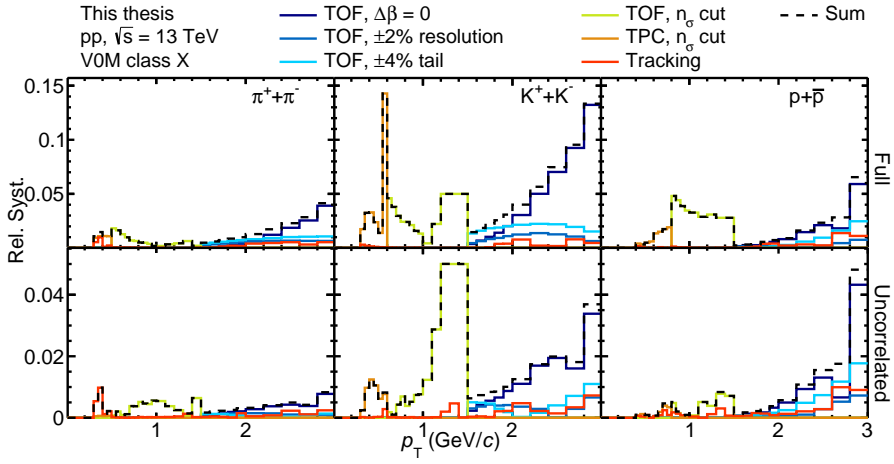


Figure C.10: Full (top panels) and multiplicity uncorrelated (bottom panels) systematic uncertainties for π , K and p in V0M multiplicity class X.

Appendix D

Blast Wave Fits in pp Collisions at $\sqrt{s} = 7$ TeV

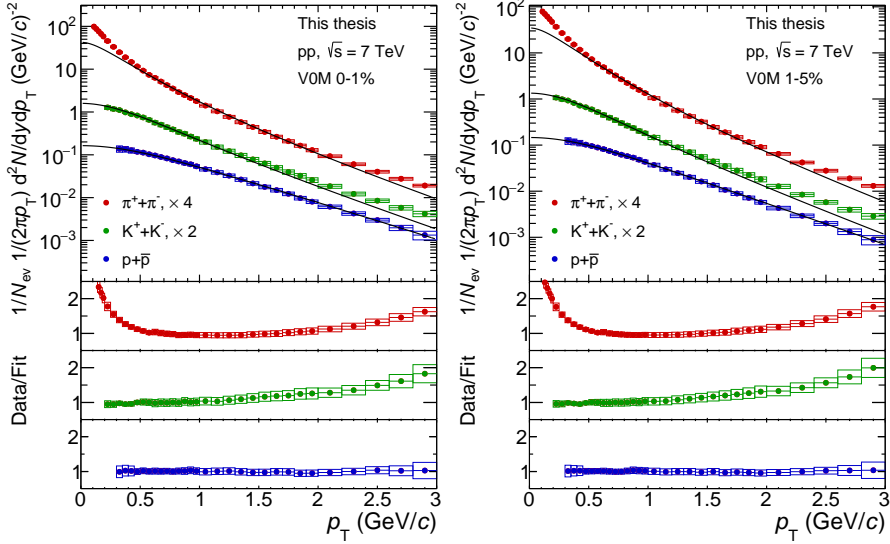


Figure D.1: Blast wave fits to π , K and p spectra measured in pp collisions at $\sqrt{s} = 7$ TeV. V0M classes I and II are shown.

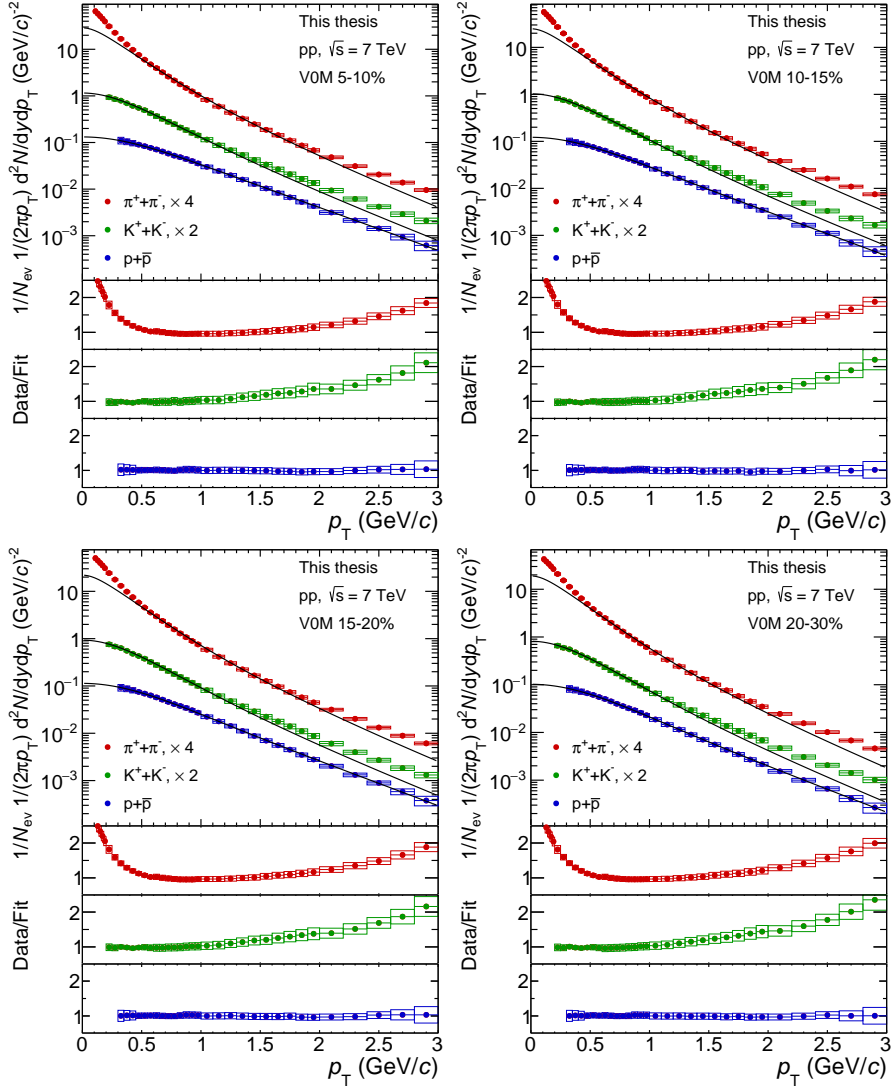


Figure D.2: Blast wave fits to π , K and p spectra measured in pp collisions at $\sqrt{s} = 7$ TeV. V0M classes III, IV, V and VI are shown.

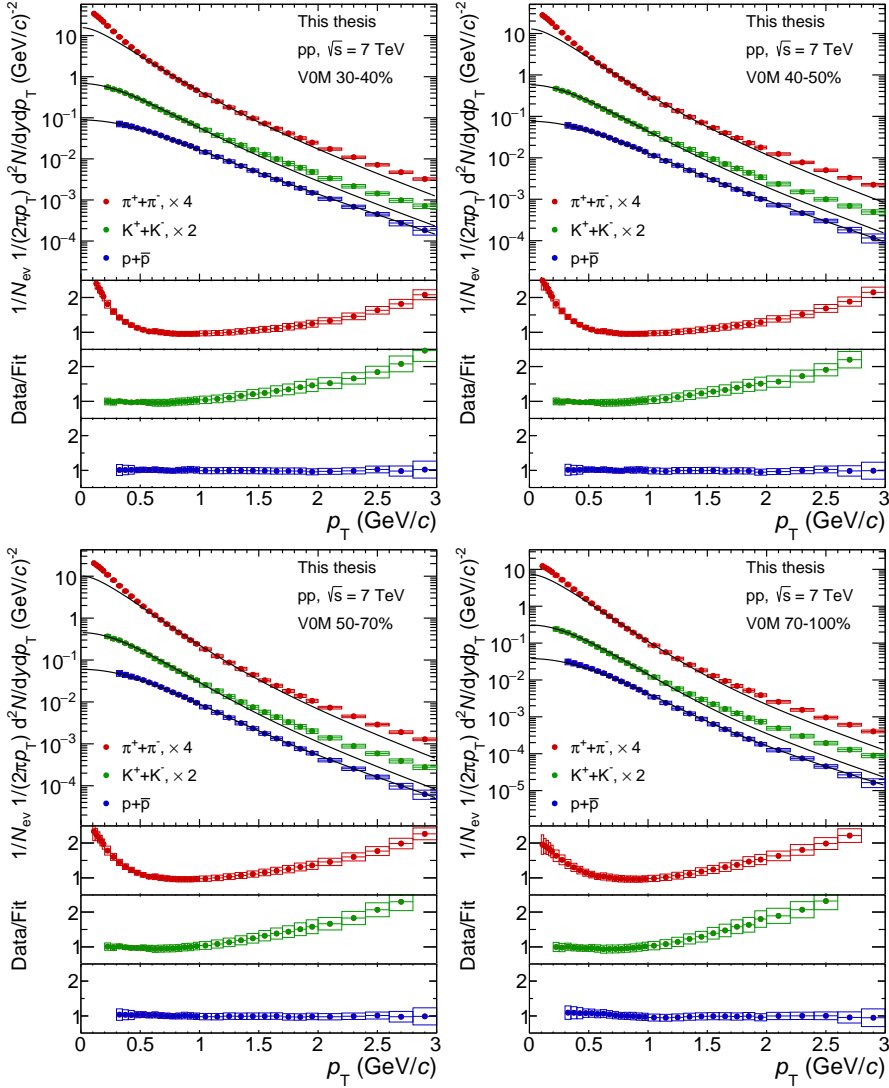


Figure D.3: Blast wave fits to π , K and p spectra measured in pp collisions at $\sqrt{s} = 7$ TeV. V0M classes VII, VIII, XI and X are shown.

Appendix E

Blast Wave Fits in pp Collisions at $\sqrt{s} = 13$ TeV

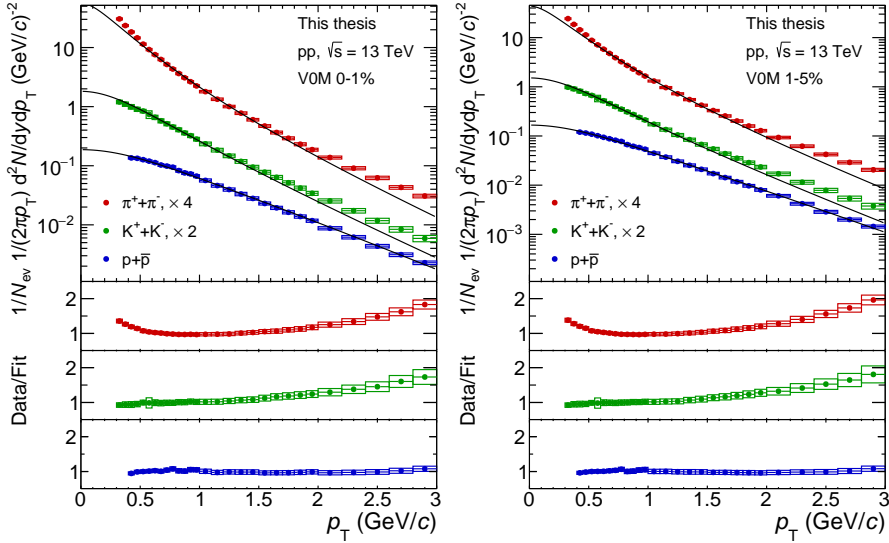


Figure E.1: Blast wave fits to π , K and p spectra measured in pp collisions at $\sqrt{s} = 13$ TeV. V0M classes I and II are shown.

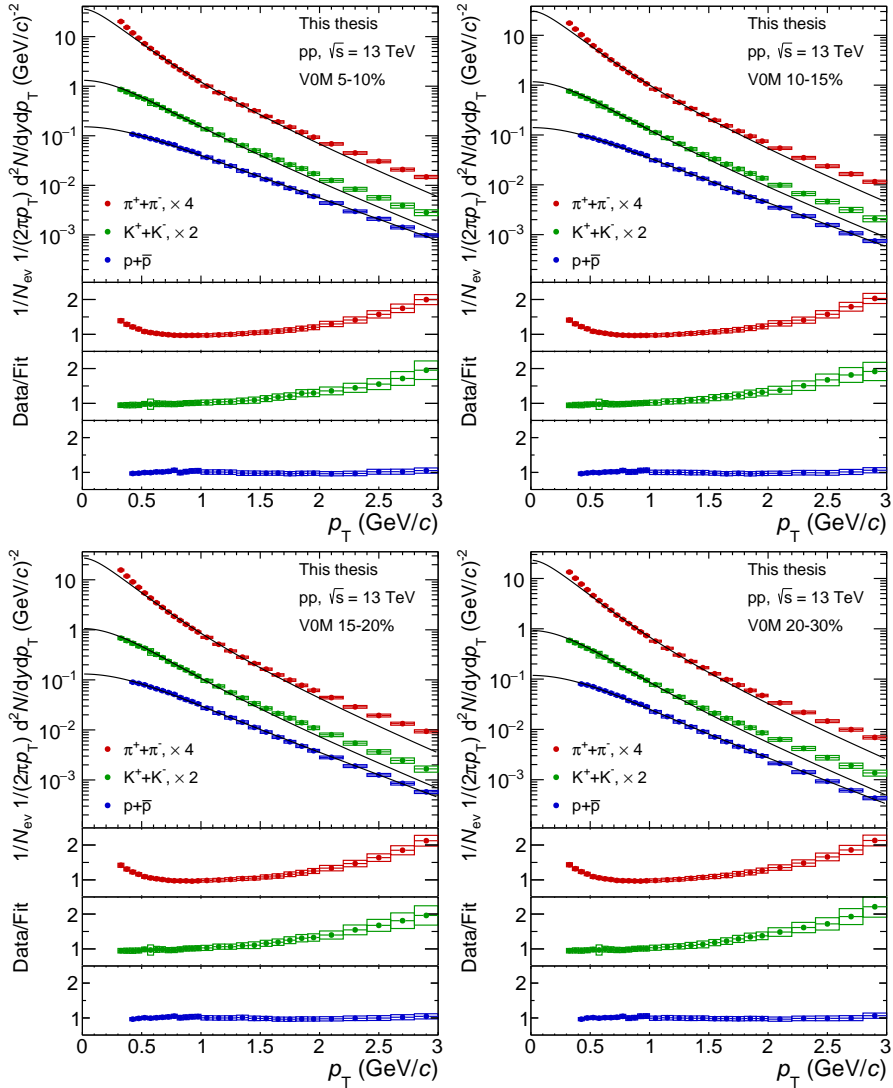


Figure E.2: Blast wave fits to π , K and p spectra measured in pp collisions at $\sqrt{s} = 13$ TeV. V0M classes III, IV, V and VI are shown.

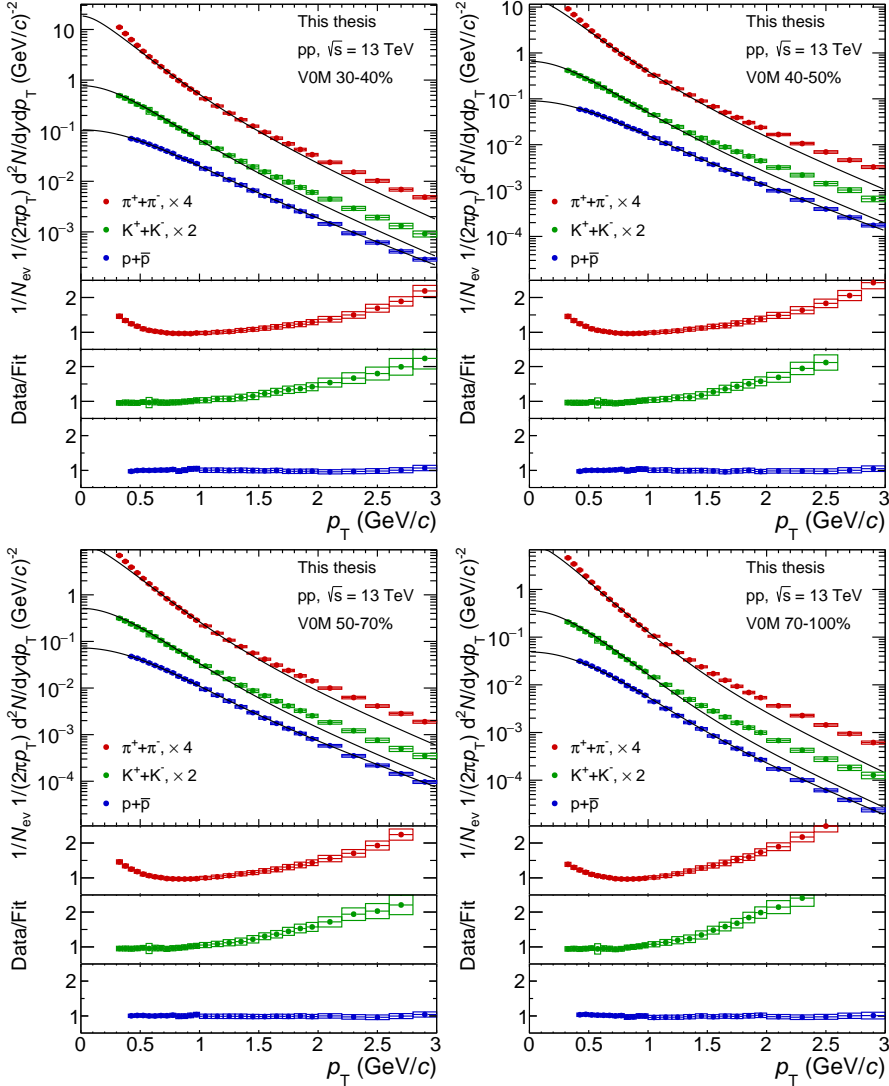


Figure E.3: Blast wave fits to π , K and p spectra measured in pp collisions at $\sqrt{s} = 13$ TeV. V0M classes VII, VIII, XI and X are shown.

